# Fundamentals and Applications of a Nanoconfined Electrochemical Reactor for Rapid Biosynthesis




**Lei Wan**

St John's College

Trinity Term 2021

A Thesis Submitted to the Board of the Faculty of Physical Sciences, for the Degree of Doctor of Philosophy

University of Oxford

© Lei Wan 2021

*Dedicated to My Parents.*

# Fundamentals and Applications of a Nanoconfined Electrochemical Reactor for Rapid Biosynthesis

Lei Wan, St John's College, University of Oxford

A thesis submitted for the Degree of Doctor of Philosophy, Trinity Term 2021

## Abstract

This thesis presents novel electrochemically driven enzyme-catalysed strategies which focus on fundamental studies and application by exploiting an established electrochemical nicotinamide cofactor recycling technology, the Electrochemical Leaf, taking it into new directions.

Inspired by nanoconfinement in Nature, in the Electrochemical Leaf, enzyme cascades are entrapped in high concentrations within the nanopores of an indium tin oxide electrode where they are driven and controlled with their rate being monitored in real time as electrical current. The key concept exploits the photosynthetic enzyme, ferredoxin-$NADP^+$ reductase (FNR) which rapidly interconverts electrons (supplied from a potentiostat) and hydride – stored on the nicotinamide cofactor, NADP(H). This activity is coupled to a second NADP(H)-dependent enzyme which recycles the cofactor back to FNR during its catalytic cycle to produce a desired product.

In this work, the 'Leaf' has been exploited to develop new 'green' strategies for redox biocatalysis (*e.g.* synthesis of an amine or an alcohol) by using either hydrogen to drive reductions, or $O_2$ in the air to drive oxidations, in each case linking the 'Leaf' to a platinised carbon electrode in a fuel cell set-up. The catalytic rate was continuously monitored through the current that flows between the two electrodes. Capitalising on the nanoconfinement and enantioselective nature of enzymes, high total turnover numbers were achieved and enantiomerically pure compounds were obtained.

Hypotheses were proposed by conducting systematic investigations into the thermodynamics, kinetics, stability and enantioselectivity of the enzyme nanoreactors

that are now emerging to be of considerable fundamental and practical significance. Three effects were found to be important: **(i)** the order of introducing FNR and E2 into the nanopores can lead to a difference in enzyme-limitation and ultimately rate determination; **(ii)** potential switch experiments were designed and used to relieve to product inhibition of the downstream E2 enzyme. The elegant convergence of timecourses when using ($S$)- and ($R$)-alcohols separately suggests that a deracemiser or racemiser might be operated using one electrode; **(iii)** the nanoconfined environment of the electrode led to a surprising result in which, unlike behaviour in dilute solution, the highly concentrated and nanoconfined enzyme system strongly favours the thermodynamic outcome, racemization. These reversible reactions occur rapidly and independently of FNR, which directly results in an acceleration of homogeneous racemisation, counteracting the enantioselective nature of E2.

Building on these results, a unique two-stage electrochemically driven deracemisation technology scheme using two enantio-complementary enantioselective alcohol dehydrogenase enzymes was proposed and successfully implemented. Enantioselective oxidation and reduction reactions were conducted sequentially on a racemic mixture of enantiopure secondary alcohols, leading to >90% enantiomeric excess in both ($R$) and ($S$).

# Collaborations

Early batches of the W110A variant of the secondary alcohol dehydrogenase from *Thermoanerobacter ethanolicus* 39E were purified and provided by Professor Nicholas J. Turner's group at the University of Manchester. In the same group, Dr Rachel S. Heath provided the plasmids encoding W110A, W110G and W110V variants of the same enzyme such that purification procedure can be carried out in Oxford later. She also analysed the chirality of samples in this thesis.

Dr Clare F. Megarity and Adam J. Sills (a part II student) within the Armstrong Group generously assisted with some electrochemical experiments. Dr Clare F. Megarity also cloned the genes and prepared the plasmids encoding ferredoxin $NADP^+$ reductase from *Chlamydomonas reinhardtii* and secondary alcohol dehydrogenase from *Lactobacillus kefir*.

# Acknowledgements

First, I want to thank Fraser for his professional supervision, constructive suggestions, insightful thinking, continuous support and encouragement in my path to pursue the D.Phil. degree. I feel really happy and lucky to undertake these stimulating, challenging, and first-rate projects in his group.

Special thanks to Dr. Clare F. Megarity and Dr. Bhavin Siritanaratkul who co-supervised me, proof read the thesis and tutored me the subjects that I was not familiar with before, *e.g.* the protein film electrochemistry, fuel cell set-up, molecular biology, and protein purification, to name a few. They both are erudite, considerate and helpful scientists. I would like to say that many years from now on, I might forget the details when I was working with them, but I would definitely not forget Bhavin's interesting self declaration: 'I am the best person of Armstrong Group!' and Clare's mantra-like saying 'My body is a real temple!'

Thanks to the kind colleagues in the Armstrong Group: Liyun, Non, Elena, Stephen, Tania, Adam, Sarah, Ros, Ryan, Giorgio and Beichen for their extra professional advice and daily talking. Some credits to Beichen and buddies in the Vincent Group as my loyal meal partners.

I would like to say thanks to: staff in the ICL for their routine maintenance of this building, Terri for the beautiful customised electrochemical cells, Dr. Rachel S. Heath and Professor Nicholas J. Turner at the Manchester University for the wonderful collaboration which is an integral part of my D.Phil. studies, China Scholarship Council for the funding, St John's College for providing me grant and support, especially the financial support during Covid, Great Britain-China Educational Trust for the student award.

Finally, the deepest appreciation to my parents. It is their unwavering and

unconditional love, encouragement, spiritual and financial support that I could manage to go through the happiness, hardships, setbacks during during my studies. This is a thesis for them.

# Symbols and Abbreviations

| | |
|---|---|
| A | ampere (SI base unit) |
| Å | angstrom (one Å= $10^{-10}$ m) |
| ADH | alcohol dehydrogenase |
| ADP | adenosine diphosphate |
| Ar | argon |
| ATP | adenosine triphosphate |
| a.u. | arbitrary units |
| BSA | bovine serum albumin |
| bpy | $2,2'$-bipyridine |
| C | coulomb (one C = one s $\cdot$ A) |
| $c$ | concentration |
| °C | degrees centigrade |
| CA | chronoamperometry/chronoamperogram |
| Cd | cadmium |
| CE | counter electrode |
| CHES | N-Cyclohexyl-2-aminoethanesulfonic acid |
| cp* | $C_5Me_5$ (pentamethylcyclopentadienyl) |
| CV | cyclic voltammetry/voltammogram |
| $D$ | diffusion coefficient |
| Da | Dalton (one Dalton = $1.660 \times 10^{-27}$kg) |
| $\delta$ | chemical shift |
| DTT | dithiothreitol |
| E | enzyme |
| *E. coli.* | *Escherichia coli* |

| | |
|---|---|
| ee | enantiomeric excess |
| E2 | second (downstream) enzyme |
| F | Faraday constant = 96485 C $mol^{-1}$ |
| FAD | flavin adenine dinucleotide |
| Fd | ferredoxin |
| FDA | Food and Drug Administration |
| FNR | ferredoxin-$NADP^+$ reductase |
| G | Gibbs free energy |
| GC | gas chromatography |
| GC-FID | gas chromatography with flame-ionisation detection |
| GLDH | L-glutamate dehydrogenase |
| G3P | glyceraldehyde 3-phosphate |
| G6PDH | glucose-6-phosphate dehydrogenase |
| HEPES | 4-(2-hydroxyethyl)-1-piperazineethanesulfonic acid |
| HER | hydrogen evolution reaction |
| HLADH | ADH from horse liver |
| HOR | hydrogen oxidation reaction |
| *i, I* | current |
| IPTG | $\beta$-D-1-thiogalactopyranoside |
| ITO | indium tin oxide |
| J | joule (one joule = 1 kg $m^2$ $s^{-2}$) |
| K | kelvin (SI base unit) |
| $k_{cat}$ | turnover number |
| $K_m$ | Michaelis constant |
| $K_i$ | inhibition constant |
| LB | Luria-Bertani |
| LIC | ligation independent cloning |
| LK | *Lactobacillus kefir* |
| L-Glu | L-glutamate |

| | |
|---|---|
| L-LDH | L-lactate dehydrogenase |
| MES | 2-(N-morpholino)ethanesulfonic acid |
| MFC | mass flow controller |
| mole | amount of substance (SI base unit) |
| MOPS | 3-(N-morpholino)propanesulfonic acid |
| MV | methyl viologen |
| $\nu$ | scan rate |
| $NAD^+$/NADH | nicotinamide adenine dinucleotide |
| $NADP^+$/NADPH | nicotinamide adenine dinucleotide phosphate |
| NMR | nuclear magnetic resonance |
| OCP | open-circuit potential |
| OD | optical density |
| OER | oxygen evolution reaction |
| ORR | oxygen oxidation reaction |
| PCP | platinised carbon electrode |
| PCR | polymerase chain reaction |
| PEM | proton exchange membrane |
| PFE | protein film electrochemistry |
| PGE | pyrolytic graphite edge |
| $P_i$ | phosphate ions |
| PTDH | phosphite dehydrogenase |
| *pri*-ADH | primary alcohol dehydrogenase |
| Pt | platinum |
| $q$, $Q$ | quantity of charges |
| QD | quantum dot |
| R | gas constant = 8.315 J $mol^{-1}$ $K^{-1}$ |
| RE | reference electrode |
| Rh | rhodium |
| RHE | reversible hydrogen electrode |

| | |
|---|---|
| rpm | rotation per minute |
| Ru | ruthenium |
| RuBisCO | ribulose-1,5-bisphosphatecarboxylase |
| RuBP | ribulose-1,5-bisphosphate |
| *sec*-ADH | secondary alcohol dehydrogenase |
| SCE | saturated calomel electrode |
| SEP | standard electrode potential |
| SHE | standard hydrogen electrode |
| TAPS | [tris(hydroxymethyl)methylamino]propanesulfonic acid |
| TbSADH | *sec*-ADH from *Thermoanaerobium brockii* |
| TeSADH | *sec*-ADH from the *Thermoanerobacter ethanolicus* 39E |
| Ti | titanium |
| TMSP | (Trimethylsilyl)propionic-2,2,3,3-$d_4$ acid |
| TOF | turnover frequency |
| TON | turnover number |
| Tris | tris(hydroxymethyl)aminomethane |
| TTN | total turnover number |
| U | unit |
| V | volt, cell voltage |
| $v$ | reaction rate |
| $v_{max}$ | maximum reaction rate |
| UV-Vis | ultraviolet–visible |
| WE | working electrode |
| Zn | zinc |
| 2-OG | 2-oxoglutarate |
| 3-PGA | glyceraldehyde 3-phosphate |
| 4P2B | 4-phenyl-2-butanol |

# Publications

1. **L. Wan**, R. S. Heath, C. F. Megarity, A. J. Sills, R. H. Herold, N. J. Turner, and F. A. Armstrong., 'Exploiting Bidirectional Electrocatalysis by a Nanoconfined Enzyme Cascade to Drive and Control Enantioselective Reactions', *ACS Catalysis*, **2021**, *11*, 6526–6533.

2. **L. Wan**, C. F. Megarity, B. Siritanaratkul, and F. A. Armstrong., 'A Hydrogen 'Fuel Cell' for Rapid, Enzyme-Catalysed Organic Synthesis with Continuous Monitoring', *Chem. Commun.*, **2018**, *54*, 972–975.

3. **L. Wan**, R. S. Heath, B. Siritanaratkul, C. F. Megarity, A. J. Sills, M. P. Thompson, N. J. Turner, and F. A. Armstrong., 'Enzyme-Catalysed Enantioselective Oxidation of Alcohols by Air Exploiting Fast Electrochemical Nicotinamide Cycling in Electrode Nanopores', *Green Chem.*, **2019**, *21*, 4958–4963.

4. C. F. Megarity, B. Siritanaratkul, R. S. Heath, **L. Wan**, G. Morello, S. R. FitzPatrick, R. L. Booth, A. J. Sills, A. W. Robertson, J. H. Warner, N. J. Turner, and F. A. Armstrong., 'Electrocatalytic Volleyball: Rapid Nanoconfined Nicotinamide Cycling for Organic Synthesis in Electrode Pores', *Angew. Chem. Int. Ed.*, **2019**, *58*, 4948–4952.

5. B. Cheng, **L. Wan**, and F. A. Armstrong., 'Progress in Scaling up and Streamlining a Nanoconfined, Enzyme-catalysed Electrochemical Nicotinamide Recycling System for Biocatalytic Synthesis', *ChemElectroChem*, **2020**, *7*, 4672–4678.

6. C. F. Megarity, B. Siritanaratkul, B. Cheng, G. Morello, **L. Wan**, A. J. Sills, R. S. Heath, N. J. Turner and F. A. Armstrong., 'Electrified Nanoconfined Biocatalysis with Rapid Cofactor Recycling', *ChemCatChem*, **2019**, *11*, 5662–5670.

# Contents

**Abstract** i

**Collaborations** iii

**Acknowledgements** v

**Symbols and Abbreviations** vii

**Publications** xi

**1 Introduction** 1

Abstract . . . 2

1.1 Enzyme-catalysed Reactions . . . 4

1.2 The Nicotinamide Cofactor NAD(P)(H) . . . 5

1.3 Typical NAD(P)(H) Regeneration Methods . . . 7

1.3.1 Enzymatic . . . 9

1.3.1.1 Reduced Form . . . 9

1.3.1.2 Oxidised Form . . . 11

1.3.2 Chemical . . . 12

1.3.2.1 Direct Redox Reaction . . . 12

1.3.2.2 Organometallic Approach . . . 13

1.3.3 Electrochemical . . . 15

1.3.3.1 Direct Electrochemical . . . 17

1.3.3.2 Indirect Electrochemical . . . 19

1.3.3.3 Direct Electroenzymatic . . . 19

1.3.3.4 Indirect Electroenzymatic . . . 20

1.3.4 Photochemical Methods . . . 21

1.3.4.1 Inorganic Photosensitiser . . . . . 21
1.3.4.2 Organic Photosensitiser . . . . . 23
1.3.5 Other Methods . . . . . 25
1.4 Photosynthesis . . . . . 27
1.4.1 Light-dependent Reactions . . . . . 27
1.4.2 Light-independent Reactions . . . . . 28
1.5 Micro- and Nano-confinement in the Natural Leaf . . . . . 29
1.6 Ferredoxin $NADP^+$-reductase (FNR) . . . . . 30
1.6.1 Flavoenzymes . . . . . 30
1.6.2 Structures and Mechanisms of FNR . . . . . 31
1.7 The Electrochemical Leaf . . . . . 34
1.7.1 Protein Film Electrochemistry (PFE) . . . . . 34
1.7.2 Different Electron Transfer Modes of FNR-catalysed Electrochemistry . . . . . 36
1.7.3 Principle of the Electrochemical Leaf . . . . . 38
1.7.4 Electrochemistry of Electrochemical Leaf . . . . . 42
1.7.4.1 Methods of Loading Enzymes . . . . . 42
1.7.4.2 Non-turnover Signals of FNR . . . . . 43
1.7.4.3 Interconversion of $NADP^+$/NADPH catalysed by FNR 45
1.7.4.4 FNR Catalysis Coupled to a Second Enzyme . . . . 48
1.7.5 Proof of Nanoconfinement . . . . . 53
1.8 Conclusion and Perspectives . . . . . 55

**2 A $H_2$-driven Fuel Cell Scheme for NADPH Regeneration 59**

Abstract . . . . . 60
2.1 Introduction: FNR-Catalysed Biosynthetic Fuel Cell . . . . . 61
2.1.1 Enzymatic Fuel Cells . . . . . 61
2.1.2 A Biosynthetic Fuel Cell using FNR and Dehydrogenases . . . 64
2.2 The Fuel cell Anode: $H_2O/H_2$ Catalysed by a Platinised Carbon Electrode . . . . . 66

2.3 Driving force for the $H_2$-driven Electrochemical Leaf . . . . . 67
2.4 Continuously Monitored $H_2$-driven NADPH Regeneration . . . . . 70
2.4.1 Exploitation of the Two-Electrode System . . . . . 70
2.4.2 $H_2$-driven, FNR-catalysed $NADP^+$ Reduction . . . . . 72
2.4.3 The Set-up for the $H_2$-driven Coupled Reaction . . . . . 74
2.4.4 Bovine L-glutamate Dehydrogenase (GLDH) . . . . . 76
2.4.4.1 Properties of GLDH . . . . . 76
2.4.4.2 NADPH Regeneration Coupled to GLDH Catalysis: Monitored by Cyclic Voltammetry . . . . . 77
2.4.5 $H_2$-driven Reductive Amination Coupled to NADP(H) Regeneration . . . . . 78
2.4.5.1 $NADP^+$ Titration for the $H_2$-driven Coupled System 78
2.4.6 The $H_2$-driven Coupled System under Different Conditions . . 81
2.5 Conclusions and Perspectives . . . . . 88

**3 An Air-driven Fuel Cell Scheme for $NADP^+$ Regeneration 89**

Abstract . . . . . 90
3.1 Introduction . . . . . 91
3.2 $O_2$ Reduction Catalysed by a Platinum Carbon Paper Electrode . . . 92
3.3 Secondary Alcohol Dehydrogenase TeSADH W110A . . . . . 93
3.3.1 Wildtype TeSADH . . . . . 93
3.3.2 TeSADH W110A Variant . . . . . 94
3.4 $NADP^+$ Regeneration Coupled to TeSADH W110A Catalysis: Monitored by Cyclic Voltammetry . . . . . 95
3.4.1 Measurements Using Various Substrates . . . . . 95
3.4.2 pH Selection for Alcohol Oxidation . . . . . 97
3.5 Driving Force for the Air-driven Cell Reaction . . . . . 99
3.6 Continuously Monitored Air-driven $NADP^+$ Regeneration . . . . . 100
3.6.1 The set-up for the Air-driven Fuel Cell Scheme . . . . . 100

3.6.2 Air-driven Enantioselective Alcohol Oxidation Coupled to $NADP^+$ Regeneration . . . 103
3.7 Feasibility of Switch between $H_2$-Driven and Air-driven Modes . . . 111
3.8 Conclusions and Perspectives . . . 113

**4 Racemisation & Kinetics Studies 115**

Abstract . . . 116
4.1 Introduction: Enantioselectivity of *sec*-ADH . . . 117
4.2 Hints from Previous Electrochemical Data . . . 123
4.2.1 Disagreement between Electrochemical Results and Kinetics Data . . . 123
4.2.2 Hypotheses Based on the Electrochemical Results and Kinetics Data of TeSADH W110A . . . 124
4.2.2.1 Racemisation . . . 124
4.2.2.2 ADH-limited and FNR-limited Scenarios . . . 125
4.3 Studies on Rate-limiting Enzyme Ratios . . . 127
4.3.1 ADH- to FNR-limited Electrodes . . . 127
4.3.2 FNR- to ADH-limited Electrodes . . . 132
4.4 Spontaneous Racemisation in the Bulk Solution . . . 134
4.5 Square-wave Potential Inversion Measurements . . . 138
4.6 Coloading of Enzymes in Different Ratios . . . 144
4.7 Titration of NADPH Using Rotating Electrodes . . . 148
4.7.1 Uncoupled NADPH Oxidation Catalysed by FNR . . . 148
4.7.2 NADPH Titration Coupled to the Oxidation of Alcohol . . . 153
4.8 Conclusion . . . 158

**5 Electrochemical Deracemisation of Secondary Alcohols 161**

Abstract . . . 162
5.1 Introduction . . . 163
5.2 Electrochemical Deracemisation to Produce (*R*)-4P2B . . . 169

5.2.1 The Two-stage Scheme to Produce (*R*)-4P2B . . . . . 169
5.2.2 (*S*)-selective Alcohol Oxidation and (*R*)-selective Ketone Reduction . . . . . 171
5.2.3 Two-stage Experiments to Produce (*R*)-4P2B . . . . . 175
5.3 Electrochemical Deracemisation to Produce (*S*)-4P2B . . . . . 179
5.3.1 The Two-stage Scheme to Produce (*S*)-4P2B . . . . . 179
5.3.2 (*R*)-selective Alcohol Oxidation and (*S*)-selective Ketone Reduction . . . . . 179
5.3.3 Two-stage Experiment to Produce (*S*)-4P2B . . . . . 185
5.4 Conclusion and Perspectives . . . . . 187

**6 Theories and Experimental Methods 189**

Abstract . . . . . 190
6.1 Electrochemical Fundamentals and Techniques . . . . . 191
6.1.1 Basic Concepts . . . . . 191
6.1.1.1 Electrode . . . . . 191
6.1.1.2 Electrode Processes . . . . . 192
6.1.1.3 Electrochemical Cell . . . . . 192
6.1.1.4 Electrode Potential . . . . . 193
6.1.1.5 The Set-up for Dynamic Electrochemistry . . . . . 195
6.1.2 Cyclic Voltammetry . . . . . 197
6.1.2.1 Non-Faradaic Current . . . . . 197
6.1.2.2 Faradaic Current I: Non-Turnover Signal . . . . . 198
6.1.2.3 Faradaic Current II: Catalytic Current . . . . . 199
6.1.2.4 Faradaic Current III: Coupled Reaction . . . . . 202
6.1.3 Chronoamperometry . . . . . 204
6.1.4 Hydrodynamic Electrodes . . . . . 206
6.2 Enzyme . . . . . 206
6.2.1 Enzyme Preparation and Purification . . . . . 206
6.2.1.1 Ferredoxin-NADP$^+$ reductase (FNR) . . . . . 206

6.2.1.2 TeSADH W110A, W110G and W110V . . . . . 207
6.2.1.3 The Secondary Alcohol Dehydrogenase L. Kefir. . . . 209
6.2.1.4 L-Glutamate Dehydrogenase (GLDH) . . . . . 210
6.2.2 Determination of Enzyme Concentration . . . . . 210
6.2.3 Enzyme Kinetics . . . . . 211
6.2.3.1 Michaelis-Menten Kinetics . . . . . 211
6.3 Experimental Methods and Materials . . . . . 212
6.3.1 Electrochemical Measurements . . . . . 212
6.3.2 Electrode Fabrication . . . . . 213
6.3.2.1 The (FNR + E2)@ITO/support Electrode . . . . . 213
6.3.2.2 The Platinised Carbon Electrode . . . . . 214
6.3.3 Analytical Methods . . . . . 214
6.3.3.1 UV-Vis Spectroscopy . . . . . 214
6.3.3.2 Nuclear Magnetic Resonance . . . . . 215
6.3.3.3 GC-FID analysis . . . . . 216
6.3.4 Buffer Solution . . . . . 216
6.3.4.1 Borate and Phosphate Buffer . . . . . 216
6.3.4.2 Good's Buffers . . . . . 217

**References** **219**

**Appendix** **243**

A Derivation of Nernst Equation . . . . . 244
B Quantification of Non-Turnover Signal . . . . . 245
C Derivation of Michaelis-Menten Equation . . . . . 247

# Chapter 1

# Introduction

## Abstract

Biocatalysis refers to a process in which chemical reactions are catalysed by the use of living systems or their components. Enzymes are the proteins that act as biological catalysts and oxidoreductases are one of the largest classes of enzymes (approx. 25% of the total) which catalyse the transfer of electrons from the reactant to the product. Coenzymes are usually required for oxidoreductase-catalysed reactions and the nicotinamide cofactors NAD(P)(H) – the natural hydride carriers and also the biological equivalent of $NaBH_4$ or $LiAlH_4$ – are among the most important kinds. The extremely high cost of nicotinamide cofactors, especially the **phosphorylated type NADP(H)**, has made their stoichiometric use impractical and partially results in the situation that the development of the overall NAD(P)(H)-dependent biosynthesis schemes largely lags behind that of cofactor-independent versions.

This chapter first presents a brief introduction to enzyme-catalysed reactions and the nicotinamide cofactor NAD(P)(H). This is followed by a review of previous studies that reported recycling methods of these nicotinamide coenzymes. Mechanisms, advantages, and disadvantages in terms of yield, cost, protocol, efficiency and so on are all discussed to present a rough overview of this field.

The Electrochemical Leaf which is inspired by the biological leaf is then systematically introduced. This technology was developed in the Armstrong group in 2017 and it is a nicotinamide cofactor recycling technology but has become much more than that and is now also considered to be an investigative tool in which the activity of enzymes which are not electroactive themselves can now be visualised using electrochemistry *via* the transducer, ferredoxin $NADP^+$-reductase (FNR).

An important reason why biosystems are so efficient in terms of enzyme-catalysed reactions and cascades is that the space where reactions occur is limited to three-dimensional micro- or nano-confined zones. Exemplary cases of nanoconfinement in nature include chloroplasts and mitochondria in living cells. Photosynthesis which converts solar energy to storable chemical energy thus fuelling living body's biological

activities, is the most important chemical process in the world. It consists of the light-dependent and the light-independent reactions and occurs in the nanozones ($<$ 100 nm diameters) of chloroplasts.[1] The FNR is an integral part of the light-dependent reactions of photosynthesis where it catalyses the regeneration of NADPH that provides reducing power for $CO_2$ fixation during of the Calvin Cycle. Due to the quasi-reversible nature of the FNR-catalysed interconversion between $NADP^+$ and NADPH, this enzyme was key to the development of derived applications of the Electrochemical Leaf.

The Leaf used in this thesis mimics the nanoconfinement of biological leaf by entrapping FNR and other NADP(H)-dependent enzymes within the nanopores which form naturally between particles of conductive indium tin oxide that have been electrophoretically deposited on a conductive electrode support. Just as in the chloroplast, this nanoconfinement of enzymes and reactants led to them being highly concentrated locally and the intersite distances over which reactants have to travel being tiny, leading to the same massive enhancement in rate as that which occurs in nature. Previously published work on the Electrochemical Leaf including the proof of nanoconfinement and other relevant electrochemical results that showcase the Leaf are also presented.

The chapters to follow this introduction present the different ways in which my work has exploited the power of this technology, the Electrochemical Leaf: in a fuel cell configuration, driven by $H_2$ and then air and in deracemisation studies which have led to the development of novel deracemising and racemising strategies.

## 1.1 Enzyme-catalysed Reactions

The value of biocatalysis has been increasingly recognised in academia and food, energy, chemical and pharmaceutical industries.[2–8] Value-added compounds can be synthesised under mild conditions with the help of enzymes – the biocatalysts that can massively speed up chemical reactions with great chemo-, regio-, stereo-, and enantio-selectivity. In short, the unique features of enzymes in stark contrast to their inorganic or organic equivalents can be summed up as:

- **Substrate specificity:** In most cases, a class of enzymes are only active on a group of specific reactions.[9–11] For instance, the primary alcohol dehydrogenase (*pri*-ADH) is active on the dehydrogenation of a primary alcohol to produce an aldehyde and its reverse reaction. However, *pri*-ADH is much less active on a secondary alcohol or ketone.

- **Enantioselectivity:** Because enzymes are themselves chiral molecules, they are therefore sensitive to the chirality of their substrates.[12, 13] This is the property that leads to many enzymes (not all) being highly enantioselective. When the substrate of enzymes is comprised by a mixture of two enantiomerically pure compounds (racemate), the enzyme is much more active on one enantiomer, leaving the other enantiomer largely unreacted.

- **High efficiency:** Enzymes are the catalysts in living systems that have been evolving for hundreds of millions of years. The rate of reactions catalysed by enzymes is orders of magnitude faster than those without enzymes.[14, 15]

- **Mild reaction conditions:** Enzyme-catalysed reactions usually occur under mild temperature and pressure. Enzymes work in aqueous conditions. This is in contrast to many catalysts used in organic chemistry which must be used in organic solvent.

- **Complex reaction mechanism:** The rate equations for enzyme-catalysed reactions are usually complex.[16] The reaction rate is highly sensitive to acidity,

and ion strength.[17–19] Some enzymes are unstable.[20] These all complicate attempts to study catalytic mechanism, electronic structure, and geometries of enzymes.

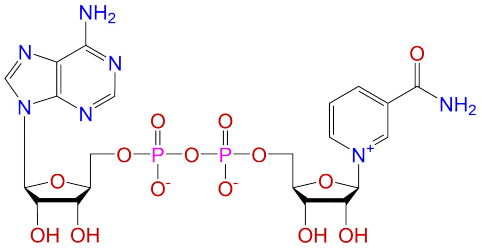
Some of these features are highly valued, particularly the pharmaceutical industry, as enzyme-catalysed synthesis of chiral products have accounted for two-thirds of commercialised new pharmaceuticals and this ratio is expected to increase further.[21, 22]

## 1.2 The Nicotinamide Cofactor NAD(P)(H)

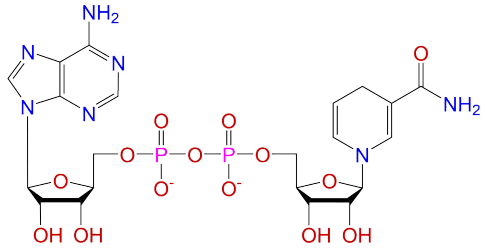
The oxidoreductases represent a large class of enzymes and act as catalysts in redox biochemical reactions by lowering the activation energy that is required. Cofactors are essential participants in many oxidoreductase-catalysed reactions. While some cofactors are self-regenerating, *e.g.* pyridoxal phosphate (vitamin $B_6$) and thiamine pyrophosphate (a derivative of vitamin $B_1$). Others are basically co-substrates that donate or accept functional groups, *e.g.* hydride or phosphate, to/from the substrate in a reaction.

The (reduced) nicotinamide adenine dinucleotide (NAD(H)) and (reduced) nicotinamide adenine dinucleotide phosphate (NADP(H)) are two important cofactors which are the hydride carriers in nature. In enzyme-catalysed reactions, they serve as the 'redox currency' *via* mediating two-electron transfer between substrates and products. Unlike the enzyme-bound cofactors like flavin adenine dinucleotide (FAD) or flavin mononucleotide (FMN), NAD(H) and NADP(H) are freely dissociated in the aqueous phase. Figure 1.1 shows the molecular structures of both cofactors, from which one can clearly distinguish their structural differences. NADP(H) is the phosphorylated version of NAD(H) where an extra phosphate group is attached to the $2'$ position of the ribose moiety. While these two cofactors share almost identical properties regarding thermodynamics and reaction mechanisms, in terms of physiological function, mostly NAD(H) is involved in catabolism (electron transfer linked to $O_2$ in respiration) and NADP(H) plays role in anabolism (electron transfer linked

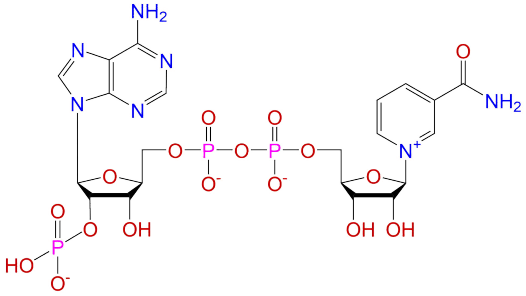
to biosynthesis).[23, 24] Also, customarily, although the oxidised form NAD(P)$^+$ is written with a superscript plus sign '+' owing to a positive charge carried by the nitrogen atom of the pyridine ring of the nicotinamide, in effect, they are charged anions at physiological pH. Their corresponding reduced forms NAD(P)H accordingly hold more negative charges due to the abstraction of a hydride.[25]



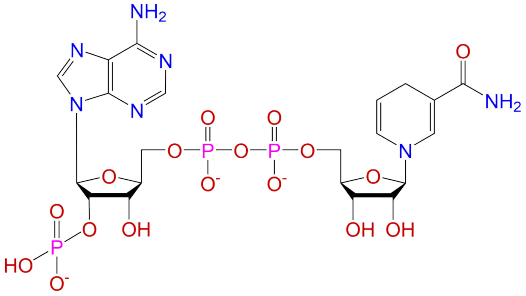
**(a)** Molecular structure of NAD$^+$.



**(b)** Molecular structure of NADH.



**(c)** Molecular structure of NADP$^+$.



**(d)** Molecular structure of NADPH.

**Figure 1.1** Molecular structures of the nicotinamide cofactor NAD(P)(H).

NAD(P)(H) is involved in hundreds of biochemical reactions, many of which are extraordinarily profitable in the pharmaceutical industry. The reduced forms are essential for a far-ranging group of reactions, *e.g.* reduction reactions catalysed by dehydrogenases and oxidation reactions like hydroxylation-, epoxidation-, or hetero atom oxidation-reactions catalysed by monooxygenases.[26] On the other hand, the oxidised forms are mainly used in dehydrogenase-catalysed oxidation of alcohols, aldehydes, amines and so on.[26] Table 1.1 shows the current cost of NAD(P)(H). It is clear that the stoichiometric supply of cofactors is unaffordable, which necessitates the need to find an efficient, clean and inexpensive method to regenerate NAD(P)(H) in the course of biosynthetic reactions.

Ten percent of known oxidoreductases require NADP(H) as the cofactor.[27] Compared to NAD(H), NADP(H) is less stable and more expensive. Also, a regeneration

**Table 1.1** Cost of nicotinamide cofactors NAD(P)(H) in anhydrous basis.

| Cofactor | Empirical formula | Molecular weight | £ $mol^{-1}$ |
|---|---|---|---|
| $NAD^+$ | $C_{21}H_{27}N_7O_{14}P_2$ | 663.43 | 52,000 |
| NADH | $C_{21}H_{27}N_7Na_2O_{14}P_2$ | 709.40 | 67,000 |
| $NADP^+$ | $C_{21}H_{26}N_7Na_2O_{17}P_3$ | 787.37 | 219,000 |
| NADPH | $C_{21}H_{26}N_7Na_4O_{17}P_3$ | 833.35 | 858,000 |

Data extracted from Sigma-Aldrich Co. Ltd., https://www.sigmaaldrich.com (on 05/2020).

scheme for NADP(H) is less developed than its non-phosphorylated form NAD(H). Under this background, it is of great practical as well as intellectual interest to find a regeneration scheme of NADP(H) that can meet the criteria for potential large-scale biosynthesis.

## 1.3 Typical NAD(P)(H) Regeneration Methods

Before moving to detailed introduction of regeneration methods, it is necessary to introduce some concepts and terminologies that are commonly referred to in this thesis.

First, as to the criteria for determining the efficiency of a cofactor regeneration system, two definitions – 'total turnover number' (TTN) and 'turnover number' (TON) – are useful:[28]

$$\text{TTN} = \frac{\text{product formed in moles}}{\text{cofactor present in moles}} = \frac{[\text{product}]}{[\text{cofactor present}]} \tag{1.1}$$

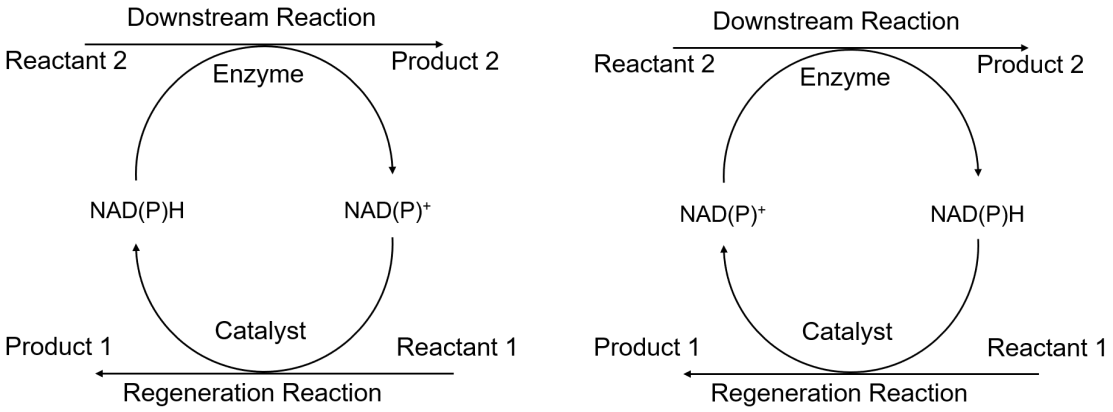
$$\text{TON} = \frac{\text{product formed in moles}}{\text{the catalyst present in moles}} \tag{1.2}$$

To be considered economically feasible, efficient and industrially sensible, a TTN ranging from $10^3$–$10^6$ is appreciated,[28–30] though the exact efficiency also depends on the cost of the catalysts and cofactors that are used.

Actually, having a TTN over 1,000 is not as easy as it seems to be. For instance,

if 50% of the catalytic activity remains after 1,000 successful cycles, the regeneration scheme must have over 99.93% efficiency for each cycle.[28] Therefore it is clear that a successful regeneration scheme must have rapid reaction rate as well as good durability.

The catalysts that regenerate the cofactors can be either inorganic, organic catalysts, or enzymes. To make a full cycle of regeneration scheme work, the reaction involved in regenerating the cofactors must be coupled with an enzymatic reaction (or downstream reaction) such that the cofactors can continuously switch their redox state back and forth. Figure 1.2a shows the basic schemes of NAD(P)H and $NAD(P)^+$ regeneration. It should be mentioned that these are oversimplified versions and the real cases vary depending on more factors.




**(a)** NAD(P)H regeneration. **(b)** $NAD(P)^+$ regeneration.

**Figure 1.2** Schematic drawings for a generic NAD(P)(H) regeneration cycle.

Methods for cofactor regeneration can be roughly subdivided into four main categories: chemical, electrochemical, enzymatic and photochemical.[29, 31] As a rule of thumb, an easy way to classify a cofactor recycling scheme is to find out the key features by asking questions like: 'where is the driving force from?' or 'what is the key catalyst'.

The next subsection will start to introduce these four methods with their merits and demerits. Based on the site that catalysis occurs, these methods can be either homogeneous or heterogeneous. Other methods like the biological (whole-cell) one will also be briefly described later.

### 1.3.1 Enzymatic

The Enzymatic method exploits enzymes to regenerate NAD(P)(H). This method is a favourable method in terms of yield, efficiency and compatibility and up to now is the only method that is practically applied in industry.

This subsection introduces some popular enzymatic methods for regenerating the reduced and oxidised form of nicotinamide cofactors separately.

#### *1.3.1.1 Reduced Form*

**Formate Dehydrogenase (FDH)** Formate dehydrogenases (EC 1.2.1.2) are a group of enzymes that catalyse the oxidation of formate to $CO_2$. The scheme of a FDH-catalysed NADH regeneration is shown in Figure 1.3.

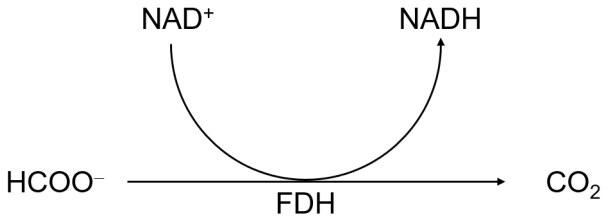



**Figure 1.3** Scheme for FDH-catalysed $NAD^+$ reduction using formate as the sacrificial substrate.

Major merits of this method are as follows:

- The reaction is strongly reducing.
- The byproduct $CO_2$ is chemically inert and can be easily removed from the reaction later.
- Formate is inexpensive and innocuous to most enzymes.
- FDH is commercially available.

NADH regeneration using FDH is one of the most commercially successful methods. A typical example is the ton-scale synthesis of L-*tert*-leucine catalysed by Leucine dehydrogenase (LeuDH, EC 1.4.1.9) from *Bacillus stearothermophius* where NADH

was regenerated by FDH.[32] Other representative applications can be seen in the following references.[33–36]

High cost and relatively low activity are two major disadvantages of FDH.[37] The first disadvantage is practically overcome considering that in most cases the stability of FDH remains stable in different forms (the immobilised,[38] soluble, or membrane-retained[39]), with a daily loss less than 3%. For the second disadvantage, large amounts of protein and extended time can be used to complete one reaction. Also, FDH is much more specific for NAD(H) than NADP(H). An $NADP^+$-dependent FDH was obtained by multipoint site-directed mutagenesis. This new variant of FDH from *Pseudomonas sp.* 101 has a specific activity of $NADP^+$ 60% of its wildtype equivalent.[40]

**Glucose Dehydrogenase (GDH)** The scheme of a reaction catalysed by GDH (EC 1.1.1.47) is shown in Figure 1.4, where the $NAD(P)^+$ is reduced to NAD(P)H accompanied with the formation of glucono $\delta$-lactone from D-glucose (gluconolactone).

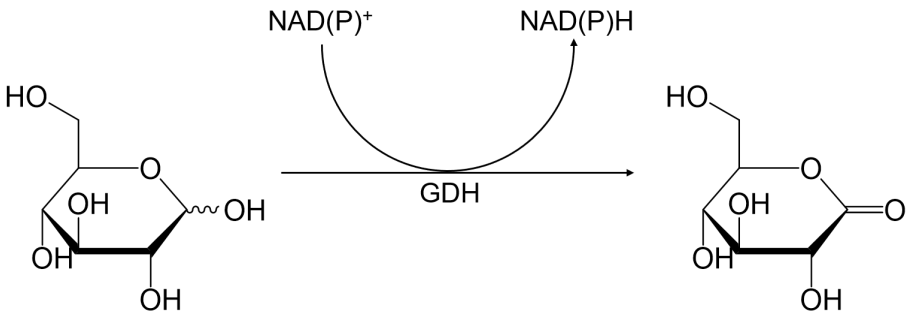



**Figure 1.4** Scheme for GDH-catalysed $NAD(P)^+$ reduction using D-glucose as the sacrificial substrate.

The GDH-catalysed reaction is strongly reducing. Also, D-glucose is inexpensive and stable. The cost of GDH, however, is still a minor concern, but is less expensive than FDH. Unlike FDH, GDH can accept both $NAD^+$ and $NADP^+$ as its substrate, making it one of the best choices for NADPH regeneration, especially at laboratory scale.[28]

A major disadvantage of GDH-catalysed method is that the byproduct gluconate

(quick hydroxylation product of gluconolactone) is difficult to isolate from the system.

Some relevant applications of GDH-catalysed NAD(P)H regeneration are available in the following references.[41–44]

**Other methods** Other commonly used enzymes for NAD(P)H regeneration include: alcohol dehydrogenase (ADH, EC 1.1.1.1/1.1.1.2),[45–48] phosphite dehydrogenase (PTDH, EC 1.20.1.1),[49–51] hydrogenase (EC 1.12.1.2),[52, 53] and glucose-6-phosphate dehydrogenase (G6PDH) (EC 1.1.1.49).[28, 54]

The G6PDH catalyses the oxidation of glucose-6-phosphate to 6-phosphogluconolactone. Its stability, and reducing capacity are similar to GDH, with the exception that G6PDH itself is inexpensive but has an expensive sacrificial reagent glucose-6-phosphate.

When hydrogenase is used in a regeneration system, NAD(P)H can be regenerated by $H_2$, with one proton being the byproduct. This reaction is very clean as protons, provided no considerable pH value is altered, having almost no side effect on the system at all. Using $H_2$ as the co-substrate is also attractive, as it is inexpensive. Hydrogenases being commercially unavailable and sensitive to $O_2$ are its disadvantages.

A feature of ADH is that this enzyme catalyses the reversible oxidation of alcohols to aldehydes or ketones, depending on whether the alcohols are in primary or secondary forms. This reaction is bidirectional, meaning that ADH-catalysed reactions can regenerate both the oxidised and the reduced forms of cofactors. ADH will be frequently used in this thesis.

#### *1.3.1.2 Oxidised Form*

Commonly used enzymes include L-glutamate dehydrogenase (GLDH, EC 1.4.1.4),[55–57] alcohol dehydrogenase (ADH),[58, 59] L-lactate dehydrogenase (LDH, EC 1.1.2.27),[60, 61] and NADH oxidase (EC 1.6.3.3)[62–64]. This section will introduce the GLDH-catalysed reductive amination as an example.

The GLDH-catalysed reductive amination of 2-oxoglutarate (2-OG, shown in

Figure 1.5) is favourable for NAD(P)$^+$ regeneration. This system could use NADH and NADPH as substrates. The reaction is thermodynamically favoured to drive most of downstream biochemical reactions. Both 2-OG and GLDH are inexpensive, as is the product L-glutamate. Moderate specific activity is a minor disadvantage for GLDH. Its activity (40 U mg$^{-1}$) is over one magnitude lower than LDH (1000 U mg$^{-1}$).[28] However, the LDH-catalysed system is thermodynamically less favourable and usually LDH cannot accept NADPH.

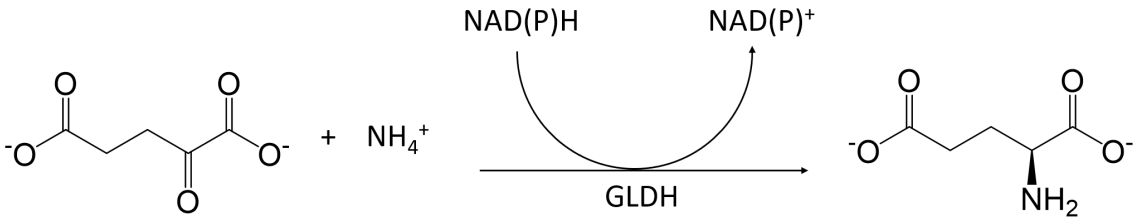



**Figure 1.5** Scheme of GLDH-catalysed NAD(P)$^+$ regeneration using 2-oxoglutarate as the sacrificial substrate.

### 1.3.2 Chemical

#### *1.3.2.1 Direct Redox Reaction*

The most straightforward way is to use a strong oxidising or reducing agent to directly alter the redox state of cofactors. Strong inorganic reducing agents like $NaBH_4$ and $Na_2S_2O_4$ are capable of reducing NAD(P)$^+$.[65] $NaBH_4$ is the one of the inorganic equivalents of NAD(P)(H) that can donate hydrides for a redox reaction, though the reactions involved usually proceed violently. Owing to the following reasons, it is not recommended to use this method for reactions involving enzymes:

- The inorganic salts are unfriendly to the coupled enzymes which tend to deactivate.[66]
- The TTN adopting this scheme is not that impressive.
- The reactions are usually not enantioselective.

- A large feed of chemicals are required, which produces waste and is not eco-friendly.

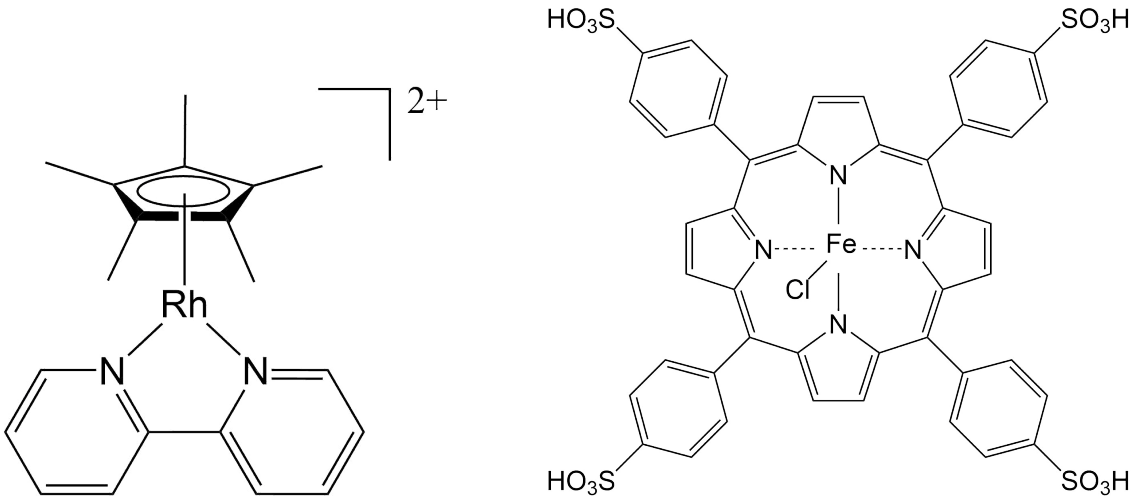
#### *1.3.2.2 Organometallic Approach*

There has been a suite of studies since 1980s on regenerating NAD(P)(H) using organometallic and biomimetic approaches.[67–70] For these organic compounds, several prerequisites should be met to be a good catalyst for NAD(P)(H) regeneration:

- The mediator should be stable in both oxidised and reduced forms.
- The turnover frequencies of the mediators should be high.
- The mediator should be soluble in the phase in which the experiment is carried out.
- The mediator should react specifically with the cofactors.

The commonly used mediators are organometallic complexes of transition metals like Rh, Ru, Ir, Fe, and so on.[37] Figure 1.6 demonstrates molecular structures of two catalysts $[Cp^*Rh(bpy)]^{2+}$ ($Cp^* = C_5Me_5$, bpy = $2,2'$-bipyridine) and iron(III) porphyrin complex. $[Cp^*Rh(bpy)]^{2+}$ can reduce $NAD(P)^+$ in a mechanism where two electrons and one proton are donated from the formate, through which $CO_2$ forms and $[Cp^*Rh(bpy)]^{2+}$ is converted to $[Cp^*Rh(bpy)H]^+$.[71] This organometallic complex mimics FDH in biology.

As for the selection of a sacrificial substrate, $O_2$ and $H_2$ are two appreciated kinds, because their complete reduction and oxidation products are $H_2O$ and protons, ruling out the formation of wasteful byproducts. The iron(III) porphyrin complex (shown in Figure 1.6b) is typically used in the regeneration of the oxidised form $NAD(P)^+$ and mimics oxidases in biology. Gröger *et al.* achieved TON of 48–50 in alcohol oxidation using ADH as the coupling enzyme.[72] One impressive result of this study is that $H_2O_2$ was not produced so that catalase was not required to decompose this toxic byproduct.




**(a)** $[Cp^*Rh(bpy)]^{2+}$ **(b)** An iron(III) porphyrin complex.[72]

**Figure 1.6** Molecular structures of two organometallic complexes for NAD(P)(H) regeneration.

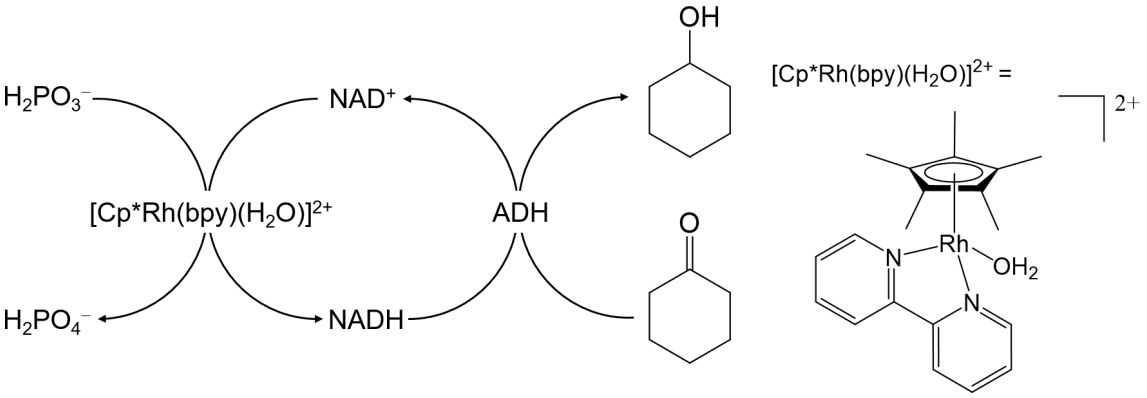



**Figure 1.7** A NADH regeneration scheme coupled with ADH and using phosphite as the sacrificial reagent.[73]

Another inexpensive sacrificial substrate is phosphite. In a NADH recycling scheme (shown in Figure 1.7), cyclohexanol was produced after the system was used in conjunction with a thermostable ADH from *Thermus sp.* ATN1.[73]

The mutual inactivation between the organometallic catalysts and downstream enzymes is a disadvantage preventing further development of this approach.[74–78] One thinking to address this issue is to compartmentalise or separate the two entities such that the mutual interaction can be largely avoided.[79–81] Sluggish diffusion issues tend to occur using the compartmentalisation techniques. However, the longevity of the overall system can be prolonged.

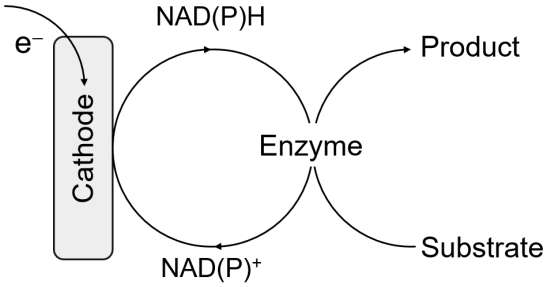
Another problem is that the TTN of the mediator-catalysed regeneration scheme is still far behind the enzymatic method.[76, 82] Also, for a potential scaled-up scenario, the exploitation of large amounts of the mediators, many of which are noble-metal-based and toxic, is inevitable. This is not economically and environmentally favourable.

### 1.3.3 Electrochemical

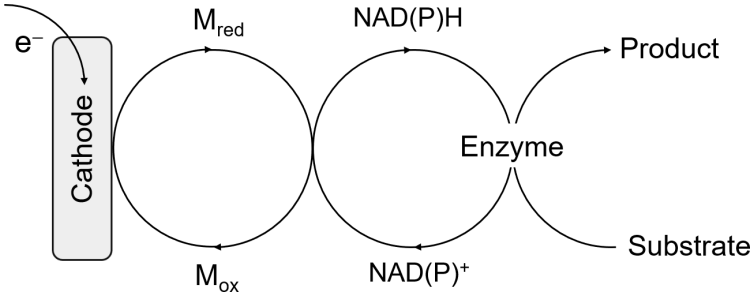
The electrochemical method has been appreciated as a promising and powerful technique to regenerate NAD(P)(H). A major advantage of this heterogeneous approach is that while other methods heavily rely on large amounts of co-substrates to donate/accept electrons to/from the NAD(P)(H), the atom efficiency of the electrochemical method is apparently high as it exchanges the mass-free electrons directly or indirectly from the power source.[26, 31, 83]

In terms of the pathways through which electrons are transferred and the mechanisms of reactions, four different approaches are available. In the case of regeneration of the reduced form NAD(P)H,[26, 83] the schematic drawings of four approaches are shown in Figure 1.8.[1] The direct cathodic NAD(P)H (shown in Figure 1.8a) is the most straightforward way, through which the oxidised nicotinamide cofactors

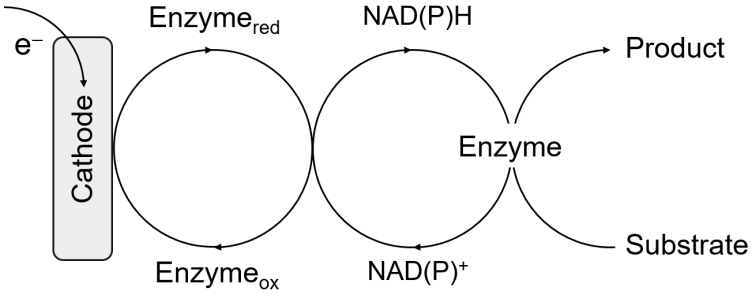
[1] As to the regeneration of the oxidised form $NAD(P)^+$, schemes follow a similar way. One can simply reverse the flow of electrons by applying an oxidative potential that is large enough to drive NAD(P)H oxidation.



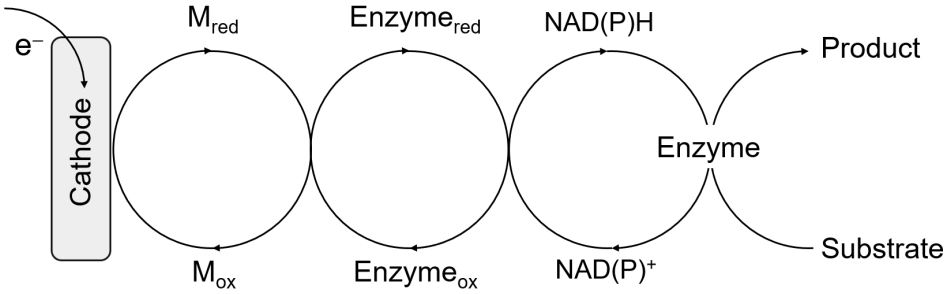

**(a)** Direct cathodic NAD(P)H regeneration.




**(b)** Indirect electrochemical NAD(P)H regeneration.




**(c)** Direct electroenzymatic NAD(P)H regeneration.




**(d)** Indirect electroenzymatic NAD(P)H regeneration.

**Figure 1.8** Schematic drawings for four electrochemical methods to regenerate NAD(P)H. The capital letter 'M' denotes a mediator.

receive electrons directly from the electrode. The second case, termed as indirect electrochemical NAD(P)H regeneration, involves the electrode that is modified by an electron mediator (shown in Figure 1.8b). By altering the redox states of the mediator, the electrons are thus transferred to the cofactors.

Figure 1.8c and 1.8d demonstrate the methods that exploit enzymes to catalyse the regeneration process, with the difference that the direct electroenzymatic approach does not need an electron mediator to carry electrons.

All these four approaches have their merits and demerits and can be used under different scenarios. The projects undertaken in this thesis are categorised into the direct electroenzymatic approach, which achieves direct electron transfer exploiting FNR entrapped within the porous electrode. Additionally, it will be demonstrated later that the essence of experiments carried out in this thesis is more than just '**direct electroenzymatic**'.

#### *1.3.3.1 Direct Electrochemical*

The earliest studies using direct electrochemical methods to regenerate NAD(P)H exploited carbon and mercury as the working electrodes.[84–86] As a non-specific method, the main problem arising is that, other than the biologically active NAD(P)H (or 1,4-NAD(P)H), a mixture of non-biologically active 1,2-, 1,6-NAD(P)H isomers and $[NAD(P)]_2$ dimers would form.[25, 26, 87–90] As shown in Figure 1.9, in the course of reduction, $NADP^+$ is first reduced to a $NAD(P)^\bullet$ radical, the following reduction and protonation of which is expected to give NAD(P)H. However, in the cases that migration of radicals occurs, 1,2-NAD(P)H and 1,6-NAD(P)H would also form. Also, two $NAD(P)^\bullet$ may dimerise to give $[NAD(P)]_2$. The same method for the regeneration of the oxidised form of $NAD(P)^+$ does not result in such complexity; however, high overpotential is still required to oxidise NAD(P)H into $NAD(P)^+$. It was reported that the inactive $[NAD(P)]_2$ can be electrochemically or biologically re-oxidised into $NADP^+$.[85, 91–93] In addition, a recent interesting discovery is that the formation of these biologically inactive NADP(H) isomers also take place in living

bodies, but are soon transformed into 1,4-NAD(P)H; this is achieved by enzymes. For instance, the primary function of renalases is to recover 1,2- and 1,6-NAD(P)H to $NAD(P)^+$.[94, 95]

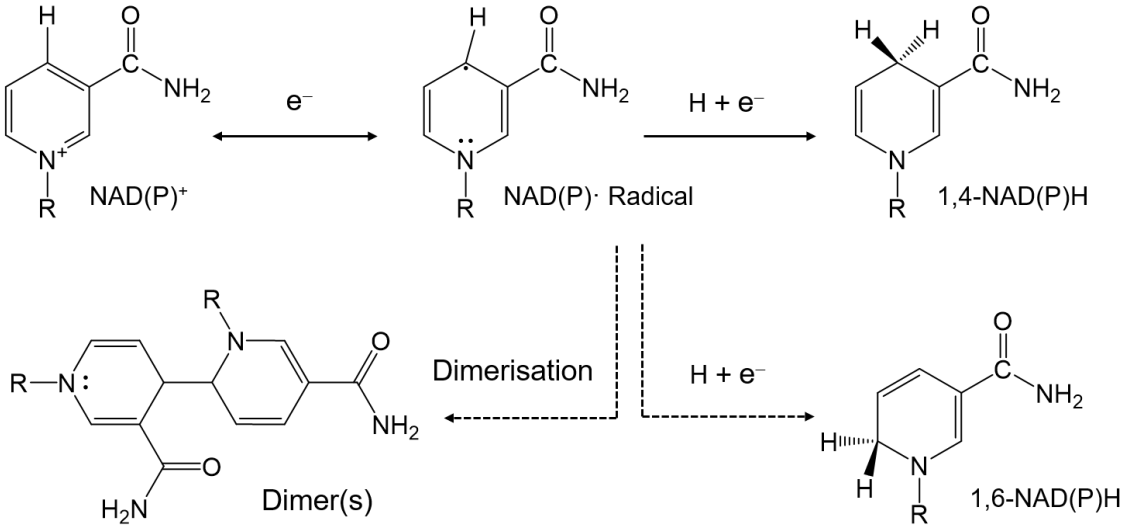



**Figure 1.9** A schematic drawing showing the mechanism of direct electrochemical $NAD(P)^+$ reduction. The R group linked to the nitrogen atom of the pyridine denotes adenosine diphosphoribose.[26, 37]

Other electrode materials, including either modified or non-modified glassy carbon, Pt, Ru, Ni, Ti, Cd, Co, Cu have been tried.[37, 96–98] For example, I. Ali *et al.* found that the rate of the protonation step shown in Figure 1.9 depends not only on the electrode potential, but also the strength of the metal-hydrogen ($M\text{-}H_{ads}$) bond. After trying a series of materials, 96–100% NADH yield was attained using bare Ti, carbon nanofiber, or nano-patterned glassy carbon/Pt electrodes.[98–100] Y. Kim *et al.* also obtained 100% NADH yield using a tin oxide electrode. E. Siu *et al.* reported 3,300 TTN of NAD(H) using an un-modified Pt electrode coupled with GLDH. For these studies, further scaled-up experiments are required to test whether such high efficiencies achieved in the laboratory can be repeated on a bulk scale.[101]

The required high overpotential and electrode fouling are the major problems to be addressed for the direct electrochemical regeneration approach.[27, 62, 78, 102–104] To circumvent these issues, the improvement of the electrode structure is important.

#### *1.3.3.2 Indirect Electrochemical*

Mediators can lower the overpotential required to oxidise/reduce NAD(P)(H). As seen in Figure 1.8b, the reduced form of the mediator molecule $M_{red}$ serves as the reductant for $NAD(P)^+$. $M_{red}$ is then recycled back *via* cathodic reduction of the oxidised form $M_{ox}$. Compared to the typical case in which mediator monomers are in the solution, mediators anchored on the electrode surface through covalent linkage reduces the difficulties of product purification and waste disposal.

It should be mentioned that in electrochemistry, the two-electron mediators, *e.g.* quinones and Rh-based complexes and their derivatives, are able to effectively avoid the problems arising from the one-electron radicals,[105–107] such as the $NAD(P)^{\bullet}$ as mentioned in the last section. On the other hand, the one-electron mediators, such as the 2,2'-azinobis(3-ethylbenzothiazoline-6-sulfonate) ($ABTS_2^-$) reported by Schröder *et al.* are chemically stable and react faster with NADH.[108]

#### *1.3.3.3 Direct Electroenzymatic*

Many oxidoreductases do not need an exogenous electron shuttle to achieve electron transfer with the electrode. Therefore, with these enzymes, direct electron transfer is realised by intramolecular and interfacial electron transfers through redox-active centres, *e.g.* heme, ferredoxin adenine dinucleotide (FAD), Mo pterin, and relays, like iron-sulphur ([Fe–S]) clusters.[109–112]

Though there are many cases of oxidoreductases being capable of direct electron transfer with the electrode typically hydrogenase, laccase, carbon monoxide dehydrogenase (CODH), FDH, and bilirubin oxidase,[113–116] the case of direct electroenzymatic regeneration of nicotinamide cofactor is rare.

Prior to the pioneering work carried out by B. Siritanaratkul *et al.*[117, 118] in this group, a typical example of direct electroenzymatic regeneration is the hydrogenase system. Cantet *et al.* found that the NADH-producing hydrogenase from *Alcaligenes eutrophus H16* (EC 1.12.1.2) adsorbed on a platinum electrode was able to reduce $NAD^+$ directly when $H_2$ was present in proximity to the electrode.[119]

This regeneration system was coupled to GLDH and the production of L-glutamate was detected.[120] Later, the hydrogenase from *Rhodococcus opacus* was exploited in a similar recycling system, with significantly higher NADH formation rates being achieved.[121] The stability and TTN need improvement further for these systems to be of use. However, electron transfer between the electrode and the metalloenzymes directly is conceptually doable and attractive.[122]

#### *1.3.3.4 Indirect Electroenzymatic*

Electron transfer between electron mediators and NAD(P)(H) can be sped up using enzymes. This is especially useful in the case where the active site of an enzyme is buried deeply within the tertiary structure.[123] An example is shown in Figure 1.10 where $NAD^+$ is regenerated using co-immobilised diaphorase (EC 1.6.99.1) and ferrocene.[124, 125] The system is coupled with HLADH to oxidise alcohols and up to 50 TTN was achieved.

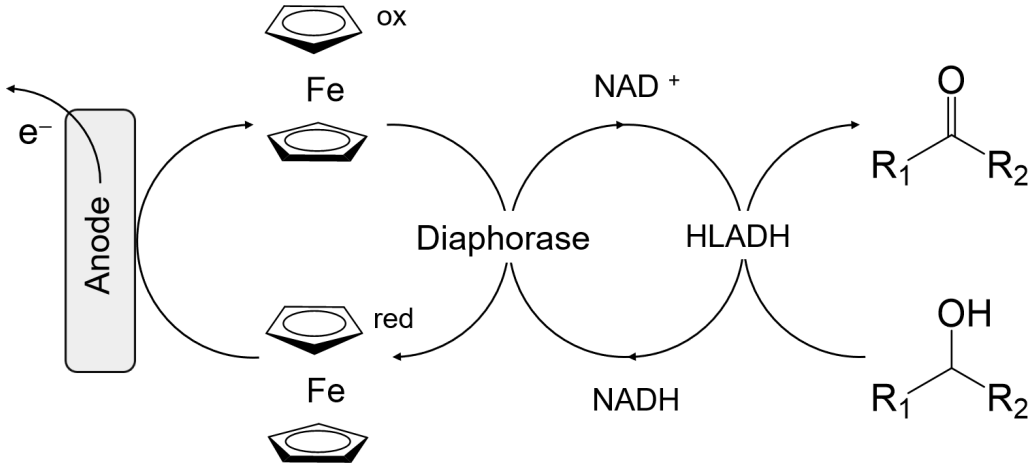



**Figure 1.10** Indirect electroenzymatic $NAD^+$ regeneration using ferrocene and diaphorase coupled to horse liver ADH (HLADH).[125]

A commonly used mediator is the one-electron N,N'-dimethyl-4,4'-bipyridinium dichloride (methyl viologen, $MV^{2+}$) and its main relay enzymes includes diaphorase,[126] FNR,[127–129] and the AMAPORs (artificial mediator accepting pyridine nucleotide oxidoreductase).[130, 131] When using FNR, ferredoxin (Fd) can replace methyl viologen since this iron-sulphur protein is the natural electron mediator of FNR.[31]

The $MV^{2+}/MV^{+\bullet}$-mediated system is stable and efficient but toxic. Another efficient alternative of methyl viologen is the natural cofactor FAD.[132–135]

### 1.3.4 Photochemical Methods

NAD(P)(H) regeneration driven by photochemical reactions has attracted great interest these years due to its eco-friendly feature.

Like natural photosynthesis (details will be introduced later in this chapter), the artificial photochemical reaction requires a photosensitiser by which excited electrons are generated under visible or ultraviolet light. These high-energy electrons are further accepted by the $NAD(P)^+$ such that NAD(P)H is produced. In this process, a mediator is often exploited to facilitate downstream electron transfer. The photocatalyst is regenerated by the electron donors like triethanolamine (TEOA) and $H_2O$.

Photosensitisers can be roughly classified into the inorganic and organic types. The selection of a correct photosensitiser is crucial for downstream reactions. The rest of this section will briefly introduce these two kinds.

#### *1.3.4.1 Inorganic Photosensitiser*

Commonly used inorganic photosensitisers include titanium oxide ($TiO_2$), cadmium sulphide (CdS), carbon nitride ($C_3N_4$), and so forth.[37] Also, a photocatalyst can also be comprised of a mixture of different photosensitisers to offer more photoexcited electrons and a broader adsorption band.

$TiO_2$ is one of the earliest examples as the photocatalyst to regenerate NADH. The original $TiO_2$ is not very efficient mainly due to its broad bad gap of ∼3.2 eV, meaning that it can only generate excited electrons from ultraviolet (UV) light. This represents approximately 4% of the total energy of sunlight and also UV light is detrimental to a system involving enzymes. To make a red shift of the adsorption band of $TiO_2$, doping the lattice with impurities like carbon, boron or phosphorus is effective, as the as-treated $TiO_2$ starts to adsorb visible light.[136–138]

In a NADH regeneration scheme using a dopamine-coordinated $TiO_2$ nanoporous film, the composite material was attached upon the surface of an ITO electrode. Photocurrent was detected and intensified in the presence of NADH. This reactor can be used to detect minute quantities of NADH as low as $1.4 \times 10^{-7}$ M.[139]

Quantum dot (QD) materials including CdS, cadmium selenide (CdSe) and zinc sulphide (ZnS), *etc.*, are a large group of inorganic photosensitisers.[140–144] These nanoscale QDs can be loaded upon a support, like silicon dioxide ($SiO_2$), $TiO_2$, $Al_2O_3$ or enzymes.[145, 146] Figure 1.11 shows the working scheme of a quantum QD-FNR biohybrid complex.[142] In this NADPH regeneration system proposed by K. Brown *et al.*, the photoexcited electrons generated by CdSe quantum dots were transferred to FNR which catalysed the reduction of $NADP^+$. The reaction was coupled with

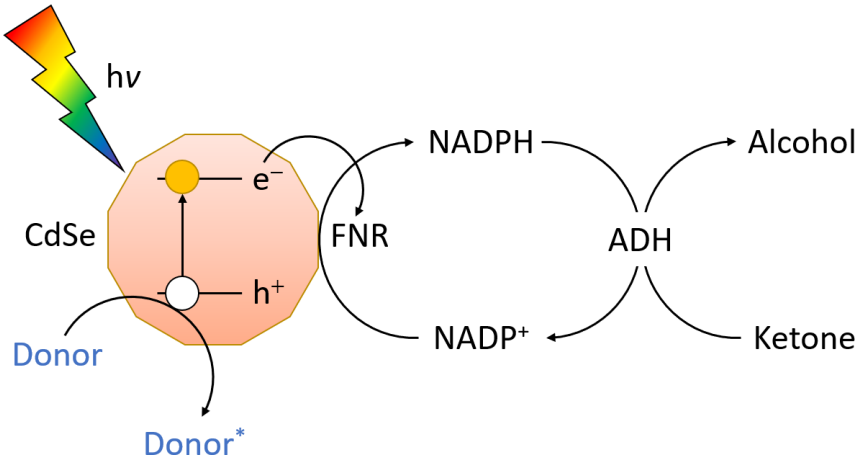



**Figure 1.11** A schematic drawing of the photo-driven QD-FNR biohybrid NADPH regeneration system. Here, the electron donor is ascorbic acid (AA).[142]

ADH such that alcohols were the final product. The resulting TTN ranged from 2–4, showing that there is still large scope for optimisation, as the value is far less than that of the enzymatic methods.

Graphitic carbon nitride (g-$C_3N_4$, Figure 1.12) is a popular newly-reported metal-free photosensitiser.[147] This material has a suite of advantages: it is easy to synthesise, it has attractive band position and is comprised of inexpensive raw materials (mostly earth-abundant), and is thermostable. Apart from sharing similar working mechanisms of photoexcitation processes with other inorganic photosensitis-

ers, it is shown that g-$C_3N_4$ can even catalyse direct reduction of $NADP^+$ free of the Rh-based complex.[148] A possible interpretation given by J. Huang *et al.* is that the $\pi$-$\pi$ stacking of the heptazine units of g-$C_3N_4$ and the adenine group of $NAD^+$, facilitate direct electron transfer with one another. Although the direct formation of NADH in the absence of a mediator is non-specific, leading to biologically inactive 1,6-NADH, this approach is still conceptually interesting. g-$C_3N_4$ can also mix with other photosensitisers like $\alpha$-$Fe_2O_3$. A newly reported g-$C_3N_4$@$\alpha$-$Fe_2O_3$/C photocatalyst can output 3.26 times higher photocurrent than the pristine g-$C_3N_4$.[149]

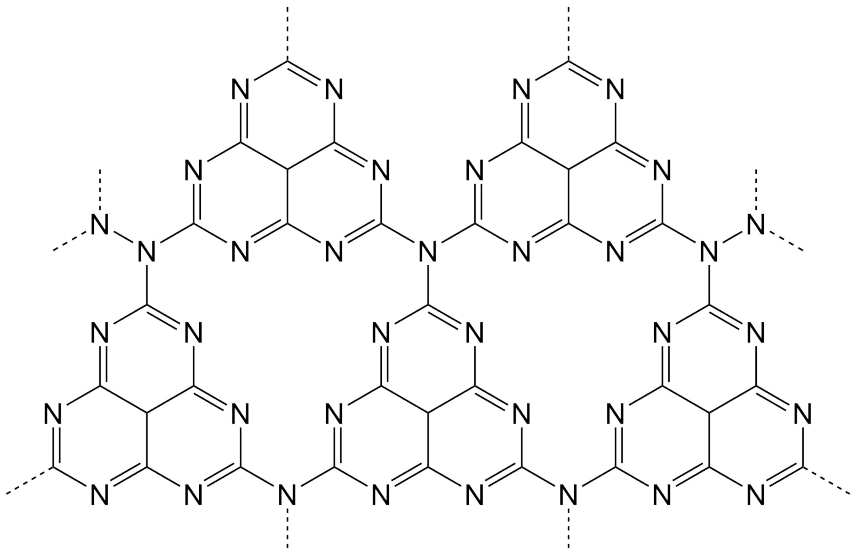


**Figure 1.12** Molecular structure of g-$C_3N_4$.

Another example of a photosensitiser for direct photocatalytically driven NADH formation, is gold nanoparticles (AuNP).[150] S. Roy *et al.* reported that the positively charged AuNPs improves the channelling and local concentration of the negatively charged $NAD^+$, thereby promoting the opportunities for multielectron transfer.

### *1.3.4.2 Organic Photosensitiser*

Organic photosensitisers derived from nature, *e.g.* proflavine, porphyrin, chlorophyll, and those are synthesised artificially are another group of photocatalysts to achieve photocatalytic NAD(P)(H) recycling schemes.[151–153]

As shown in Figure 1.13, when using proflavine as the photocatalyst, photo-induced nicotinamide cofactor regeneration occurs under visible light ($\lambda > 420$ nm) in the presence of the Rh-based complex $[Cp^*Rh(bpy)(H_2O)]^{2+}$.[151] This reaction was coupled to the GLDH-catalysed reductive amination to produce L-glutamate. While the authors found that the efficiency of photochemical reaction depends on the wavelength and intensity of light, choosing an optimal photosensitiser also helps. Despite shared similar structures and properties, flavin derivatives like FAD, flavin mononucleotide (FMN), riboflavin and lumichrome can only speed up the rate of NADH oxidation, not the rate of $NAD^+$ reduction.

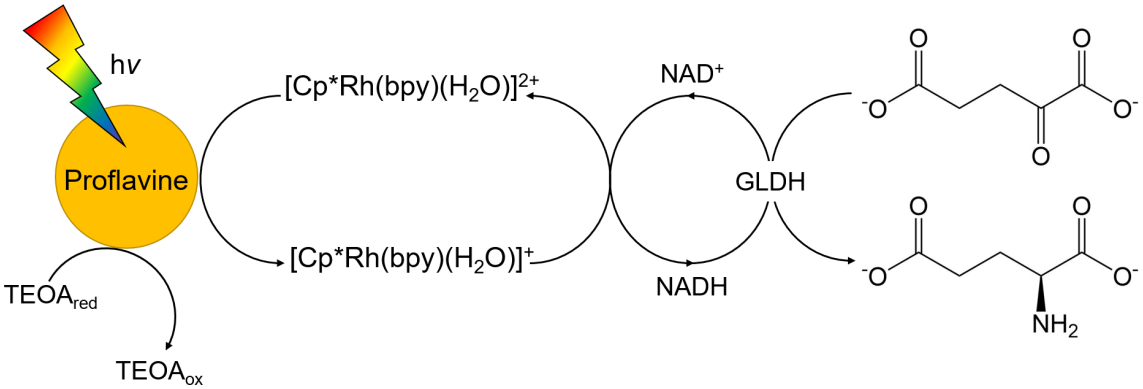



**Figure 1.13** Photocatalytic NADH regeneration using proflavine as the photosensitiser. Electron transfer is mediated by the Rh-based complex $[Cp^*Rh(bpy)(H_2O)]^{2+}$.[151]

Organic photosensitisers usually show high efficiency regarding photoexcitation. However, as small molecules, instability in structure, poor re-usability and difficulty in separation need solving first for this system to be viable. Two workable methods are physical entrapment and chemical grafting.[37] A representative of physical entrapment used the synthetic wood. M. Lee *et al.* encapsulated porphyrins in the porous support matrix made from wood whereby the hybrid acquired light-harvesting ability under visible light.[154] Likewise, the photoexcited electrons were then mediated by $[Cp^*Rh(bpy)(H_2O)]^{2+}$ through which a hydride was transferred to $NAD^+$. As for chemical grafting, a typical case is the covalently bonded multi-anthraquinone-substituted porphyrin with the chemically converted graphene.[155] The mixture as a whole can act as both electron donor and acceptor. The downstream

components of this scheme also included $[Cp^*Rh(bpy)(H_2O)]^{2+}$ and a NADH-linked FDH, through which NAD(H) is regenerated and formic acid is produced.

To summarise, the photochemical NAD(P)(H) regeneration scheme is conceptually intriguing as it deals with free and eco-friendly solar energy as the driving force. However, the efficiency of this method needs improving as the TTN reached in most cases was far below than those in enzymatic method. Also, the reliance on electron donors means that the oxidised byproduct needs to be separated from the final product.

### 1.3.5 Other Methods

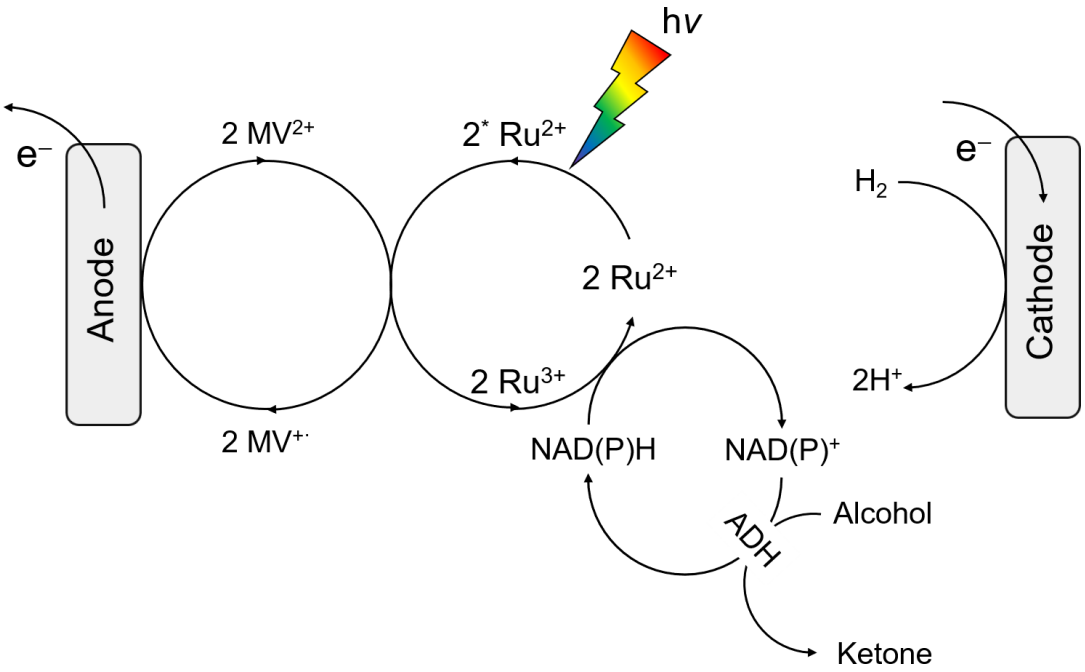



**Figure 1.14** Photoelectrocatalytic $NAD(P)^+$ regeneration using tris(2,2′-bipyridyl)ruthenium(II) as the photosensitiser. During catalytic cycle, this complex is excited under illumination, oxidised by $MV^{2+}$ by, and regenerated by NAD(P)H.[156]

The classification of different NAD(P)(H) regeneration methods makes it easy to categorise newly reported work. However, there are methods that share the key characteristics of at least two main methods and therefore are difficult to classify into a definite method.

Figure 1.14 illustrates the schematic drawing of the work performed by E. Steckhan *et al.*[156] It is a photoelectrochemical $NAD^+$ regeneration experiment, indicating

that it is both 'photochemical' and 'electrochemical'. Here, the photosensitiser is the Ru-based complex tris(2,2′-bipyridyl)ruthenium(II) (abbreviated as $Ru^{2+}$), which converted to Ru(II)* after photoexcitation under visible light. The Ru(II)* was then oxidised by the electron mediator $MV^{2+}$ to give $Ru^{3+}$ which regenerated $NAD^+$ by oxidising NADH. On the anode, the reaction occurred was the regeneration of $MV^{2+}$, while on the cathode, protons were reduced to molecular $H_2$. The downstream enzyme used was HLADH by which alcohol oxidation was catalysed to give a ketone as the final product.

**Whole-Cell Method** The whole-cell method can be seen as a parallel alternative to the enzymatic method. This method exploits cells, *e.g.* yeast or *E. coli.* as the biocatalysts. When isolated enzymes are used, they may be more prone to destabilisation in organic solvents and sensitive to the change of experimental conditions. Also, the purification of enzymes is more time-consuming than just exploiting whole cells directly. On the other hand, stability of enzymes can be improved dramatically within live cells, since the host cells provide a shelter to protect enzymes from external environment. A great advantage of the whole-cell method lies in the fact that the cells are self-sufficient in terms of nicotinamide cofactors, since they contain an intracellular pool to use. However, hundreds of enzymes that can catalyse the same reaction may be present in the cell, as a result, it is harder for the cell-catalysed reactions to produce enantiomerically pure compounds. So far, recombinant DNA techniques have provided a workable solution to increase the stereoselectivity of a whole-cell-catalysed reaction.[31]

A typical example exploiting the whole-cell method is the asymmetric reduction of 4-fluoroacetophenone to (*R*)-4-fluorophenylethan-1-ol based on the (*R*)-selective *sec*-ADH from *Lactobacillus kefir.*[157, 158] A recombinant *E. coli.* that has been engineered to contain this (*R*)-selective ADH and a GDH was used in aqueous phase, resulting in with good yield (87%) and very high enantiomeric excess (ee, 97% (*R*)).

## 1.4 Photosynthesis

Solar energy provides the driving force for continuous recycling of $O_2$ and $CO_2$ in the biosphere and ultimately the production of an energy source in the form of reductive substrate, *e.g.* glucose that living organisms must live on.

Photosynthesis by green plants consists of two main processes – the light-dependent reactions (or simply light reactions) and the light-independent reactions (also called dark reactions, Calvin Cycle, carbon-fixation or -assimilation reactions).

A simplified version of the net reaction of photosynthesis can be written as:

$$CO_2 + H_2O \xrightarrow{\text{Light}} (CH_2O) + O_2 \tag{1.3}$$

### 1.4.1 Light-dependent Reactions

As shown in Figure 1.15, the electron pathway during photosynthesis commences at protein complex photosystem II. Under light illumination, an electron in the chlorophyll pigment molecules P680 is photoexcited to a higher energy level. From photosystem II, electrons are transferred to the plastocyanin – a copper protein in the thylakoid – one at a time. The plastocyanin then carries the electrons to the adjacent pigment P700 in photosystem I. The lost electron in P680 is compensated by oxidising water molecule using a strong oxidant manganese centre through which $O_2$ evolves. After receiving one electron, P700 is photoexcited and passes this electron to the iron-sulphur protein ferredoxin (Fd) and two Fd molecules that have received electrons then sequentially transfer their electrons to FNR by which $NADP^+$ is catalysed to NADPH. The complete route of electron flow from $H_2O$ to NADPH is known as the Z-scheme. Also, the proton gradient that evolves across the thylakoid membrane is contributed by Cytochrome *b6f*. The adenosine triphosphate (ATP) synthase then exploits this gradient to convert adenosine diphosphate (ADP) and phosphate ions ($P_i$) into ATP.

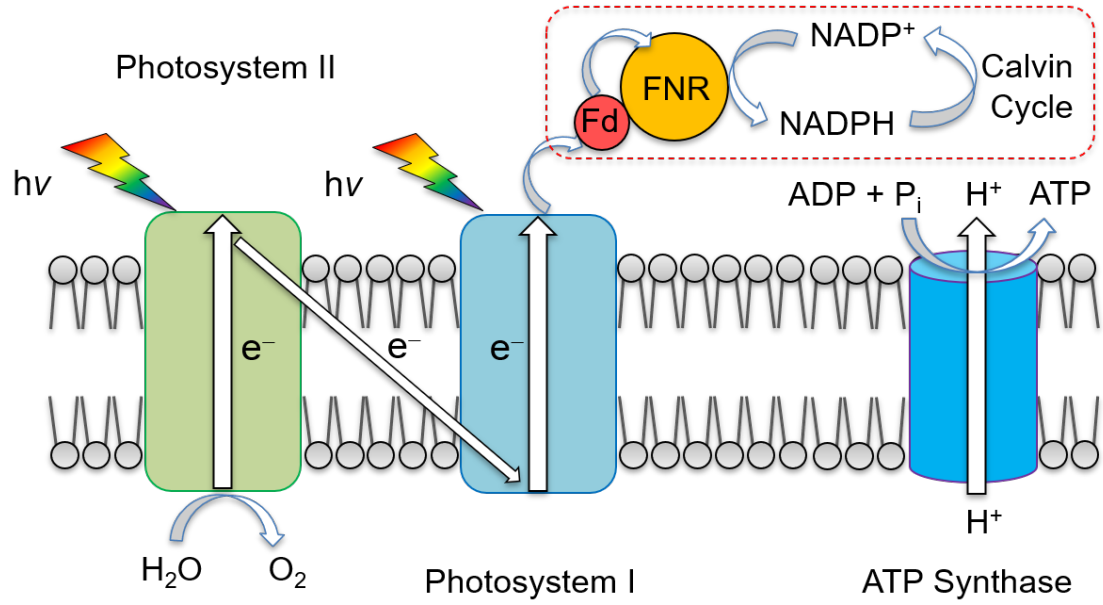



**Figure 1.15** A simplified schematic drawing of photosynthesis, particularly the light-dependent reactions. The icons and arrows that are enclosed in red dash-line frame is the process involving NADP(H) regeneration.

The net equation resulting from light-dependent reactions can be written as:

$$2\,H_2O + 2\,NADP^+ + 3\,ADP + 3\,P_i \xrightarrow{\text{Light}} O_2 + 2\,NADPH + 2\,H^+ + 3\,ATP \quad (1.4)$$

### 1.4.2 Light-independent Reactions

The light-independent reactions use ATP and NADPH that are regenerated in the light-dependent reactions as the driving force. This process as a whole mainly encompasses the following stages:

1. The carboxylation of a five-carbon intermediate ribulose-1,5-bisphosphate (RuBP) with molecule of $CO_2$ is catalysed by the enzyme RuBP carboxylase (RuBisCO) to form an unstable six-carbon compound which splits into two molecules of the three-carbon compound 3-phosphoglycerate (3-PGA).

2. Through phosphorylation and reduction in sequence, the 3-PGA is converted into glyceraldehyde 3-phosphate (G3P). In this step, every one 3-PGA molecule reacts with one molecule of ATP and one molecule of NADPH, producing one molecule of G3P, $P_i$, ADP and $NADP^+$, respectively.

3. Following a series of complicated steps, five molecules of G3P react with three molecules of ATP. This regenerates three molecules of RuBP, together with three molecules of ADP and two molecules of $P_i$.

In total, for every six molecules of G3P produced, five of them are used to regenerate three molecules of RuBP, leaving only one used for the next-step reaction to produce glucose. This requires nine molecules of ATP, three molecules of $CO_2$, and six molecules of NADPH. Apart from one molecule of G3P, nine molecules of ADP, six molecules of $NADP^+$ and eight molecules of $P_i$ are produced. The net reactions can be written as:

$$3\,CO_2 + 6\,NADPH + 6\,H^+ + 9\,ATP \longrightarrow 6\,NADP^+ + 9\,ADP + 3\,H_2O + 8\,P_i + G3P \tag{1.5}$$

## 1.5 Micro- and Nano-confinement in the Natural Leaf

Photosynthesis is crucial to life, as all living creatures on earth depend on the sugar produced to live on directly or indirectly and the usable $O_2$ produced from the water split during this process.

A factor contributing to fast catalysis in plants is the effect of micro- and nano-confinement that is common in living organisms. Chloroplasts, mostly existing in the leaves of land plants (a typical schematic drawing shown in Figure 1.16), are organelles where the reactions of photosynthesis occur. The number of chloroplasts a cell contains varies from one in unicellular algae to 100 in plants. The chloroplasts of land plants are often lens- or ellipsoid-shaped, with 3–10 $\mu$m diameter and 1–3 $\mu$m thick.[159]

Thylakoids are the core components inside chloroplasts in which the protein complexes photosystem I, photosystem II and photosynthetic pigments (different kinds of chlorophyll in particular) are embedded (as shown in Figure 1.15). The very close range or close packing of these protein complexes, pigments and inorganic and organic reagents with one another, all whilst confined within nano-zones and therefore

concentrated next to the membrane, substantially facilitates many cascade reactions which occur. For instance, for the energy gained from the photoexcited electrons are to be catalysed by independent and distant photosensitisers, it is highly likely that the energy would dissipate into heat as the electron returns to ground state. Within the nanozones of chloroplasts, in particular the thylakoid nearby, on the contrary, a useful electron acceptor nearby ensures that electrons can be smoothly and rapidly passed to the acceptor and thus leads to highly efficient reaction chains.[160]

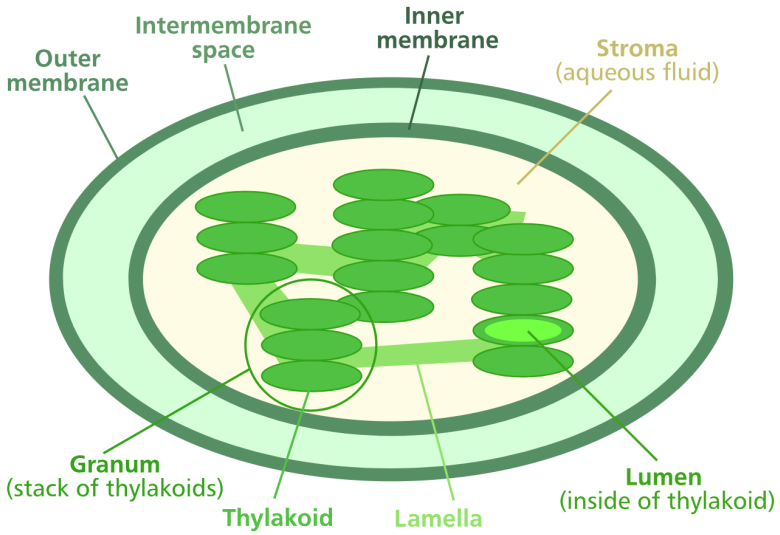



**Figure 1.16** A schematic drawing of chloroplasts in plants[2].

## 1.6 Ferredoxin NADP$^+$-reductase (FNR)

### 1.6.1 Flavoenzymes

Flavoenzymes are a group of enzymes that contain a flavin mononucleotide (FMN) or flavin adenine dinucleotide (FAD) as their coenzymes to realise catalytic functions. Flavin is the general term for a class of organic compounds having the heterocyclic isoalloxazine ring.

The flavin group is capable of mediating one-electron or two-electron transfers by accepting or losing protons and electrons to or from its three redox states of isoalloxazine ring. As shown in Figure 1.17, after accepting one electron and one

[2]This figure was contributed by Ollin in English Wikipedia who granted its usage for any purpose. (https://en.wikipedia.org/wiki/File:Chloroplast_diagram.svg#filelinks)

proton, the hydroquinone (fully-reduced, or $FADH_2$) is converted from the semi quinone (semi reduced, or $FADH^\bullet$) state which itself is reduced from quinone state (fully oxidised, or FAD) through the same process as before.

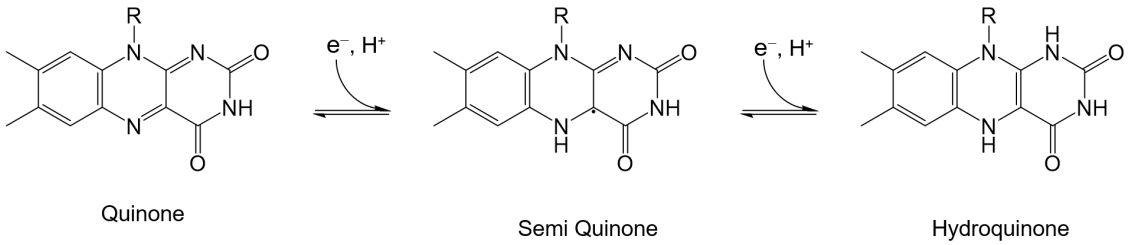



**Figure 1.17** Chemical structures of three redox states of the flavin group, *i.e.* the quinone (fully oxidised), semi quinone (semi-reduced) and hydroquinone (fully reduced) states.

### 1.6.2 Structures and Mechanisms of FNR

As mentioned before, in photosynthetic reactions, FNR is the enzyme that catalyses the production of NADPH by using two electrons previously accepted (one at a time) from reduced ferredoxin (Fd):

$$2\,Fd_{red} + NADP^+ + H^+ \overset{FNR}{\rightleftharpoons} 2\,Fd_{ox} + NADPH \tag{1.6}$$

The fact that FAD can accept one electron first and be in the highly unstable semiquinone radical state whilst 'waiting' for the second electron is very important. Normally this radical is very unstable because of the highly crossed or inverted reduction potentials. But when bound inside FNR, it is stabilised which allows for the two sequential separate single electron transfer events taking the quinone to semiquinone and then to hydroquinone.[161]

The FNR utilised in this thesis is from a single-cell green alga *Chlamydomonas reinhardtii*. It production was optimised by Dr. C. F. Megarity who overexpressed the recombinant enzyme in *E. coli.* (details in Chapter 6).

FNR is a flavoenzyme and the earliest report of it can trace back to 1963 when Shin *et al.* extracted 'impure' FNR from the acetone precipitate of lysed spinach

chloroplasts.[128, 162] By then, NADPH was still referred as the old nomenclature 'triphosphopyridine nucleotide' so that the newly discovered FNR was named ferredoxin-TPN-reductase. FNR is monomeric and hydrophilic with a molecular weight of approximately 38 kDa.[163] The structure of the holoenzyme (FNR in complex with its cofactor, FAD) from *Nostok sp.*, is shown in Figure 1.18. It should be noted that the structure of FNR from *Chlamydomonas reinhardtii* has not been solved yet, but similarity between *Chlamydomonas reinhardtii* and *Nostok sp.* FNR in terms of structure and reaction mechanisms is expected.

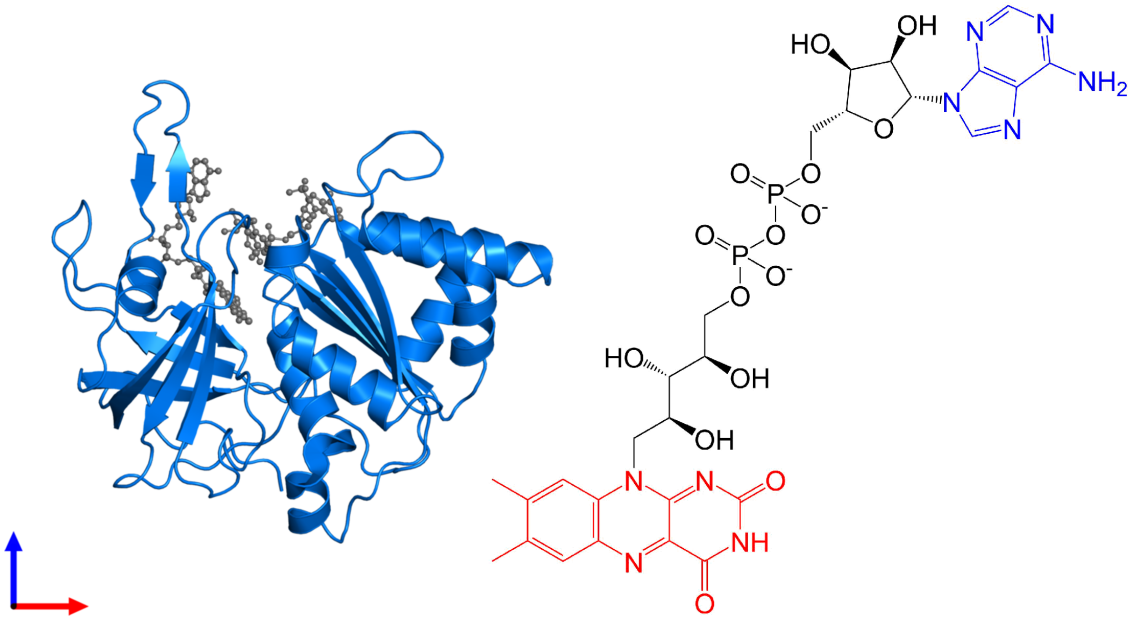



**Figure 1.18 Left:** X-ray diffraction image of FNR from *Nostok sp.*, PDB 1GJR, with the bound FAD and $NADP^+$ shown in gray.[164] **Right:** chemical structure of FAD. The isoalloxazine ring and adenine are shown in red and blue, respectively.

As indicated by Equation 1.6, FNR requires both Fd and $NADP^+$ to carry out catalysis. For plant-type FNRs, their N-terminal and C-terminal, each containing approximately 150 amino acids, are responsible for the binding of FAD and $NADP^+$, respectively.[165]

The binding site for the adenine moiety of FAD (shown in blue in Figure 1.18) differs between FNR variants, whereas the binding site for the isoalloxazine ring moiety (shown in red in Figure 1.18) is highly conserved.[166] The tightly bound FAD is held in place by intermolecular forces *e.g* hydrogen bonds, van der Waals

forces and $\pi$-stacking between the aromatic isoalloxazine ring system and the phenol ring of a tyrosine residue. The properties of FAD change when it is bound in the enzyme. For instance, in the aqueous phase, the free flavin semi-quinone tends to disproportionate but is stabilised by FNR. Also, the standard reduction potential of the bond FAD shifts from –0.22 V to –0.35 V (vs SHE) at pH 7.0.[161]

The adenine moiety of NADP$^+$ is connected to the phosphorylated sugar moiety where the negative charge interacts with positively charged amino acids (lysine, *etc.*). In addition, in order for efficient hydride transfer from FAD to NADP$^+$, the nicotinamide moiety of NADP$^+$ and the isoalloxazine ring of FAD need to be aligned coplanar to each other. For this aligned conformation to happen, a tyrosine residue in the C-terminal that blocks it must be displaced. The electrostatic attraction between the 2'-phosphate group of NADP$^+$ and positively charged residues provides an anchor which ultimately allows NADP$^+$ to remain bound whilst the tyrosine is displaced. On the other hand, the NAD$^+$ lacks the 2'-phosphate anchor; therefore it is unable to overcome the stereo-hindrance due to tyrosine.[161, 167, 168] This is the reason why FNR features much higher selectivity towards NADP(H) over NAD(H) (approx. 30,000 times).[167] Enhanced activity of FNR with NAD$^+$ can be realised by site-directed mutagenesis of the wildtype FNR. In the situation that the tyrosine is replaced by smaller non-aromatic residues like glycine or serine, enhanced interaction between the new FNR variants and NAD$^+$ is obtainable.[168, 169] However, NADP$^+$ can still bind to FNR (but not productive) and thus becomes an inhibitor for NAD$^+$.

The Fd is negatively charged with an excess of amino acids that contain acidic side chains. As for FNR, there is a positive patch to which the negatively charged Fd binds.[170] As a result, electrostatic forces are established to ensure interaction between Fd and FNR. The electrostatically driven binding as described between Fd and FNR facilitates the close alignment of the [2Fe-2S] cluster in Fd to the FAD in FNR, which is *ca.* 6 Å.[170]

The steps of catalytic mechanism for FNR, proposed by C. Batie *et al.* which involves a ternary complex, are as follows:[171–173]

- $NADP^+$ binds with FNR.
- Two reduced $Fd_{red}$ molecules donate their single electron sequentially, through which FNR is reduced (FAD in the hydroquinone state $FADH_2$).
- NADPH regeneration occurs. Hydride transfer is processed through $N_5$ of the reduced $FADH_2$ of FNR and $C_4$ of the nicotinamide ring of $NADP^+$.
- NADPH is released from FNR.

During hydride transfer, the isoalloxazine ring of $FADH_2$ and nicotinamide moiety of $NADP^+$ are almost co-planar with the shortest distance being *ca.* 3.3 Å.[161, 167] This definitely facilitates the reduction of $NADP^+$.

For this mechanism, an interesting and counterintuitive result observed was that the binding of either Fd or $NADP^+$ tends to destabilise the binding of the other with FNR by altering the dissociation constant of FNR with Fd and $NADP^+$. It is thought that this phenomenon could facilitate the release of the oxidised $Fd_{ox}$ following its electron donation to FNR.

## 1.7 The Electrochemical Leaf

### 1.7.1 Protein Film Electrochemistry (PFE)

This laboratory has developed a powerful electrochemical technology – protein film electrochemistry (PFE) over the past several decades, with many pioneering studies being carried out using electroactive oxidoreductases as the electrocatalysts.[114–116, 174] The enzymes adsorbed upon the electrode can form stable protein films where direct interfacial electron transfer (electrode to enzyme) takes place directly without the use of any electron mediator.

As for electrode materials, those possessing biocompatible functionalities including carboxylates and oxides are ideal candidates. On the contrary, many bare metals which tend to denature enzymes are not recommended. A commonly used electrode in PFE is the pyrolytic graphite edge (PGE) electrode.[175–178] After further

modifications, such as the use of carbon nanotubes, and amide linkages,[179–182], stabilisation and immobilisation can be further improved.[183]

PFE allows for the study of redox active enzymes directly. As shown in Figure 1.19, The study of enzymes using PFE involves consideration of:

- The mass transfer of either substrates or products to or away from the active site of the enzymes.
- Interfacial electron transfer between the electrode surface and the redox active centre of the enzyme. This is the step in which the electrons cross a phase boundary.
- Intramolecular electron transfer within the enzymes *via* relay centres, *e.g.* iron-sulphur (Fe-S) clusters.
- Substrate conversion catalysed by the active site of the enzymes.

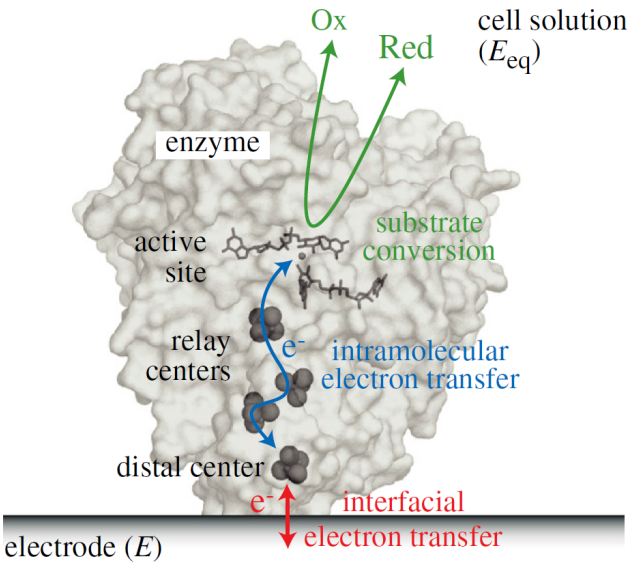



**Figure 1.19** The scheme demonstrating electron flow pathway of an immobilised enzyme upon an electrode surface. $E_{eq}$ denotes the potential where no net current flows through the electrode (*i.e.* the equilibrium potential). Reprinted with permission from F. A. Armstrong *et al.* Copyright 2011, United States National Academy of Sciences.[115]

All these steps can be rate-determining. Cyclic voltammetry, chronoamperometry, electrochemical impedance spectrum and so forth are all useful techniques of PFE. By controlling experimental parameters and variables, informative data regarding thermodynamics, kinetics, as well as inherent properties of enzymes can be extracted.

### 1.7.2 Different Electron Transfer Modes of FNR-catalysed Electrochemistry

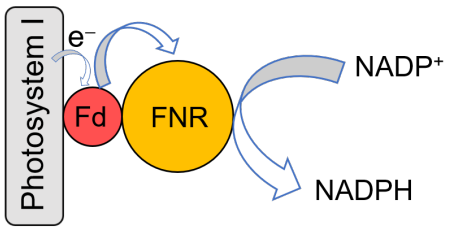
Prior to the pioneering work carried out by Dr. B. Siritanaratkul *et. al.* in this laboratory, most of FNR-related studies using electrochemical methods required an electron mediator as the intermediary agent, *i.e.* in the indirect electroenzymatic mode. This process resembles nature if we consider the Fd to be the mobile mediator (Figure 1.20a), such as the methyl viologen (1.20b).[127–129] We can also draw a parallel between nature and the direct electron transfer by the Electrochemical Leaf (Figure 1.20c) in which the ITO replaces Fd.

One of the most commonly used mediators for FNR are the methyl viologens (MV) (Figure 1.20b). This mediator was chosen since it demonstrates a favourable $E^{0\prime}$ close to that of Fd. As seen in Table 6.1, the reduction potential for the $MV^{2+}/MV^{+\cdot}$ couple is –0.446 V (*vs.* SHE),[184–186] compared to –0.42 V of Fd in spinach FNR.[187] The reduction potentials for other Fds were reported within the range from –0.417 to –0.490 V, which are also similarly close to that of MV.

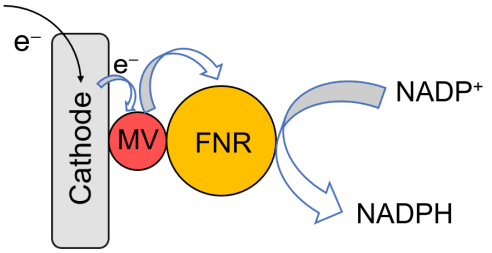
**Table 1.2** Electrode potentials of some half reactions.

| Half reaction | $E^{0\prime}$ / V *vs.* SHE |
|---|---|
| $MV^{2+} + e^- = MV^{+\bullet}$ | –0.446 |
| $MV^{+\bullet} + e^- = MV^0$ | –0.88[128] |
| $Fd_{ox} + e^- = Fd_{red}$ (spinach) | –0.42 |
| $NADP^+ + 2\,e^- + H^+ = NADPH$ | –0.32[24, 188] |

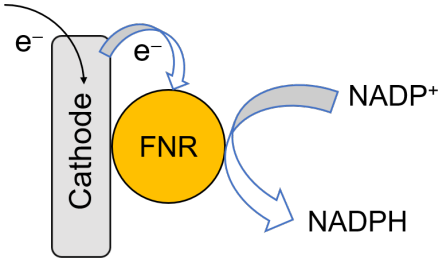
In 1971, T. Kuwana *et al.* detected an appreciable $NADP^+$ reduction current using a MV-mediated system. The experiments were performed using a tin oxide transparent electrode and the catalytic rate was found to be first-order for FNR.[128]




**(a)** In photosynthesis, electron transfer is mediated by Fd.




**(b)** In indirect electroenzymatic approach, a mediator is required and MV is a representative electron mediator.




**(c)** Direct transfer in the Electrochemical Leaf. FNR can mediate electrons directly to/from the electrode. It should be noted that this figure just shows an oversimplified model which does not reflect the true microscopic geometry of the electrode surface. This includes the nanoporous electrode entrapping enzymes within the pores just like the internal nanozones created by chloroplasts. Details will be shown later in this thesis.

**Figure 1.20** Electron transfer to FNR. Also, as for electrochemical methods, one can easily reverse this process by applying a potential more positive than $E_{eq}$ to achieve a $NADP^+$ regeneration scheme such that the electrode turns from an electron source to sink.

An early application of NADPH recycling system for practical organic synthesis was reported by G. Whitesides *et al.*[127] In this case, tungsten and MV served as the electrode materials and electron mediator respectively. This is exactly the case shown in Figure 1.20b. The GLDH was utilised as the cofactor scavenger that consumed NADPH regenerated by FNR. 120 mmol 2-OG was converted to L-glutamate within seven days in a 600 mL reactor containing $NADP^+$ equivalent to 200 mM in the cell solution. The conversion was reported to be 96% with 1,000 as the TTN. Other than MV, electron mediators that can mediate one-electron transfer (for example, like ferrocenemethanol) are also available for FNR. V. Fernández *et al.* reported the surface-modified gold electrode using ferrocenemethanol as the mediator to perform kinetic investigations of FNR-catalysed NADPH oxidation.[189, 190] Here, a mutated FNR was anchored upon the gold surface by the self-assembled monolayer of thiols and electron transfer was mediated by ferrocenemethanol. By doing these experiments, key parameters of heterogeneous catalysis, *e.g.* $k_{cat}$ in different elementary steps were measured and found to be comparable to those measured in homogeneous solution assays, with the conclusion that the immobilisation of FNR would not alter its catalytic function.

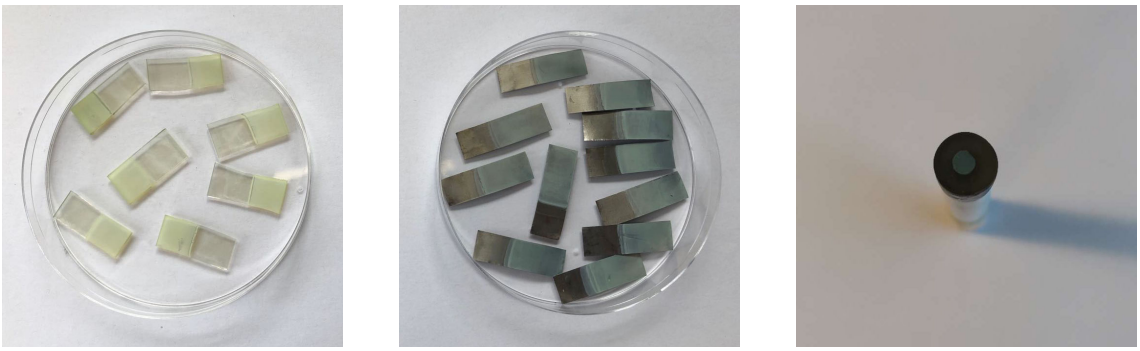
The avoidance of electron mediators allows one to study the direct electron transfer between FNR and the electrode; the Electrochemical Leaf (Figure 1.20c) facilitates this.

### 1.7.3 Principle of the Electrochemical Leaf

The electrode fabricated *via* electrophoretic deposition of ITO nanoparticles upon a conductive support, *e.g.* pyrolytic graphite edge (PGE), titanium foil, or transparent ITO glass (shown in Figure 1.21, hereafter referred as ITO/PGE, ITO/Ti-foil and ITO/ITO-glass), is capable of transferring electrons *via* a potentiostat to/from FNR.[3] This obliterates the need for mediators like Fd and MV exploited in natural photosynthesis and indirect electroenzymatic approaches. In previous work by

[3]Electrochemical results and the process of enzyme immobilisation will be shown later in this chapter and details of electrode formation will be shown in Chapter 6.

Siritanaratkul *et al.*,[118] an attempt was made to adsorb FNR directly onto a PGE electrode (*i.e.* without an ITO coating). FNR failed to show activity using this electrode. A reasonable hypothesised explanation was that the $\pi$-$\pi$ stacking between the graphite and the isoalloxazine ring system promoted the dissociation of the FAD cofactor. Unlike the PGE electrode, the surface of electrophoretically deposited ITO is hydrophilic like Fd; thus the binding of FNR is favoured. The isoelectric point of ITO is 6.0, meaning that at higher pH than 6.0, the surface of ITO is negatively charged. This resembles the negatively charged Fd which allows FNR to bind using the positively charged area on its surface. Figure 1.22 shows scanning electron microscopy (SEM) images of the surface morphology of the ITO/ITO-glass. This clearly demonstrates the rough and nanoporous nature of the ITO layer.



**(a)** ITO/ITO-glass **(b)** ITO/Ti-foil **(c)** ITO/PGE

**Figure 1.21** Photographs of ITO coated electrode supports. **Left:** ITO deposited on ITO glass, **Middle:** ITO deposited on Ti foil, **Right:** ITO deposited on PGE.

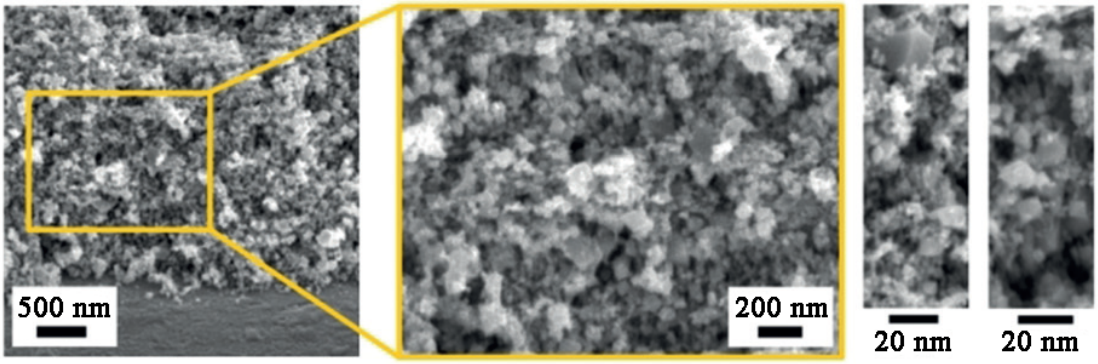



**Figure 1.22** The cross-section of the scanning electron microscopy images of ITO layer deposited upon the conductive support *via* electrophoresis. Reprinted with permission from C. F. Megarity *et al.* Copyright 2019, Wiley.[169]

The fact that the nanopores of ITO electrode can entrap a large number of FNR and downstream enzyme molecules is markedly different from the situation where a mono-layer of enzyme molecules are simply immobilised upon the electrode surface. In the latter case, as reported by many studies before, enzymes are anchored on a two-dimensional plain and the diffusion of reactants and products to and from the electrode respectively, is three-dimensional. For the nanoporous electrode of the Electrochemical Leaf, the space that holds the enzymes and reactants is a three-dimensional matrix, just like the nanoconfined space in the natural leaf. The diffusion pattern for the reactants and products now becomes one-dimensional.[191]

Figure 1.23 illustrates the processes with respect to NADP(H) regeneration in the biological leaf directly compared to the Electrochemical Leaf. For the biological leaf, the details of the mechanism have been introduced previously. For the Electrochemical Leaf, the potentiostat serves as the electron source/sink and electrons are mediated to/from the electrode by the NADP(H) transducer FNR – the E1 of the cascade. The second enzyme (abbreviated as E2) and possibly the third, fourth or even fifth enzymes (E3, E4, E5) together with FNR ideally are all randomly close-packed and confined within the tiny nanozones. The reduced and oxidised forms of the nicotinamide cofactor can thus be rapidly shuttled between FNR and the downstream NADP(H)-dependent enzyme. Along with the enzymes, the cofactor molecules are also partially retained within the nanopores and the distance they must travel between enzymes is shortened substantially, much resembling a volleyball that is passed by players back and forth within the playing field.

The nanoporous ITO layer upon the conductive support, FNR, together with E2 is the basic unit of the Electrochemical Leaf and hereafter is referred to as (FNR + E2)@ITO/support for simplicity.

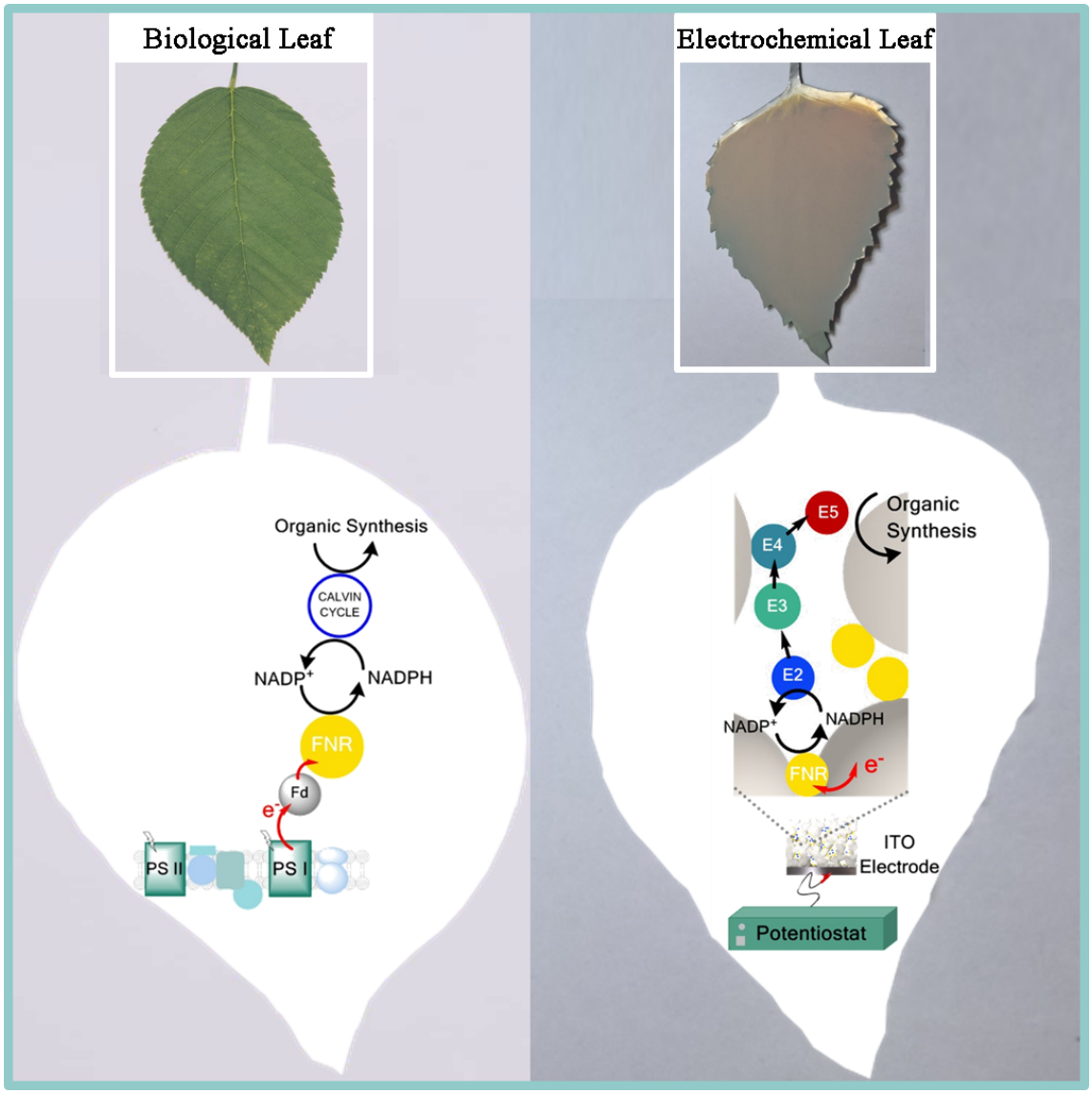



**Figure 1.23** Schematic drawings for the NADP(H) recycling in **Left:** the biological leaf and **Right:** the Electrochemical Leaf. Reprinted with permission from C. F. Megarity *et al.* Copyright 2019, Wiley.[169]

### 1.7.4 Electrochemistry of Electrochemical Leaf

#### *1.7.4.1 Methods of Loading Enzymes*

In this thesis, there are mainly two methods to immobilise enzymes into the ITO nanopores.

**By dropcasting** An aliquot of concentrated enzyme is dropped upon the bare ITO/support electrode, and then uniformly cast or painted across the surface of the ITO layer to make sure that enzyme droplets fully cover the whole area of the electrode. This process is usually operated using a pipette tip and care should be taken not to scrape off any of the ITO surface. After incubation for a while, the electrode is rinsed by either Milli-Q water or buffer to wash away any unbound enzymes.

**From dilute enzyme solution** The electrode is suspended inside a vial containing stirred dilute enzyme solution. The whole set-up is placed in the cold room (4 °C) overnight to allow enzyme adsorption into the ITO nanopores. The electrode should be rinsed by either Milli-Q water or buffer before use, again, to remove any unbound enzyme molecules. Enzyme adsorption from dilute solution can also be monitored by placing a bare ITO electrode in an electrochemical cell and measuring the increase in current (enzyme catalytic rate) over time as enzyme molecules adsorb into the pores until a maximum current is obtained.

These two methods both have their advantages and are exploited for different purposes in this thesis. The immobilisation of enzymes by dropcasting is more straightforward and the time required is very short, varying from several seconds to one hour. When electrochemical measurements are initiated after the implementation of this method, the best achievable catalytic current for the exact reaction can be obtained shortly. This is because all enzyme molecules required for catalysis have been in position within the nanopores. While for the second method, the immobilisation process might take hours to finish. When the introduction of enzymes is carried out

during the electrochemical measurement, as mentioned before, this process can be visualised using electrochemical methods. In this thesis, while both FNR and E2 can be loaded together using either the 'by dropcasting' or the 'from dilute enzyme solution' method, experiments can be operated using a combination of these two methods. As will be shown repeatedly later, one can first immobilise one enzyme (either E2 or FNR) and monitor the process that the incoming enzyme molecules are immobilised (by injection) using electrochemistry.

#### *1.7.4.2 Non-turnover Signals of FNR*

As shown in Figure 1.24, the cyclic voltammetry (CV) measurement of a piece of bare ITO/ITO-glass electrode (black trace, active surface area = 1 $cm^2$) carried out at pH 9.0 in 50 mM TAPS buffer, with 1 mV $s^{-1}$ as the scan rate, does not display any catalysis-linked signal. The trapezoid-like background derives from the charging and discharging behaviour of capacitance.[4] As no interfacial electron transfer occurs, this portion of current is generally termed as non-faradaic current.

When FNR is adsorbed, the faradaic current encompasses two forms: the non-catalytic (non-turnover) current and catalytic (turnover) current. The non-catalytic (non-turnover) peaks (red trace of Figure 1.24) corresponds to the cooperative two-electron reduction and oxidation of the FAD cofactor (Figure 1.17). The redox peaks occur at approximately –0.42 V *vs* SHE is the electrode potential for the flavin group. The area under each peak after subtracting the baseline can be calculated by integration and the average area for the two peaks links to the amount of FNR (in a redox active conformation) adsorbed. The area under the peaks is proportional to the number of FNR molecules entrapped within the ITO nanopores with the relation:[5]

$$\int I \mathrm{d}E = nFA\Gamma_0^*\nu \tag{1.7}$$

where $n$ is the number of electron transferred in the chemical equation, $F$ is the

[4]Details are available in Section 6.1.2 of Chapter 6.
[5]Derivation of this equation is available in Appendix B.

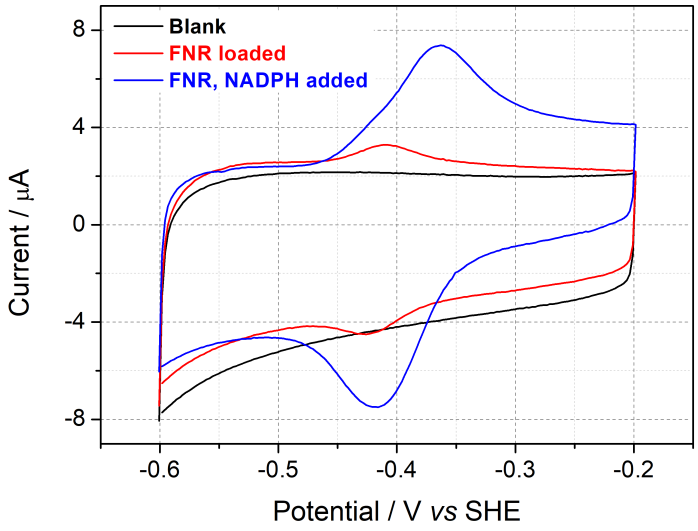



**Figure 1.24** Non-turnover and turnover signals for FNR. **Black trace:** the cyclic voltammogram of a bare ITO/ITO-glass electrode. **Red trace:** the cyclic voltammogram after FNR was loaded upon the electrode. **Blue trace:** the cyclic voltammogram after NADPH was injected to give a final concentration of 50 $\mu$M. FNR was introduced *via* dropcasting. The cell solution was purged by Ar prior to the measurement. Experimental conditions: active surface area of FNR@ITO/ITO-glass electrode = 1 cm$^2$, buffer = 50 mM TAPS, pH =9.0, 25 °C, scan rate = 1 mV s$^{-1}$.

Faraday constant, $\Gamma_0^*$ refers to the surface coverage of FNR and $\nu$ is the scan rate. In the case shown in Figure 1.24, the coverage of FNR is 230 ± 20 nM $cm^{-2}$. Generally speaking, the coverage of FNR is pH- and ionic-strength-dependent. The FNR coverage being linked to pH is partially due to electrostatic attraction. As mentioned before, at pH values higher than the isoelectric point 6.0, the ITO layer is negatively charged, which is ideal for the adsorption of FNR. At lower pH values the ITO surface charge becomes less negative thus the adsorption of FNR becomes less favourable.[117, 118]

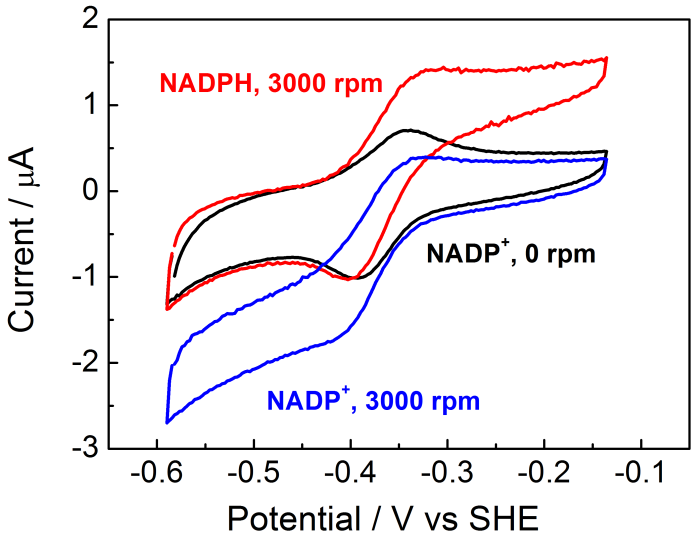
#### *1.7.4.3 Interconversion of NADP$^+$/NADPH catalysed by FNR*

The injection of NADPH to 50 $\mu$M in the bulk solution (blue trace of Figure 1.24) leads to much larger current corresponding to the FNR-catalysed quasi-reversible interconversion between $NADP^+$ and NADPH. As direct electron transfer occurs without the use of Fd, the reaction becomes:

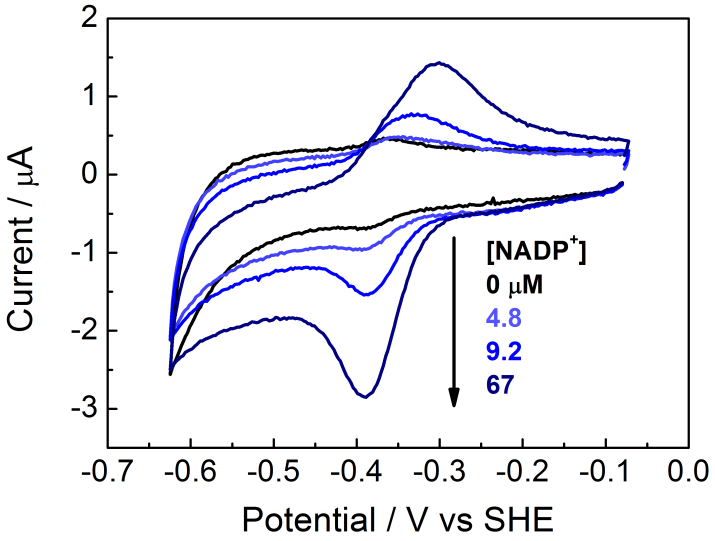
$$NADP^+ + H^+ + 2\,e^- \overset{FNR}{\rightleftharpoons} + NADPH \tag{1.8}$$

It should be noted that the cofactor added was the reduced form NADPH which undoubtedly gives rise to a sharp oxidation peak; an equally large reduction peak corresponding to $NADP^+$ reduction is also observed on the return scan, because for a stationary electrode, *i.e.* diffusion-controlled, the $NADP^+$ produced in the oxidative scan is not spun away from the electrode and therefore is available for the FNR to reduce in the reductive scan. The shape of CV is almost the same when using $NADP^+$ as the initially injected cofactor (not shown here).

On the other hand, when the electrode is rotated at adequately fast speed such that the rate-determining step is no longer diffusion-controlled, the substrate or product of FNR is dispelled into the bulk solution, making it unavailable as a substrate for FNR on the return scan. In this situation, the shape of cyclic voltammogram corresponding to NADPH production would differ from the one for $NADP^+$ production when initiating with different redox forms. This was proved




**(a) Black trace:** stationary electrode with 50 $\mu$M $NADP^+$ present. **Blue trace:** electrode with 50 $\mu$M $NADP^+$ present, 3,000 rpm. **Red trace:** electrode with 50 $\mu$M NADPH present, 3,000 rpm. Scan rate = 1 $mV^{-1}$.




**(b)** Effects of $NADP^+$ concentration, stationary electrode. Scan rate = 5 $mV^{-1}$.

**Figure 1.25** Cyclic voltammograms showing the FNR-catalysed interconversion between $NADP^+$ and NADPH using an FNR@ITO/PGE electrode. Experimental conditions: buffer = 25 mM MES + 25 mM TAPS, pH = 8.0, 20 °C. Measurements were performed after the solution was purged by Ar. Reprinted with permission from B. Siritanaratkul *et al.* Copyright 2017, Royal Society of Chemistry.[117]

by B. Siritanaratkul *et al.*[117] As shown in Figure 1.25a, the peak-like CVs for FNR catalysis of $NADP^+$ reduction (blue trace) and NADPH oxidation (red trace) collapse to sigmoidal waves when the electrode was rotated.[117] When the electrode was stationary (black trace, with $NADP^+$ as the substrate introduced), the peak-like feature of the CV would reappear. The magnitude of the catalytic peaks was also related to the [$NADP^+$]. As expected (Figure 1.25b), the increase of [$NADP^+$] led to enhanced reduction current and oxidation current on the return scan.

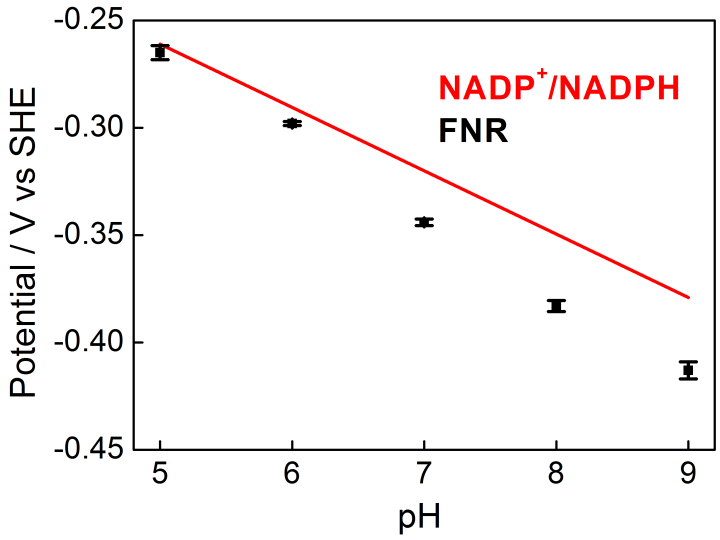



**Figure 1.26** The comparison of the reduction potential for FNR (black trace) to that for the $NADP^+$/NADPH couple (red trace). Reprinted with the permission from B. Siritanaratkul *et al.* Copyright 2017, Royal Society of Chemistry.[117]

This reduction potential of the $NADP^+$/NADPH couple is pH-dependent with –30 mV for every pH decrease as this process involves one proton for two electrons that are transferred. FNR and $NADP^+$/NADPH reduction potentials at different pH are shown in Figure 1.26. At pH values higher than 5.0, the reduction potential of FNR starts to become more negative than that of the $NADP^+$/NADPH couple and this trend tends to expand at more basic pH values. This suggests that at physiological pH, the FNR-catalysed reaction slightly favours $NADP^+$ reduction than NADPH oxidation.

#### *1.7.4.4 FNR Catalysis Coupled to a Second Enzyme*

When a NADP(H)-dependent second enzyme along with the substrates are introduced into the pores, the downstream reaction occurs and meanwhile, FNR starts to regenerate the cofactor required by E2 such that fast enzyme-catalysed cascades are established (Figure 1.23). Depending on the applied potentials, the reaction can be either **reduction** (*i.e.* NADPH is regenerated by FNR from $NADP^+$) or **oxidation** (*i.e.* $NADP^+$ is regenerated by FNR from NADPH). The downstream reaction catalysed by the second enzyme consumes the regenerated nicotinamide cofactor molecules, whilst produces the product.

**NADPH regeneration** I here take the GLDH-catalysed reductive amination as an example. The reaction catalysed by the GLDH from *E. coli.* is:

$$\text{2-oxoglutarate} + {NH_4}^+ + \text{NADPH} \longrightarrow \text{L-glutamate} + H_2O + NADP^+ \tag{1.9}$$

The electrode process – the FNR-catalysed $NADP^+$ reduction (Equation 1.8) – is coupled to the downstream reaction catalysed by E2 (GLDH). Because its product is NADPH which serves as the substrate for the coupling reaction shown in Equation 1.9 through which NADPH is oxidised back to $NADP^+$, NADPH can thus be regenerated continuously, with the reductive amination product L-glutamate being the net product. The net reaction after coupling Equations 1.8 and 1.9 is:

$$\text{2-oxoglutarate} + {NH_4}^+ + H^+ + 2\,e^- \longrightarrow \text{L-glutamate} + H_2O \tag{1.10}$$

This regeneration scheme resembles the so-called EC′ mechanism,[6] in which E stands for an electrochemical process, C is a homogeneous reaction and the 'prime' (′) refers to a catalytic process.

Figure 1.27 shows CVs for the coupled catalysis of an (FNR + GLDH)@ITO/PGE electrode. In this experiment the adsorption of GLDH to the porous electrode was

[6]Details of the EC′ mechanism is introduced in Section 6.1.2.4 of Chapter 6.

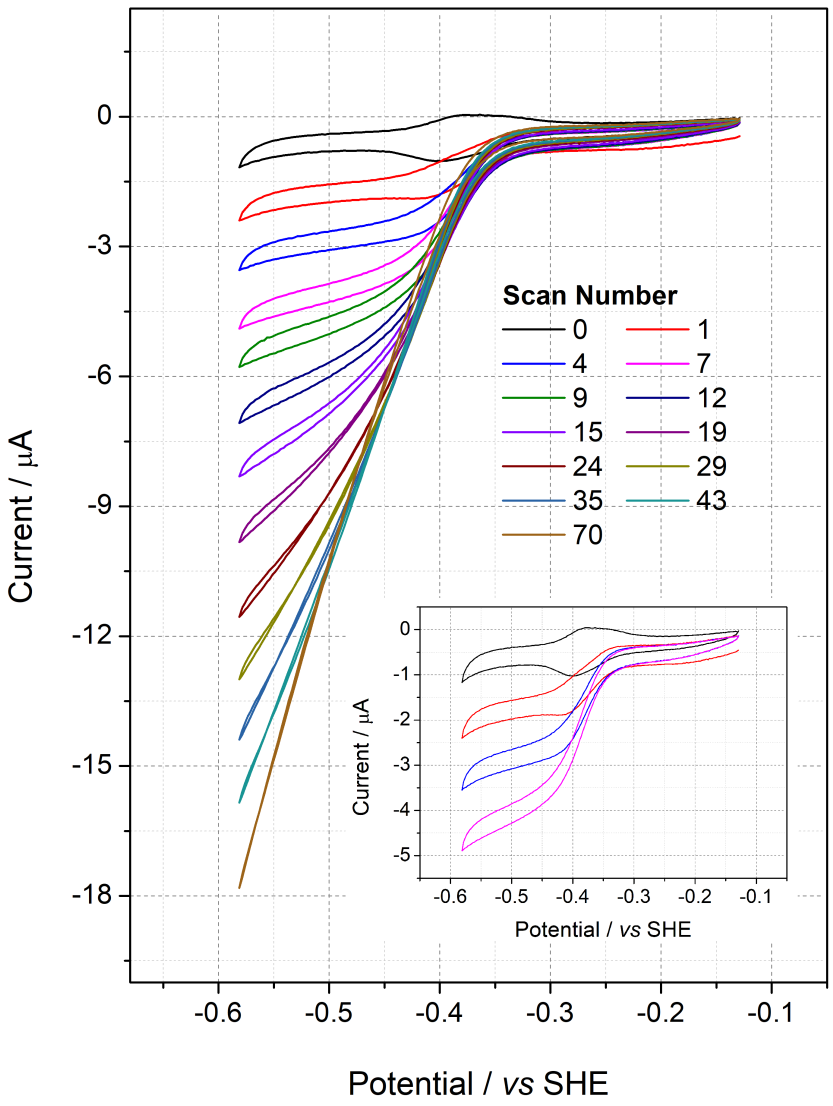



**Figure 1.27** Cyclic voltammograms of reductive amination of 2-oxoglutarate (2-OG) catalysed by an (FNR + GLDH)@ITO/PGE electrode at pH 8.0. A aliquot of 10 $\mu$L FNR (775 $\mu$M) was dropcast on the PGE electrode (0.06 $cm^2$) for 3 minutes, the surface of which was then rinsed by required buffer before use. Catalysis was initiated by injecting 10 $\mu$L GLDH to give final concentration of 870 nM in the cell solution which had been pre-charged with 20 mM 2-OG, 30 mM $NH_4Cl$ and 20 $\mu$M $NADP^+$. The whole measurement last for 70 scans among which the representative ones are plotted. Argon was used to purge the headspace of the cell throughout. Other experimental conditions: scan rate 3 mV $s^{-1}$, cell volume 3 mL, 50 mM TAPS buffer, 25 °C. Adapted with permission from B. Cheng *et al.* Copyright 2020, Wiley.[192]

monitored by cyclic voltammetry (rather than the typical approach of preloading and rinsing so that no E2 enzyme is present in solution). The FNR@ITO/PGE electrode (surface area = 0.06 $cm^2$) was fabricated by dropcasting an aliquot of concentrated FNR solution (775 $\mu$M) upon the PGE electrode, which was rinsed thoroughly before use. The cell (3 mL) was charged with 20 mM 2-OG and 30 mM $NH_4Cl$ initially and the injection of $NADP^+$ gave rise to the quasi-reversible interconversion between $NADP^+$ and NADPH (the black trace, scan 0). The live injection of an aliquot of 10 $\mu$L GLDH (260 $\mu$M, equivalent to 870 nM in the cell solution) then triggered an enhancement of current due to fast regeneration of NADPH, as $NADP^+$ – the byproduct of reductive amination – was continuously replenished to FNR. Compared to a classical EC′ model where the coupled homogeneous catalytic reaction C′ occurs in the bulk solution, the gradual enhancement of current cycle after cycle should be exclusively due to the adsorption of GLDH in the pores where both enzymes are confined. When more GLDH molecules are present in the nanozone, one would expect larger current to be observed because there are more homogeneous catalysts available. As GLDH was initially injected into the bulk solution, it took time for GLDH molecules diffusing into the pores. This results in the increase of reduction current scan by scan. As shown in the inset, the red, blue and magenta traces correspond to the results of scan 1, 4, and 7, and it is clear that the electrocatalytic current continuous increased. This trend continued in the rest of the measurement, with the largest reduction current reaching 18 $\mu$A at scan 70. As each scan took three minutes to go through, approximately 3.5 hours were required to achieve a sweet point where the ratio of FNR:GLDH can support the best achievable activity. Also, it is observed that this cascade was eventually limited by FNR that regenerates NADPH. However, this does not necessarily mean that GLDH is inherently more active than FNR, since the actually ratio of FNR:GLDH is still unknown.

**$NADP^+$ regeneration** In this scheme, the coupled reaction requires $NADP^+$ as the cofactor. A typical reaction is the oxidation of secondary alcohols catalysed by *sec*-ADH. I here use a variant of the *sec*-ADH from *Thermoanerobacter ethanolicus*

39E (TeSADH W110A) as an example.[7] The reaction to be catalysed by ADH is as follows:

$$(S)\text{-4-phenyl-2-butanol} + \text{NADP}^+ \rightleftharpoons \text{4-phenyl-2-butanone} + \text{NADPH} + \text{H}^+ \quad (1.11)$$

Similar to NADPH regeneration, the $NADP^+$ required for this coupled reaction can be continuously supplied by FNR *via* applying an oxidative potential such that 4-phenyl-2-butanone is produced as the net product. The net reaction after coupled Equations 1.8 and 1.11 is:

$$(S)\text{-4-phenyl-2-butanol} \rightarrow \text{4-phenyl-2-butanone} + 2\text{H}^+ + 2\text{e}^- \quad (1.12)$$

Figure 1.28 shows the CV for the (FNR+ADH)@ITO/ITO-glass-catalysed electrocatalysis. In contrast to the example shown in Figure 1.27, the electrode here was formed by dropcasting an aliquot of concentrated FNR and TeSADH W110A mixture. The electrode was incubated at 4 °C for 10 minutes and rinsed thoroughly by buffer before use. The black trace shows the interconversion of $NADP^+$/NADPH by FNR with 50 $\mu$M NADP(H) present. The measurement was paused and an aliquot of pure $(S)$-4-phenyl-2-butanol was injected to give a final concentration of 5 mM. Upon resuming the measurement the plot shows an immediate large oxidation current due to alcohol oxidation (which in turn replenishes NADPH back to FNR giving rise to the oxidative current). In this case, the dropcasting method ensures there are no enzyme molecules in solution and therefore the same growth in current observed in Figure 1.27 does not occur here, which results in the best achievable electrocatalytic current at the very beginning of the measurement.

[7] The *sec*-ADH TeSADH W110A will be frequently used in this thesis. Detailed experiments and properties of this enzyme will be shown in later chapters.

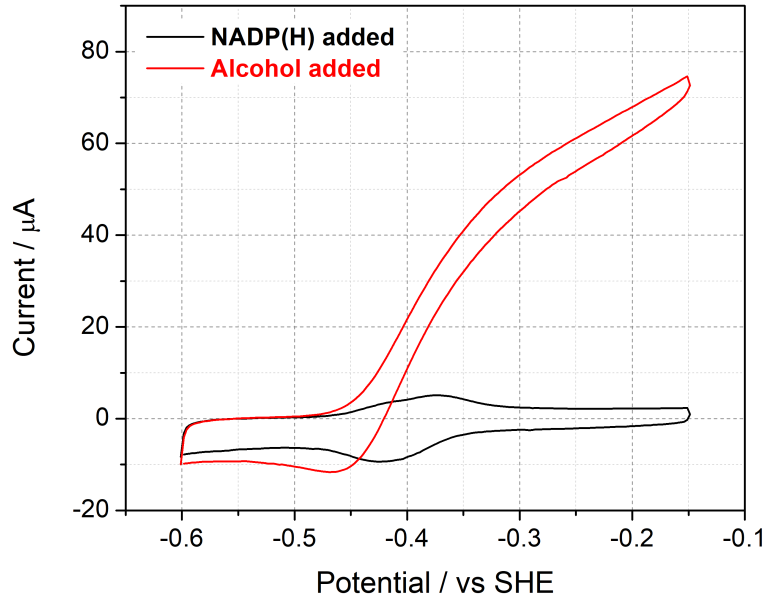



**Figure 1.28** The cyclic voltammogram of alcohol oxidation to ketone catalysed by an (FNR + *sec*-ADH)@ITO/ITO-glass electrode at pH 9.0. An aliquot of 2.4 $\mu$L FNR (1.96 mM) and 6.2 $\mu$L (70.5 $\mu$M) TeSADH W110A was dropcast upon a piece of ITO glass (1.0 $cm^2$), which was incubated in a glass vial on ice for 10 min. The electrode surface was rinsed thoroughly by TAPS (pH = 9.0) buffer before use. **Black trace:** a 1:1 mixture of $NADP^+$:NADPH (25 + 25 $\mu$M) in the cell solution. **Red trace:** the measurement after an aliquot of (*S*)-4-phenyl-2-butanol (equivalent to 5 mM) was injected into the cell solution. Experimental conditions: scan rate 1 mV $s^{-1}$, cell volume 8 mL, 50 mM TAPS buffer, 25 °C. Ar was used to purge the headspace of the cell throughout.

### 1.7.5 Proof of Nanoconfinement

In previous sections, the basic concepts and observable phenomena of the (FNR + E2)@ITO/support electrode under nanoconfinement that mimics the natural leaf have been outlined using previously published work that employed cyclic voltammetry. This section again uses previously published work by C. F. Megarity *et al.*[163] to outline the work which provided direct and convincing proof of nanoconfinement, this time employing chronoamperometry.

The result of experiment investigating the nanoconfinement of whether enzymes and NADP(H) molecules in the ITO pores during measurement is shown in Figure 1.29. Compared to cyclic voltammetry, results from chronoamperometric test are more intuitive and straightforward. With this technique, the electrocatalytic reaction rates at steady state are quantifiable with the relation '$r \propto \frac{I}{2F}$'[8] where $r$ stands for reaction rate, $F$ is the Faraday constant 96,485 A mol$^{-1}$, and $I$ is the current that is monitored. This method will be frequently used in this thesis for electrochemically driven biosynthesis.

The growth in current observed was attributable to the adsorption of ADH into the pores and that at maximum current the buffer was exchanged to remove the ADH in solution (whilst maintaining the alcohol substrate). Despite the fact that the NADPH was not maintained after buffer exchange, the current did not return to zero indicating that some must still have been present in the pores (and also E2 must have been retained as well). When NADPH was re-introduced again to its original concentration the current was restored despite there now being no ADH in solution. This work provided the first evidence that indeed both enzymes were nano-confined in the pores and that reactants were also partially retained.[163]

This experiment had confirmed the following facts:

- Both FNR and ADH are not required in the solution for the building of electrocatalysis. After the exchange of new buffer and thorough rinsing of the electrode, the cell solution does not contain enzymes anymore. On this occasion,

[8]Details of this relation are available in Section 6.1.3 in Chapter 6.

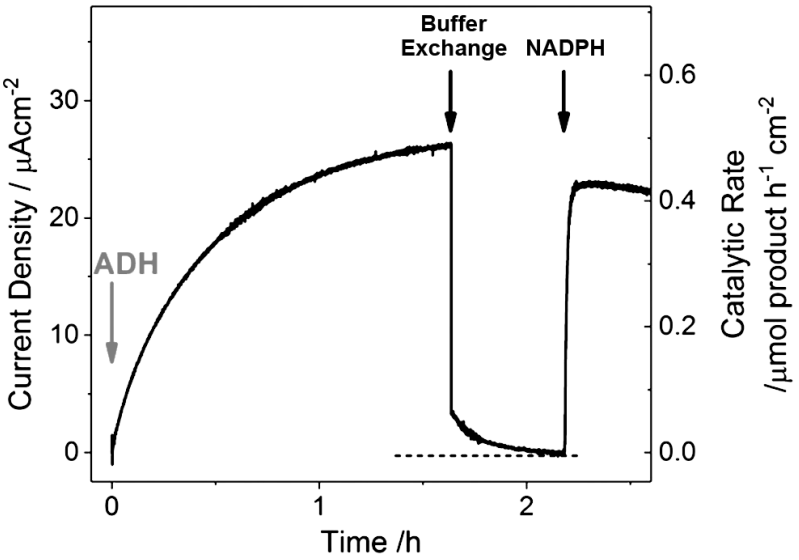



**Figure 1.29** The timecourse to study confinement of TeSADH W110A and retention of $NADP^+$ within the ITO nanopores before and after buffer exchange. The measurement was carried out using a rotating PGE electrode. The substrate (20 mM (*S*)-4-phenyl-2-butanol) and cofactor (5 $\mu$M NADPH) were present at the start. This was followed by TeSADH W110A injection to give a final concentration of 0.3 $\mu$M. After buffer exchange, the [NADPH] was re-injected to a final concentration of 5 $\mu$M where indicated by an arrow. Argon was used to purge the headspace of the cell throughout. Experimental Conditions: potential = +0.08 V *vs* SHE, TAPS (50 mM) + MES (50 mM) buffer, pH = 8.0, cell volume = 3 mL, 20 °C. Reprinted with permission from C. F. Megarity *et al.* Copyright 2019, Wiley.[163]

the resurgence of large current after the re-injection of NADPH suggested that the electrocatalytic current did not originate from anything but from enzymes bound within the pores.

- Only a tiny amount of NADP(H) ranging from 5–20 $\mu$M is required to drive rapid electrocatalytic reaction. This is an intriguing result due to nanoconfinement as the working [NAD(P)(H)] of other classical systems usually ranges from micro- to milli-molar.

- Compared to FNR and E2, NADP(H) tends to be loosely retained within the ITO nanopores.

The current that is monitored using chronoamperometry technique is an important metric to see how fast the reaction rate is changed by live intervention *via* the altercation of experimental parameters. This includes the injection of enzyme/substrate/product/inhibitor, the introduction of hydrodynamic force to the electrode (rotating the electrode or stirring the cell solution), the increase/decrease of temperature, *etc.*

## 1.8 Conclusion and Perspectives

A self-sufficient nicotinamide recycling process is critical for biosynthetic reactions involving NAD(P)H-requiring enzymes. Compared to NAD(H), the regeneration scheme of the phosphorylated version NADP(H) is less developed, which is partly because NAD(H) accounts for a larger group of oxidoreductase-catalysed reactions and NAD(P)(H) is much more precious and less stable.

This chapter has introduced common methods for NAD(P)(H) regeneration and by far the most successful method is the enzymatic method. The unique features of enzymes have avoided many side effects that could be encountered in other methods. For NADP(H) alone, the well-studied enzyme to recycle the reduced form NADPH is GDH, while for the oxidised form GLDH has been one of the best choices. However, as mentioned before, the enzymatic method is not flawless. The cost of

the raw materials, including the enzymes and the recycled NAP(P)(H) has been an issue, which is aggravated when the scale of biosynthesis is increased. A stark difference between chemical science on the bench and chemical science engineered on a large scale is that many fancy laboratory-scale experiments cannot be replicated in larger scale, as the reaction rate usually fails to scale up linearly. Therefore, when considering a scaled-up scheme for NAD(P)(H)-dependent biosynthesis, one must consider the following factors:

- **Cost** A trade-off has to be made between the cost and efficiency in many cases to make a chemical reaction 'cost-effective'.
- **TTN** A TTN that is larger than 1,000 is the benchmark for an efficient nicotinamide cofactor regeneration system. The point of this criterion is clear, as the cost of nicotinamide cofactor is very high, especially for the reduced form NAD(P)H.
- **Durability** The enzymes and cofactors involved in the biosynthesis should be stable during the reaction. For this purpose, the pH, temperature, solvent, as well as bio-compatibility all have to be considered.
- **Product separation** As the title suggests, a biosynthetic reaction is better to be as much 'clean' as possible. This is the reason why using $H_2$ or $O_2$ as the electron donor or acceptor is conceptually interesting, as after electron transfer, ideally the only byproduct would be $H_2O$ or protons.
- **Environment** The use of toxic and eco-unfriendly reactants should be avoided. This is also an advantage of biocatalysts.

Taking the above factors into consideration, a strategy combining advantages of different methods has been increasingly appreciated. Recently, in the Armstrong group, a flavoenzyme FNR has been proven to be an electrocatalyst for direct quasi-reversible interconversion of $NADP^+$/NADPH on the electrode. The enzyme and the modified electrode as a whole is coined the 'Electrochemical Leaf', which itself mimics

the mechanisms of the natural leaf. In nature, FNR relies on the Fe-S protein Fd to mediate electrons. In the Leaf system, this is replaced by the negatively charged and bio-compatible ITO nanoporous layer that is electrophoretically deposited on conductive supports, such as graphite, ITO glass, or Ti. The essence of the Electrochemical Leaf is that biosynthetic enzymes are entrapped along with the transducer FNR within the nanoporous indium tin oxide (ITO) layer such that coupled catalysis can be dramatically sped up by the effect coined as 'nanoconfinement'.

As opposed to traditional homogeneous biosynthesis, the Electrochemical Leaf has the following advantages:

- Usually only 5–20 $\mu$M precious NADP(H) is required to establish efficient catalysis.
- In tandem with electrochemical methods, reactions can be controlled and monitored *in situ*, especially the rate and yield.
- Competent total turnover numbers (TTN) are attainable. This fact will be shown later.
- The raw materials of electrodes are inexpensive, eco-friendly and recyclable.
- Enzymes are not required in the bulk solution for effective electrochemistry.

From the next chapter, interesting applications and analytical measurements of the Electrochemical Leaf will be presented, which include the hydrogen-driven and the air-driven biosynthetic reactions operated under the fuel cell mode, detailed kinetic studies and the development of novel deracemising and racemising strategies.

# Chapter 2

# A $H_2$-driven Fuel Cell Scheme for NADPH Regeneration

## Abstract

The oxidation of hydrogen ($\frac{1}{2}\mathbf{H_2} \rightarrow \mathbf{H^+} + \mathbf{e^-}$) is a very important reaction. In this chapter, a series of exciting experiments in which the Electrochemical Leaf is powered, for the first time, by $H_2$, are demonstrated. The reactor works in a fuel-cell mode with a two-electrode and one-pot set-up. The Electrochemical Leaf works as the cathode which **(i)** uses electrons to interconvert $NADP^+$/NADPH; **(ii)** couples the cofactor recycling to a second entrapped enzyme that requires NADPH. The anode is a piece of platinised carbon paper (PCP) which catalyses the oxidation of $H_2$. The quasi-reversible FNR-catalysed $\mathbf{NADP^+ + H^+ + 2e^- \rightarrow NADPH}$ is kinetically fast, demonstrated by a minimal overpotential requirement and more than 10,000 TNN being achieved.

## 2.1 Introduction: FNR-Catalysed Biosynthetic Fuel Cell

### 2.1.1 Enzymatic Fuel Cells

By definition, a fuel cell is an electrochemical device that converts chemical energy into electrical energy by oxidation of the fuel. The overall reaction requires a pair of redox reactions and continuous supply of fuel and oxidant. Fuel cells are operated under a two-electrode set-up: an **anode** where oxidation of fuel occurs and a **cathode** where reduction of the oxidant occurs. Figure 2.1 shows the scheme that illustrates the interrelationship between potential and current when measuring the polarisation curves of anode and cathode reactions separately. When overlaying the corresponding polarisation curves on a current *vs* potential plot or *I*-*V* plot, the open circuit potential (OCP) reflects the potential difference when no net current flows through the two electrodes. As the name OCP suggests, ideally its value can be measured when the switch is off. The cell potential is the working potential of the cell and the value is smaller than the OCP because some driving force is used due to the polarisation behaviour of both electrodes to allow the flow of current.

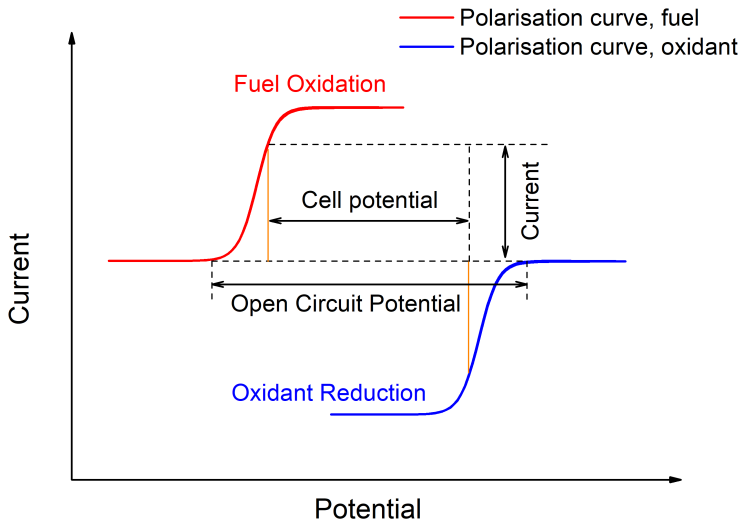



**Figure 2.1** An illustration of the separate oxidation and reduction half reactions of a fuel cell as a function of potential.

Fuel cells can be classified by the electrolyte used, such as alkaline fuel cells,[193,

194] phosphoric acid fuel cells,[195, 196] and solid oxide fuel cells.[197] Fuel cells can also be classified based on their catalysts, for example, conventional (using inorganic or organic synthetic catalyst) fuel cells, microbial fuel cells [198, 199] or, as presented in this chapter, enzyme-based fuel cells which use purified enzymes as the electrocatalyst.[200–202] The latter are distinct from microbial fuel cells which take a whole-cell approach.

While the same underlying electrochemical rules are shared by all types of fuel cells, the enzyme-based fuel cell has some unique features due to intrinsic properties of redox enzymes, with both merits and demerits.

**Advantages** **First**, enzymes are highly selective and efficient catalysts. For example, as used in this work, the secondary alcohol dehydrogenases (*sec*-ADH) are especially active on secondary alcohols with only limited activity on primary alcohols. Hydrogenase enzymes, as their name suggests, exclusively use hydrogen or protons – a feature that leads to a simplified and much less expensive fuel cell as it rules out the necessity for an ion-exchange membrane barrier because the crossover of fuel and oxidant is no longer a concern.[203, 204] **Second**, enzymes are kinetically efficient. Many enzymes can substantially lower the overpotential required to drive a reaction.[115, 161] When using electroactive enzymes as electrocatalysts, the cases of fully reversible and quasi-reversible reactions are common, like the interconversion of the $2H^+/H_2$ couple catalysed by [NiFe]-hydrogenase and the interconversion of the $NADP^+$/NADPH couple catalysed by FNR in this thesis. Even the kinetically sluggish four-electron reduction of $O_2$ is made efficient by the enzyme bilirubin-oxidase, requiring an overpotential of only 0.3 V, outperforming the well-established Pt.[205] **Third**, enzymes are eco-friendly electrocatalysts. Currently, the main component of conventional electrocatalysts contain transition noble metals like Pt, Ir, Ru, *etc.* In contrast, the chief elements that make up the skeleton of enzymes are C, H, O, N and S. Trace elements like Ni, Fe, Zn are also sometimes required as cofactors, but only in minute amounts. For example, [NiFe]-hydrogenase contains Ni and Fe in its active site.

**Disadvantages** **First**, in terms of activity per catalytic unit, enzymes are more active than many conventional electrocatalysts. However, enzymes are macromolecules, with molecular weights in the kDa range, this inevitably lowers the number of enzyme molecules (catalytic units) that can be loaded onto an electrode. **Second**, some enzymes are sensitive to temperature, pH or organic solvent. This may narrow down the future application of enzymes in fuel cells. **Third**, not all redox enzymes are electroactive and of those that are, some exhibit inefficient intramolecular or interfacial electron transfer when adsorbed on an electrode surface. For example, chicken liver sulphide oxidase, for which interfacial electron transfer from the electrode surface to its heme group is highly efficient, exhibits sluggish intramolecular electron transfer because the Mo pterin active site is not close enough to the heme.[116, 206] Also, when adsorbed on an electrode, it is likely that some enzyme molecules are not in an optimal conformation for the heme to act as a relay to the active site. **Fourth**, the purification process of enzymes is sometimes time-consuming and expensive.

There are strategies to overcome the aforementioned problems. To increase the enzyme loading, the introduction of electrode materials with large effective surface area is a solution. L. Xu *et al.* exploited a three-dimensional electrode comprised of graphite and multi-walled carbon nanotubes to hold an $O_2$-tolerant [NiFe]-hydrogenase and bilirubin oxidase in a $H_2$ fuel cell scheme which achieved 2 mW $cm^{-3}$ at 1.22 V.[207] To increase the stability of purified enzymes under harsh conditions, the search for suitable strains of microorganisms is an option. Many natural enzymes are derived from extremophilic organisms which inhabits environments that are unfriendly to most living creatures. For example, the *sec*-ADH from the *Thermoanerobacter ethanolicus* can withstand 30% organic solvent and reaches its best activity at 80 °C.[208] Interestingly, the source of this bacterium was from hot springs in the Yellowstone National Park, US.[209] Also, immobilisation of enzymes can be helpful to the overall performance and durability of the enzyme-modified electrode.[210, 211] As for poor interfacial electron transfer, the exploitation of electron mediator would work by introducing an intermediary to channel electrons,

though this might complicate the situation as well. The cost of enzyme purification procedure can be largely overcome by optimising the purification protocol and scaling-up.[212, 213]

The commonly used fuels include glucose,[214] methanol,[215–217] ethanol,[215, 218] and hydrogen.[181, 204, 207, 219, 220] The oxidation of organic compounds like sugar and alcohol usually requires NAD(P)(H)-dependent dehydrogenases to catalyse downstream reactions. There are also reports of new-type fuel cells, such as the $H_2/N_2$ fuel cell exploiting nitrogenase to catalyse the reduction of $N_2$ to $NH_3$ through which the bioelectrochemical Haber-Bosch process was achieved.[110, 221]

### 2.1.2 A Biosynthetic Fuel Cell using FNR and Dehydrogenases

Apart from electricity generation, exploiting the driving force of redox reactions for biosynthesis provides an alternative application for enzymatic fuel cells. Figure 2.2 shows three overlaid CVs that were recorded at pH 9.0. The red and blue traces show the $H_2O/H_2$ and $O_2/2\,OH^-$ half reactions catalysed by a platinised carbon electrode and the black trace which lies between them shows the interconversion of alcohol/ketone couple catalysed by an (FNR + *sec*-ADH)@ITO/support electrode. While the experimental details of these CVs will be discussed later, the point of this overlaid plot is to illustrate that a combination of any two of these traces, each representing a half reaction, results in a full cell reaction, through which the useful driving force can be used in a fuel cell scheme.

A combination of the red and blue traces gives the cell reaction of a hydrogen fuel cell $\mathbf{H_2} + \frac{1}{2}\mathbf{O_2} \rightarrow \mathbf{H_2O}$, with $\Delta E_1 + \Delta E_2$ as the driving force. The anode and cathode reactions are:

$$H_2 + 2\,OH^- \rightarrow 2H_2O + 2\,e^- \tag{2.1}$$

$$\frac{1}{2}\,O_2 + H_2O + 2\,e^- \rightarrow 2\,OH^- \tag{2.2}$$

Similarly, a combination of the red and black traces gives the cell reaction **Ketone + $\mathbf{H_2}$ → Alcohol**, with $\Delta E_1$ as the driving force. The anode and cathode reactions

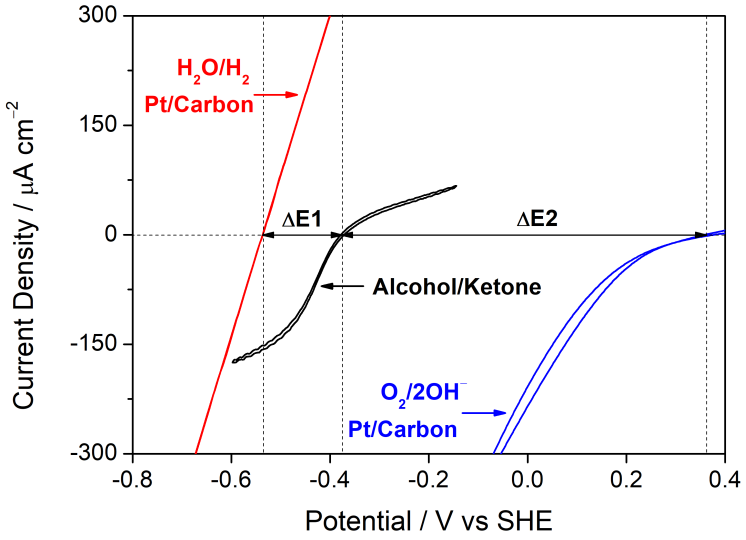



**Figure 2.2** Overlaid CVs of the $H_2O/H_2$, $O_2/2OH^-$ reactions (catalysed by a platinised carbon electrode) and the organic synthetic reaction, alcohol/ketone catalysed by an (FNR + *sec*-ADH)@ITO electrode at pH 9.0. Experimental details shown later in Figures 2.3, 3.2, and 3.4.

are:

$$H_2 + 2\,OH^- \rightarrow 2H_2O + 2\,e^- \tag{2.3}$$

$$\text{Ketone} + 2\,H^+ + 2\,e^- \rightarrow \text{Alcohol} \tag{2.4}$$

where Equation 2.4 is the coupled reaction between FNR ($\mathbf{NADP^+ + H^+ + 2e^-} \rightarrow \mathbf{NADPH}$) and ADH ($\mathbf{Ketone + NADPH + H^+} \rightarrow \mathbf{Alcohol + NADP^+}$).

On the other hand, a combination of the black and blue traces gives the cell reaction $\mathbf{Alcohol + \frac{1}{2}O_2} \rightarrow \mathbf{Ketone + H_2O}$, with $\Delta E_2$ as the driving force. The anode and cathode reactions are:

$$\text{Alcohol} \rightarrow \text{Ketone} + 2\,H^+ + 2\,e^- \tag{2.5}$$

$$\frac{1}{2}\,O_2 + H_2O + 2\,e^- \rightarrow 2\,OH^- \tag{2.6}$$

where Equation 2.5 is the coupled reaction between FNR ($\mathbf{NADPH} \rightarrow \mathbf{NADP^+ + H^+ + 2e^-}$) and ADH ($\mathbf{Alcohol + NADP^+} \rightarrow \mathbf{Ketone + NADPH + H^+}$).

Based on the aforementioned discussions, a $H_2$-driven ($H_2$ as fuel, ketone as oxidant) fuel cell to produce alcohol and an $O_2$-driven (alcohol as fuel, $O_2$ as oxidant) fuel cell to produce ketone can be easily envisaged. The use of FNR is necessary since it transduces electrons supplied from the electrode to electrons on the mobile hydride carrier – NADP(H), but the selection of the NADP(H)-dependent enzyme (E2) is flexible.

The results of the $H_2$-driven experiments will be discussed in this chapter and those for the $O_2$-driven experiments will be shown in the next chapter.

## 2.2 The Fuel cell Anode: $H_2O/H_2$ Catalysed by a Platinised Carbon Electrode

Since platinum is an expensive resource, there is great interest to replace it by developing efficient and cost-effective catalysts for the hydrogen evolution reaction (HER), the hydrogen oxidation reaction (HOR), the oxygen evolution reaction (OER), and the oxygen reduction reaction (ORR) as a replacement for Pt. New candidates include Pt-based alloys, Rh-based alloys and phosphides, sulphides, selenides of transition metals, many of which have delicate nano-structures with hundreds of well-designed complex surface morphologies and impressive catalytic properties regarding either HER, HOR, OER or ORR.

Here, the anode material used in this $H_2$-driven fuel cell is a piece of platinised carbon paper (PCP). As the focus of this thesis is the performance of the enzyme-based electrode, the foremost criteria for the selection of the auxiliary electrode are that it should be kinetically fast and durable over longtime measurement, *i.e.* it must not be rate-determining. Therefore, the well-established platinum or platinum-modified materials easily meet our requirements. The fabrication of the PCP electrode is described in Section 6.3.2.

The electrocatalytic $H_2O/H_2$ interconversion catalysed by a PCP electrode at pH 8.0 and 9.0 under 1 atm $H_2$ is shown in Figure 2.3. Within the potential range, the CVs recorded at both pH 8.0 and pH 9.0 are visibly straight lines, indicating a

high faradaic/capacitance ratio of the PCP electrode. The potential values that the CVs cross the horizontal axis at pH 8.0 and pH 9.0 are recorded to be –0.47 and –0.53 V respectively, which are very close to the theoretical values for a Pt electrode at these corresponding pH values. Both CVs cut sharply through the X axis at these values, a feature indicating that the $H_2O/H_2$ interconversion is fully reversible.

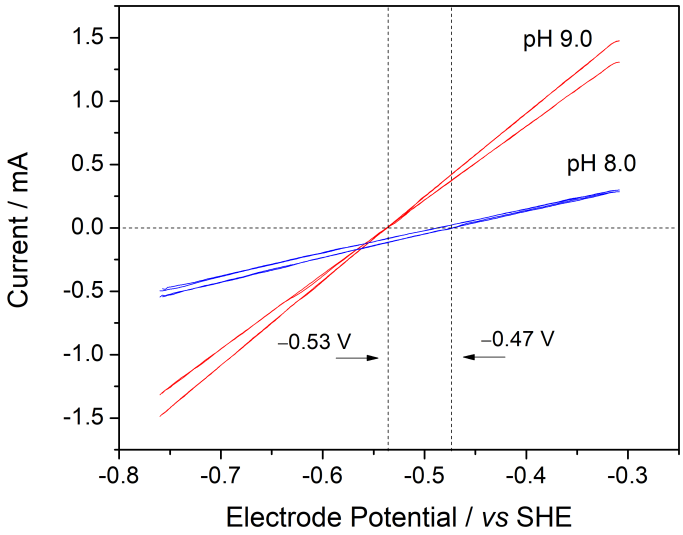



**Figure 2.3** Cyclic voltammograms (CVs) showing the interconversion of $H_2O/H_2$ at pH 8.0 (blue) and pH 9.0 (red). The solution was bubbled with mild flow of $H_2$ ($p_{H_2}$ = 1 atm) throughout. The CVs are shown in duplicate. Other experimental conditions: 25 °C, buffer = 50 mM borate, scan rate = 5 mV $s^{-1}$.

## 2.3 Driving force for the $H_2$-driven Electrochemical Leaf

Figure 2.4 shows the CVs for the interconversion of $H_2O/H_2$ at pH 8.0 (presented in Figure 2.3), overlaid with those for the interconversion of $NADP^+$/NADPH catalysed by an FNR@ITO/ITO-glass electrode at pH 8.0. Importantly, rapid $NADP^+$ reduction observed at $-420 \pm 5$ mV shows that $NADP^+$ is reduced at least 50 mV more positive than the onset potential for the $H_2O/H_2$ interconversion. The cell reaction after combining two half reactions can be expressed as:

$$NADP^+ + H_2 + 2\,e^- \rightarrow NADPH + H^+ \tag{2.7}$$

from which the driving force is estimated to be 90 ± 5 mV.

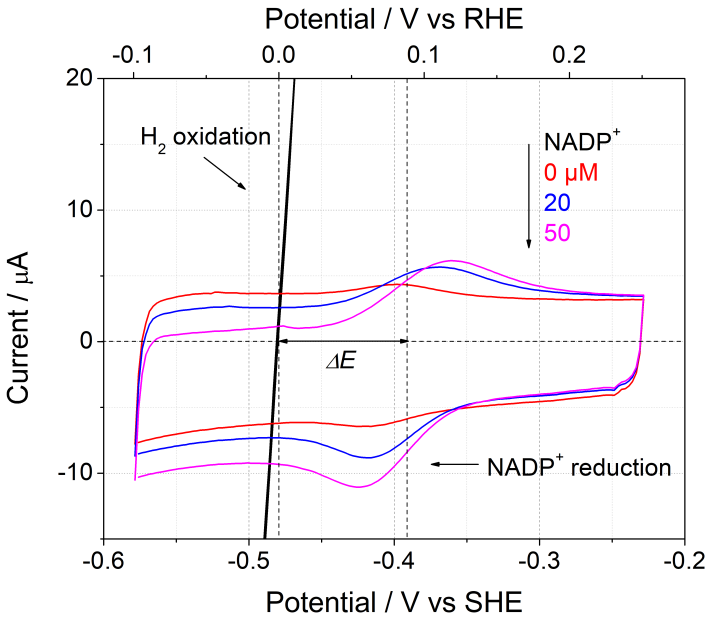
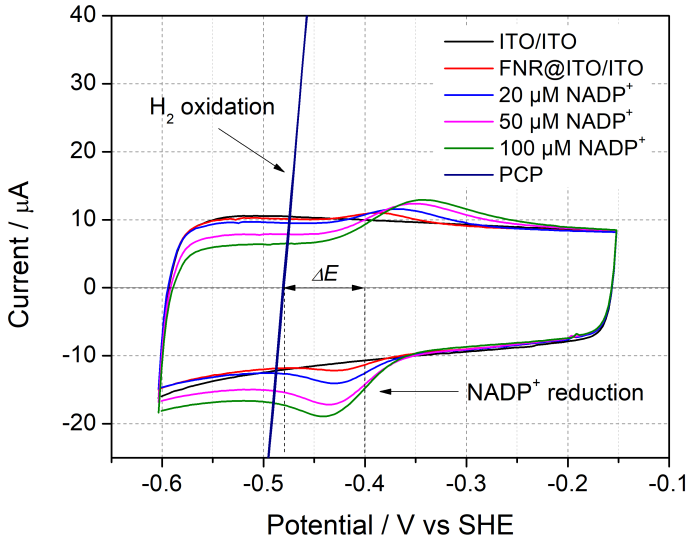
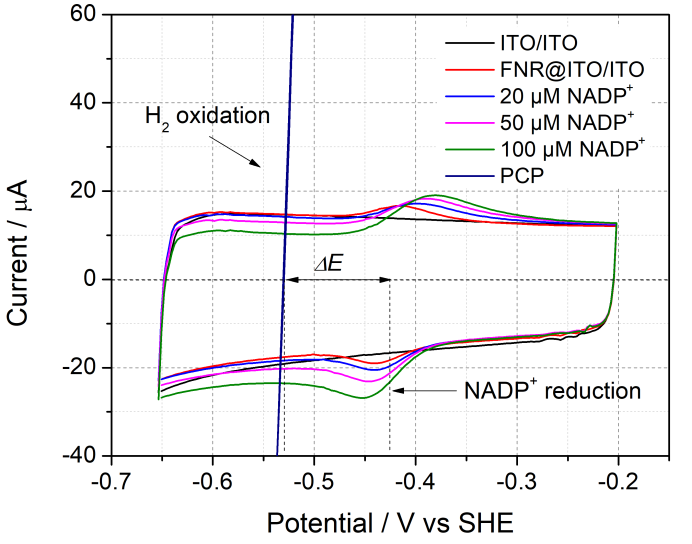



**Figure 2.4** Cyclic voltammograms (CVs) showing the interconversion of $H_2O/H_2$ (experimental conditions shown in Figure 2.3), overlaid with $NADP^+$/NADPH interconversion catalysed by an FNR@ITO/ITO-glass electrode (1.1 $cm^2$). The solution was bubbled with Ar before the measurement to remove traces of oxygen. Experimental conditions: pH = 8.0, 25 °C, buffer = 50 mM borate, cell volume = 8 mL, scan rate = 1 mV $s^{-1}$, stationary electrode, not stirred. Adapted with permission from L. Wan *et al.* Copyright 2018, Royal Society of Chemistry.[222]

Figure 2.5 demonstrates a group of control experiments recorded at pH 8.0 (Figure 2.5a) and pH 9.0 (Figure 2.5b), in which the activity of FNR at increasing concentrations of $NADP^+$ was monitored by cyclic voltammetry and overlaid with cyclic voltammograms for $H_2/H_2O$ interconversion. It is clear that at pH 9.0, the coupled reaction has larger driving force than that at pH 8.0, with 110 ± 5 mV *vs* 90 ± 5 mV.




**(a)** Recorded at pH 8.0




**(b)** Recorded at pH 9.0

**Figure 2.5** Cyclic voltammograms (CVs) showing the interconversion of $H_2O/H_2$ (conditions outlined in Figure 2.3), overlaid with $NADP^+$/NADPH interconversion catalysed by FNR@ITO/ITO-glass electrodes (1.5 $cm^2$) at pH 8.0 and pH 9.0. The solution was bubbled by Ar before measurements, to remove traces of oxygen. Experimental conditions: 25 °C, buffer = 50 mM borate, scan rate = 2 mV $s^{-1}$, electrodes stationary, solution not stirred.

Both $H_2O/H_2$ and $NADP^+$/NADPH interconversion are pH dependent and the plot reflecting this relationship is shown in Figure 2.6. The reduction potentials for $NADP^+$ (red trace) at pH 7.0, pH 8.0 and pH 9.0 are –0.32 V, –0.35 V and –0.38 V respectively; the potential shifts by 30 mV per pH unit. In contrast, the potential for the $2H^+/H_2$ reaction (black trace) shifts by 59 mV per pH unit indicating that the driving force for oxidation is greater at a higher pH. This is consistent with the result shown in Figure 2.5, where the $\Delta E$ at pH 9.0 is 20–30 mV greater than that at pH 8.0.

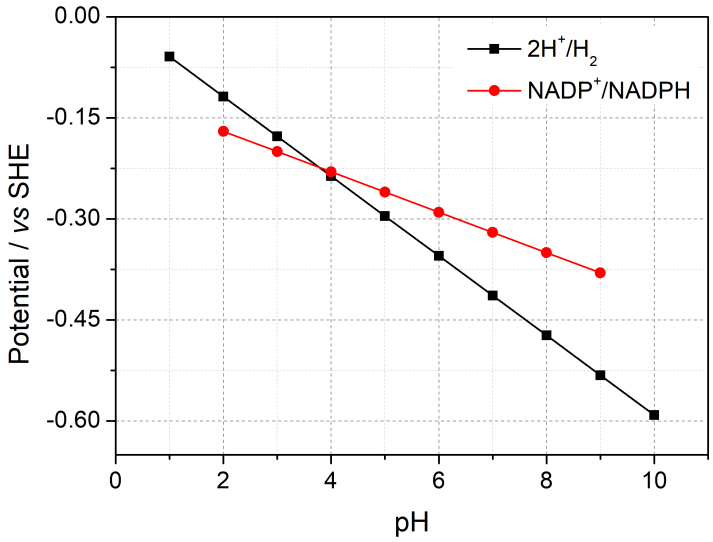



**Figure 2.6** pH dependence of the reduction potential for the $NADP^+$/NADPH (red trace) and $H_2O/H_2$ (black trace) couples.

## 2.4 Continuously Monitored $H_2$-driven NADPH Regeneration

### 2.4.1 Exploitation of the Two-Electrode System

To build a fuel cell in practice, a resistor is connected between the anode and cathode in the external circuit. This set-up is also equipped with an amperemeter and voltmeter to measure the resulting voltage across the two electrodes and the current

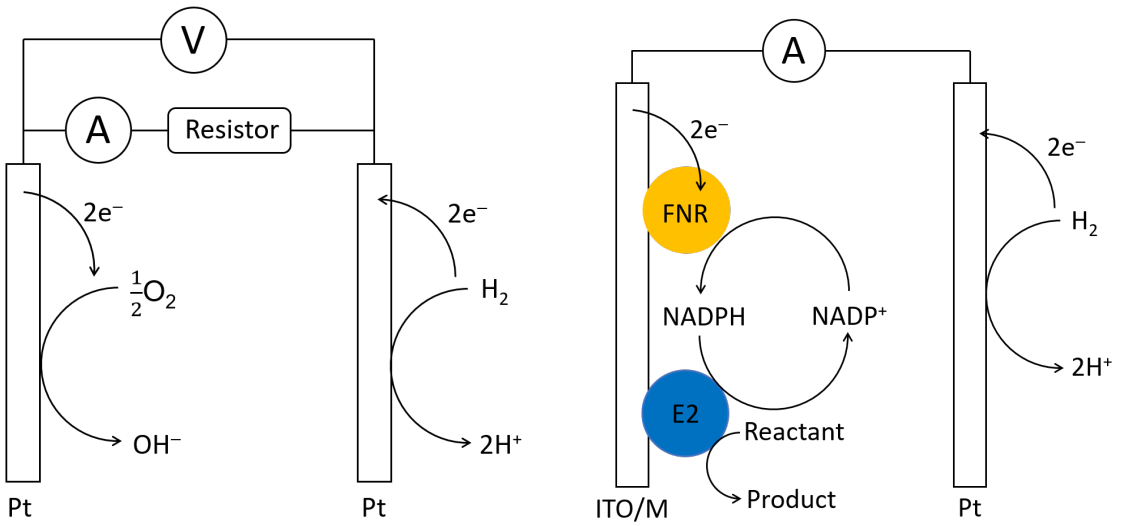
that flows. Power is calculated using the equation:

$$P = I^2R = IV \tag{2.8}$$

where $P$ is the power, $I$ is the current, $R$ is the cell resistance and $V$ is cell potential. To guarantee the largest possible power output, a trade-off between $I$ and $V$ has to be made.

For our bioorganic synthetic fuel cell scheme, instead of the largest power that can be achieved, what we really pursue is the largest faradaic current flowing through the (FNR + E2)@ITO/support electrode. Therefore, there is no need for an external resistor in the circuit and to reach this goal, a direct way is by simply short-circuiting the anode and cathode. An amperemeter in this case is still useful to measure the current because its magnitude is directly proportional to the catalytic rate of the (FNR + E2)@ITO electrode. In our case, a smart way to record the current is to use a potentiostat which, under the 'chronoamperometry' mode, monitors the current flowing through a working electrode (WE) and counter electrode (CE) at an applied potential E (in a set-up that is not a fuel cell); for the case of this $H_2$-driven fuel cell, there is no external potential applied because it is the $2H^+/H_2$ couple at Pt which provides the driving force. In other words, since the driving force is provided by the $2H^+/H_2$ couple, it translates as 0 V vs Pt.

Figure 2.7 illustrates the schematic drawings for a typical $H_2$ fuel cell and the $H_2$-driven biosynthetic cell in this thesis. Unlike the typical $H_2$ fuel cell, the $H_2$-driven biosynthetic cell does not require a proton exchange membrane (PEM). As mentioned before, this is because the reactants and products do not interfere with one another, ruling out the necessity to introduce such a physical barrier to prevent the crossover of chemicals.




**(a)** The scheme of a typical $H_2$ fuel cell. A resistor provides a means to control the power output, an amperemeter measures the current and a voltmeter measures the potential difference across the two electrodes.

**(b)** The $H_2$-driven biosynthetic cell. Only an amperemeter is required to measure the current that flows. The current is directly proportional to the catalytic rate of the (FNR + E2)@ITO/support electrode.

**Figure 2.7** A comparison of a $H_2$ fuel cell and the $H_2$-driven biosynthetic cell.

### 2.4.2 $H_2$-driven, FNR-catalysed $NADP^+$ Reduction

As a proof of concept, this subsection shows control experiments carried out to confirm that $NADP^+$ can indeed be reduced with a driving force of approximately 100 mV and also to confirm that it is $H_2$ oxidation that provides this driving force. Figure 2.8 shows the chronoamperograms (CAs) under four different conditions. A facile two-electrode system was exploited, with a piece of FNR@ITO/ITO-glass electrode as the WE and a Pt wire as both CE and reference electrode (RE). The cell was simply a one-pot glass vial containing the two electrodes which were connected to the potentiostat. As seen in the figure legend, the variables applied were $NADP^+$ and $H_2$. When there was no $H_2$ supply, Ar was used to purge the cell solution as a control. For the measurements where $NADP^+$ was absent, the currents corresponding to the experiments with $H_2$ bubbling (black trace) or with Ar bubbling (red trace) both converged to virtually zero in 100 seconds. For the experiment in the absence of $H_2$ but with $NADP^+$ present (blue trace), no visible reduction current was recorded

either. It was only when the gas flow was switched to $H_2$ in the presence of $NADP^+$ (magenta trace) that a stable reduction current of –5 $\mu$A was observed. These control experiments confirm that both $NADP^+$ and $H_2$ are indispensable for the FNR-catalysed reduction of $NADP^+$.

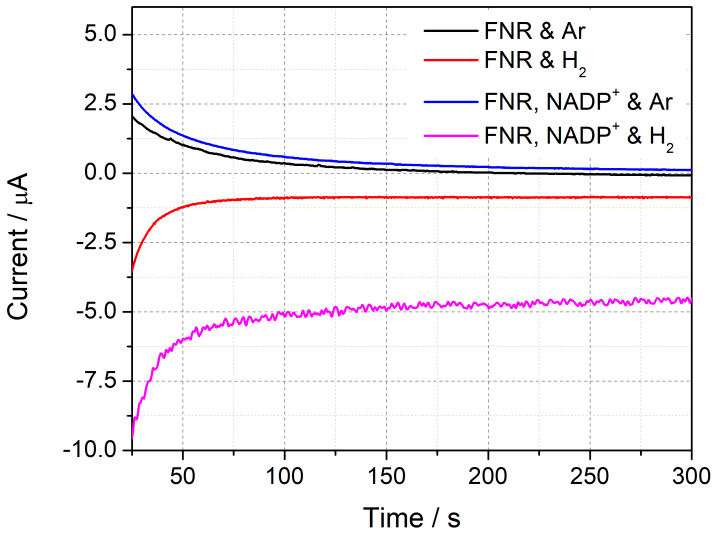


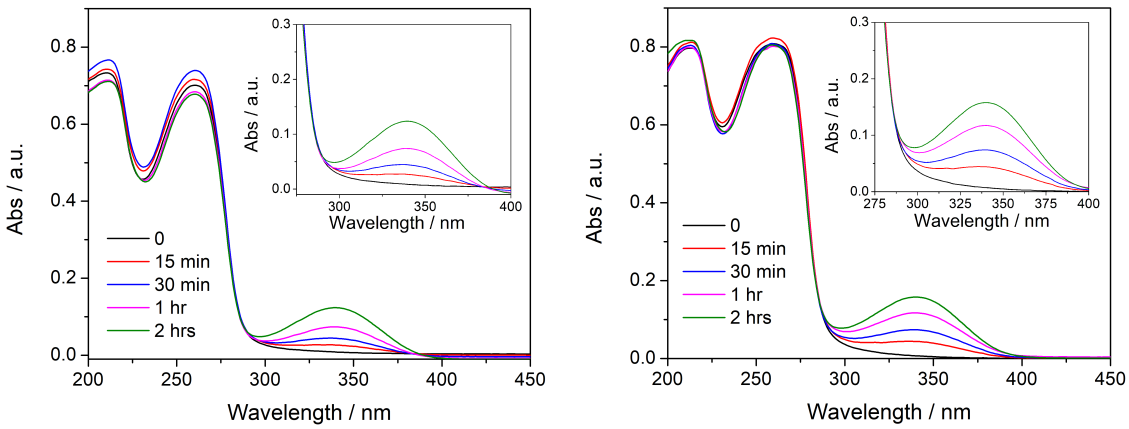

**Figure 2.8** Chronoamperograms for an FNR@ITO/ITO-glass electrode (1.5 $cm^2$) under different conditions. Ar was bubbled the cell solution before the measurement. Experimental conditions: CE = Pt wire, [$NADP^+$] = 50 $\mu$M, cell volume = 8 mL, 25 °C, pH = 8.0, 50 mM borate buffer.

To confirm the production of NADPH at pH 8.0 and pH 9.0, two additional $H_2$-driven experiments were carried out. The samples were taken periodically from the cell solution and analysed using UV-Vis spectroscopy to quantify the NADPH by measuring its absorbance at 340 nm. The calculation of NADPH concentration is performed using the Beer-Lambert law:

$$A = \varepsilon l c \tag{2.9}$$

where A is the optical attenuation of the species (the output of UV-Vis), $\varepsilon$ is the molar extinction coefficient, $l$ is the optical path length and $c$ is the concentration of the species in question. Here, the $l$ is 1 mm and $\varepsilon$ for NADPH is 6,220 L $mol^{-1}$ $cm^{-1}$. Figure 2.9 and Table 2.1 demonstrate the UV-Vis results. At both pH 8.0

and 9.0, the conversions were around 20% after 2 hours.




**(a)** Recorded at pH 8.0. **(b)** Recorded at pH 9.0.

**Figure 2.9** UV-Vis spectra of NADPH production catalysed by FNR@ITO/ITO-glass electrodes (1.5 $cm^2$). The insets show an enlarged view of the spectra from ~300 to ~400 nm. The cell volume collected from analysis each time was 400 $\mu$L. Experimental conditions: cell volume = 8 mL, [$NADP^+$] = 100 $\mu$M, 25 °C.

**Table 2.1** UV-Vis spectroscopy results for the timepoints throughout the $H_2$-driven FNR-catalysed NADPH production at pH 8.0 and pH 9.0.

| **pH 8.0** | | | **pH 9.0** | | |
|---|---|---|---|---|---|
| Time / min | Absorbance / a.u. | [NADPH] /$\mu$M | Time / min | Absorbance / a.u. | [NADPH] /$\mu$M |
| 0 | 0.00854 | \ | 0 | 0.00712 | \ |
| 15 | 0.02664 | 4.3 | 15 | 0.04409 | 7.1 |
| 30 | 0.04417 | 7.1 | 30 | 0.0741 | 11.9 |
| 60 | 0.07385 | 11.9 | 60 | 0.1173 | 18.8 |
| 120 | 0.12369 | 19.9 | 120 | 0.15789 | 25.4 |

### 2.4.3 The Set-up for the $H_2$-driven Coupled Reaction

A schematic drawing for the set-up is shown in Figure 2.10. As mentioned before, both the NADPH-recycling cathode and the $H_2$-oxidising anode are specific to their substrates, meaning that a PEM is not required. On the right we can see that

FNR and E2 co-adsorb and are randomly distributed within the nanoporous ITO layer. Another rule of thumb in designing the set-up is that since the $H_2O/H_2$ reaction catalysed by the PCP electrode is fully reversible, it is unlikely that the this electrode is rate determining; therefore, a large FNR@ITO/support electrode should be fabricated to match the activity of the PCP electrode. Here, instead of the ITO glass, I chose Ti foil with much larger available surface area as the conductive base for the Electrochemical Leaf. Ti is highly anti-corrosive and can be easily cleaned and recycled. This makes it an ideal candidate as the electrode material for a scaling-up scheme in the future. The FNR@ITO/Ti electrode was constructed by combining several pieces of ITO/Ti-foil together and pre-loading it with FNR before use by stirring in dilute FNR solution. Pictures of the PCP and FNR@ITO/Ti electrodes are shown in Figure 2.11.

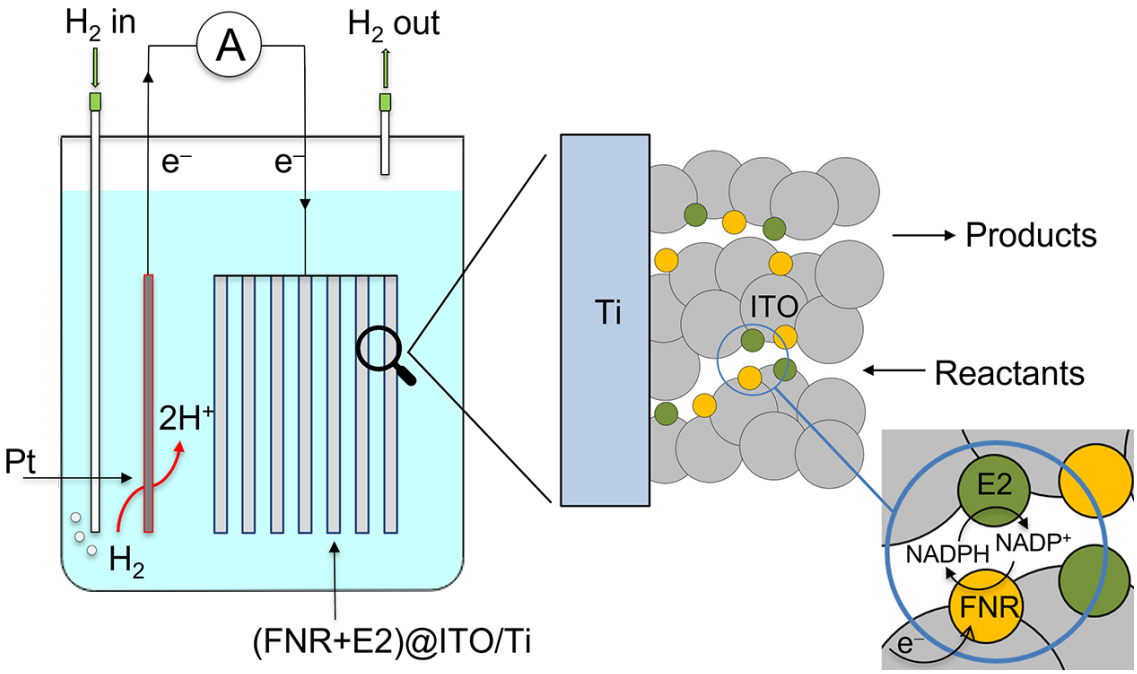
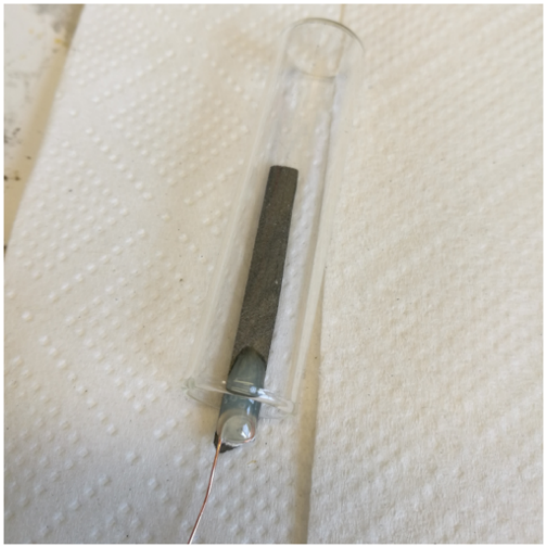



**Figure 2.10** A schematic drawing demonstrating the bioorganic synthetic fuel cell. Current can be continuously monitored using a two-electrode system under chronoamperometry mode.



**(a)** The platinised carbon paper (PCP) electrode.



**(b) Left:** the FNR@ITO/Ti-foil electrode; **Right:** the raw Ti conductive base.

**Figure 2.11** Pictures of the anode and cathode for the $H_2$-driven set-up. Adapted with permission from L. Wan *et al.* Copyright 2018, Royal Society of Chemistry.[222]

### 2.4.4 Bovine L-glutamate Dehydrogenase (GLDH)

#### *2.4.4.1 Properties of GLDH*

The downstream enzyme (E2) chosen for the coupled reaction was the commercially available L-glutamate dehydrogenase from bovine liver (EC 1.4.1.3), which catalyses the reductive amination of 2-oxoglutarate (2-OG) to L-glutamate (L-Glu):

$$\text{L-glutamate} + H_2O + NADP^+ \rightleftharpoons \text{2-oxoglutarate} + {NH_4}^+ + NADPH \qquad (2.10)$$

Despite the lack of an industrially important reaction, GLDH was chosen as a test enzyme because it is well-characterised, inexpensive, commercially available, and robust. Interestingly, although L-Glu is itself inexpensive, its monosodium salt L-Glu is widely used in East Asian countries as a flavour enhancer to give the taste of umami.

Bovine GLDH exists as a hexamer at concentrations lower than 0.1 mg $mL^{-1}$, with 332 kDa molecular weight (approx. 55.3 kDa per subunit). The 332 kDa of the hexamer is the lowest possible molecular weight form that GLDH can be active and

stable in the aqueous phase.[223] At higher concentrations, GLDH further associates to even higher oligomeric.[223–225] In living organisms, the deamination of L-Glu to 2-OG is the natural reaction for this enzyme. However, the reverse reaction was chosen for this system since it is much faster in this direction. The enzyme is active upon both NADP(H) and NAD(H) with published $K_m$ values of 2.4 ± 0.8 mM, 6.5 ± 1.8 mM and 0.022 ± 0.007 mM for 2-OG, $NH_4^+$ and NADPH, respectively.[223, 226, 227] The enzyme may incur substrate inhibition as well, at concentrations of NADPH and 2-OG much higher than their $K_m$.[226]

#### *2.4.4.2 NADPH Regeneration Coupled to GLDH Catalysis: Monitored by Cyclic Voltammetry*

This subsection describes previously published work by B. Siritanaratkul *et al.* in which the FNR-catalysed regeneration of NADPH was first coupled to bovine GLDH.[117] Unlike the work to come in the remainder of this chapter in which a fuel cell approach is taken, in this previous work the authors drove the reaction by applying a potential using a potentiostat and showed efficient coupling to GLDH as monitored by cyclic voltammetry. The shape of the CV should echo the so-called EC′ mechanism,[228] which has been mentioned in the previous chapter where E stands for an electrode process, *i.e.* the $NADP^+$ reduction in our case, and C′ represents a homogeneous catalytic process, which is the amination of 2-OG to L-Glu and regeneration of $NADP^+$.

The CVs are shown in Figure 2.12. The electrode was pre-loaded with FNR and the measurement was initiated by injecting GLDH into the cell solution which was charged with 20 mM $NH_4^+$, 50 $\mu$M NADPH and 20 mM 2-OG. The catalytic current increased with the increase of [GLDH]. As discussed in the last chapter, the scale of the catalytic current depends on the substrate concentration and also the reaction rate of the coupled reaction. Due to the nanoconfinement, NADP(H) is partially retained inside the ITO nanopores and shuttled between GLDH and FNR, making the recycling system even more efficient.

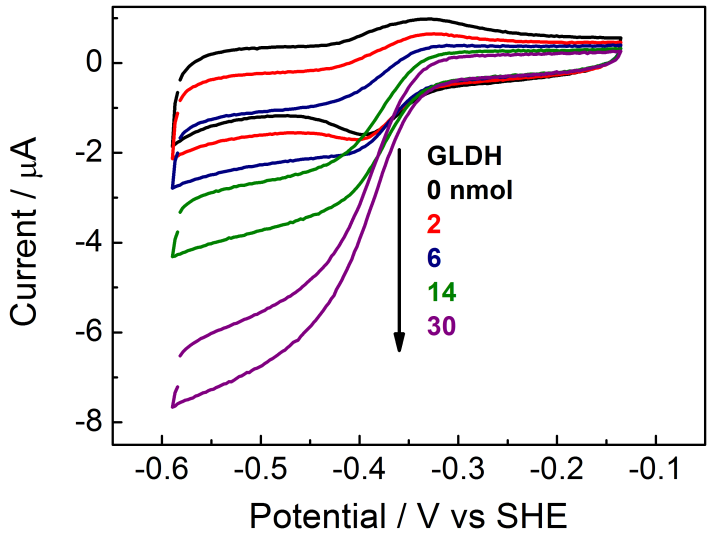



**Figure 2.12** Cyclic voltammograms showing the coupled reaction between FNR-catalysed recycling of NADP(H) and the amination of 2-OG catalysed by GLDH. Experimental conditions: effective surface area of the (FNR + GLDH)@ITO/PGE electrode = 0.09 $cm^2$, $[NH_4{}^+]$ = 20 mM, [2-OG] = 10 mM, $[NADP^+]$ = 50 $\mu$M. Reprinted with permission from B. Siritanaratkul *et al.*, Royal Society of Chemistry.[117]

### 2.4.5 $H_2$-driven Reductive Amination Coupled to NADP(H) Regeneration

#### *2.4.5.1 $NADP^+$ Titration for the $H_2$-driven Coupled System*

After combining the cathode reaction shown in Figure 2.12 and the $\mathbf{H_2 + 2OH^- \rightarrow 2H_2O + 2e^-}$ at the anode, the net cell reaction is written as:

$$\text{2-oxoglutarate} + NH_4{}^+ + H_2 \rightarrow \text{L-glutamate} + H_2O + H^+ \qquad (2.11)$$

To obtain the optimal working $[NADP^+]$ range for this $H_2$-driven scheme, an electrochemical titration measurement was performed with consecutive injections of $NADP^+$ in every 500 seconds using the chronoamperometry mode. An FNR@ITO/Ti-foil electrode (4 $cm^2$) was placed into the cell solution (50 mM borate buffer charged with 50 mM 2-OG, 60 mM $NH_4{}^+$ and bovine 90 $\mu$L GLDH (9.3 mg $mL^{-1}$)). After

bubbling with Ar for five minutes to remove $O_2$, the CA measurement was initiated – as expected zero current flowed. The gas flow was then switched to $H_2$ to induce the coupled reaction ($H_2$ bubbling was allowed to continue for five minutes to saturate the cell solution before resuming measurement). This was followed by a series injections of $NADP^+$, each of which was followed with a 5-minute pause before the resume of measurement in order to remove traces amount of oxygen. The current increased with each successive $NADP^+$ injection and the titration was terminated when no significant increase in current was observed. The full results are shown in Figure 2.13 and Table 2.2.

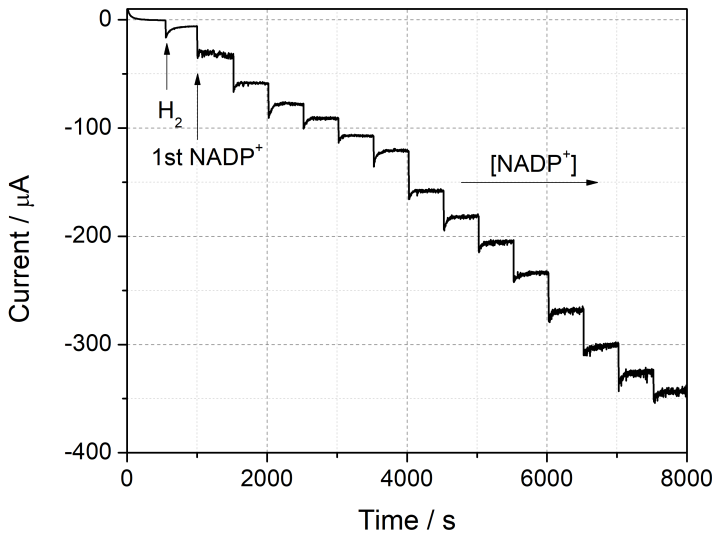



**Figure 2.13** The chronoamperogram of the titration experiment. All substrates were injected in the cell solution before the measurement except for $NADP^+$. Ar was bubbled the solution first followed by $H_2$, the flow rate of which was controlled by a mass flow controller (MFC). Experimental conditions: applied potential = 0 V *vs* Pt, buffer = borate (50 mM, pH = 9.0), 25 °C, initial cell solution = 4 mL, added GLDH volume = 90 $\mu$L (9.3 mg $mL^{-1}$), [2-OG] = 50 mM, [$NH_4^+$] = 60 mM, surface area of the FNR@ITO/Ti-foil electrode = 4 $cm^2$, surface area of the PCP electrode = 3 $cm^2$.

Using the data from this experiment (Figure 2.13 and Table 2.2) the current (rate) was plotted as a function of [$NADP^+$] in Figure 2.14a from which we can see that the catalytic current increased very fast at low [$NADP^+$] and this growth

slowed down after [$NADP^+$] surpassed 30 $\mu$M. The data (red points) were fitted to the Michaelis-Menten equation (fitted curve shown in black). The resulting $K_m$ for $NADP^+$ was determined to be 25.6 $\mu$M, which is very close to the published value 0.022 $\pm$ 0.007 mM of GLDH. It should be noted that the Michaelis-Menten kinetics mostly describes homogeneous enzyme-catalysed reactions. This enzyme-catalysed electrochemical reaction, however, is much more complex and therefore the $K_m$ could be thought of as a working $K_m$ for the coupled system.

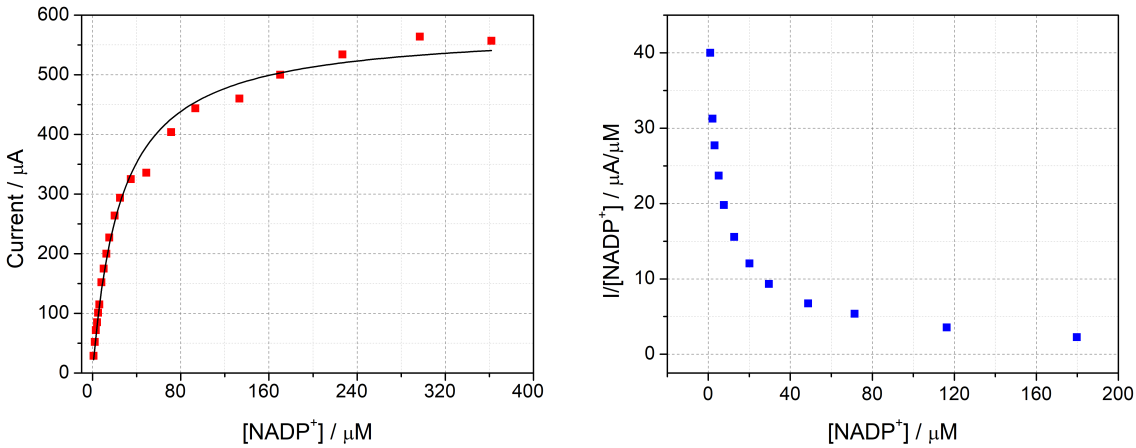
**Table 2.2** Results of the titration experiment.

| [$NADP^+$] / $\mu$M | Current / $\mu$A | [$NADP^+$] / $\mu$M | Current / $\mu$A |
|---|---|---|---|
| 1.02 | 29 | 25.00 | 294 |
| 2.05 | 52 | 34.65 | 325 |
| 3.07 | 72 | 48.78 | 336 |
| 4.09 | 85 | 71.43 | 404 |
| 5.10 | 101 | 93.23 | 444 |
| 6.12 | 115 | 133.30 | 460 |
| 8.14 | 152 | 170.21 | 500 |
| 10.15 | 175 | 226.80 | 534 |
| 12.66 | 200 | 297.01 | 564 |
| 15.15 | 227 | 361.92 | 557 |
| 20.10 | 264 | | |

**First**, what the timecourse in Figure 2.13 really reflects is the rate of the electrode process $\mathbf{NADP^+ + H^+ + 2e^- \rightarrow NADPH}$ catalysed by FNR, which is a heterogeneous electrode process. This is significantly accelerated by the coupled homogeneous GLDH-catalysed reaction within the ITO nanopores ($\mathbf{2\text{-}oxoglutarate + NH_4^+ + NADPH \rightarrow L\text{-}glutamate + H_2O + NADP^+}$), which recycles $NADP^+$ back to FNR and gives rise to the enhancement in current.

**Second**, the catalytic current was only contributed by the enzymes confined within the nanopores and it is difficult to determine the concentration of GLDH which is not electroactive and thus is not quantifiable. Due to its FAD cofactor, FNR

is electroactive and quantifiable; the FNR coverage averages at 5 pmole $cm^{-2}$ and it has previously been concluded that the coverage equates to significantly more than a monolayer which means that it is likely that some deeply buried FNR molecules are redundant.




**(a)** Current measured in Figure 2.13 plotted against the corresponding [$NADP^+$]. The data were fitted to the Michaelis-Menten kinetics equation.

**(b)** A curve showing the 'efficiency' of added $NADP^+$. The independent variable is [$NADP^+$] and the dependent variable is the (catalytic current)/([$NADP^+$]).

**Figure 2.14** Plots to analyse the $H_2$-driven (FNR + GLDH)@ITO-catalysed system. The data points were extracted from Table 2.2.

Figure 2.14b reveals another interesting fact: by plotting (catalytic current)/[$NADP^+$] against the corresponding [$NADP^+$], a measure of the efficiency of the system can be obtained. As expected, this efficiency factor decreases with the increasing [$NADP^+$], with the steepest decreasing trend occurring within the lower concentration range. Based on this, a trade-off should be made between sizable catalytic current and the efficiency of $NADP^+$ and it is clear that 5–20 $\mu$M is an appropriate range.

### 2.4.6 The $H_2$-driven Coupled System under Different Conditions

Figure 2.15 demonstrates a model chronoamperometry experiment, which was carried out with the following conditions: a PCP anode (1.6 $cm^2$) and a 'book' (see Figure 2.11) of FNR@ITO/Ti-foil cathode (total active surface area = 14 $cm^2$) were placed into a glass vial containing 50 mM MES buffer, pH 7.0. This one-pot reactor was

charged with 40-50 mM 2-OG and 60 mM $NH_4Cl$. The vial was then sealed by a rubber septum through which thin gas tubes or needles could be inserted. Prior to $NADP^+$ and GLDH additions, the introduction of $H_2$ by gently bubbling of the cell solution originally brought about a large current that decayed quickly within minutes to a constant low baseline level. As can be seen in the inset, a number of control intervention steps prove that the initial spike upon introduction of $H_2$ must have been attributable to trace oxidising materials trapped in the electrode. After purging with Ar for a while, subsequent purging of $H_2$ did not cause this spike in current again.

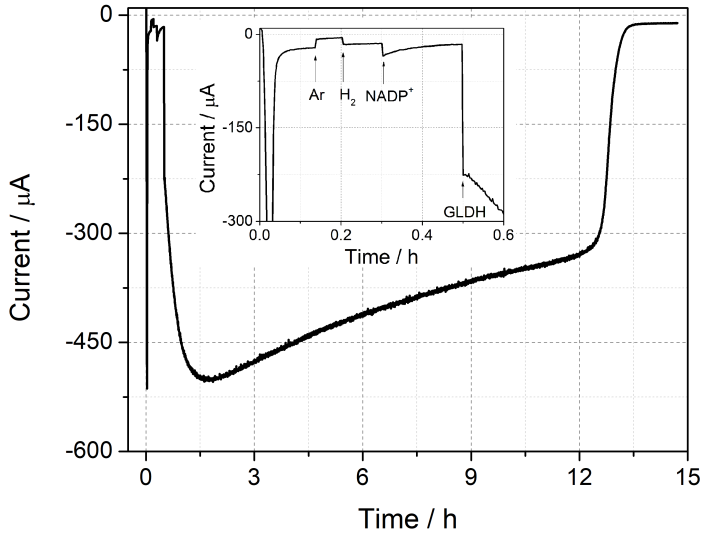



**Figure 2.15** An exemplary chronoamperogram of L-glutamate synthesis in a single-compartment $H_2$-fuel cell using an FNR@ITO/Ti-foil electrode. The inset shows an amplified view of the beginning 0.6 hour during which $H_2$ was 'burnt' to remove the oxidising materials and $NADP^+$, GLDH were subsequently injected. Experimental conditions are shown in entry H of Table 2.3. Adapted with permission from L. Wan *et al.* Copyright 2018, Royal Society of Chemistry.[222]

The injection of $NADP^+$ to a final concentration of 20 $\mu$M led to a sudden increase in current due to FNR-catalysed $NADP^+$ reduction. The coupled reaction was triggered by the injection of an aliquot of GLDH to give final concentration of 0.209 mg $mL^{-1}$ in the cell solution. After the five minutes' pause, a large initial current was observed. The timecourse was then monitored for more than 13 hours,

with the following essential features:

1. An initial biphasic increase in current (a virtually instantaneous increase followed by a much slower one). In fact, the first steeper increase was mainly due to the five-minute pause between GLDH injection and the resume of CA, the purpose of which was to avoid convolution from the trace amount of $O_2$ present in the aliquot of enzyme that was injected. This pause can be avoided if the catalytic reaction is oxidative instead of reductive, for instance, the CA shown in Figure 1.29 of the previous chapter.

2. A gradual decrease over approximately 10 hours. This can be explained by the consumption of substrate (the charge passed is 17.4 C which equates to 82.9 $\mu$moles of product formed; there might also be a slow deactivation of the system which also causes a gradual decrease in current over time).

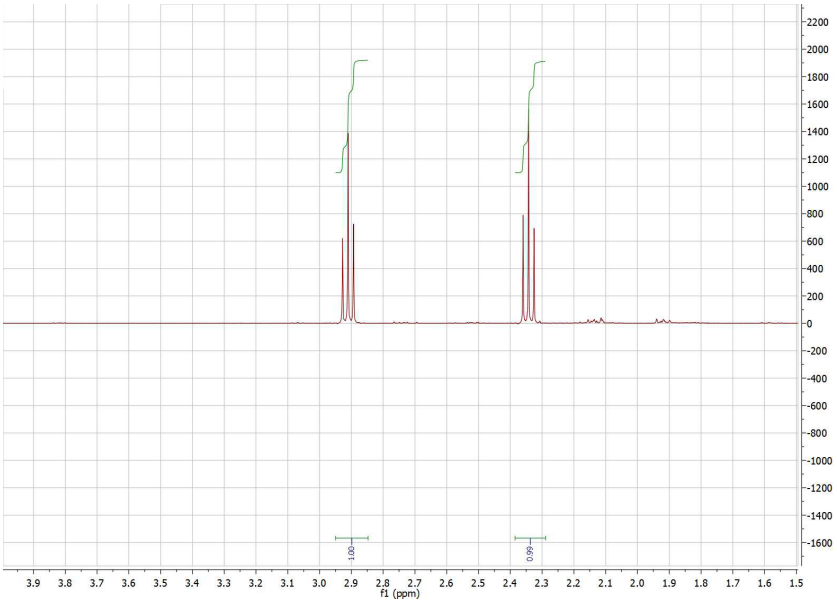
3. Following the previous stage, a slump in current to the background (virtually zero) within 1 hour. This is a clear signal that 2-OG approached to being fully consumed.

A set of experiments performed over a range of pH values and [$NADP^+$] in details are listed in Table 2.3. The variable 'total FNR coverage' was determined by calculating the peak areas (background subtracted) under 'non-turnover' conditions, *i.e.* $NADP^+$ absent. In all experiments, the product from the resulting solution was quantified using $^1$H NMR to determine the yield and conversion, which was compared to those calculated from charge passed through the electrodes (coulometry). Borate buffer was used for most cases (entries A−G), aiming at attaining clear and distinct peaks in the NMR spectra. Results of $^1$H NMR analysis for entry C in Table 2.3 showed that 100% conversion of 2-OG to L-Glu had been achieved (Figure 2.16), which was consistent with 98.6% conversion obtained from coulometry. The rest (1.4%) was probably due to loss during sample collection and set-up installation. Some measurements were carried out using MES or TAPS buffer (entries H, J and K) to double-check whether borate complexation with $NADP^+$ lowered the rate, as borate

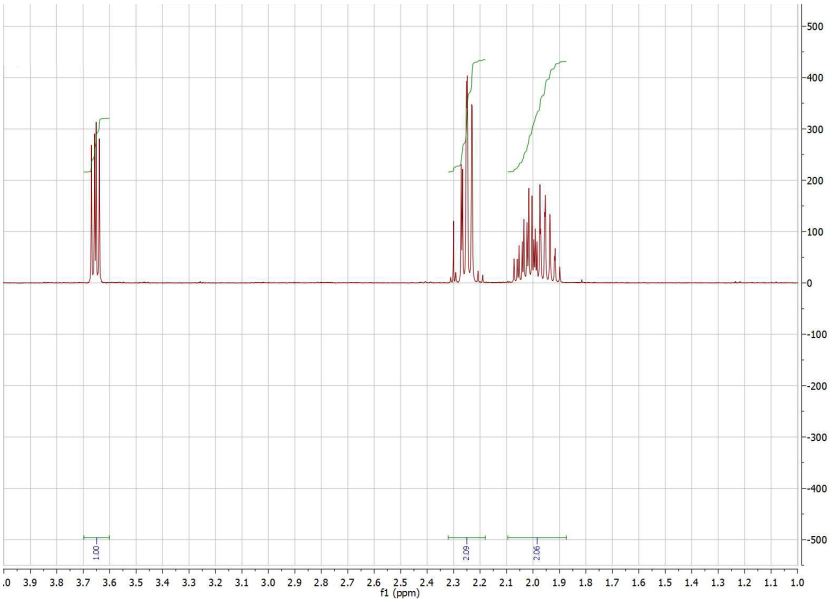
**Table 2.3** Compilation of data for the reductive amination of 2-OG to L-Glu, catalysed by GLDH, using an FNR@ITO/Ti-foil cathode in a $H_2$ fuel-cell mode.

| | | | Total FNR coverage | | | L-Glu[a] (NMR) | | L-Glu | TON[b] (NMR) | TTN[c] | | Rate |
|---|---|---|---|---|---|---|---|---|---|---|---|---|
| | | Reactant amount | pmoles cm$^{-2}$ | NADP$^+$/$\mu$M | Duration/h | mM | $\mu$moles | (Coulometry) | product/FNR | product/NADP$^+$ | | $\mu$moles h$^{-1}$ cm$^{-2}$ |
| | pH | (2-OG, $\mu$moles) | | | | | | $\mu$moles | | NMR | Coulometry | (NMR) |
| A | 9.0 | 94.6 + 98.0 | 423 | 5 | 31.9 + 81.6 | 61.9 | 139.3 | 157.6 ± 5.0 | 23,337 | 13,926 | 15,759 | 0.087 |
| B | 9.0 | 89.6 | 433 | 100 | 11.0 | 34.5 | 81.1 | 90.4 ± 0.6 | 13,428 | 406 | 452 | 0.527 |
| C | 9.0 | 98.0 | 382 | 20 | 19.3 | 37.9 | 83.4 | 94.7 ± 1.0 | 15,595 | 2,085 | 2,367 | 0.309 |
| D | 9.0 | 89.6 | 420 | 5 | 35.0 | 35.8 | 78.8 | 88.5 ± 3.0 | 13,401 | 7,875 | 8,851 | 0.161 |
| E | 9.0 | 98.0 | 373 | 2.5 | 82.9 | 30.6 | 61.2 | 65.2 ± 5.2 | 11,720 | 12,247 | 13,040 | 0.053 |
| F | 8.0 | 98.0 | 168 | 20 | 19.4 | 38.4 | 84.5 | 96.9 ± 0.5 | 35,927 | 2,113 | 2,423 | 0.311 |
| G | 8.0 | 98.0 | 185 | 5 | 36.1 | 48.4 | 94.5 | 97.2 ± 1.0 | 36,486 | 9,447 | 9,720 | 0.187 |
| H | 7.0 | 91.3 | 37 | 20 | 13.4 | 32.5 | 82.9 | 90.1 ± 0.2 | 160,004 | 2,072 | 2,253 | 0.442 |
| I | 7.4 | \ | 145 | 20 | 32.2 | 43.6 | 97.7 | 111.1 ± 1.3 | 48,128 | 2,442 | 2,777 | 0.217 |
| J | 9.0 | 95.7 | 262 | 20 | 21.4 | 39.7 | 89.3 | 93.6 ± 0.6 | 24,346 | 2,232 | 2,339 | 0.298 |
| K | 8.0 | \ | 98 | 20 | 17.5 | 37.3 | 87.6 | 92.4 ± 1.0 | 63,848 | 2,190 | 2,309 | 0.358 |

Surface area of the FNR@ITO/Ti-foil electrode = 14 cm$^2$ in all experiments. Solution conditions (2 mL volume): 50 mM borate (for A–G), 50 mM MES (for H), no buffer added (for I), 50mM TAPS (for J and K); 40 − 50 mM 2-OG (concentrations of the stock solutions were measured by $^1$H NMR); 60 mM $NH_4Cl$ (A–H and J–K) and 25 mM $(NH_4)_2SO_4$ (for I); [GLDH] = 0.209 mg mL$^{-1}$; 25 °C. Experiment for entry A includes a second injection of 2-OG, 60 mM $NH_4Cl$ and GLDH. [a] Moles L-Glu product have been corrected to allow for volume change. The small errors given for L-Glu (charge passed) reflect the uncertainty in taking a correct baseline which is small compared to the large current that is observed over a long-time period. [b] Defined as moles L-Glu/moles FNR. [c] Defined as moles L-Glu/moles NADP$^+$; moles L-Glu calculated from $^1$H NMR and CA. Adapted with permission from L. Wan *et al.* Copyright 2018, Royal Society of Chemistry.[222]




**(a)** The starting solution at time zero, showing peaks corresponding to 2-OG ($\delta$ 2.34 (t, 2H), 2.91 (t, 2H)).




**(b)** After CA for 19 hours, the peaks corresponding to 2-OG have completely disappeared. The peaks shown corresponded to L-Glu ($\delta$ 1.99 (m, 2H), 2.25 (m, 2H), and 3.65 (q, 1H)

**Figure 2.16** $^1$H NMR spectra of cell solutions at time zero and after the 19-hour CA experiment for entry C of Table 2.3.

complexation with $NAD^+$ is known to inhibit enzymatic reactions.[229–231] In fact, CVs in Figures 2.5 did imply that a small negative shift of FNR-catalysed $NADP^+$ reduction (approx. 10−20 mV) took place compared with other buffers. Also, the extent of such shift was more noticeable at pH 9.0, at which point more borate takes the form $B(OH)_4{}^-$.[231] The reaction was able to proceed in an unbuffered mode (entry I) with equally impressive results: 100% conversion and high efficiency. Two reasons might account for the results of the experiment under unbuffered condition: **(i)** The substrates 2-OG and $NH_4{}^+$ have some buffering capacity, since 2-OG is basic and $NH_4{}^+$ is acidic; **(ii)** Both GLDH and FNR are active over a wide pH range; thus small pH fluctuations have no noticeable impact upon the coupled system.

Figure 2.17 demonstrates CA results for experiments carried out at different [$NADP^+$] in 2 mL of 50 mM borate buffer (pH 9.0) containing 40–50 mM 2-OG and 60 mM $NH_4Cl$. Other than the lowest [$NADP^+$] (2.5 $\mu$M), all reactions were complete within 35 hours with the shortest case being finished in 11 hours when 100 $\mu$M $NADP^+$ was used. A comparison of these experiments shows that at higher [$NADP^+$], the time taken to reach a maximum current is shorter with much higher rate of increase of current. A plausible hypothesis for this fact is that at high levels of [$NADP^+$], the release of FNR from the ITO nanopores is accelerated, which simultaneously facilitates the adsorption of GLDH in close proximity to FNR molecules. This thereby substantially enhances the overall catalytic rate.

An important metric to evaluate the performance of a cofactor regeneration system is the 'total turnover number' (TTN), defined as the moles of product divided by the moles of cofactor added. As shown in Table 2.3, the TTN corresponding to each experiment varies from 400 using 100 $\mu$M $NADP^+$ to as many as 12,000 using 2.5 $\mu$M $NADP^+$.

After closer inspection of the results presented in Table 2.3, it was observed that even though the FNR coverage increases with increasing pH as expected (30 pmole $cm^{-2}$ at pH 7.0, compared with $>$ 400 pmole $cm^{-2}$ at pH 9.0),[117] there was no corresponding increase in electrocatalytic rate (current). In other words, the reaction

was not limited by FNR but was E2-limited under our experimental conditions. This is because a large proportion of FNR molecules being deeply buried inside the ITO nanopores are redundant in terms of NADPH recycling. As a consequence, the smallest turnover number (TON) was recorded at pH 9.0 (11,000–24,000) and the largest TON (160,000) was achieved at pH 7.0 where quite fewer FNR molecules were confined in the pores. Also, the lower amount of FNR adsorbed at pH 7.0 suggests that there was more 'room' for more E2 molecules to adsorb.

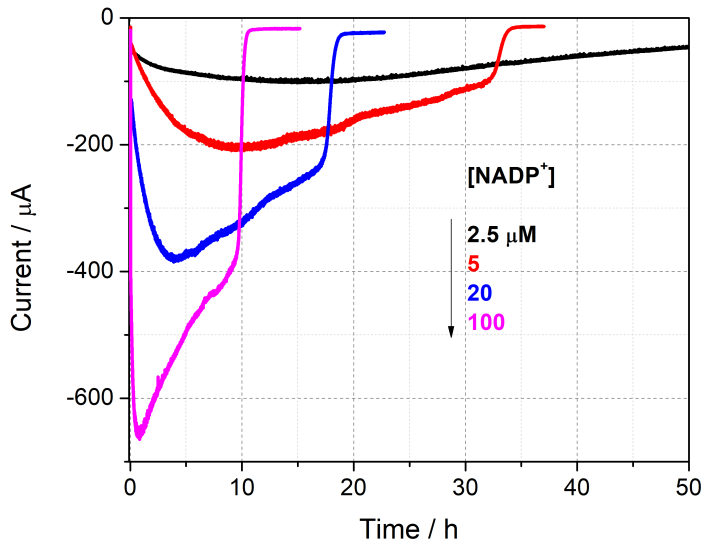



**Figure 2.17** Chronoamperograms ($i$-t curve) for the synthesis of L-Glu catalysed by GLDH. Numbers in the figure legend refer to [$NADP^+$] in $\mu$M. Experimental conditions are listed in entries B–E of Table 2.3. Adapted with permission from L. Wan *et al.* Copyright 2018, Royal Society of Chemistry.[222]

Here, a new metric defined as the average current during the reaction (after GLDH injection and before abrupt drop of current in the end) divided by the total active cathode surface area ($\mu$moles $h^{-1}$ $cm^{-2}$) is introduced as an empirical 'operational' rate constant for this particular biosynthetic fuel cell (right hand column in Table 2.2).

By plotting rate constants against [$NADP^+$], a 'Michaelis-Menten' type curve is generated (Figure 2.18), which is independent of pH and buffer solution. From this new curve we can observe that $> 50\%$ of the maximum rate is achieved at 20 $\mu$M

$NADP^+$, thereby providing a useful guide for potential applications in the future.

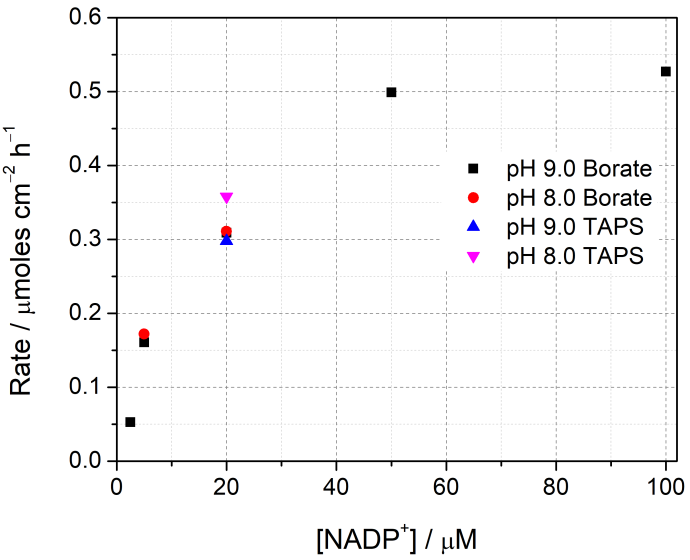



**Figure 2.18** A operational 'rate' *vs* [$NADP^+$] plot. The rate is defined as $\mu$moles L-Glu produced divided by active electrode area and total reaction time (from the point when GLDH was injected until the moment before current plummets (substrate depletion)). Adapted with permission from L. Wan *et al.* Copyright 2018, Royal Society of Chemistry.[222]

## 2.5 Conclusions and Perspectives

This chapter exploits the (FNR + GLDH)@ITO/support electrode as the cathode in a $H_2$-driven fuel cell to recycle NADPH. Electrons provided by the oxidation of $H_2$ at the anode are transduced by FNR at the cathode to form a hydride on the mobile electron carrier, NADPH. Subsequently, the co-entrapped downstream enzyme, GLDH captures the NADPH and catalyses the production of L-Glu, releasing $NADP^+$ which is then recycled back to FNR. In this fuel cell, both the (FNR + GLDH)@ITO/support cathode and PCP anode are reversible such that only a minimal overpotential is required to drive rapid diffusion-controlled NADPH recycling. In this system, 100% conversion and more than 10,000 TTN can be achieved in a series of continuously monitored measurements.

# Chapter 3

# An Air-driven Fuel Cell Scheme for $NADP^+$ Regeneration

## Abstract

This chapter introduces another extension of the enzyme-catalysed Electrochemical Leaf system. Precisely speaking, the idea originates in thinking reversely of the $H_2$-driven biosynthetic fuel cell that under appropriate conditions, the Electrochemical Leaf transforms into an anode and the FNR entrapped within the nanopores is switched to a hydride consumer. The resulting $NADP^+$ is then accepted by a NADP(H)-dependent enzyme – undoubtedly, also bound within the nanopores – to carry out downstream reactions that in turn produce chemicals and NADPH. This interesting $NADP^+$ recycling system is capable of enantioselective conversion of secondary alcohols to ketones when the second enzyme coupled with FNR is enantioselective. The significant enhancement of catalytic rate arising from nanoconfinement is fulfilled using an air-driven fuel cell scheme, which like its $H_2$-driven equivalent, requires no complicated control features yet still allows continuous monitoring of the rate in real time through the current that flows between the anode ((FNR + ADH)@ITO/support: bioorganic chemistry) and cathode (Pt: $O_2$ from air). Also informed interventions can be made, such as recharging with reactant. This clean, air-driven process should be widely applicable to oxidations catalysed by $NADP^+$-dependent dehydrogenases.

## 3.1 Introduction

As shown in Section 2.1.2 of the previous chapter, an air-driven fuel cell can be envisaged when the **cathodic** reaction – the reduction of dioxygen catalysed by a platinised carbon electrode, and the **anodic** reaction – the oxidation of NADPH catalysed by FNR are combined. A concise illustration of an air-driven fuel cell for biosynthesis is shown in Figure 3.1. The electrode material for the cathode – ITO deposited conductive base (ITO/support) – can display $O_2$ reduction (though limited) under a broad range of comparatively negative potentials. As a result, the net flow of electrons that passes through the two electrodes can be partially counteracted by the $O_2$ reduction occurring on the ITO/support, leading to underestimated coulometry that can be monitored. Here, a proton exchange membrane (PEM) is introduced to separate the anodic and cathodic reactions, with the purpose of avoiding the intervention from $O_2$, whilst the movement of protons is still available. This fuel cell can drive downstream biosynthetic reactions when the oxidation of NADPH is coupled with an NADPH-requiring E2 within the pores.

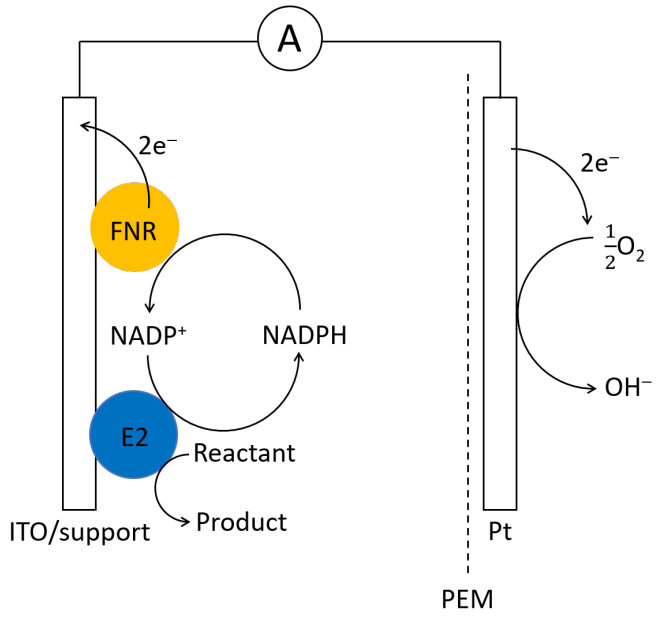



**Figure 3.1** An illustration of the working principle of an air-driven bioorganic fuel cell.

## 3.2 $O_2$ Reduction Catalysed by a Platinum Carbon Paper Electrode

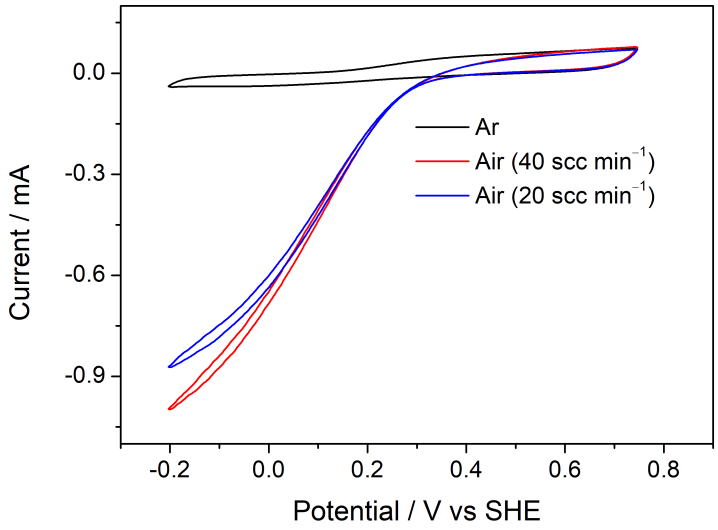



**Figure 3.2** Cyclic voltammograms showing $O_2$ (in air) reduction operated by a PCP electrode under Ar (black trace) and air bubbling under different flow rates (blue and red traces). Experimental conditions: cell solution = 8 mL, buffer = 50 mM TAPS (pH = 9.0), active surface area of the PCP = 2.4 $cm^2$, 25 °C, scan rate = 5 mV $s^{-1}$.

Figure 3.2 shows $O_2$ (in air) reduction catalysed by a piece of platinised carbon paper (PCP) electrode that was used for HOR in Chapter 2. The cell solution was bubbled by either Ar (black trace) or air (red and blue traces) throughout measurements. pH 9.0 was chosen to meet the optimal condition for alcohol oxidation that will be discussed later. Under such mild alkaline condition, the chief reaction that occurs is expressed by the equation:

$$O_2 + 2\,H_2O + 4\,e^- \rightarrow 4\,OH^- \tag{3.1}$$

As expected, when only Ar was present (air absent), virtually no effective catalysis occurred as there was only non-faradaic current due to capacitance being observed. The introduction of air flow (20 scc $min^{-1}$) soon 'activated' the PCP electrode with

clear signal of $O_2$ reduction commencing from approximately 0.5 V vs SHE. The catalytic current arising from $O_2$ reduction then increased as the applied potential approached more negatively and reached a value slightly less than 0.9 mA at –0.2 V vs SHE. Theoretically, at pH 9.0, the onset potential for $O_2$ reduction should start at 0.7 V vs. SHE. The approximately 0.3 V required overpotential recorded is mainly attributable to slow kinetics of ORR which involves the transfer of four electrons. The measurement with higher air flow rate at 40 scc $min^{-1}$ was also performed but with limited catalytic enhancement.

## 3.3 Secondary Alcohol Dehydrogenase TeSADH W110A

### 3.3.1 Wildtype TeSADH

The Food and Drug Administration (FDA) of the US has been increasingly interested in chiral purity of drugs, of which up to 90% are offered in racemic form.[232] While it is acceptable that usually only one enantiomer is biologically useful for humankind, there were cases that the other enantiomer could be toxic.[233–235] As most enzymes are inherently enantioselective, they are widely used as biocatalysts to synthesise enantiomerically pure compounds. The synthesis of enantiomers of secondary alcohols catalysed by enantioselective *sec*-ADH is a typical example for this purpose.

TeSADH, the secondary ADH (*sec*-ADH) from *Thermoanerobacter ethanolicus* 39E is an NADP(H)-dependent zinc-containing tetrameric oxidoreductase and highly active on (*S*)-2-butanol, (*S*)-2-propanol and their corresponding ketones.[208] In a typical TeSADH-catalysed reaction initiated with a racemic mixture of chiral alcohols, the (*S*)-enantiomer tends to be transformed much more rapidly, leading to the slower substrate (*R*)-enantiomer accumulating in the bulk solution, the process of which is called kinetic resolution. Conversely, the reverse reaction initiating with ketones favours the production of (*S*)-enantiomer, *i.e.* asymmetric reduction.[59]

TeSADH has overcome shortcomings of many previously commercially available ADH. As *Thermoanerobacter ethanolicus* 39E itself is a thermophilic bacterium,

TeSADH is thermostable and has 1.7 hour half-life even at temperature as high as 90 °C. Also, it can survive in moderate concentrated organic solvents.[208]

### 3.3.2 TeSADH W110A Variant

TeSADH W110A (hereafter sometimes referred to as ADH in this chapter) is the E2 for demonstrating the scope of air-driven fuel cell system in this chapter.[1] This recombinant enzyme is a variant of TeSADH, in which Trp-110 is substituted by alanine. This results in a larger pocket of the active site that is able to accommodate phenyl ring-containing (*S*)-alcohols and ketones,[59] especially (*S*)-4-phenyl-2-butanol, (*S*)-1-phenyl-2-propanol, 4-phenyl-2-butanone (benzylacetone) and , phenylacetone which are valuable precursors or building blocks for pharmaceuticals.[232, 236] The TeSADH-W110A-catalysed interconversion of (*S*)-4-phenyl-2-butanol and 4-phenyl-2-butanone which will be frequently used in this chapter is written as:

$$(S)\text{-4-phenyl-2-butanol} + \mathrm{NADP^+} \rightleftharpoons \text{4-phenyl-2-butanone} + \mathrm{NADPH} + \mathrm{H^+} \quad (3.2)$$

It should be mentioned that when a racemic mixture of 4-phenyl-2-butanol, *i.e.* (*rac*)-4-phenyl-2-butanol serves as the substrate, the oxidation of (*R*)-4-phenyl-2-butanol also occurs, albeit a much slower kinetics is expected.

TeSADH W110A has been used in hydrogen-borrowing cascades for synthesising amines, initiating from either racemic alcohols or alkanes.[237, 238] Following site-directed mutagenesis, its stability at high temperature and in organic solvent remains roughly unchanged.[59]

Currently, 'green' options for carrying out such chiral alcohol production on a large scale are either chemical, using $H_2O_2$, $O_2$ or N-oxyl reagents, together with a transition-metal catalyst,[239–241] or enzymatic, using $O_2$ with alcohol oxidases or laccases.[242, 243]

[1] The mechanisms of enantioselectivity of the wild-type TeSADH and the W110A variant will be discussed in the next chapter.

## 3.4 $NADP^+$ Regeneration Coupled to TeSADH W110A Catalysis: Monitored by Cyclic Voltammetry

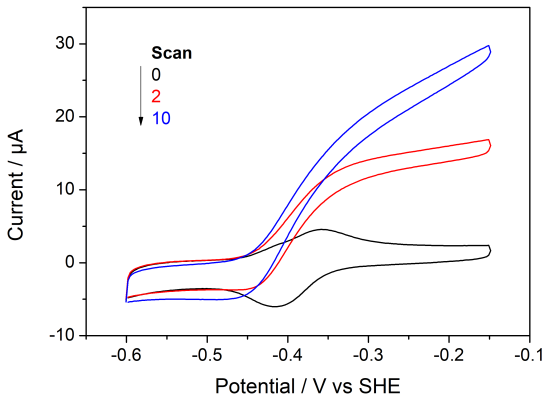
### 3.4.1 Measurements Using Various Substrates

Figure 3.3a illustrates CVs of the TeSADH-W110A-catalysed (*rac*)-4-phenyl-2-butanol oxidation coupled with FNR-catalysed $NADP^+$/NADPH interconversion. The measurement was carried out using a piece of stationary FNR@ITO/ITO-glass electrode (dropcasting method, [FNR] = 1.25 mM, 3 $\mu$L, 30 seconds incubation) placed in a vial containing 8 mL 50 mM TAPS (pH = 9.0) buffer, 50 $\mu$M NADPH, and 5 mM (*rac*)-4-phenyl-2-butanol (4P2B). The starting cyclic voltammogram (scan 0, black trace) is the quasi-reversible $NADP^+$/NADPH interconversion. Once introducing ADH into the cell solution to give 0.7 $\mu$M final concentration, the current of the oxidation of NADPH started to increase steadily as the incoming ADH formed catalytic unit with FNR in the nanopores. The overall coupled reaction occurring at the working electrode is written as:

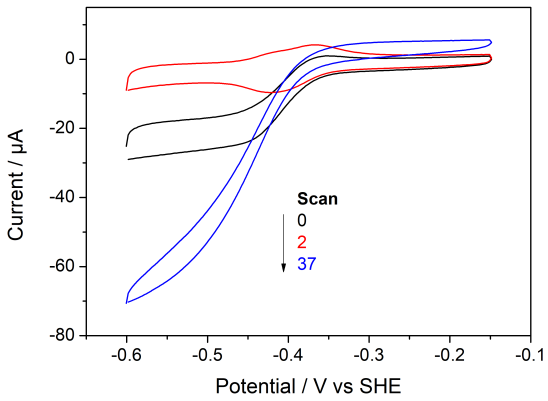
$$(S)\text{-4-phenyl-2-butanol} \rightarrow \text{4-phenyl-2-butanone} + 2\,\mathrm{H^+} + 2\,\mathrm{e^-} \tag{3.3}$$

The CV of its reverse reaction, the reduction of 4-phenyl-2-butanone to (*S*)-4-phenyl-2-butanol is shown in Figure 3.3b. Likewise, upon introducing $NADP^+$, the cathodic current increased progressively due to ADH binding. Also, at scan 37 when activity of ketone reduction reached an optimal point, it is interesting to see that within the comparatively positive potential range, some current due to the oxidation of alcohol also emerged. This indicates that following long-time cyclic voltammetry measurement, some amounts of alcohol molecules are also produced and retain within the pores.

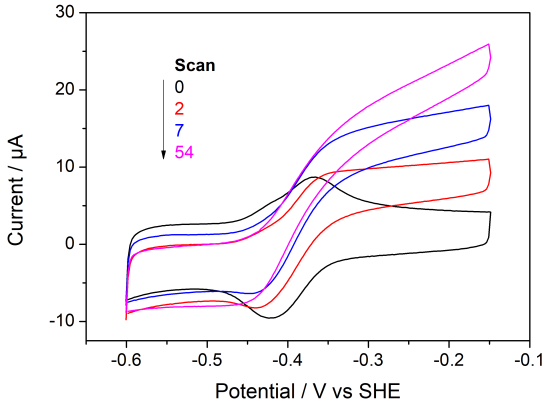
Similarly, Figure 3.3c and 3.3d demonstrate CVs of cyclohexanol oxidation and cyclohexanone reduction, respectively. It is not surprising to observe appreciable activities for both as the pocket of TeSADH W110A can also contain the cyclohexyl



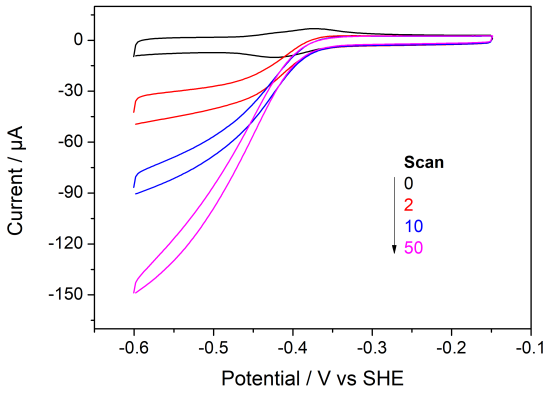

**(a)** Oxidation of (*rac*)-4-phenyl-2-butanol (5 mM).



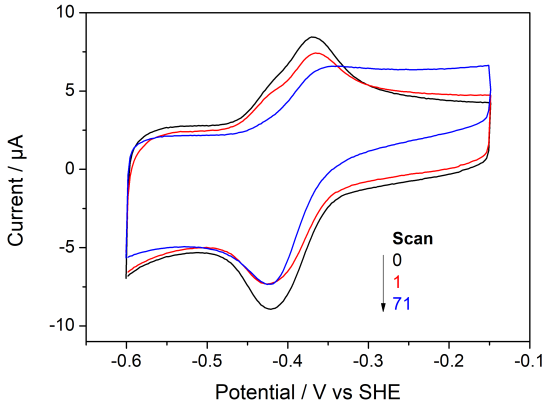

**(b)** Reduction of 4-phenyl-2-butanone (5 mM).



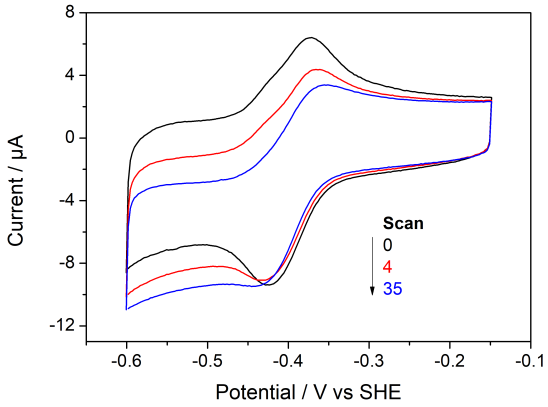

**(c)** Oxidation of cyclohexanol (50 mM).




**(d)** Reduction of cyclohexanone (50 mM).




**(e)** Oxidation of 1-hexanol (50 mM).




**(f)** Reduction of hexanal (50 mM).

**Figure 3.3** Cyclic voltammograms showing the interconversion of NADP$^+$/NADPH coupled to TeSADH-W110A-catalysed reactions with different substrates, recorded using FNR@ITO/ITO-glass electrodes (1.1–1.25 cm$^2$, dropcasting method, [FNR] = 1.25 mM, 3 $\mu$L, 30 seconds incubation); cycles are indicated in the legend of subfigures where '0' cycle means the one being recorded before the injection of TeSADH W110A, *i.e.* the CV prior to coupling. Experimental conditions: cell volume = 8 mL, buffer = TAPS (pH =9.0), 25 °C, [TeSADH W110A] = 0.7 $\mu$M, [NADP(H)] = 50 $\mu$M, scan rate = 1 mV s$^{-1}$. The cell solution was bubbled with Ar for five minutes before resuming the measurement.

group.

On the other hand, as the TeSADH family is not designed for primary alcohol and aldehyde, poor activities were observed when using 1-hexanol and hexanal (Figure 3.3e and 3.3f).

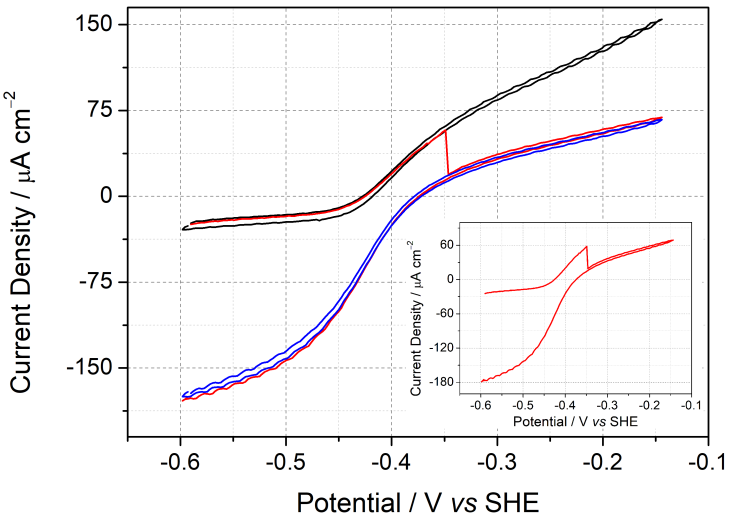
### 3.4.2 pH Selection for Alcohol Oxidation

Experiments were also carried out under hydrodynamic control to discover the system's overall response, kinetics and reversibility towards product inhibition at different pH values. In each case, an (FNR + ADH)@ITO/PGE rotating disc electrode was fabricated *via* dropcasting an aliquot of concentrated FNR (705 $\mu$M) and TeSADH W110A (42 $\mu$M) onto the ITO layer for approximately three minutes. The electrode was then rinsed by Milli-Q water repeatedly before use.

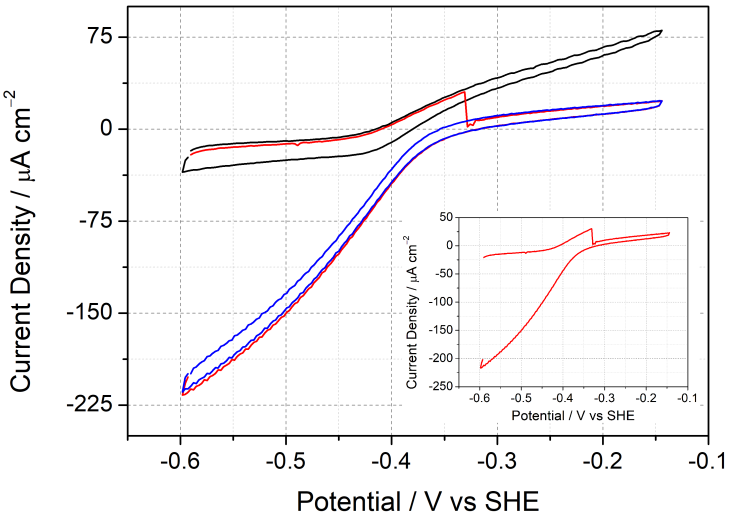
The upper cyclic voltammogram (black trace) in Figure 3.4a shows the oxidation of 5 mM (*S*)-4P2B at pH 9.0 with 50 $\mu$M NADP(H) present in cell solution (equivalent ratio of $NADP^+$:NADPH was applied in this experiment). As expected, a large anodic current due to alcohol oxidation appeared. Following the injection of 4-phenyl-2-butanone (the product) to give a final concentration of 5 mM (red trace), the anodic current dropped sharply and remained inhibited at a level *ca.* 1/3 of that was recorded prior to ketone introduction. In the reductive half cycle, even larger cathodic current owing to ketone reduction was recorded. The subsequent cycle (blue trace) then showed a classical electrochemically driven interconversion of alcohol and ketone. It is clear from this figure that in a 1:1 mixture of alcohol:ketone at pH 9.0, ketone reduction is slightly more favoured than alcohol oxidation.

The control experiment carried out at pH 8.0 is illustrated in Figure 3.4b. Again, the upper CV was recorded before injecting ketone. A clear trend observed is that as pH was switched from 9.0 to 8.0, reduction was much more favoured. The reduction current was large, with approximately 220 $\mu$A $cm^{-2}$, compared to 20 $\mu$A $cm^{-2}$ for the oxidation current.

It is clear that at higher pH, kinetics of alcohol oxidation is much faster and




**(a)** Recorded at pH 9.0.




**(b)** Recorded at pH 8.0.

**Figure 3.4** Cyclic voltammograms to monitor the enzyme-catalysed electrochemical interconversion of (*S*)-4P2B/4-phenyl-2-butanone using a (FNR + ADH)@ITO/graphite rotating disc electrode. pH 9.0 (panel **a**) and pH 8.0 (panel **b**) were used to compare reversibility, catalytic bias, and product inhibition (ketone). The measurement was initiated with 5 mM (*S*)-4P2B in the cell (black trace). In each case during the measurement, 4-phenyl-2-butanone was injected (to give 5 mM final concentration) during the scan (also shown in the inset). The cycle following ketone injection is shown in blue. The inset shows an enlarged view of the cycle where the injection of ketone was carried out. Experimental conditions: buffer = 50 mM TAPS + 50 mM MOPS + 50 mM CHES, [NADPH] = 25 $\mu$M, [$NADP^+$] = 25 $\mu$M, 20 °C, scan rate = 3 mV $s^{-1}$, rotation speed = 500 rpm. Adapted with permission from L. Wan *et al.* Copyright 2019, Royal Society of Chemistry.[236]

also experiences less product inhibition. This is in consistent with previous studies[232]. Therefore, pH 9.0 is chosen as the standard condition for electrochemical measurements in the rest of this chapter.

## 3.5 Driving Force for the Air-driven Cell Reaction

After obtaining the electrochemical results for the cathode and anode reactions of the air-driven electrochemical cell, a plot recording CVs for $O_2$ reduction catalysed by the PCP electrode and alcohol oxidation catalysed by an (FNR + ADH)@ITO/ITO-glass electrode is shown in Figure 3.5.

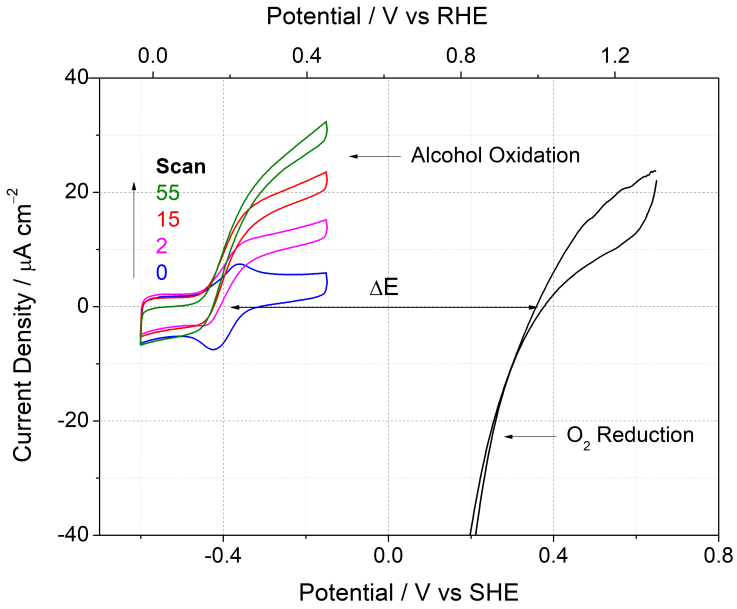



**Figure 3.5 Left:** Cyclic Voltammograms showing the interconversion of $NADP^+$/NADPH coupled to the TeSADH-W110A-catalysed oxidation of (*rac*)-4P2B obtained at an FNR@ITO/ITO-glass electrode (active surface area = 1.0 $cm^2$), [FNR] = 1.25 mM (dropcasting method, 3 $\mu$L, 30 seconds incubation); cycle numbers are shown in proximity with the CVs where '0' indicates the scan of uncoupled reaction. **Right:** A CV for $O_2$ (in air) oxidation at a PCP electrode. The CVs were measured at scan rate 1 mV $s^{-1}$ for the FNR@ITO/ITO-glass electrode, and 5 mV $s^{-1}$ for the PCP electrode. Experimental conditions: cell volume = 8 mL, buffer = 50 mM TAPS (pH 9.0), 25 °C, [TeSADH W110A] = 0.13 $\mu$M, [NADPH] = 50 $\mu$M, [(*rac*)-4P2B] = 10 mM. Adapted with permission from L. Wan *et al.* Copyright 2019, Royal Society of Chemistry.[236]

Experimental details are similar to those described before and are shown in the figure caption. Compared to the $H_2$-driven fuel cell which only has approximately 0.1 V driving force, a useful driving potential of 0.7–0.8 V is available for this air-driven fuel cell ($\Delta E$ in Figure 3.5).

## 3.6 Continuously Monitored Air-driven $NADP^+$ Regeneration

### 3.6.1 The set-up for the Air-driven Fuel Cell Scheme

Figure 3.6 is a detailed scheme showing the two-compartment cell together with a cartoon depicting the nanoconfinement, in which the (FNR + E2)@ITO/Ti-foil electrode is situated in the main compartment. During measurement, a stream of compressed air is gently introduced into the smaller platinum-containing compartment which is separated from the main compartment by a Nafion 115 PEM. Like its $H_2$-driven counterpart, progress of the reaction, which is represented by the current that flows, is continuously monitored. In our case, the potentiostat would in principle work as an amperemeter.

The self-made biosynthetic electrochemical cell being used in this experiment is demonstrated in Figure 3.7. As seen in panel **a**, compared with the main compartment, the platinum-containing compartment is a very thin cylindrical vial and the bottom of it is attached with a piece of PEM to which is pasted by epoxy. Panel **b** shows the bench for the experiment. The cell as a whole is placed into a waterbath which itself is placed on a magnetic stirrer.

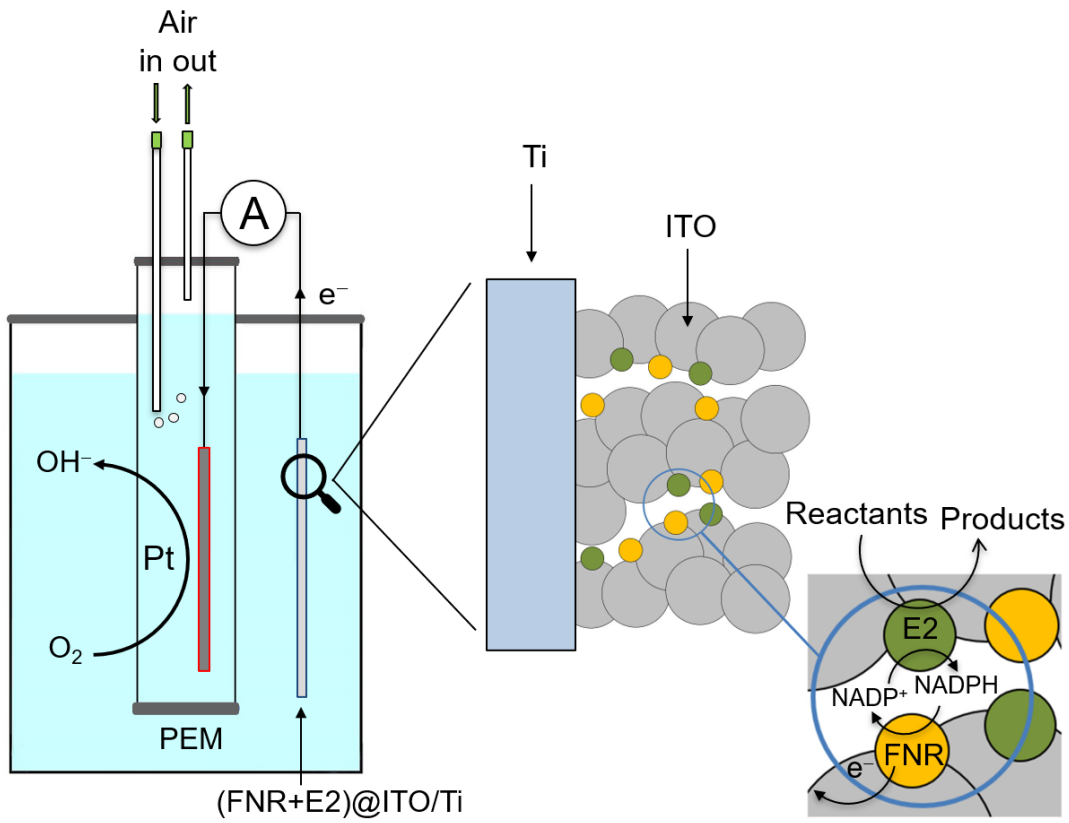
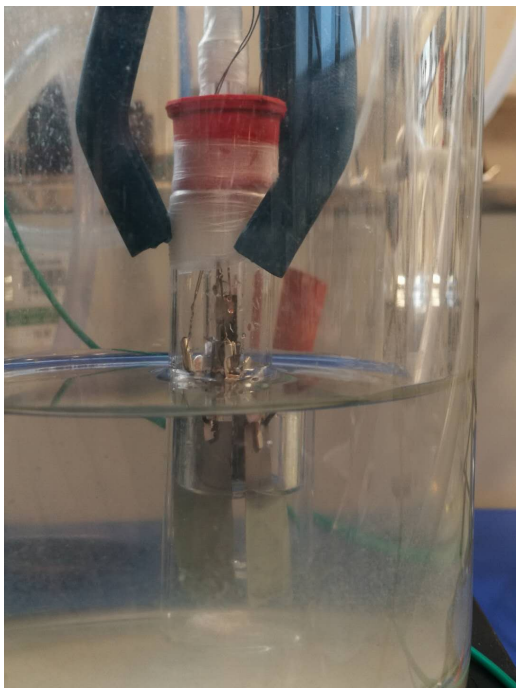



**Figure 3.6** A schematic drawing showing the set-up of the two-compartment air-driven enzymatic fuel cell for biosynthesis and the nanoconfinement effect underpinning the action of an (FNR + E2)@ITO/support electrode. A Nafion proton exchange membrane is placed between the main compartment and the platinum-containing compartment. The current flowing through the two chambers yields the reaction rate. Adapted with permission from L. Wan *et al.* Copyright 2019, Royal Society of Chemistry.[236]



**(a) Left:** the main compartment (a glass vial). **Right:** the platinum-containing compartment (a smaller cylindrical glass vial).



**(b)** The set-up during measurement. The cell is placed into a waterbath under constant temperature.

**Figure 3.7** The photographs showing the components of the cell and the set-up exploited in air-driven the fuel cell. Adapted with permission from L. Wan *et al.* Copyright 2019, Royal Society of Chemistry.[236]

### 3.6.2 Air-driven Enantioselective Alcohol Oxidation Coupled to $NADP^+$ Regeneration

After combining the cathode reaction (Equation 3.1) catalysed by platinum (PCP in this case) and the anode reaction (Equation 3.3), the overall cell reaction is written as:

$$(rac)\text{-4-phenyl-2-butanol} + \frac{1}{2}\,O_2 \rightarrow \text{4-phenyl-2-butanone} + H_2O \qquad (3.4)$$

As the presence of protons or hydroxide ions are eliminated in the formula, a pH neutral reaction is obtained. Due to the high enantioselectivity of TeSADH W110A favouring the (*S*)-enantiomer as its chief substrate, when the electrochemical oxidation is initiated with (*rac*)-alcohol and approaches completion, most of the (*S*)-4-phenyl-2-butanol is expected to be converted into 4-phenyl-2-butanone, leaving the relatively slower substrate (*R*)-4-phenyl-2-butanol accumulating in the bulk solution. Ideally, this would expect to result in 50% ketone and 50% (*R*)-enantiomer as the final product.

All air-driven alcohol oxidation runs were performed at pH 9.0 and 25 °C. Unlike the cyclic voltammetry measurement, a much larger electrode (active surface area = 7.2 $cm^2$) was used to obtain quantifiable products for further analysis. Additional insight was also obtained by loading FNR first and then introducing ADH to enter the ITO nanopores from the bulk solution. Figure 3.8 shows results of electrooxidations using (*rac*)-, (*S*)- and (*R*)-4P2B, monitored as a function of time after the introduction of ADH into the gently stirred cell solution of the main compartment in which an FNR@ITO/Ti-foil electrode was placed. This electrode was pre-treated by dropcasting a 24 $\mu$L aliquot of concentrated FNR ([FNR] = 425 $\mu$M, 30 seconds incubation) onto a piece of fresh ITO/Ti-foil electrode. Each run was initiated by injecting a 25 $\mu$L aliquot of TeSADH W110A into the main compartment to attain a final concentration of 0.44 $\mu$M. Prior to ADH injection, the cell had already been charged with all reactants and $NADP^+$ as indicated. Concentrations of different enantiomers of 4P2B being added, determined by $^1$H NMR, were limited by their

solubility in aqueous phase (approximately 10 mM). Similar to the $H_2$-driven fuel cell scheme, four pieces of valuable information are contained in these *i-t* curves:

1. The current that is monitored at given time is proportional to an empirical catalytic turnover constant $k'$ (mole $s^{-1}$ $cm^{-2}$ (per unit area of electrode)) *via* the equation $i = 2k'FA$, in which $F$ is the Faraday constant and $A$ is the active surface area of the (FNR + ADH)@ITO/Ti-foil electrode.

2. The slope of the initial increase of current reflects the rate at which nanozones comprised of the ADH and FNR become progressively assembled in the ITO layer.

3. The total integral under each curve gives the total charge passed, which is directly related to the yield of chemical *via* the relation $\int i\mathrm{d}t = 2F \times$ total yield according to the Faraday's laws of electrolysis. Also, the progress of the reaction at any time point can be obtained from the segment of the integral.

4. The current experiences enduring decrease after reaching a maximum due to several reasons: **(i)** the reaction approached to completion; **(ii)** it was gradually product-inhibited as products accumulate in proximity; **(iii)** slow inactivation of enzymes occurred.

Coulometry (charge passed), $^1$H NMR, and GC-FID (gas chromatography with flame-ionization detection) were used to quantify results of measurements over a series of $NADP^+$ concentrations and reactants. Detailed data shown in Table 3.1 and 3.2 in which entries A–C were charged with racemate, while D and E were carried out with (*S*)- and (*R*)-enantiomers. A Typical NMR result after the experiment (entry A of Table 3.1) is shown in Figure 3.9 which shows spectra and characteristic peaks corresponding to the buffer, alcohol and ketone. As expected, peaks for both (*rac*)-4P2B ($\delta$ 1.18, m, 3H) and 4-phenyl-2-butanone ($\delta$ 2.18, m, 3H) exist in the spectrum after the electrooxidation run. The very large peaks ranging from 1.9–2.05 correspond to the TAPS buffer, while those standing at 0.0 are the signals for the

internal standard (Trimethylsilyl)propionic-2,2,3,3-$d_4$ acid sodium salt (TMSP) with fixed concentration.

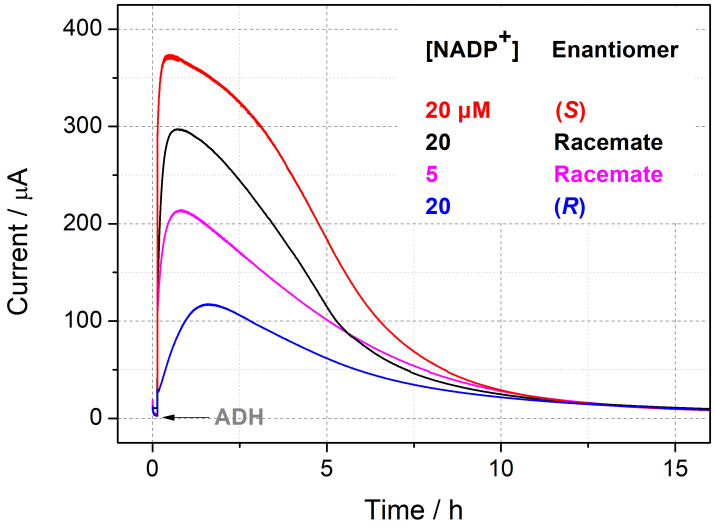



**Figure 3.8** *i-t* curves (timecourses or chronoamperograms, CA) illustrating electrooxidation of (*rac*)-, (*S*)- and (*R*)-4P2B under air-driven fuel cell mode. Experimental conditions: buffer = TAPS, pH = 9.0, 25 °C, [ADH] = 0.44 $\mu$M, cell volume = 5 mL for the main compartment and 1 mL for the PCP-containing compartment, active surface area of the (FNR + ADH)@ITO-Ti foil electrode = 7.2 $cm^2$ ([FNR] = 0.43 $\mu$M, 24 $\mu$L, by dropcasting, 30 seconds incubation), air flow rate = 2.6 scc $min^{-1}$, [(*rac*)-4P2B] = 11.6 mM, [(*S*)-4P2B] = 10.5 mM, [(*S*)-4P2B] = 9.7 mM. Concentrations of $NADP^+$ and types of enantiomers utilised for each run are shown in the legend. More detailed results for these four curves are listed in entries A, B, D and E of Table 3.1. Adapted with permission from L. Wan *et al.* Copyright 2019, Royal Society of Chemistry.[236]

**Table 3.1** Compilation of data for the air-driven TeSADH-W110A-catalysed electrooxidation of different enantiomers of 4-phenyl-2-butanol using an FNR@ITO/Ti electrode in an air-driven fuel-cell scheme.

| | Reactant | Reactant amount[a]/mM | NADP$^+$/$\mu$M | conversion[b]/% Charge passed | conversion[b]/% NMR | conversion[b]/% GC | ee[c] / % | TTN[d]/product/NADP$^+$ (approx.) Charge passed | TTN[d]/product/NADP$^+$ (approx.) NMR | TTN[d]/product/NADP$^+$ (approx.) GC |
|---|---|---|---|---|---|---|---|---|---|---|
| A | (*rac*)-4-phenyl-2-butanol | 11.6 | 5 | 38.7 | 39.7 | 38.3 | 85 (R) | 898 | 922 | 889 |
| B | (*rac*)-4-phenyl-2-butanol | 11.6 | 20 | 48.4 | 48.5 | 48.5 | 99 (R) | 279 | 281 | 282 |
| C | (*rac*)-4-phenyl-2-butanol | 11.6 | 50 | 50.4 | 55.4 | 43 | 96 (R) | 117 | 129 | 123 |
| D | (*S*)-4-phenyl-2-butanol | 10.5 | 20 | 71.1 | 68.3 | 60.7 | 99 (S)[e] | 372 | 360 | 319 |
| E | (*R*)-4-phenyl-2-butanol | 9.9 | 20 | 27.3 | 36.9 | 33.8 | 99 (R) | 135 | 182 | 167 |

Experimental conditions: FNR@ITO/Ti-foil anode (7.2 cm$^2$), PCP cathode (2.4 cm$^2$), T = 25 °C, pH = 9.0, 0.2 M TAPS buffer, [TeSADH W110A] = 0.44 $\mu$M (in solution), solution volume in the main compartment = 5 mL, solution volume in the PCP-containing compartment = 1 mL, air flow rate in the PCP-containing compartment = 2.6 scc min$^{-1}$. [a] Concentrations of reactants determined by $^1$H NMR. [b] Defined as [product]/[reactant] × 100 %. The product has been normalised due to volume change (details shown in Table 3.2). [c] Defined as $\left|\frac{c^{\mathrm{R}}-c^{\mathrm{S}}}{c^{\mathrm{R}}+c^{\mathrm{S}}}\right| \times 100\%$. [d] Defined as [product]/[NADP$^+$]. [e] This result will be discussed in the next chapter. Adapted with permission from L. Wan *et al.* Copyright 2019, Royal Society of Chemistry.[236]

**Table 3.2** Supplementary data for results in Table 3.1.

| | Reactant | Final cell volume[a] / mL | [Ketone] / mM | | Normalised[b] [Ketone] / mM | | [Alcohol] / mM | | Normalised[b] [Alcohol] / mM | | Loss[c] / % | |
|---|---|---|---|---|---|---|---|---|---|---|---|---|
| | | | NMR | GC | NMR | GC | NMR | GC | NMR | GC | NMR | GC |
| A | (*rac*)-4-phenyl-2-butanol | 6.3 ± 0.1 | 3.66 | 3.53 | 4.61 | 4.44 | 4.57 | 4.47 | 5.75 | 5.63 | 10.69 | 13.19 |
| B | (*rac*)-4-phenyl-2-butanol | 6.5 ± 0.1 | 4.34 | 4.33 | 5.63 | 5.63 | 2.55 | 2.27 | 3.32 | 2.95 | 22.84 | 26.03 |
| C | (*rac*)-4-phenyl-2-butanol | 6.4 ± 0.1 | 5.03 | 4.80 | 6.44 | 6.15 | 1.88 | 1.72 | 2.41 | 2.23 | 23.71 | 27.76 |
| D | (*S*)-4-phenyl-2-butanol | 6.45 ± 0.15 | 5.57 | 4.94 | 7.19 | 6.38 | 0.56 | 0.45 | 0.73 | 0.59 | 24.57 | 33.61 |
| E | (*R*)-4-phenyl-2-butanol | 6.2 ± 0.1 | 2.94 | 2.68 | 3.65 | 3.32 | 3.47 | 3.32 | 4.31 | 4.11 | 19.60 | 24.95 |

All entries in this table correspond to those in Table 3.1. [a] The final cell volumes are the volume of the main compartment plus that of the PCP-containing compartment after the CA measurement. [b] The term 'normalised' here means that the concentration measured is calculated by multiplying a volume factor 'final volume/5 mL'. [c] Defined by (1 – (normalised [ketone] + normalised [alcohol])/[initial reactant]) × 100 %. Adapted with permission from L. Wan *et al.* Copyright 2019, Royal Society of Chemistry.[236]

Taking the black trace in Figure 3.8 as an exemplary case where [$NADP^+$] = 20 $\mu$M and [(*rac*)-4P2B] = 11.6 mM, the anodic current increases continuously for 40 minutes after ADH injection, before peaking at 360 $\mu$A and eventually decreasing to a low level after 15 hours, at which point the conversion was equivalent to 48.4% based on coulometry. Meanwhile, the product analysed by $^1$H NMR, and GC-FID gave similar conversion values of 48.5% (Table 3.1). These results are very encouraging, considering the fact that crossover (leakage of substrates and products into the PCP-containing chamber) and volatility (the cell is not fully airtight and the chemicals are volatile). Upon lowering the [$NADP^+$] to 5 $\mu$M (magenta trace in Table 3.1), the run with (*rac*)-4P2B still secured a decent peak current at 0.2 mA, which approximately corresponded to 70% of the value achieved using 20 $\mu$M $NADP^+$. As expected, the total turnover number (TTN, defined as [ketone]/[$NADP^+$]), achieved the highest value when $NADP^+$ concentration was lower, and was also limited by the amount of alcohol available for conversion due to low solubility. Enantiomeric excess (ee) levels of 85, 99 and 96% for (*R*)-enantiomer were realised at 5, 20, and 50 $\mu$M [$NADP^+$], respectively. These results confirm our prediction that if (*S*)-4P2B is oxidised much faster than (*R*)-4P2B, electrochemically driven kinetic resolution to produce (*R*)-enantiomer is feasible. The control experiment using the favoured enantiomer (*S*)-4P2B (red trace, Figure 3.8) revealed that a much higher yield and rate are obtained. Interestingly, the measurement using pure (*R*)-4P2B (blue) showed that significant conversion also occurred, albeit with a decreased yield and lower reaction rate. Also, using (*R*)-4P2B alone, much longer time is required for the current to reach an optimal level, indicating that the lower natural activity of TeSADH W110A upon this enantiomer – as suggested in the enantiomeric ratio E determined from solution assays,[2] is partially compensated when a great number of ADH molecules go into the pores.

To have further insight into the factors that can control the overall electrocatalytic activity, experiments were performed to observe the response of the system following

[2]The enantiomeric ratio E in this case is 50.0 favouring the (*S*)-enantiomer. Detailed results regarding enantioselectivity of TeSADH W110A will be discussed in Chapter 4.

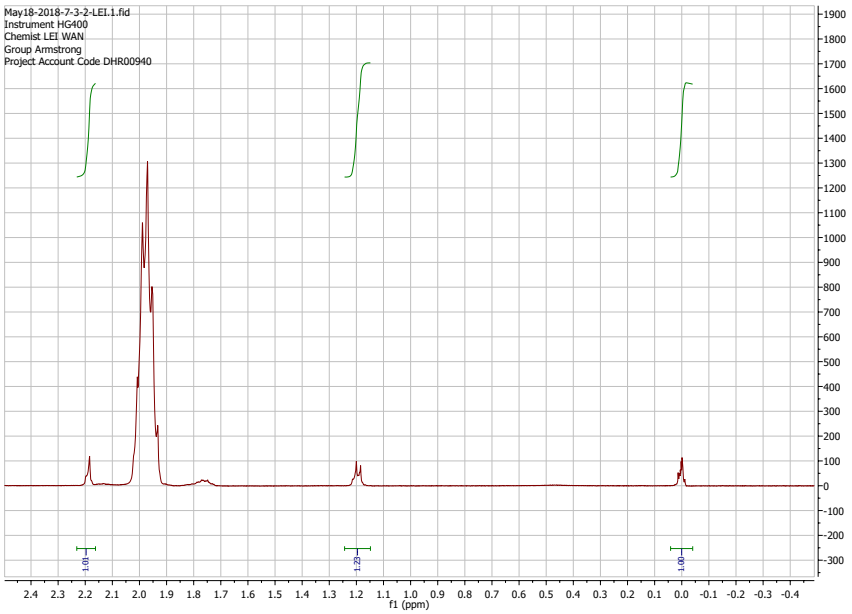



**Figure 3.9** $^1$H NMR spectrum of the cell solution for entry A in Tables 3.1 and 3.2. Apart from the peaks for TAPS buffer and TMSP standard solution for referencing, peaks at $\delta$ 1.18 (m, 3H) correspond to 4-phenyl-2-butanol and those at $\delta$ 2.18 (m, 3H) correspond to 4-phenyl-butanone. Adapted with permission from L. Wan *et al.* Copyright 2019, Royal Society of Chemistry.[236]

intended interventions, such as injections of more substrate, product, cofactor or enzyme. A chronoamperometry experiment monitoring these interventions over 18 hours is shown in Figure 3.10, where the measurement was initiated by injecting ADH into the cell to give a final concentration 0.19 $\mu$M. At the time point when the current had decreased to approximately 25% of its highest value, an aliquot of the substrate (*rac*)-4P2B equivalent to 2.5 mM in the cell solution was injected (or short circuit), leading to an immediate increase in current. Next was the injection of the ketone (the product, also inhibitor, and again equivalent to 2.5 mM in the cell solution) which resulted in a drop of current by a third. More interventions involved introductions of ADH, FNR, NADP$^+$, and second additions of alcohol and ketone. While more ADH molecules which increased the its concentration in the cell by 0.11 $\mu$M caused a rise in current, the addition of FNR caused virtually no change at all and the injection of NADP$^+$, which doubled the initial concentration to 100 $\mu$M, resulted in less than 10% increase in current. The second introductions of alcohol

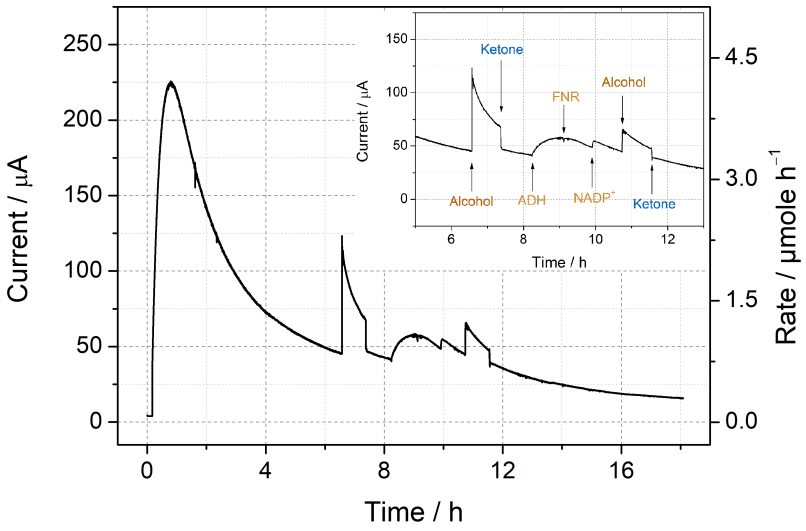



**Figure 3.10** *i-t* curve demonstrating the response of the system upon which different interventions exerted. Experimental methods: buffer = TAPS (pH =9.0, 200 mM), 25 °C, [(*rac*)-4P2B] (initial, in the main compartment) = 2.5 mM, [$NADP^+$] (initial) = 50 $\mu$M, [ADH] (following injection into solution) = 0.19 $\mu$M, air flow rate in the Pt-containing compartment = 10 scc $min^{-1}$, volume of cell solution = 9 mL for the main compartment and 1.2 mL for the PCP-containing compartment, active surface area of the FNR@ITO/Ti-foil electrode = 3.6 $cm^2$ (dropcasting method, [FNR] = 425 $\mu$M, 12 $\mu$L, 30 seconds incubation), surface area of the PCP electrode = 2.4 $cm^2$. The main compartment was bubbled with Ar throughout. The inset is an enlarged view of the period during which intensive interventions were made. Inside this inset, every injection of (*rac*)-4P2B and 4-phenyl-2-butanone increased their concentrations by 2.5 mM, injection of $NADP^+$ increased its concentration by 50 $\mu$M, injection of ADH increased its concentration by 0.11 $\mu$M, and injection of FNR increased its concentration by 0.57 $\mu$M. Adapted with permission from L. Wan *et al.* Copyright 2019, Royal Society of Chemistry.[236]

and ketone rendered a rise and drop in current, respectively.

## 3.7 Feasibility of Switch between $H_2$-Driven and Air-driven Modes

Dissimilar to GLDH which is mainly efficient in reductive amination direction[117, 222], TeSADH can catalyse the interconversion of the alcohol/ketone couple rapidly in either oxidation or reduction direction. Therefore, it is reasonable to think that when working with 4-phenyl-2-butanone, the application of a reductive potential could drive ketone reduction. Due to high enantioselectivity of this system, the (*S*)-4P2B will be the main product. Figure 3.11 shows the $H_2$-driven 4-phenyl-2-butanone reduction using a similar two-electrode set-up described in the previous chapter. The original 4 mL cell solution contained 5 mM 4-phenyl-2-butanone, a PCP cathode and an as-prepared FNR@ITO/Ti-foil electrode. The cell was gently bubbled by $H_2$ flow throughout. The run was initiated by introducing 50 $\mu$M $NADP^+$ into the cell, resulting in a increase in current due to $NADP^+$ reduction. This can be clearly observed in the inset in which the first 3.2 hours of the run is enlarged. Soon after the current kept stable in a low level, TeSADH W110A was injected, after which an enduring activating period mainly due to ADH entering into the ITO nanopores and forming a catalytic couple with FNR was observed. To accelerate the electrocatalytic rate, this time some potential biases were applied after the current reached a plateau (the initial applied potential was 0 V *vs* Pt). For every 500 seconds, a more –30 mV reductive potential bias was applied to the (FNR + ADH)@ITO/Ti-foil cathode until –150 mV *vs* Pt was reached. These operations increased the current step by step until –300 $\mu$A was achieved at –150 mV *vs* Pt, after which a lasting deactivating periods was followed. Enantiomeric excess of 55.7% *(S)* for the final product was determined by GC-FID.

After checking the system's capability of performing both $H_2$-driven NADPH regeneration and air-driven $NADP^+$ regeneration, it is clear that the role of the (FNR + E2)@ITO/support electrode and platinum electrode can be switched with one

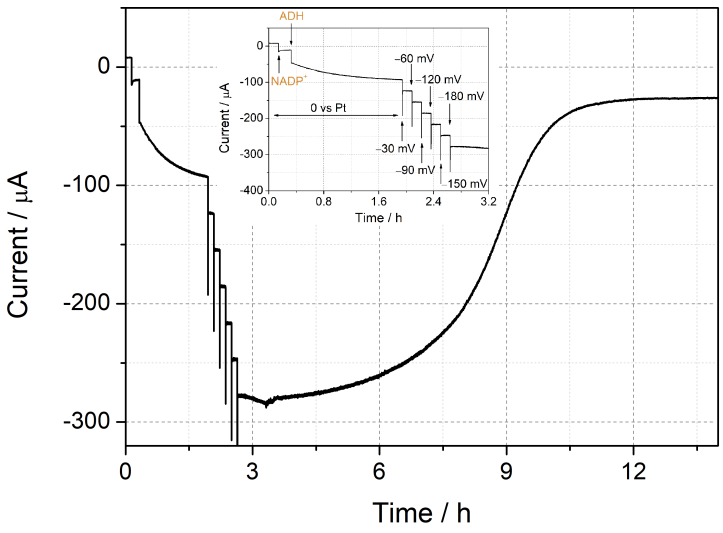



**Figure 3.11** The *i*-*t* curve showing the reduction of 4-phenyl-2-butanone driven by $H_2$ under different potential biases. Experimental conditions: cell solution = 4 mL, buffer = 50 mM MES, pH = 7.0, 25 °C, [4-phenyl-2-butanone] = 5 mM, [$NADP^+$] = 50 $\mu$M, [ADH] = 0.24 $\mu$M , active surface area of the FNR@ITO/Ti-foil electrode = 3.6 $cm^2$, active surface area of the PCP electrode = 2.4 $cm^2$, $H_2$ flow rate = 15 scc $min^{-1}$. The inset shows an enlarged view of the time period over which intensive interventions were made. This experiment was carried out using a membraneless one-compartment cell set-up, being introduced in Chapter 2.

another. As seen in Figure 3.12 which shows a schematic drawing of an electrochemical cell, one could easily achieve this goal by switching the gas flow to $H_2$/air, after which the sign of the current monitored will switch oppositely as the direction of electron flow changes.

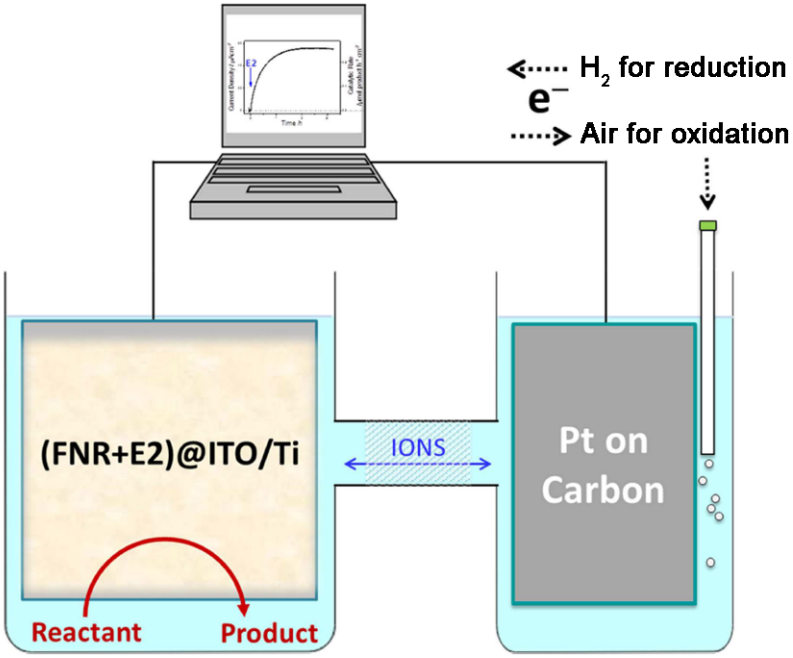



**Figure 3.12** This schematic drawing demonstrates that the $H_2$-driven and air-driven modes can be easily switched with one another by changing the gas to $H_2$/air. The progress of reaction represented by current can be monitored throughout. Re-printed with permission from C. F. Megarity *et al*, 2020, Wiley.[169]

## 3.8 Conclusions and Perspectives

Results analysed in this chapter represent a novel and facile method to realise enzyme-catalysed enantioselective oxidation of valuable chemical compounds – an approach that can conduct *in situ* monitoring and control.

A key contributor of high catalytic rate is the extremely high local concentration of FNR and ADH being entrapped within the ITO nanopores, through which NADP(H) is recycled more rapidly than without the nanoconfinement. Like the $H_2$-driven fuel cell scheme, the air-driven fuel cell reactor here has also been simplified which only requires an anode, cathode and PEM to form a full circuit. The reduction of $O_2$

(in air) catalysed by platinum is well-established, clean and provides a large, steady overpotential to drive the efficient, quasi-reversible alcohol oxidation at the anode.

After and between experiments, the enzyme-entrapped ITO layer ($\leq 3$ $\mu$m) is easily removed, cleaned, and replaced, while the ITO glass, Ti foil and platinum are all stable and can be reused continually. Unlike many traditional nicotinamide cofactor regeneration schemes that were carried out in homogeneous environment, the systems introduced in this thesis works with low concentration of NADP(H) ($\leq$ 20 $\mu$M *vs* 0.5 mM for typical analytical scale reactors).

Real-time monitoring (*via* current shown in *i-t* curves) enables continuous probing of the reaction when new additions of substrates, products, and enzymes are implemented. One can use this feature to optimise experimental conditions for synthesis, to conduct manual investigations, and to monitor bioorganic reactions.

# Chapter 4

# Racemisation & Kinetics Studies

## Abstract

The enantioselectivity of the Leaf when exploiting enantioselective dehydrogenases together with FNR is discussed in this chapter. A typical example is a variant of *sec*-ADH from *Thermoanerobacter ethanolicus* 39E (TeSADH W110A) which was also used in Chapter 3 and has an enantiomeric ratio (E value) value 50.0 (on 4-phenyl-2-butanol). This suggests that kinetically, this enzyme strongly favours (*S*)-4-phenyl-2-butanol over (*R*)-4-phenyl-2-butanol. In practice, however, electrochemical results show that when working with (*R*)- and (*S*)-4-phenyl-2-butanol separately, less than 10 times difference of catalytic rate was always monitored, which is much lower than the reported E value.

This chapter will show that the nanoconfined environment of the Leaf leads to an ADH-rich environment which strongly favours the thermodynamically favoured racemisation process. Also, the ratio between FNR and ADH in the pores casts significant influence on the final electrocatalytic current. This could be observed either by loading FNR and ADH sequentially (or *vice versa*) within the pores, with the resulting electrochemical reactions being limited by ADH and FNR at different stages or by co-loading FNR and ADH under different ratios. In the end of this chapter, some NADPH titration experiments will also be shown.

## 4.1 Introduction: Enantioselectivity of *sec*-ADH

TeSADH W110A is a variant of the *sec*-ADH from the thermophilic bacterium *Thermoanerobacter ethanolicus* 39E. This enzyme is (*S*)-selective, preferring the (*S*)-enantiomer of a mixture of enantiomerically pure secondary alcohols. In terms of the molecular basis that determines the enantioselectivity of *sec*-ADH, although there have been quite a few studies over the past few decades, the mechanisms are still not clear. A rule-of-thumb model is the so-called 'Prelog rules' that was proposed by V. Prelog in 1960s when he studied the stereochemistry of a suite of ketone reduction reactions using the culture that was rich in the fungus *Curvularia falcata*.[244] The Prelog's rule states that the *pro*-(*S*) or *pro*-(*R*) hydride is delivered from the *re* face of a prochiral ketone such that the (*S*)-configured alcohol is formed (as shown in the left hand side of Figure 4.1). Most known *sec*-ADH enzymes follow the Prelog rules, like the yeast ADH, ADH from horse liver (HLADH),[245] ADH from *Thermoanaerobium brockii* (TbSADH) [246] as well as TeSADH. Some *sec*-ADH enzymes follow the anti-Prelog's rule, like the ADH from *Lactobacillus brevis*[247] and from *Lactobacillus kefir*.[36, 248, 249]

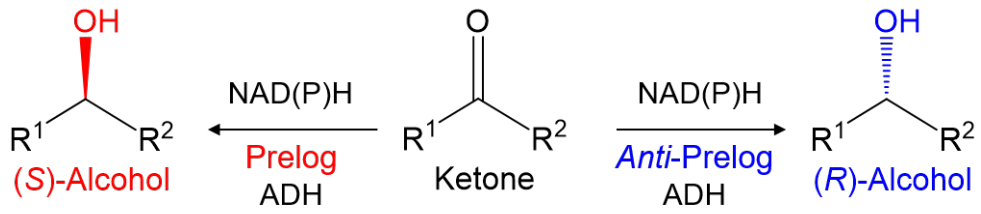



**Figure 4.1** A scheme of the 'Prelog's rule' and '*anti*-Prelog's rule' for *sec*-ADH-catalysed ketone reduction. Here, $R^1$ is sterically more hindered than $R^2$.[244]

In enzymology, a metric to reflect the intrinsic kinetic enantioselectivity of enzymes is the enantiomeric ratio E, defined as $(k_{cat}^{S}/K_{m}^{S})/(k_{cat}^{R}/K_{m}^{R})$[1], where $k_{cat}$ is the turnover number and $K_m$ is the Michaelis constant. These kinetic parameters can be determined by carrying out a solution assay for enzymes under a range of experimental conditions.

[1]Instead, the definition of E value for the (*R*)-selective enzyme should be $(k_{cat}^{R}/K_{m}^{R})/(k_{cat}^{S}/K_{m}^{S})$.

In this thesis, in addition to TeSADH W110A, two other (*S*)-selective *sec*-ADH variants from the TeSADH family – TeSADH W110G and W110V – were also used for electrochemical experiments. These three enzymes are all active on the (*S*)-alcohol but vary in $K_m$,[2] $k_{cat}$ and more importantly, their E values. According to literature, results of ketone reduction catalysed by the wild-type TeSADH share high similarity with those of a highly homologous, NADPH-dependent TbSADH.[250] It was proposed that this enzyme has two hydrophobic sites (or pockets, a large one and a small one) which exhibit different affinities for the alkyl groups on ketone substrates with the smaller site having a higher affinity. The hypothesis accounting for the enantioselectivity of TeSADH by E. Keinan *et al.* is that (*R*)-alcohols are produced from pro-chiral ketones when their larger alkyl groups fit into the small pocket. On the other hand, the (*S*)-alcohols are produced when the larger alkyl group of ketones fit into the larger pocket, which is definitely easier to occur.[251, 252] For example, when 2-butanone, one of the most active substrates of the wild-type TeSADH, binds with the enzyme, it is the larger ethyl group fits into the larger pocket, leaving the smaller methyl group fits into the smaller pocket, such that the (*S*)-2-butanol is produced. This mechanism of size-dependent enantioselectivity was confirmed by mutations S39T and C295A, with one shrinking the size of the larger alkyl-binding pocket (S39T) and one enlarging the smaller pocket (C195A).[253, 254] These led to the enantioselectivity of the wild-type TeSADH shifting to (*R*)-selective. Based on this fact, M. Musa *et al.* successfully made a highly active (*R*)-selective I86 variant of TeSADH, which has an enlarged small pocket.[255]

The site-directed mutagenesis of the wild-type TeSADH Trp-110 by K. Ziegelmann-Fjeld *et al.* was based on the orientation of p-bromobenzyl alcohol in a solved ternary complex structure of HLADH.[232] In this case, the sterically hindered Trp-110 in the large pocket was replaced by alanine (W110A variant) such that the binding site can contain the phenyl-ring containing substrates like 4-phenyl-2-butanone and phenylacetone. The variants W110G and W110V share similar principles, but gave

[2]This is actually $K_{m,app}$ which is the $K_m$ value for alcohol/ketone at a single and fixed [NADPH].

subtle changes to the exact size and orientation of the larger pocket, leading to different extents of enantioselectivity favouring the (*S*)-enantiomer.[256] The plasmids of TeSADH W110A, W110G and W110V were offered by Dr. R. S. Heath in N. J. Turner's group at the University of Manchester.

For a *sec*-ADH that is enantio-complementary to the TeSADH family, the (*R*)-specific ADH *Lactobacillus kefir* (hereafter ADH LK) was purified and analysed. This enzyme has a broad substrate range, shows high enantioselectivity for the (*R*)-alcohol and is stabilised by $Mg^{2+}$.

Key kinetic parameters for the above-mentioned enzymes, including the $K_m$, $k_{cat}$, $K_i$, and E values for the oxidation of alcohols ((*S*)-4P2B and (*R*)-4P2B) and the reduction of the ketone 4-phenyl-2-butanone are shown in Table 4.1. These experiments were carried out by solution assays using a UV-Vis spectrophotometer; the data were fitted based on the modified Michaelis-Menten kinetics model:

$$v = v_{max}[S]/(K_m + [S] + \frac{[S]^2}{K_i}) \tag{4.1}$$

where $v$ is the first-order reaction rate, $K_m$ is the Michaelis constant, [S] is the concentration of substrate, and $K_i$ is the substrate inhibition constant.

The W110A variant has an E value of 50.0, compared to the less enantioselective W110G variant (E = 17.0). These two variants both have decent activities on (*S*)-4P2B and 4-phenyl-2-butanone. The W110V variant, on the other hand, is not as active as the W110A and W110G variants in oxidising (*S*)-4P2B. However, due to the fact that W110V has almost no detectable activity on the (*R*)-4P2B, a very high E value is expected (> 100), which is consistent with the reported studies (E = 134 ± 27.7 when using another phenyl-containing alcohol 1-phenyl-2-propanol). ADH LK, is the enantio-complementary *sec*-ADH of TeSADH. This enzyme has good activity on (*R*)-4P2B instead but no detectable activity on (*S*)-4P2B, which would hopefully give it a very large E value (> 100) too.

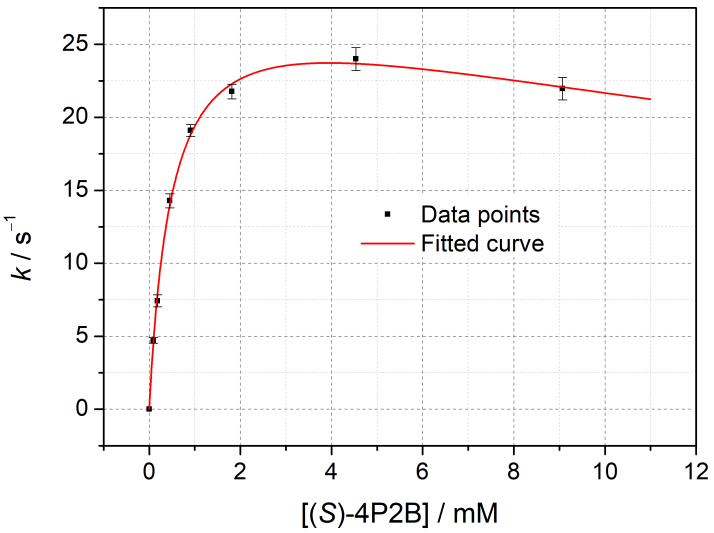
**Table 4.1** Kinetics data for the (*S*)-selective TeSADH W110A, W110G, and W110V enzymes, and the (*R*)-selective ADH LK.

| | TeSADH | | | ADH LK[b] |
|---|---|---|---|---|
| | W110A | W110G[a] | W110V[b] | |
| $k_{cat}$ (*S*) / $s^{-1}$ | 29.8 | 55.5 | 6.20 | \ |
| $K_m$ (*S*) / mM | 0.50 | 1.26 | 0.13 | \ |
| $K_i$ (*S*) / mM | 30.9 | 23.8 | 60.5 | \ |
| $k_{cat}$ (*R*) / $s^{-1}$ | 0.68 | 1.92 | \ | 29.0 |
| $K_m$ (*R*) / mM | 0.57 | 0.74 | \ | 1.58 |
| $K_i$ (*R*) / mM | 25.1 | 23.5 | \ | \ |
| E value | 50.0 | 17.0 | \ | \ |
| $k_{cat}$ (ketone) / $s^{-1}$ | 48.4 | \ | 20.1 | 32.8 |
| $K_m$ (ketone) / mM | 0.29 | \ | 0.12 | 0.13 |
| $K_i$ (ketone) / mM | 2.20 | \ | 1.58 | \ |

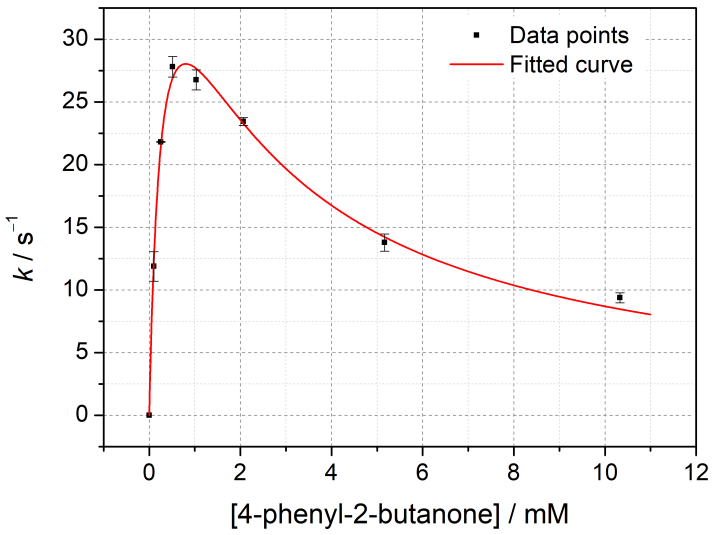
Kinetic parameters determined by solution assays for ADH-catalysed alcohol oxidation ((*S*)-4-phenyl-2-butanol and (*R*)-4-phenyl-2-butanol, at pH 9.0) and ketone reduction (4-phenyl-2-butanone at, pH 7.5), with substrate concentration ranging from 0.09–11 mM. Measurements were carried out using UV-Vis spectroscopy method. Initial rates were obtained (in triplicate) by monitoring the production (for the alcohol oxidation reaction, initiated with $NADP^+$) or consumption (for the ketone reduction reaction, initiated with NADPH) of NADPH by measuring the linear increase or decrease at $A_{340}$. Non-linear curve-fitting was operated using the 'lsqcurvefit' nonlinear model of MATLAB. [a] The kinetic parameters for the W110G-catalysed ketone reduction were not given, since there was no parallel electrochemical experiment performed using this variant. [b] The E values for ADH LK and TeSADH W110V are not shown because the specific activities with their less favoured alcohols were too low to monitor accurately but it is reasonable to assume that, based on this, both will have very high E values. Experimental conditions: $25 \pm 2^\circ$ C , [NADPH] = 200 $\mu$M, [$NADP^+$] = 300 $\mu$M, cuvette volume = 400 $\mu$L, buffer for alcohol oxidation: pH 9.0, 50 mM TAPS + 1 mM $MgCl_2$, buffer for ketone reduction: pH 7.5, 50 mM TAPS + 1 mM $MgCl_2$ + 25 mM NaCl. Adapted with permission from L. Wan *et al.*, Copyright 2021, American Chemical Society.[257]

The $K_\mathrm{i}$ presented in the Equation 4.1 reflects the extent that the enzymatic reactions are inhibited by the substrates being added. Substrate inhibition occurs in approximately 25% of known enzymes and accounts for the most common deviation from the model of Michaelis–Menten kinetics.[258–260] Enzymes which have substituted enzyme or ordered ternary complex mechanisms may exhibit the phenomenon of substrate inhibition where high concentration of the second substrate (in our case the alcohol or the ketone) may bind and act as inhibitors with respect to the first substrate. Figure 4.2 shows Michaelis-Menten plots in which the kinetics data have been fitted to the modified Michaelis-Menten equation (Equation 4.1). Panel **a** illustrates the plot of the results corresponding to the oxidation of (*S*)-4P2B by TeSADH W110A (data presented in Table 4.1). It is clear that the rate measured at *ca.* 10 mM alcohol is lower than that at *ca.* 5 mM which is most likely explained by substrate inhibition. After curve-fitting, the inhibition constant $K_\mathrm{i}$ was determined to be 26.3 mM. Based on the mathematical expression of Equation 4.1, the smaller the substrate inhibition constant $K_\mathrm{i}$, the more significant the inhibition effect. Panel **b** shows a seriously substrate-inhibited case where the determined $K_\mathrm{i}$ is 2.20 mM (reduction of 4-phenyl-2-butanone at pH 7.5, data shown in Table 4.1). The highest activity is achieved at 0.5 mM above which the turnover frequency $k$ decreases dramatically. Mathematically, when $K_\mathrm{i}$ approaches $+\infty$, or in other words, there is no inhibition effect, Equation 4.1 then simplifies to the basic Michaelis-Menten equation:

$$\frac{v_\mathrm{max}[\mathrm{S}]}{K_\mathrm{m} + [\mathrm{S}]} \tag{4.2}$$




**(a)** Oxidation of (*S*)-4P2B.




**(b)** Reduction of 4-phenyl-2-butanone.

**Figure 4.2** Kinetics data for TeSADH W110A. Data fitted to the modified Michaelis-Menten Equation 4.1. Experimental conditions and determined kinetic parameters are shown in Table 4.1.

## 4.2 Hints from Previous Electrochemical Data

### 4.2.1 Disagreement between Electrochemical Results and Kinetics Data

Based on the E values from solution assays (Table 4.1), it was expected that when using TeSADH W110A, the oxidation of (*S*)-4P2B should be 50 times faster than that of (*R*)-4P2B. Similarly, the reduction of 4-phenyl-2-butanone should give predominately (*S*)-4P2B (*ca.* ee 96.1% (*S*)). This prediction which is totally based on kinetics data, is however not consistent with the electrochemical results obtained in the previous chapter. The surprising results worth paying special attention to are:

- Figure 3.8 in the previous chapter shows the CAs of enantioselective oxidation of (*S*)-, (*R*)- and (*rac*)-4P2B driven by air. Instead of 50 times, the maximum current achieved for (*S*)-4P2B was only approximately three times than that for (*R*)-4P2B.

- In the same experiments, the electrodes were formed by pre-loading FNR, followed by the injection of TeSADH W110A into the bulk solution. The activation of the (FNR + ADH)@ITO/Ti-foil electrode was then continuously visualised by looking at the growing of current which corresponds to the process that ADH goes into the ITO nanopores.[163] However, it took *ca.* 3 times longer to reach the maximum current for the case initiated with (*R*)-4P2B than its chiral counterpart.

- Coming back to the GC-FID analysis results of electrochemical oxidation of (*S*)-4P2B described in Figure 3.8, it was surprising to see that the chirality outcome gave an (*R*) majority.

- The results of $H_2$-driven reduction of 4-phenyl-2-butanone (Figure 3.11) shows that the ee was only 55.7% (*S*). This implied that a certain amount of (*R*)-4P2B was produced.

If the reactions using the Leaf were controlled strictly by kinetics, these counter-intuitive results would not be observed. It was therefore hypothesised that the

nanoconfined environment of the porous electrode must have influenced the outcome compared to the results obtained from traditional solution assays.

### 4.2.2 Hypotheses Based on the Electrochemical Results and Kinetics Data of TeSADH W110A

#### *4.2.2.1 Racemisation*

By definition, racemisation is a process that forms a racemic mixture of enantiomers from its enantiomerically pure form without affecting the chemical constitution of the compound. In the case for our ADH-catalysed reaction, this corresponds to the case where either enantiopure (*S*)-4P2B or (*R*)-4P2B is converted to (*rac*)-4P2B. Thermodynamically, racemisation is favoured by a value of free energy $\Delta G = -RT \ln 2$ equalling to –1.7 kJ mol$^{-1}$ at 298 K.[261]

The enantiomeric ratio E values, on the other hand, is a kinetic metric to reflect the inherent enantioselectivity of enzymes. As thermodynamics always favours racemisation, when a reaction is carried out using enantioselective enzymes as the catalyst, the ratio between the two enantiomers could be much lower than the E value. As shown in Figure 4.3, a homogeneous reaction to racemise enantiomerically pure (*S*)-alcohol or (*R*)-alcohol can be performed using an one-pot reactor which contains $NADP^+$, NADPH, and TeSADH W110A. M. Musa *et al.* achieved partial racemisation of a set of phenyl-containing enantiopure secondary alcohols using this scheme. In this work, in the experiment exploiting (*S*)-4P2B or (*R*)-4P2B as the starting compounds, after 48 hours of incubation at 50 °C, 82.4% (*S*) and 34.5% (*R*) can be achieved.

The experimental conditions for the above reactions required relatively concentrated cofactors (1 mM) and enzymes (0.3 mg mL$^{-1}$). In our case, enzymes, chemical species, and cofactors are entrapped/retained in high concentrations within the nanopores of the Electrochemical Leaf's porous electrode. It is sensible to think that the Leaf might have an parallel version of racemisation.

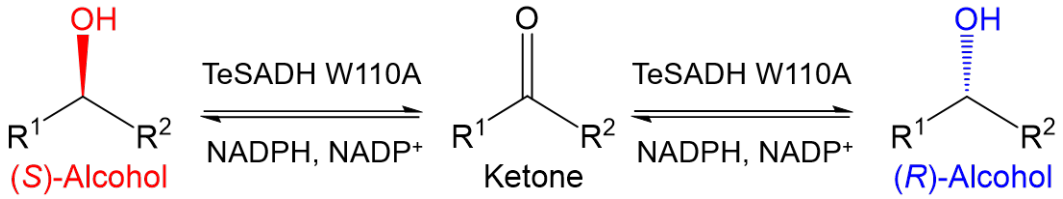



**Figure 4.3** A scheme of racemisation of secondary alcohols catalysed by TeSADH W110A starting with either enantiomerically pure (*S*)-alcohol or (*R*)-alcohol. Here, $R^1$ is sterically more hindered than $R^2$.[262]

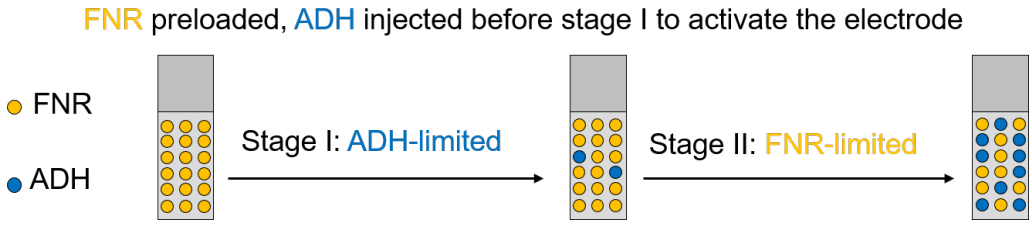
#### *4.2.2.2 ADH-limited and FNR-limited Scenarios*

Different ratios of FNR and the downstream enzymes that are entrapped within the nanopores could influence the overall electrocatalytic activity and lead to different rate-limited situations.

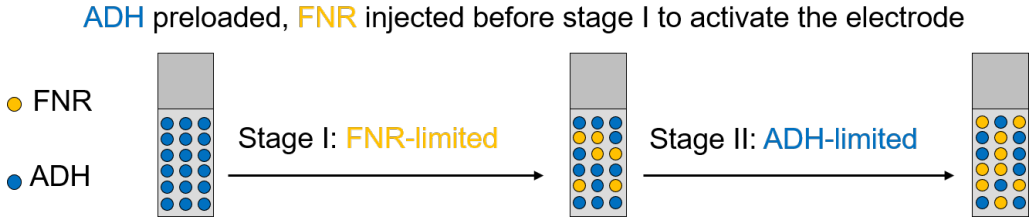
I here take an example using FNR and TeSADH as the catalytic couple. The first case is shown Figure 4.4a where FNR is preloaded on the electrode and ADH is then injected into the bulk solution later to initiate the activation of the (FNR + ADH)@ITO/support electrode. At first, the nanoporous zones contain only FNR molecules. Following the introduction of ADH, the rate-limiting factor over the initial stage is ADH, since the number of FNR molecules in the pores are in excess. As more and more ADH molecules adsorb in the pores, the coupled catalytic current increases until it reaches a maximum (achieved at the optimal ratio of FNR:ADH). After this point as more ADH molecules goes into the pores, the dominant enzyme now becomes ADH. At this stage, the reaction starts to be limited by FNR. Conversely, when the preloaded enzyme is ADH and FNR is the incoming enzyme, as shown in Figure 4.4b, the system will initially be limited by FNR, followed by an ADH-limited step later.

When working with the faster substrate (*S*)-4P2B and the slower substrate (*R*)-4P2B separately, two following scenarios can be envisaged:

- In the situation following Figure 4.4a where FNR is loaded first and ADH is the incoming enzyme, it would take a shorter time for the experiment initiated with (*S*)-4P2B to reach the maximum current, with the reasoning being that




**(a)** The shift from the ADH-limited to FNR-limited step.




**(b)** The shift from the FNR-limited to ADH-limited step.

**Figure 4.4** Schemes show two scenarios in which an FNR-limited or an ADH-limited electrode, is formed.

ADH is much more active on (*S*)-4P2B than (*R*)-4P2B, so to overcome the inherently slow rate of (*R*)-enantiomer, the adsorption of many more ADH molecules is required. This hypothesis is partially confirmed by previous results (Figure 3.8).

- For the situation following Figure 4.4b, ADH is loaded first and FNR serves as the incoming enzyme. During the initial stages (immediately after injecting FNR into the bulk solution), ADH molecules in the pores are in far excess of the incoming FNR and as such, the system is FNR-limited. As more and more FNR molecules adsorb, the current will increase (regardless of which enantiomer substrate for ADH is used) until it levels off at a maximum value. But, unlike the previous experiment in which the order of enzyme addition was reversed, this time, the experiment with the (*R*)-enantiomer should reach its maximum current earlier (in other words less FNR needs to adsorb) than the experiment using the (*S*)-enantiomer. This is because ADH is much more active with (*S*)-4P2B and therefore requires more FNR molecules to adsorb in order to 'keep up' with its inherently fast rate with this enantiomer.

Two separate CA measurements, one following the scheme shown in Figure 4.4a, one

in 4.4b would verify these hypotheses.

## 4.3 Studies on Rate-limiting Enzyme Ratios

In this section, to verify the hypothesis that the order of enzyme loading will lead to distinct limitations by each enzyme and thus different rate-limiting behaviour, a rotating PGE electrode and the W110G variant of TeSADH variant were used. Compared to the W110A variant, this W110G variant is kinetically faster in oxidising (*R*)- and is much less enantioselective (E value $< 20$) than the W110A variant (Table 4.1, but still faster with the (*S*)-enantiomer compared to (*R*)).

This section shows the chronoamperometric measurements where FNR is preloaded first, and then ADH is injected to activate the (FNR + TeSADH W110G)@ITO/PGE electrode. The coupled reactions are as follows:

$$(R)\text{-4-phenyl-2-butanol} \longrightarrow \text{4-phenyl-2-butanone} + 2\,H^+ + 2\,e^- \quad (\textbf{slow}) \tag{4.3}$$

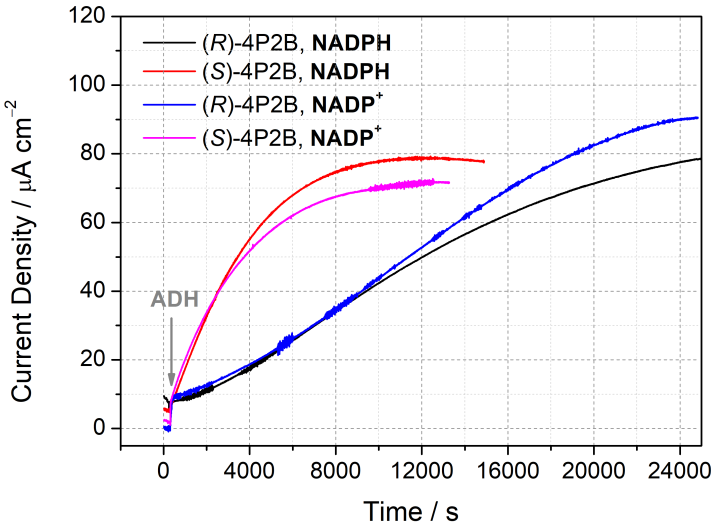
$$(S)\text{-4-phenyl-2-butanol} \longrightarrow \text{4-phenyl-2-butanone} + 2\,H^+ + 2\,e^- \quad (\textbf{fast}) \tag{4.4}$$

### 4.3.1 ADH- to FNR-limited Electrodes

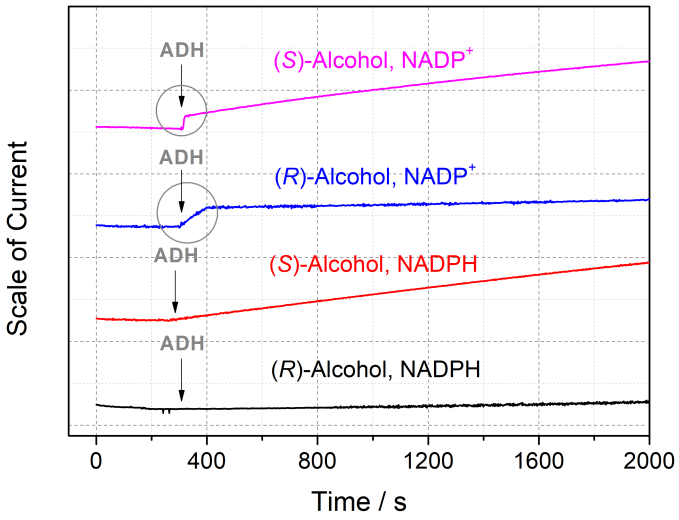
The results of CAs using rotating electrodes are shown in Figure 4.5a. Prior to the experiment, the PGE electrode preloaded with FNR was placed into a 3 mL electrochemical cell that was charged with 10 mM alcohol (either (*S*)- or (*R*)-4P2B) and 20 $\mu$M NADP(H) (either NADPH or $NADP^+$). This made four control experiments in total. The magenta trace shows the CA for (*S*)-4P2B oxidation using $NADP^+$ as the starting cofactor. The run was initiated by injecting TeSADH W110G to give the final concentration of 220 nM. The electrode was rotated at 1,000 rpm and the activity, represented as current density, rapidly grew over three hours before reaching a maximum of approximately 72 $\mu A\ cm^{-2}$. The control experiment carried out using the (*R*)-4P2B (blue trace), instead, shows a more enduring activation phase. The current density reached a steady state at 90 $\mu A\ cm^{-2}$ but took 7 hours.

Compared to the (*S*)-4P2B, this doubled the time required to reach the highest activity. As discussed in Figure 4.4a, (*R*)-enantiomer is the slower substrate, so the low activity must be compensated by introducing more ADH into the nanopores to reach an optimal ratio between FNR and ADH, which in practice obviously took more time to fulfil.

In addition, an interesting phenomenon can be observed in Figure 4.5b (the magnified views of the starting 2,000 seconds of the CAs). The increase of current density shortly after the injection of ADH was biphasic which consists of two mathematically discrete activation stages. Regarding the oxidation of (*R*)-4P2B (blue trace, $NADP^+$ as the cofactor), the first-stage activation last for 80–100 seconds with the current density increasing from virtually 0 to *ca.* 10 $\mu$A cm$^{-2}$. This was followed by the second stage – an enduring activation due to ADH going into the pores as described before. Similarly, for (*S*)-4P2B (magenta trace, $NADP^+$ as the cofactor), the injection of ADH also saw a sudden increase of current, but over a much shorter period (*ca.* 10 seconds). The hypothesis for this biphasic feature is that the injected ADH rapidly catalysed $NADP^+$ to NADPH in the bulk solution and the FNR-confined electrode thus oxidises this homogeneously produced NADPH portion. The reason why the measurement using (*S*)-4P2B had a much shorter first-stage activation than the one using (*R*)-4P2B (*ca.* 10 vs 80−100 seconds) is that in the bulk solution, the (*S*)-4P2B was oxidised faster; thus the production of NADPH for the subsequent FNR-catalysed NADPH oxidation was faster, compared to the slower rate using (*R*)-4P2B which provided the NADPH to FNR more slowly. Still, at this stage, the regeneration of cofactor by FNR for both was kinetically slow because the two enzymes stayed in different areas – FNR in the pores and ADH in the bulk solution. In the following second-stage activation, when ADH molecules started to go into the pores, the reaction started to be sped up and the contribution of the enhanced activity was predominantly due to the electrocatalytic units confined within the pores.




**(a)** The overlaid CAs of electrochemical oxidation using different starting enantiomers and redox forms of NADP(H).

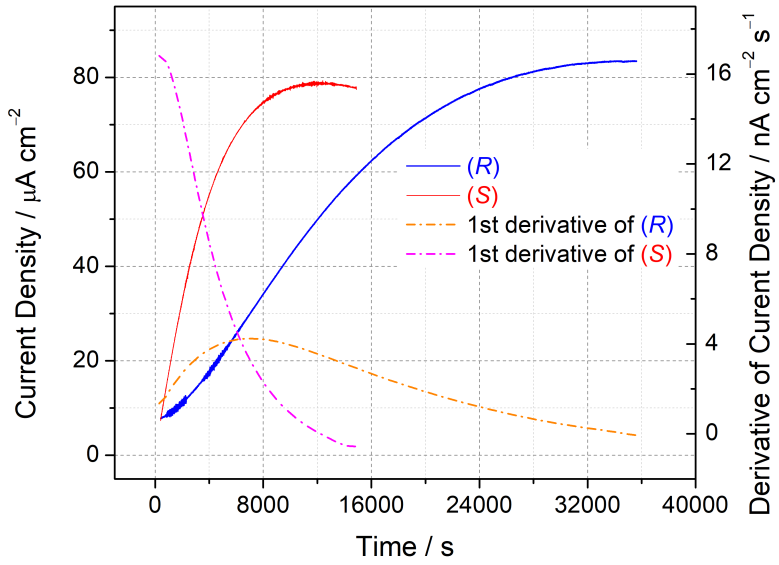



**(b)** Zoomed-in view of the CAs in panel **a** over the initial 2,000 seconds. The Y axis is adjusted to show the relative scale of current for comparison. The sites where the biphasic increase feature occurred are highlighted by gray circles.

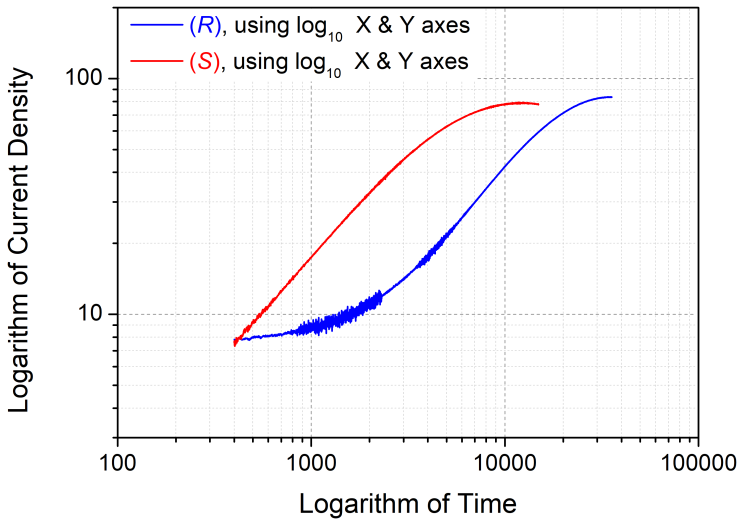
**Figure 4.5** Chronoamperograms showing electrochemical oxidation of (*R*)- and (*S*)-4P2B using either $NADP^+$ or NADPH as the starting cofactor. The electrode was formed by dropcasting an aliquot of 10 $\mu$L concentrated FNR (775 $\mu$M) on the PGE electrode (active surface area = 0.028–0.035 $cm^2$). This was incubated for three minutes and rinsed with buffer before use. Experimental conditions: [alcohols] = 10 mM, pH = 9.0, buffer = 25 mM TAPS + 25 mM MES, 26 °C, [$NADP^+$] = 20 $\mu$M, rotating speed = 1,000 rpm, [TeSADH W110G] (final concentration) = 220 nM, cell volume = 3 mL, applied potential = +0.11 V vs SHE.

This hypothesis is proved by control experiments using NADPH as the starting cofactor. The results are shown in the same figure (the red and black traces). From panel **a**, it is shown that the overall performance of electrocatalysis was independent of the initial redox state of NADP(H) as the trend of curves was highly repeatable. From panel **b**, it is clear that the biphasic feature no longer occurred. As expected, these two CAs showed initial electrochemical activity at *ca.* 10 $\mu$A due to direct FNR-catalysed NADPH oxidation and the ensuing growth of current was solely from the coupled reaction which can only occur due to the nanoconfinement of ADH.

For detailed analysis, the data from experiments using NADPH as the starting cofactor were extracted and plotted again in Figure 4.6a. The curves were processed using $\log_{10}$ X and Y axes (Figure 4.6b) from which it is clearer to see the increase in current after the injection of ADH. Compared to the red trace (oxidation of (*S*)-4P2B), the blue trace (oxidation of (*R*)-4P2B)) shows a lag phase over the first several thousand seconds. These curves were further processed using the 'polynomial fit' method of the OriginLab to determine their first-order derivatives which reflect the rate of change of the current. The magenta dash dot line, linked to the right Y axis, is the resulting first derivative of the red trace (oxidation of (*S*)-4P2B), from which we can see that following the injection of TeSADH W110G, the rate of change value was immediately obtained at 16.5 nA $cm^{-2}$ $s^{-1}$, suggesting that at this point the increase in current was rapid. This value then decreased throughout and crossed the X axis after 3.5 hours, at which point the current levelled off and started to decline. On the other hand, the corresponding curve for (*R*)-4P2B (orange trace) did not display a fast rate of change initially with only 1.3 nA $cm^{-2}$ $s^{-1}$. Over the next two hours, this value kept increasing and finally reached 4.2 nA $cm^{-2}$ $s^{-1}$, more than tripling its initial value.




**(a)** Chronoamperograms of electrochemical oxidation of (*R*)- (blue trace) and (*S*)-4P2B (red trace) (linked to the left Y axis), and their first derivatives (the orange dash dot line for (*R*) and the magenta one for (*S*), linked to the right Y axis).




**(b)** Logarithmic plots of the red and blue traces in panel **(a)** using log10 type X and Y axes.

**Figure 4.6** Detailed analysis of the (FNR + TeSADH W110G)@ITO-catalysed electrochemical oxidation of (*R*)- and (*S*)-4P2B (data extracted in Figure 4.5). The starting cofactor was NADPH.

### 4.3.2 FNR- to ADH-limited Electrodes

As predicted in Figure 4.4b, for an initially ADH-rich electrode, the injection of FNR to activate the (FNR + ADH)@ITO/support coupled catalysis is expected to trigger a gradual switch from being FNR- to ADH-limited. For the experiment charged with the faster substrate (*S*)-4P2B, more FNR is needed to reach the highest activity than for (*R*)-4P2B. This predicts that the activation phase following the injection of FNR should last longer since more FNR is required to adsorb into the pores in order to 'keep up' with the very fast reaction of ADH with the (*S*)-enantiomer.

Results of CA experiments using a PGE electrode preloaded with TeSADH W110G initiated by injecting FNR is shown in Figure 4.7, with red and blue traces illustrating the cases for (*S*)-4P2B and (*R*)-4P2B, respectively. The as-prepared electrodes were placed into the electrochemical cell which was charged with 10 mM alcohol and 20 $\mu$M $NADP^+$. Catalysis was initiated by injecting FNR into the cell to give the final concentration of 1.03 $\mu$M. Throughout the measurement, the electrode was rotated at 1,000 rpm with applied potential +0.11 V vs SHE. For (*S*)-4P2B, after the injection of FNR, the current started to increase due to FNR going into the nanopores and this stage of activation last for more than six hours, at which point a new aliquot of FNR to give a total concentration of 1.03 $\mu$M in the cell was injected. This extra operation had no noticeable influence on electrode activity, as the current density once achieved at 90 $\mu$A $cm^{-2}$ stayed unchanged afterwards, suggesting that at this point an ADH-limited situation had been reached (or the system was no longer limited by FNR). The control experiment using (*R*)-4P2B instead, took approximately 12,000 seconds to reach the maximum current. That is half that of (*S*)-4P2B. The largest current density once achieved was 50 $\mu$A $cm^{-2}$ or a bit more than half of the highest activity achieved using (*S*)-4P2B. Also, further injection of FNR did not change the activity anymore.

Unlike the experiments described in the last section, following the injection of FNR, the initial rate of change was almost the same for both cases. Based on the hypothesis, it would be sensible to envisage that during the FNR-limited stage, the

amount of ADH within the nanopores was in excess, which would compensate for the slow specific activity of TeSADH W110G on (*R*)-4P2B. As more and more FNR molecules go into the nanopores, the ADH-limited step approaches when the ratio of ADH:FNR is not high enough to support the maximum achievable activity anymore. However, as the case charged with (*S*)-4P2B definitely requires more FNR to match with the activity of ADH, it took longer for the current to level off (*i.e.* for more FNR to adsorb).

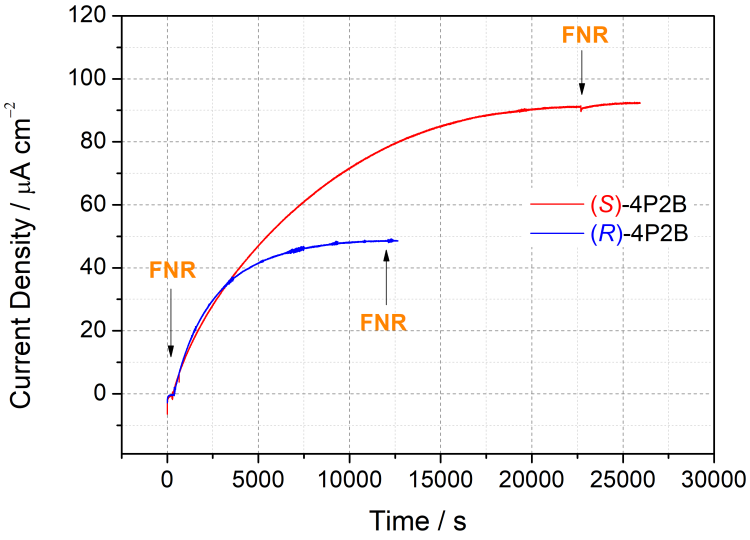



**Figure 4.7** Chronoamperograms for electrochemical oxidation of (*S*)- (red trace) and (*R*)-4P2B (blue trace). A 10 $\mu$L aliquot of concentrated TeSADH W110G (65.8 $\mu$M) was preloaded on the PGE electrode (active surface area = 0.028–0.035 cm$^2$) and incubated for 30 minutes. The electrode was rinsed in pH 9.0 buffer before use. Experimental conditions: [alcohols] = 10 mM, pH 9.0, buffer = 25 mM TAPS + 25 mM MES, 26 °C, [NADP$^+$]= 20 $\mu$M, rotating speed = 1,000 rpm, [FNR] = 1.03 $\mu$M (after the first injection) and an extra 1.03 $\mu$M (to give a total 2.06 $\mu$M after the second injection), cell volume = 3 mL, applied potential = +0.11 V vs SHE.

## 4.4 Spontaneous Racemisation in the Bulk Solution

The experiments presented in the previous section have partially confirmed the hypotheses that the order of introducing enzymes sequentially can lead to different rate-determining outcomes during the formation of the (FNR + E2)@ITO/support electrode. There is one exception, however, that the electrocatalytic current of the CA charged with (*R*)-4P2B was higher than expected and in most cases could reach 50−100% of the activity to the control experiments charged with (*S*)-4P2B. This is contradictory to the fact that TeSADH W110G has an E value of 17.0. Also, an especially counterintuitive result demonstrated in the Subsection 4.3.1 shows that the injection ADH (FNR-preloaded) can lead to a lag phase in current growth. In other words, the increase in current was slow at first and soon started to accelerate. After close inspection of these counterintuitive results, it is now reasonable to think that apart from different enzyme-limited stages, the results are also convoluted by the thermodynamically favoured process: **racemisation**.

Previously, the enzymes, especially the E2 were injected to initiate the measurement, so these macromolecules were present in both bulk solution and the ITO nanopores. This section will try to figure out any contribution of racemisation from the bulk solution, aiming at ruling out this variable for future experiments. The results of a CA measurement with designed buffer exchange and electrode cleaning processes are shown in Figure 4.8. The red trace shows the result of the electrochemical oxidation of (*S*)-4P2B at pH 9.0. The run was initiated by co-injecting an aliquot of FNR and TeSADH W110A mixture into the cell being charged with 9.3 mM (*S*)-4P2B and 20 $\mu$M $NADP^+$ (here, the electrode is a piece of bare ITO/Ti-foil without preloaded enzymes). Soon after the current peaked at approximately 370 $\mu$A, a series of operations were carried out: **(i)** the CA was paused and the electrode was withdrawn, rinsed thoroughly with buffer, and stored to one side in buffer; **(ii)** the cell solution which contained the injected enzymes was removed and the cell was rinsed to ensure complete removal of traces of enzymes; **(iii)** the cell was replenished

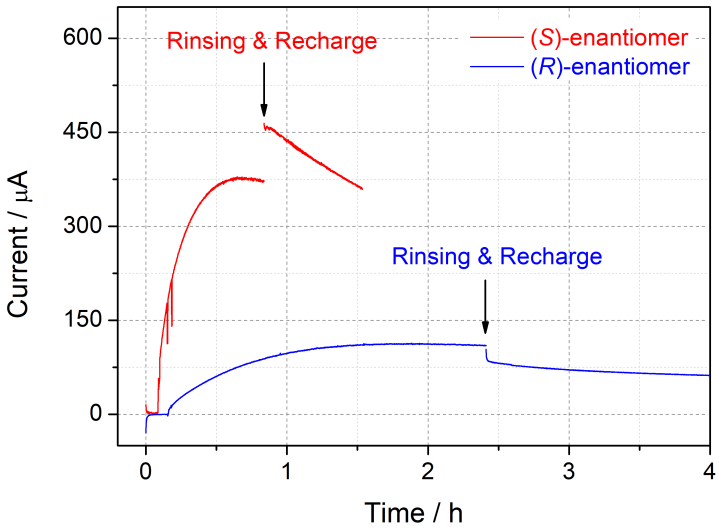



**Figure 4.8** Chronoamperograms of electrochemical oxidation of (*S*)- (red trace) and (*R*)-4P2B (blue trace) using (FNR + TeSADH W110A)@ITO/Ti-foil electrodes. The raw ITO/Ti-foil electrode (surface area = 7.2 $cm^2$) was placed into the electrochemical cell which was charged with alcohol ((*S*)-4P2B (9.3 mM) or (*R*)-4P2B (10.8 mM)) and 20 $\mu$M $NADP^+$. The measurement was initiated by injecting an aliquot of FNR and TeSADH W110A mixture to give the final concentrations of 2.33 $\mu$M and 1.35 $\mu$M in the cell, respectively. After the currents reached the accordingly highest levels, the electrodes were taken out and rinsed thoroughly by the pH 9.0 buffer before being placed into the electrochemical cell which was cleaned and recharged (buffer exchange) with new pH 9.0 buffer containing (*S*)-4P2B or (*R*)-4P2B and 20 $\mu$M $NADP^+$. The ensuing electrochemical oxidation was carried out under the same oxidation potential. Experimental conditions: buffer = 50 mM TAPS + 1 mM $MgCl_2$, pH = 9.0, 26 °C, potential = +0.071 V vs SHE.

with fresh cell solution containing all reactants (apart from enzymes) at the same concentrations as used initially; **(iv)** the electrode was placed back to the cell; **(v)** the CA was resumed. The restarting of the CA saw a sudden jump from the previously achieved current, 370 $\mu$A to 450 $\mu$A which took another one hour to decrease back to the previous highest value. The increase of the largest current was likely due to the relief of product inhibition, as based on coulometry, prior to the buffer exchange, more than 1 mM ketone was produced. The control experiment using (*R*)-4P2B shows a slightly different scenario. Following the exchange of buffer, the current dropped by 25% from the previous highest value from 110 $\mu$A to 85 $\mu$A. The reaction was allowed to proceed until 1 mM yield was achieved as determined by coulometry. The cell solutions for both experiments before and after the exchange of buffer were collected and chiral analyses of these samples are shown in Table 4.2, from which it is clear that during the first-stage electrolysis of both alcohols with enzymes present in the bulk solution, significant racemisation occurred. This resulted in ee 86.5% (*R*) and 92.2% (*S*), respectively. On the other hand, after the buffer exchange which washed away the enzyme in the bulk solution, the racemisation effect during the second-stage oxidation was much weaker. For the experiment charged with (*S*)-4P2B, no (*R*)-enantiomer was detected and for the case initiated with (*R*)-4P2B, the ee was 97.1% (*R*).

**Table 4.2** Chirality results for the experiments described in Figure 4.8.

| Measurement | [Alcohol] | Duration | GC Peak Area[a] | | Conversion[b] | ee / % |
|---|---|---|---|---|---|---|
| | / mM | / s | (*R*) | (*S*) | / % | |
| (*S*), 1st stage | 9.3 | 2,700 | 5.4 | 74.4 | 12.1 | 86.5 (*S*) |
| (*S*), 2nd stage | 9.3 | 2,500 | \ | 91.0 | 14.3 | > 99 (*S*) |
| (*R*), 1st stage | 10.8 | 8,000 | 121.3 | 4.9 | 9.0 | 92.2 (*R*) |
| (*R*), 2nd stage | 10.8 | 10,000 | 137.7 | 2.0 | 7.8 | 97.1 (*R*) |

[a] data from the integral of peak areas corresponding to the species in interest. [b] Based on charge passed.

A series of independent homogeneous ADH-catalysed reactions (*i.e.* traditional assays in solution) were then carried out to confirm that spontaneous racemisation occurred in the bulk solution when the total [NADP(H)] was 20 $\mu$M. The replacement reactor was an Eppendorf tube of which the cell volume was 1 mL. Each tube contained approximately 10 mM (*R*)- or (*S*)-4P2B, ADH (either TeSADH W110A or W110G at different concentrations), 10 $\mu$M NADPH and 10 $\mu$M $NADP^+$ in pH 9.0 buffer. The tube was attached to a large flask and rotated in a shaking incubator at 250 rpm and 24−28 °C. Results are shown in Table 4.3 from which we can conclude that racemisation does occur in solution, but the rate is relatively slow. For the TeSADH-W110A-catalysed reaction, it was only when the concentration of [ADH] exceeds 1 $\mu$M that a significant effect was observed over 24 hours. When using dilute enzyme, in most cases the chirality of alcohols largely stayed unchanged. As TeSADH W110G has better activity on (*R*)-4P2B, the effect of racemisation is more significant than using TeSADH W110A.

The fact that spontaneous racemisation occurs in the bulk solution gives a good explanation of the results in Figure 3.8 and 4.6 where experiments of both were initiated by injecting ADH into the bulk solution. Here, the result in Figure 4.6 is taken as an example. When using (*R*)-4P2B, the largest current density achieved was almost 100% its chiral counterpart (*S*)-4P2B. This implies that the local concentration of (*S*)-4P2B in the cell might have well exceeded the $K_m^S$ (1 mM, Table 4.1), which could only have been fulfilled through significant racemisation.

However, the solution assays cannot well explain the results in Figure 4.7 where the CA was initiated by injecting FNR into the bulk solution and the electrode was preloaded with TeSADH W110G. In this case, there was no ADH in the bulk solution, meaning that no racemisation occurred in the cell solution. Still, the ratio of (*S*) vs (*R*) in terms of best electrocatalytic activity being achieved was approximately 2:1. This implies that the local concentration of (*S*)-4P2B within the pores could still be high. Considering that at the very beginning, the electrode was preloaded with ADH and should give an ADH-rich environment in the pores, a sensible hypothesis

is that racemisation also occurs in the pores.

**Table 4.3** Chirality outcomes of homogeneous ADH-catalysed reactions.

| No. | TeSADH variant | [ADH] / nM | Time / h | Starting enantiomer | GC peak area ($S$) | GC peak area ($R$) | ee / % |
|---|---|---|---|---|---|---|---|
| 1 | W110A | 1,200 | 24 | ($R$) | 22.3 | 124.4 | 69.6 ($R$) |
| 2 | W110A | 12 | 24 | ($R$) | 1.4 | 141.5 | 98.0 ($R$) |
| 3 | W110A | 1,200 | 24 | ($S$) | 108.1 | 28.9 | 57.8 ($S$) |
| 4 | W110A | 12 | 24 | ($S$) | 126.2 | \ | > 99 ($S$) |
| 5 | W110A | 300 | 6 | ($R$) | 4.4 | 136.7 | 93.8 ($R$) |
| 6 | W110A | 3 | 6 | ($R$) | 0.8 | 147.3 | 98.9 ($R$) |
| 7 | W110A | 300 | 6 | ($S$) | 115.8 | 5.1 | 91.6 ($S$) |
| 8 | W110A | 3 | 6 | ($S$) | 140.9 | \ | > 99 ($S$) |
| 9 | W110G | 260 | 6 | ($R$) | 7.4 | 118.3 | 88.2 ($R$) |
| 10 | W110G | 2.6 | 6 | ($R$) | 1.0 | 142.8 | 98.6 ($R$) |
| 11 | W110G | 260 | 6 | ($S$) | 117 | 12.3 | 81.0 ($S$) |
| 12 | W110G | 2.6 | 6 | ($S$) | 131.4 | \ | > 99 ($S$) |

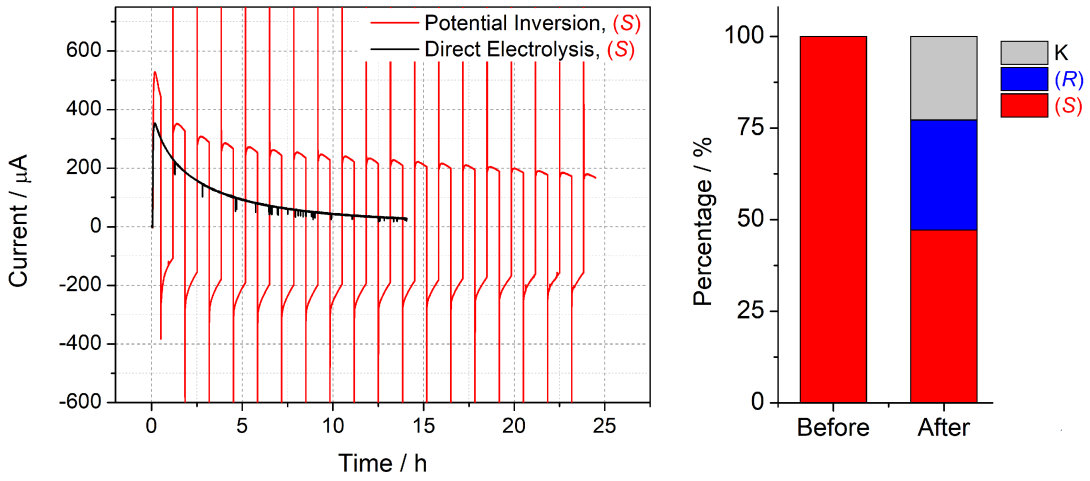
The solution assays were carried out using a 1 mL Eppendorf tube as the reactor which was attached to a flask and rotated at 250 rpm in a shaking incubator. Experimental conditions: 24–28 °C, pH = 9.0, buffer = 1 mM $MgCl_2$ + 50 mM TAPS. [($S$)-4P2B] = 9.4 mM, [($R$)-4P2B] = 10.2 mM, [NADPH] = 10 $\mu$M, [$NADP^+$] = 10 $\mu$M.

## 4.5 Square-wave Potential Inversion Measurements

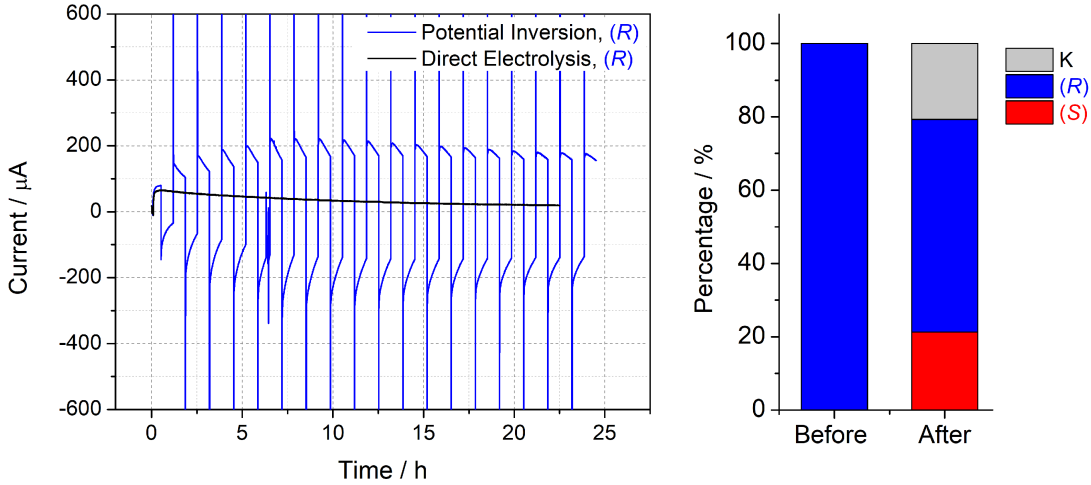
From the previous results, it is known that spontaneous racemisation effect in the bulk solution was strong when [ADH] was well over 1 $\mu$M. It is thought that racemisation also occurs within the ITO nanopores under some conditions. However, more experiments were required to figure out the details and the rate of racemisation. The speculation is, similar to the case in the bulk solution, that an ADH-rich environment in the pores is necessary. This is to assure that the alcohol/ketone couple can be interconverted with one another in a decent rate to favour local chemical

equilibration. The reasoning is that although the electrochemical potential applied is important as it drives reaction in either one of the directions, the interactions among FNR, ADH, alcohols/ketones and $NADP^+$/NADPH also play an important role in determining local equilibration within the pores. From this section, to rule out any contribution from spontaneous racemisation in the bulk solution, electrodes formed for experiments are all preloaded with both FNR and ADH and rinsed thoroughly before use such that no enzyme was present in the cell solution.

The oxidation of secondary alcohols to ketones catalysed by *sec*-ADH is thermodynamically uphill. Also, these reactions are seriously inhibited by the ketone product. This makes the complete enzyme-catalysed oxidation of secondary alcohols hard and an appropriate way to relieve product inhibition is needed. A typical illustration of product inhibition is seen in the black trace of Figure 4.9a, which plots the timecourse of electrochemical oxidation of (*S*)-4P2B monitored as a function of time. The (FNR + TeSADH W110A)@ITO/Ti-foil electrode formed previously by dilute solution (the electrode was rinsed with buffer thoroughly before use to remove any unbound enzyme and details are available in the figure caption) was placed into a stirred electrochemical cell charged with 10.2 mM (*S*)-4P2B at pH 9.0. The potential was held at –0.109 V vs SHE and the measurement was initiated by injecting $NADP^+$ to give a final concentration of 20 $\mu$M in the cell after which the maximum current was reached shortly afterwards at 350 $\mu$A. The overall activity then declined progressively to a low level in 16 hours at which point approximately 66% conversion was achieved based on charge passed. This loss of activity is largely due to product inhibition but can be substantially relieved by the technique referred as 'square-wave potential recycling'. The result of the chronoamperometric measurement using this approach is overlaid in the same panel (red trace). The run was initiated by applying the same oxidative potential (–0.109 V vs SHE). Soon after the CA was started for approximately 30 minutes, the applied potential was switched to a reductive (–0.649 V vs SHE) value, forcing the system to carry out reduction and to start consuming ketone, thus relieving product inhibition. After 40 minutes,




**(a)** Results for (*S*)-4P2B.




**(b)** Results for (*R*)-4P2B.

**Figure 4.9 Left:** chronoamperograms for enantiopure alcohols that were either oxidised throughout or experienced square-wave potential cycling. **Right:** the bar charts demonstrate the composition (in %) of the cell solution in the main compartment. Here K = 4-phenyl-2-butanone. Electrodes were formed by placing the raw ITO/Ti-foil electrode into a vial (vial volume =2.5 mL) containing dilute FNR (3.1 $\mu$M) and TeSADH W110A (2.16 $\mu$M) overnight, during which the solution was gently stirred. The electrodes were rinsed thoroughly by buffer before use. Experimental conditions: [(*R*)-4P2B] = 10.2 mM, [(*S*)-4P2B] = 10.7 mM, active surface area of the (FNR + TeSADH W110A)@ITO/Ti-foil = 7.2 $cm^2$, cell volume = 4.02 mL, buffer = 50 mM TAPS + 1mM $MgCl_2$, pH = 9.0, 26 °C, [$NADP^+$] = 20 $\mu$M. Ar was purged the headspace of the cell throughout. Applied potential = –0.109 and –0.649 V vs SHE for oxidation and reduction half-cycles. Adapted with permission from L. Wan *et al.*, Copyright 2021, American Chemical Society.[257]

the potential was switched back to the original oxidative value (–0.109 V vs SHE) such that the system restarted to perform electrochemical oxidation and produce ketone. This 80-minute reduction-oxidation cycle was repeated over 24 hours. As a reference, every 40-minute half cycle with 200 $\mu$A average is expected to consume *ca.* 2.4 $\mu$moles of alcohol to ketone or *vice versa*, equalling to 6% total substrate. The average oxidation current decreased slowly throughout the measurement and the average reduction current increased in the first 6–7 cycles before experiencing slow decrease. Eventually, the average reduction and oxidation currents converged at approximately the same values.

Likewise, results of the control experiments using (*R*)-4P2B are shown in panel **b**. The unidirectional electrolysis of ((*R*))-4P2B (black trace), as expected, experienced product inhibition and finished 35% conversion eventually based on coulometry. On the other hand, for the square-wave potential cycling run (blue trace), when the first 80-minute reduction-oxidation cycle was finished, the average oxidation and reduction currents in the ensuing 7–8 cycles both experienced continuous increase before decreasing slowly. This implies that during the starting cycles for (*R*)-4P2B, a considerable amount of (*S*)-enantiomer and 4-phenyl-2-butanone were produced, which in turn further increased the current in the next cycle. It is even more interesting to observe that when overlaying the results of panel **a** and **b** (the one-day long reduction-oxidation cycles), the two timecourses converged after 8–9 cycles (Figure 4.10). An intuitive thinking is that the components of the cell solution for both somehow reach an equilibrium, as in dynamic electrochemistry, the catalytic current should be correlated to the relative ratios of reactants and products that are involved. As a control, Figure 4.11 shows the timecourse of an experiment operated under the same square-wave cycling mode but using (*rac*)-4P2B instead. As expected, it is clear that the activity decreased very slow and the average oxidation and reduction currents remained equal throughout.

The chiral GC results of the above experiments are shown in Table 4.4. Rows 1 and 2 show the results of (*S*)- and (*R*)-4P2B under the square-wave potential

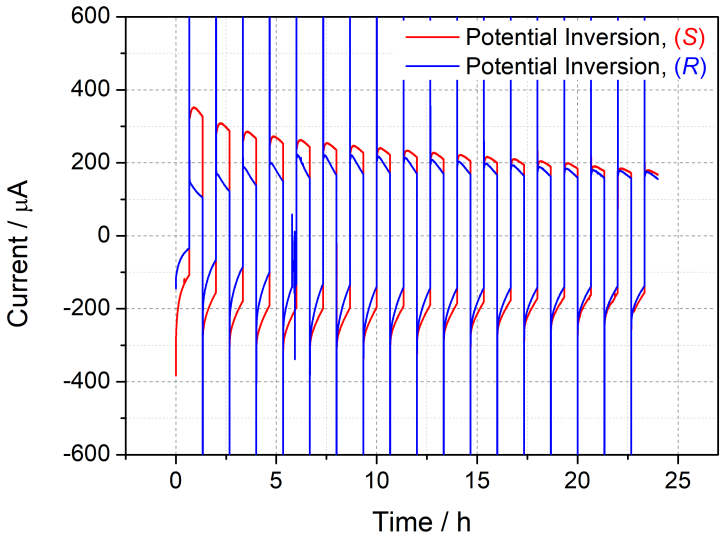



**Figure 4.10** The overlay of CAs that (*S*)-4P2B and (*R*)-4P2B are under square-wave potential cycling mode in Figure 4.9a and 4.9b. Adapted with permission from L. Wan *et al.*, Copyright 2021, American Chemical Society.[257]

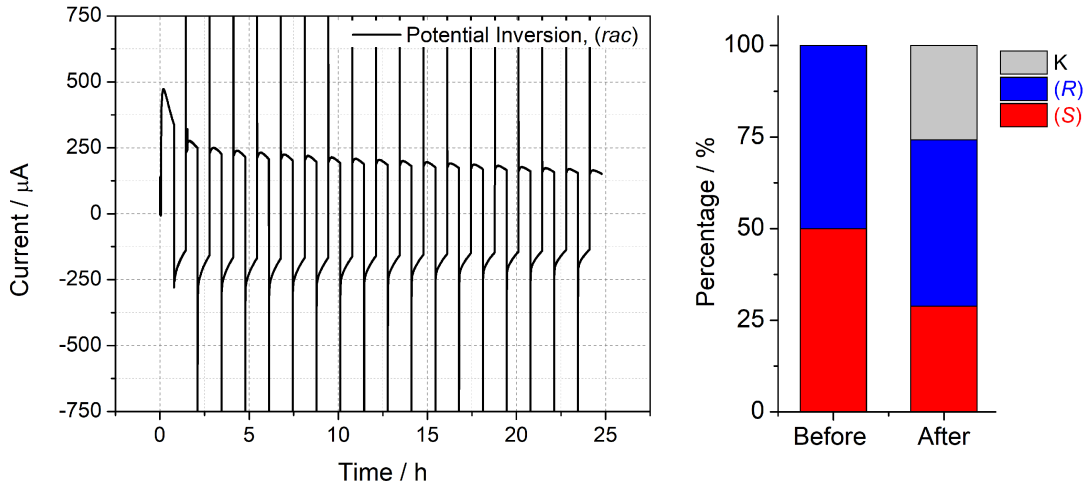



**Figure 4.11 Left:** chronoamperometric results under the square-wave potential cycling mode, initiated with 10.5 mM (*rac*)-4P2B. **Right:** the composition of the cell solution before and after measurement (K = 4-phenyl-butanone). Experimental conditions can refer to those in Figure 4.9. Adapted with permission from L. Wan *et al.*, Copyright 2021, American Chemical Society.[257]

**Table 4.4** Chirality outcomes of electrochemical reactions under square-wave potential cycling or unidirectional modes, catalysed by (FNR + TeSADH W110A)@ITO/Ti-foil electrodes.

| Experiment[a] | FNR coverage | [reactant][b] | Composition[c] / % | | | ee / % |
|---|---|---|---|---|---|---|
| | pmole cm$^{-2}$ | / mM | (*S*) | (*R*) | Ketone | |
| (*S*), square-wave potential cycling | 166 | 10.7 | 47.0 | 30.3 | 22.7 | 21.6 (*S*) |
| (*R*), square-wave potential cycling | 180 | 10.2 | 21.3 | 58.0 | 20.7 | 46.3 (*R*) |
| (*S*), oxidation | 120 | 10.7 | 23.3 | 6.3 | 70.4 | 57.4 (*S*) |
| (*R*), oxidation | 168 | 10.8 | 2.7 | 62 | 35.3 | 91.6 (*R*) |
| (*rac*), square-wave potential cycling | 216 | 10.5 | 28.8 | 45.5 | 25.7 | 22.5 (*R*) |
| Ketone, reduction | 49 | 10.7 | 94.6 | 5.4 | \ | 89.1 (*S*) |

[a] Experiments in row 1–5 were described in Figure 4.9 and 4.11. The data shown in row 6 are results of electrochemical reduction of 4-phenyl-2-butanone at pH 7.5. Details will be shown in Figure 4.12. [b] Concentrations were determined by $^1$H NMR. [c] Results were determined by GC-FID analyses. Data correspond to samples collected from the main compartment of the cell. There were minor losses during measurements, mainly due to crossover and evaporation. Adapted with permission from L. Wan *et al.*, Copyright 2021, American Chemical Society.[257]

cycling mode. It is clear that significant racemisation occurred over the one-day-long measurement, with final ee 21.6% (*S*) and 46.3% (*R*), respectively. Results for the control experiment charged with (*rac*)-4P2B, suggest that the final (*S*):(*R*) ratio was roughly unchanged, in view of some (*S*)-4P2B being converted to the ketone temporarily because the CA was terminated at an oxidation half-cycle. The racemisation of (*R*)-4P2B is not hard to imagine, as TeSADH W110A is highly (*S*)-selective which means that (*S*)-4P2B can be easily produced within cycles. For (*S*)-4P2B, the chiral purity was changed towards a racemate, implying that under this reduction-oxidation cycling mode, the nanoconfinement of enzymes just creates an environment strongly favouring racemisation (the conversion from the faster substrate (*S*)-4P2B to the slower substrate (*R*)-4P2B). Equally interesting, the results corresponding to the unidirectional electrochemical oxidation of (*S*)- (row 3) and (*R*)-4P2B (row 4) also suggest partial racemisation has occurred, with 57.4% ee (*S*) and 91.6% ee (*R*). Table 4.4 also includes the data of a control experiment of electrochemical reduction of 4-phenyl-2-butanone catalysed by an (FNR + TeSADH W110A)@ITO/Ti-foil electrode at pH 7.5. As usual, the electrode was thoroughly rinsed before use to make sure no catalysis occurring due to the possibility of enzymes in the cell solution. The potential was held at –0.649 V vs SHE and the resulting CA is shown in Figure 4.12. Running the experiment in this direction also produced some (*R*)-4P2B, with final ee 89.1% (*S*). Considering the fact that TeSADH W110A has a E value 50.0 favouring (*S*)-4P2B, the results of these unidirectional experiments suggest that the alcohols and ketones were converted to one other back and forth, leading to the acceleration of racemisation.

## 4.6 Coloading of Enzymes in Different Ratios

When discussing the experiments using ADH- or FNR-limited rate-limiting electrodes in Section 4.3, the activation of an (FNR + TeSADH W110G)@ITO/PGE electrode was always initiated by injecting enzyme into the bulk solution. By monitoring the increase of current, the build-up of electrocatalytic rate was continuously monitored

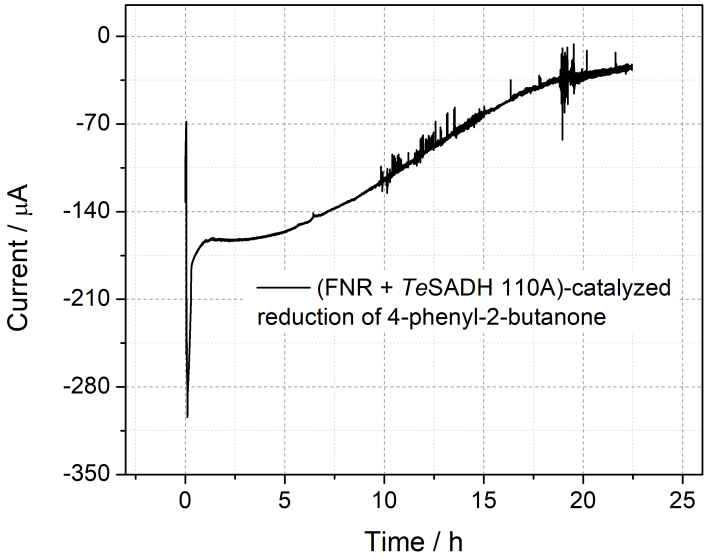
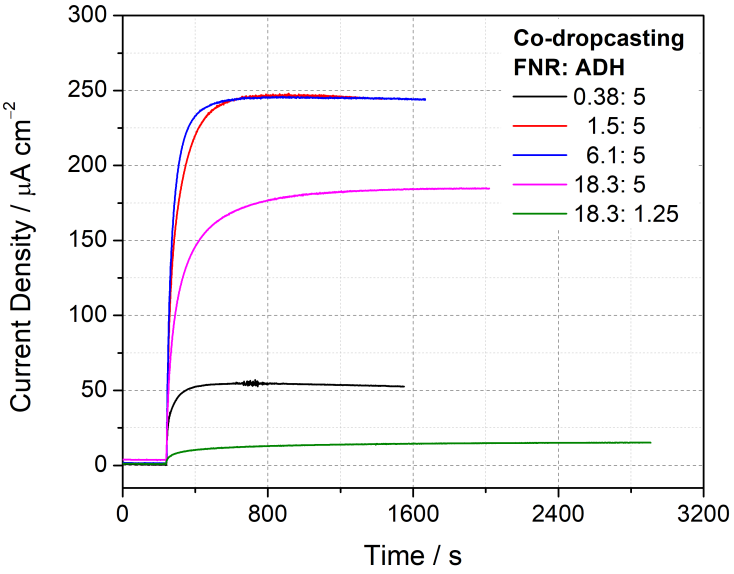


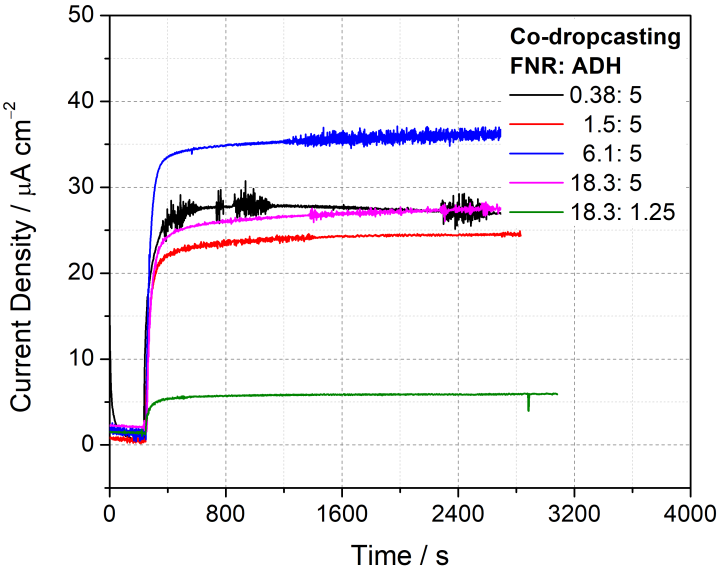

**Figure 4.12** The chronoamperogram of 4-phenyl-2-butanone reduction catalysed by an (FNR + TeSADH W110A)@ITO/Ti-foil electrode (active surface area = 7.2 $cm^2$) which was formed by placing the raw electrode into a vial (vial volume = 2.5 mL) containing stirred dilute FNR (4.96 $\mu$M) and TeSADH W110A (1.68 $\mu$M) in the cold room overnight. The electrode was rinsed repeatedly with buffer before use. Experimental conditions: cell volume = 4.02 mL, [$NADP^+$] = 20 $\mu$M, [4-phenyl-2-butanone] = 10.7 mM, 25 °C, applied reductive potential = –0.649 V vs SHE, pH = 7.5, buffer = 1 mM $MgCl_2$ + 50 mM TAPS + 25 mM NaCl. Ar was purged the headspace of the cell throughout. Adapted with permission from L. Wan *et al.*, Copyright 2021, American Chemical Society.[257]

as the enzymes adsorb in the ITO nanopores. However, as we know now, when enzymes are also present in the bulk solution, the fidelity of the experiment is questionable because homogeneous catalysis occurs in parallel in the aqueous phase. This will definitely convolute the results of electrochemical processes occurring in the pores. This section will display a series of measurements where the electrodes were coloaded by enzymes in a specific set of ratios. As before, to avoid the racemisation effect in the bulk solution, electrodes were under thorough rinsing before use.

The timecourses of electrochemical oxidation of (*S*)-4P2B at different FNR:ADH ratios are shown in Figure 4.13a. The electrode was formed by dropcasting a 10 $\mu$L aliquot of concentrated FNR + TeSADH W110G on the raw ITO/PGE electrode. The as-prepared electrode was then incubated for 30 minutes and rinsed thoroughly by pH 9.0 buffer (25 mM MES + 25 mM TAPS) before use. Here the number '1' in the figure legend equals to 63.5 $\mu$M in one aliquot. For example, 0.38:5 means that in the 10 $\mu$L aliquot, [FNR] = 0.38 $\times$ 63.5 $\mu$M, [TeSADH W110G] = 5 $\times$ 63.5 $\mu$M. The measurements were initiated by injecting $NADP^+$ to give the final concentration of 20 $\mu$M in the cell which was charged with 10 mM (*S*)-4P2B. The results of CA carried out using five ratios of FNR:ADH are shown in Figure 4.13. Unlike the runs that were initiated by injecting enzyme, the current following $NADP^+$ injection usually quickly increased to the maximum achievable value. Results corresponding to two extreme ratios 0.38:5 and 18.3:1.25 did not show good electrocatalysis, with monitored current density at only 50 and 20 $\mu$A $cm^{-2}$, respectively (Figure 4.13a black and green traces). The 0.38:5 case was seriously FNR-limited and the 18.3:1.25 one was seriously ADH-limited suggesting that to have a good coupled reaction, a suitable FNR:ADH ratio must be used. Electroactivities as high as 250 $\mu$A $cm^{-2}$ were observed at ratios 1.5:5 and 6.1:5, implying that moderate increase of FNR loading is helpful to the overall electroactivity. Further increase of FNR:ADH ratio to 18.3:5 led to substantial decrease in activity. This case was ADH-limited. The data for the electrochemical oxidation of (*R*)-4P2B using different FNR:ADH ratios, shown in panel **b**, indicate that the results were less sensitive to the FNR loading




**(a)** Results for (*S*)-4P2B.




**(b)** Results for (*R*)-4P2B.

**Figure 4.13** Chronoamperograms of electrochemical oxidation of (*S*)- or (*R*)-4P2B catalysed by (FNR + TeSADH W110G)@ITO/PGE electrodes at different FNR:ADH ratios. In the figure legend, '1' equals to 63.5 $\mu$M in an aliquot of 10 $\mu$L enzyme. Experimental conditions: active surface area of the electrode = 0.028–0.034 cm$^2$, [alcohol] = 10 mM, pH 9.0, buffer = 25 mM MES + 25 mM TAPS, 26 ± 1 °C, [$NADP^+$] = 20 $\mu$M, rotating speed = 1,000 rpm, applied potential = +0.11 V vs SHE.

when ADH loading was fixed. The values of current density achieved at ratios 0.38:5, 1.5:5, 6.1:5, and 18.3:5 varied from 25−35 $\mu$A cm$^{-2}$. This is understandable since the rate of reaction using the slow substrate (*R*)-4P2B is limited by the amount of ADH in the pores rather than FNR. When the loading of ADH largely stays fixed, the loading of FNR is less expected to have large influence on the rate of reaction. A decrease of ADH loading from ratio 18.3:5 to 18.3:1.25, on the other hand, sharply slashed the current density from 25 $\mu$A cm$^{-2}$ to only 5 $\mu$A cm$^{-2}$ at which point the (FNR + TeSADH W110G)@ITO-catalysed system was seriously limited by ADH. When the ratio FNR:ADH was 1.5:5, the largest activity difference between (*S*)- and (*R*)-4P2B was achieved with 10 times difference (approximately 250 vs 25 $\mu$A cm$^{-2}$) – a value close to the natural E value of TeSADH W110G (17.0, Table 4.1).

## 4.7 Titration of NADPH Using Rotating Electrodes

The concentration of nicotinamide used in most one-pot schemes is usually from 0.5 to several millimolar. Conversely, the Electrochemical Leaf is capable of working with high efficiency at concentrations orders of magnitude lower at 5–50 $\mu$M NADP(H). This is due to nanoconfinement by which the enzymes, cofactors and reactants are concentrated within the pores.

This section introduces titrations of NADPH using rotating electrodes. Under the chronoamperometric mode, the currents monitored at a range of [NADPH] are recorded, aiming at fitting these data to Michaelis-Menten kinetics to obtain a 'working $K_{\mathrm{m}}$' for the Leaf. The titration of NADPH using the UV-Vis spectroscopy is usually hard to perform because at low NAD(P)(H) concentration, obtaining a measurable initial reaction rate is often not accurate. On the hand other, the enzyme-confined electrodes are sensitive to NADP(H) even at very low concentrations.

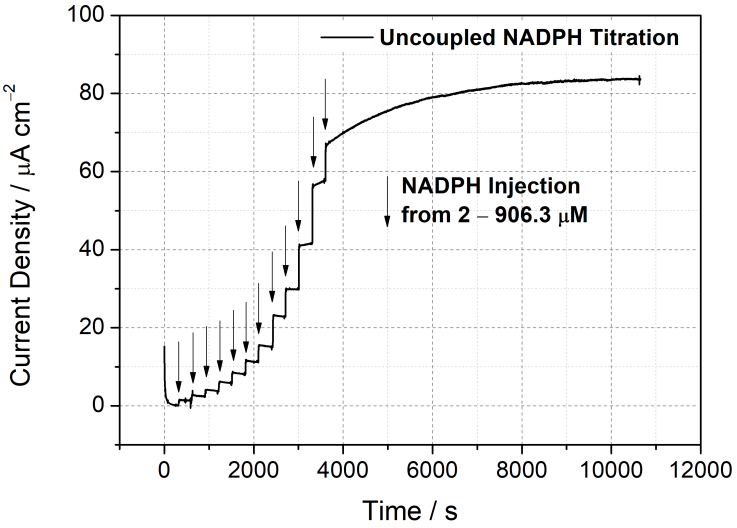
### 4.7.1 Uncoupled NADPH Oxidation Catalysed by FNR

The experiment was carried out using the PGE electrode formed by dropcasting a 5 $\mu$L aliquot of FNR (1,550 $\mu$M) by three minutes. The as-prepared electrode was

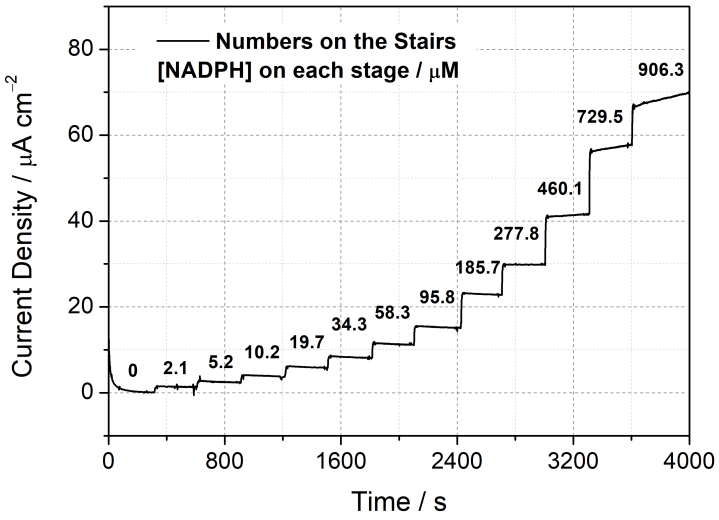
rinsed by buffer before use. Based on the non-turnover peaks for FNR, the coverage of approximately 320 pmole $cm^{-2}$ was determined.

At an applied potential +0.11 V vs SHE and 1,000 rpm rotating speed, the CV measurement was started (Figure 4.14a) and the first injection of NADPH gave the concentration of 2.1 $\mu$M in the cell. Following the initial injection, the new addition of NADPH was conducted every 300 seconds. As expected, each injection gave rise to an immediate increase in current, following which, the current stabilised before the next injection. Panel **b** is the magnified version of the CA over the first 4,000 seconds which includes all the sections where injections were made. The numbers shown in the figures indicate the real-time NADPH concentration at each stage. Some extraordinary phenomena were observed after [NADPH] reached 460.1 $\mu$M, at which point the current started to slightly increase over the next 300-second period. This trend was further enhanced after the following NADPH injections. When [NADPH] stood at 729.5 $\mu$M, the current density increased by almost 3 $\mu$A $cm^{-2}$. Then a new injection of NADPH brought the final cofactor concentration to 906.3 $\mu$M and surprisingly, an enduring increase of activity was observed. As seen in panel **a**, it took two hours before the value of current density finally levelled off, reaching 83 $\mu$A $cm^{-2}$ from 67 $\mu$A $cm^{-2}$.

This unique feature is not observable in most electrochemical experiments. As mentioned in Chapter 1, in most traditional electrochemical experiments, electroactive materials simply stay in the bulk solution or are immobilised on the electrode surface as a thin layer. On the other hand, one can imagine that the Electrochemical Leaf is a 3-dimensional nanoporous matrix like a sponge. The FNR molecules are bound from the surface to the deeply buried pores of the ITO multi-layers. In this case, a proposed hypothetic model is like this: following each NADPH injection, the sudden increase of current should be accredited to NADPH being consumed by FNR bound at the outer surface of ITO layers. As the measurement continues, the more incoming NADPH molecules could start to diffuse into the pores to activate deeply buried FNR. The value of current that the system can output also highly depends on the




**(a)** The overall view of the CA.




**(b)** The zoomed-in view of CA within the starting 4,000 seconds during which successive injections of NADPH were carried out.

**Figure 4.14** Chronoamperograms of electrochemical oxidation of NADPH catalysed by an FNR@ITO/PGE electrode. The concentration of the 5 $\mu$L aliquot of FNR to load was 1,550 $\mu$M. Experimental conditions: active surface area of the electrode = 0.031 cm$^2$, pH = 8.0, buffer = TAPS (25 mM, MES + 25 mM), 26 $\pm$ 1 °C, electrode rotation speed = 1,000 rpm, applied potential = +0.11 V vs SHE.

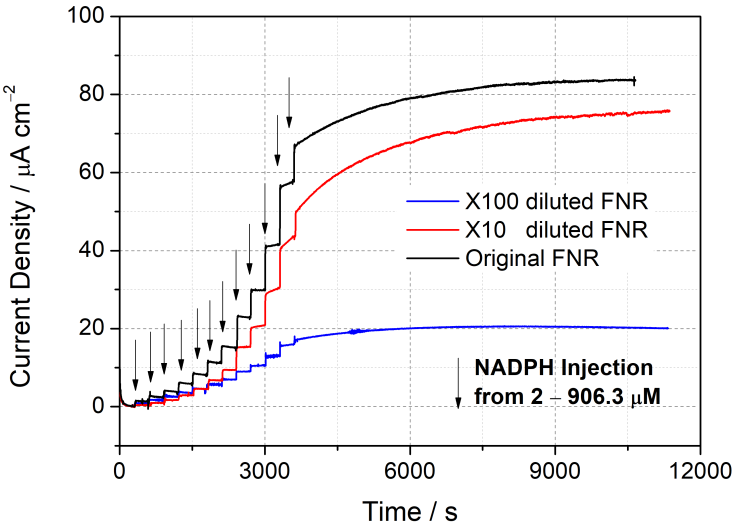
concentration gradient of NADPH. With dilute NADPH, the concentration gradient from the bulk solution to the outer surface of ITO layers was not large enough to cast significant influence and this portion of NADPH molecules tends to be consumed rapidly by FNR near the electrode surface. On the other hand, as [NADPH] reaches as high as 700 $\mu$M, the NADPH molecules were over-saturated on the outer surface of ITO layers. This might result in the process that the excess NADPH molecules penetrated into the inner ITO layers to be accessible for FNR. However, this would take some time to reach a maximum catalytic current later.

In this hypothesised model, the enduring growth of current with concentrated NADPH is attributable to the activation of deeply buried FNR. The adjustment of FNR loading in the Leaf should thus alter the current and the resulting activation process.

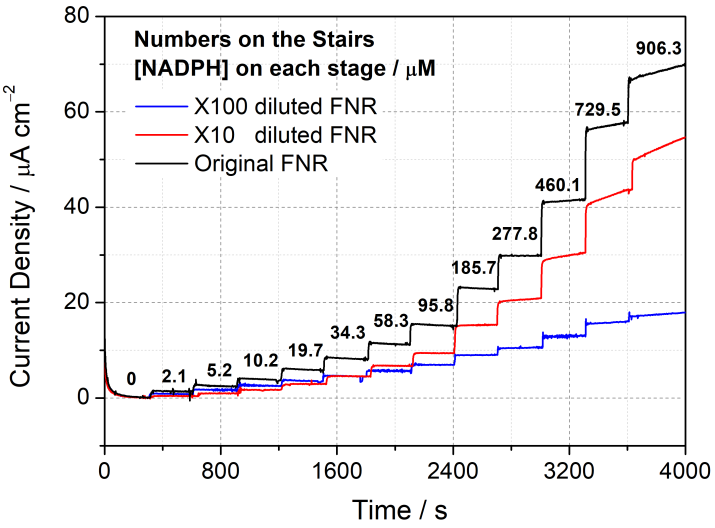
Control experiments were then designed to test this hypothesis, using the FNR@ITO/PGE electrodes preloaded with diluted FNR. In contrast to the concentrated 1,550 $\mu$M FNR being used before, two sets of [FNR] 155 and 15.5 $\mu$M (in a 5 $\mu$L aliquot) were used to form two separate electrodes. Before the chronoamperometric measurements, the corresponding FNR coverages were determined to be 190 and 70 pmole $cm^{-2}$ (compared to 320 pmole $cm^{-2}$ as before), respectively. The resulting CAs together with the one described in the last figure (Figure 4.14) are overlaid in Figure 4.15. It is clear that lower amounts of FNR led to much lower currents. Still, at high NADPH concentration, the enduring increase of current was observable for the cases using dilute FNR.

These results seem to complicate the initial purpose of the NADPH titration experiment: fitting the curves using Michaelis-Menten kinetics model to obtain a working $K_m$. As the current that is monitored is convoluted by nanoconfinement, one can never know at each NADPH concentration, the real proportion of FNR molecules that are really turning over.

Still, an attempt was made to plot the Michaelis-Menten-like figure. The scattered points based on the above chronoamperometric results are plotted in Figure 4.16,




**(a)** The overall view of the CAs.




**(b)** The zoomed-in view of CAs over the starting 4,000 seconds during which successive injections of NADPH are carried out.

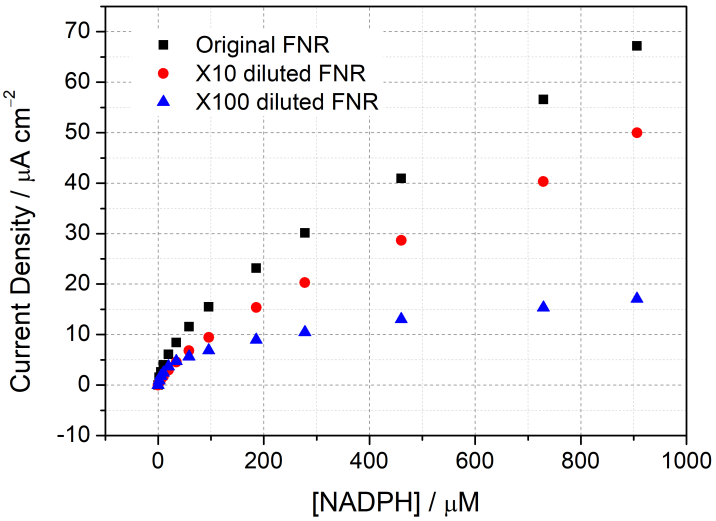
**Figure 4.15** Chronoamperograms of electrochemical oxidation of NADPH catalysed by an FNR@ITO/PGE electrode. The experimental conditions are almost the same to the experiment described in Figure 4.14 except for the [FNR] that was dropcast during for electrode formation. The figure legends for both panels **a** and **b**: 'Original' = 1,550 $\mu$M, 'X10 Diluted' = 155 $\mu$M and 'X100 Diluted' = 15.5 $\mu$M in the 5 $\mu$L aliquot FNR to load. This gave FNR coverage 320, 190, and 70 pmole cm$^{-2}$, respectively.

with each point corresponding to the current density at each stage right after the injection of NADPH. After a first glimpse of these scatter diagrams, it is clear that their shapes (the would-be fitted curves) are far from the ideal version of what a standard Michaelis-Menten plot should be. When [NADPH] approaches relatively high values, the current densities for the 'Original' and 'X10 diluted FNR' runs in panel **a** fail to level off. The 'X100 diluted FNR' run which exploited only 15.5 $\mu$M FNR to form the electrode, is not ideal either but at least looks closer to a standard Michaelis-Menten-like plot. As seen in panel **b**, all data points of the 'X100 diluted FNR' measurement are fitted into the red trace. Based on the fact that the activity tends to be convoluted seriously at high [NADPH], two more fitted curves are also plotted, one omitting the last two data points (one at 729.5 $\mu$M and the other at 906.3 $\mu$M, the blue trace) and the other (the magenta trace) omitting the last three data points (points at 460.1, 729.5 and 906.3 $\mu$M). Looking closely at these three fitted curves, the shapes more and more approach to the version that follows the Michaelis-Menten kinetics when more data points at high [NADPH] are not included. Based on these curves, the working $K_{\mathrm{m}}$ determined are 146, 75 and 49 $\mu$M.

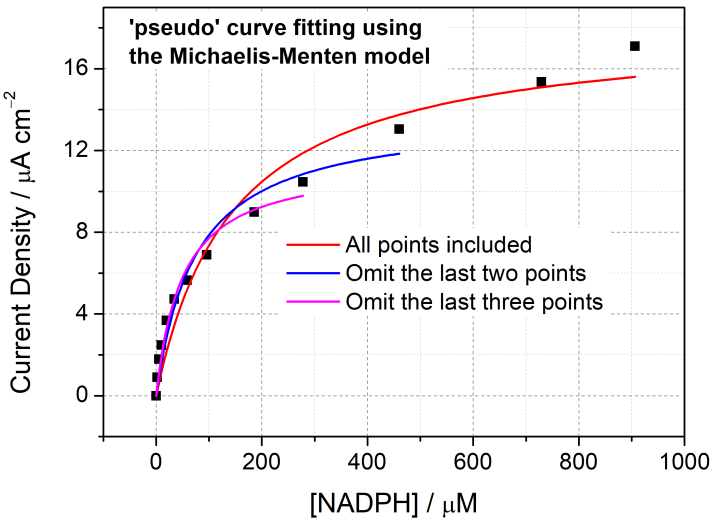
To summarise, this experiment also indirectly demonstrates the difference between the Electrochemical Leaf which entraps enzymes within 3-dimensional nanozones and conventional electrodes which simply immobilise enzymes on a 2-dimensional plain as in our case the enduring growth of current at concentrated [NADPH] was correlated to the coverage of FNR and nanoporous feature of the ITO layer. More experiments are required to study this in depth.

### 4.7.2 NADPH Titration Coupled to the Oxidation of Alcohol

Before moving on to the NADPH titration (this time using the coupled reaction, compared to the previous section referred to FNR catalysis alone) of (FNR + TeSADH W110G)@ITO-catalysed alcohol oxidation, it should be mentioned that a similar titration measurement was actually described in Figure 2.14a of Chapter 2 in which a standard Michaelis-Menten-like plot was obtained with the $H_2$-driven reductive




**(a)** The scatter plot with data points collected in the last figure.



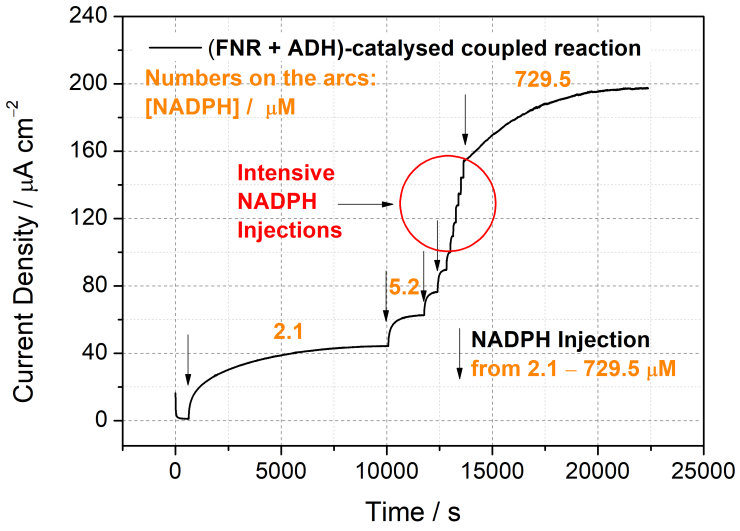

**(b)** The fitted curves using the Michaelis-Menten kinetics model. The set of data points are collected from the blue trace (X100 diluted FNR) in panel **a**.

**Figure 4.16** The current density vs [NADPH] scatter diagram. The data points are collected from the experiments described in the last figure (Figure 4.15) and were recorded immediately after the injection of NADPH at each stage.

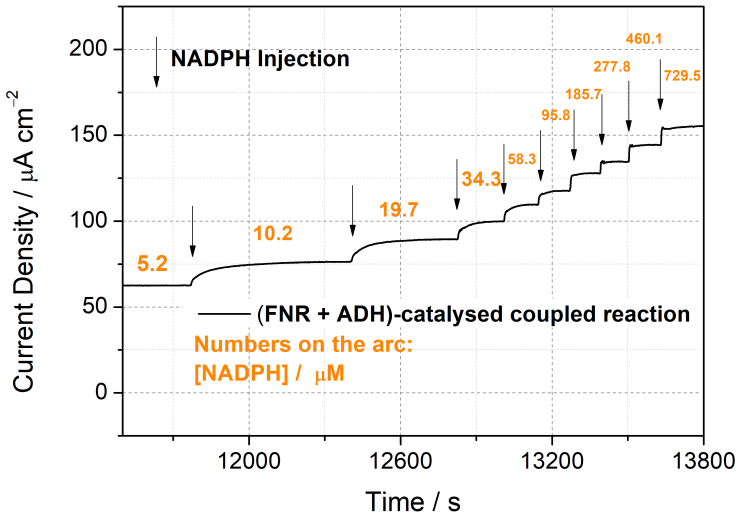
amination scheme. In the $H_2$-driven fuel cell, the reactor was bubbled with $H_2$, which was the only method to mix the reactants in the cell. In this subsection, the titration experiment is carried out using rotating electrodes, meaning that there is adequate hydrodynamic force to promote mass transport of the reactants. In other words, the current will not be limited by mass transport.

Figure 4.17a shows the timecourse of the experiment. The electrode was formed by dropcasting a 5 $\mu$L aliquot of concentrated (FNR + TeSADH W110G) on the surface, incubated for 30 minutes, and was rinsed with buffer before use. The cell was charged with 10 mM (*S*)-4P2B as the substrate and the electrode was rotated at 1,000 rpm. The first injection of NADPH gave a concentration of 2.1 $\mu$M and surprisingly, this brought about a long activation phase which last for almost three hours until the current density levelled off at 45 $\mu$A cm$^{-2}$. Then, consecutive new injections of NADPH were performed when the resulting current due to the previous injection reached new high levels. For every new injection, the time to reach a new plateau and the enhancement of activity both decreased by degrees. Figure 4.17b shows a zoomed-in view of panel **a** where intensive NADPH injections were made (the red circle in panel **a**). At [NADPH] = 5.2 $\mu$M, it took 1,000 seconds or so to reach 60 $\mu$A cm$^{-2}$ from the previous 45 $\mu$A cm$^{-2}$ level. Then, at [NADPH] = 10.2 $\mu$M, the time required for a new plateau further decreased to 500 seconds and the enhancement of activity was 15 $\mu$A cm$^{-2}$. This trend was conserved until the very last injection to give 730 $\mu$M before which the time required for activation was as short as several ten seconds and less than 10 $\mu$A cm$^{-2}$ increment at [NADPH] = 460 $\mu$M. Unexpectedly, a new long activation phase started over the next three hours and the final activity reached 200 $\mu$A cm$^{-2}$ from 160 $\mu$A cm$^{-2}$.

The enduring activation phase at very high [NADPH] in this case quite resembles the experiment of uncoupled NADPH oxidation described in Figure 4.14a. Figure 4.18 shows the overlay of these two CAs. Based on the EC′ mechanism, it is clear that the coupled reaction is much more efficient than the uncoupled NADPH oxidation (as mentioned in Chapter 1, the flux of NADPH back to FNR that gives the current




**(a)** Electrochemical oxidation of (*S*)-4P2B.




**(b)** The zoomed-in view of panel **a** where successive injections of NADPH were made.

**Figure 4.17** Chronoamperograms of electrochemical oxidation of (*S*)-4P2B catalysed by an (FNR + TeSADH W110G)@ITO/PGE electrode. The concentrations of the mixed FNR and TeSADH W110G in a 5 $\mu$L aliquot to load were 155 and 114 $\mu$M. Experimental conditions: active surface area of the electrode = 0.031 cm$^2$, pH = 8.0, buffer = TAPS (25 mM MES + 25 mM), 25.5 ± 0.5 °C, electrode rotation speed = 1,000 rpm, applied potential = +0.11 V vs SHE.

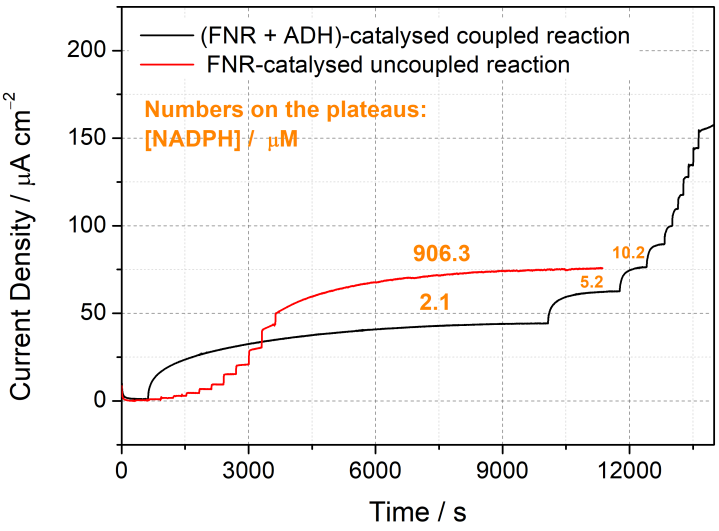



**Figure 4.18** The overlay of CAs in Figure 4.17a and 4.14a. The FNR coverage for the two electrodes exploited for each run were both 190 pmole $cm^{-2}$ with the exception that the one for the coupled reaction was loaded with TeSADH W110G.

enhancement compared to the uncoupled system). In terms of the oxidation current, at [NADPH] as low as 10 $\mu$M, the activity of the coupled reaction is on a level to which the uncoupled reaction exploited more than 900 $\mu$M NADPH to reach. Unlike the uncoupled NADPH oxidation, the activation feature at a given [NADPH] for the coupled reaction starts from the very first injection of NADPH. It is thought that the growth of current before the last NADPH injection was mainly due to fast coupled alcohol oxidation which can rapidly consume $NADP^+$ and produce NADPH back to the NADPH-oxidising electrode. And the NADPH molecules that have attended catalytic cycles then keep retaining in the pores since then. This effect is especially strong at low NADPH concentration. It still remains a question what could account for the enduring growth of current at concentrated NAPDH. A hypothesis is that this is due to direct (uncoupled) oxidation of NADPH catalysed by FNR molecules bound at the inner surface of the pores. Some of these deeply bound FNR do not attend catalytic cycle efficiently due to poor mass transport conditions but start to catalyse NADPH oxidation when [NADPH] is very high.

Again, the values of steady current at each [NADPH] of the coupled reaction are

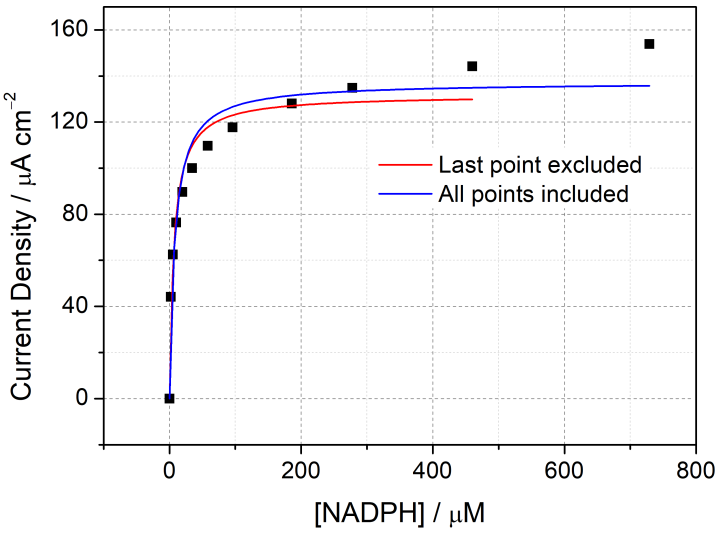



**Figure 4.19** The fitted curves of the data shown in Figure 4.17a using the Michaelis-Menten model.

recorded and an attempt is made to fit these points based on the Michaelis-Menten kinetics (Figure 4.19), as the activity at [NADPH] = 729.5 $\mu$M is an odd value anyhow, two separate curves are fitted, with one excluding the last point. The determined working $K_{\mathrm{m}}$ for this coupled reaction are 6.9 (red trace) and 8.1 $\mu$M (blue).

## 4.8 Conclusion

The enantioselective TeSADH W110A and W110G are the main downstream enzymes that were exploited in this chapter. Based on the results of solution assays, these two *sec*-ADH strongly favour (*S*)-alcohols, with much slower activity on (*R*)-alcohols. However, when the ADH-catalysed reactions were moved to the Electrochemical Leaf using (*R*)-4P2B, larger than expected electroactivity was always observed for two reasons:

**Racemisation Effect** Racemisation is thermodynamically favourable with $\Delta G$ = –1.7 kJ mol$^{-1}$. Racemisation occurs spontaneously in the bulk solution and also in the pores within which TeSADH is concentrated such that an ADH-rich environment

is created.

**ADH- & FNR-limited Situations** FNR and ADH should work concertedly to ensure good catalysis and the ratio between these two enzymes in the pores determines the catalytic current which, depending on the ratio of FNR and ADH, can be either FNR-limited or ADH-limited. In terms of electrode formation, one can pre-load either FNR or ADH to create an FNR- or ADH-rich environment in the nanopores first and initiate the electrochemical measurement by injecting the other enzyme. As the incoming FNR or ADH gradually goes into the nanopores, the electrode in each case progressively shifts from being either limited by FNR or ADH or *vice versa* to the other. As TeSADH has disparate activities on (*S*)- and (*R*)-enantiomers, the time required for this shift varies. Generally speaking, for the faster (*S*)-alcohol, a smaller ADH:FNR ratio is required to reach the maximum activity.

The last several sections introduced a series of NADPH titration experiments. The results show that the monitored electrocatalytic signals deviate from an ideal Michaelis-Menten kinetics model. The hypothesis is that with concentrated NADPH in the cell, more NADPH molecules tend to gradually move into the deeply buried ITO nanopores to be accessible for FNR bound there. This portion of FNR molecules might not efficiently turn over NADPH before due to poor mass transport.

# Chapter 5

# Electrochemical Deracemisation of Secondary Alcohols

## Abstract

The concept of deracemisation is highly appreciated, as potentially it can surpass the 50% yield limits of traditional kinetic resolution method starting with racemic secondary alcohols or asymmetric reduction method starting with pro- or meso-chiral ketones.

In this chapter, based on previous experiments exploiting the enantioselective *sec*-ADH to produce enantiopure alcohols in unidirectional electrolysis, a novel and versatile electrochemical approach is presented to deracemise racemic secondary alcohols. The key to fulfil this scheme is the exploitation of two enzyme-confined electrodes that are enantio-complementary enantioselective to each other, one being (*R*)-selective and the other being (*S*)-selective.

This electrochemical deracemisation scheme can be decomposed into two separate stages. To obtain enantiopure (*R*)-alcohol, (*S*)-selective oxidation is first carried out starting with the a racemic mixture of enantiomerically pure alcohols, *i.e.* the racemate. By applying an oxidative potential, the enantioselective oxidation results in (*S*)-alcohol being catalysed into the prochiral ketone, leaving the slower (*R*)-alcohol mostly unreacted in the bulk solution. Next, the electrode is replaced by an (*R*)-selective one and the applied potential is inverted to be reductive. This forces the system to reduce the prochiral ketone that is produced in the previous stage back into (*R*)-alcohol to finish deracemisation. The deracemisation of (*rac*)-alcohol to obtain enantiopure (*S*)-alcohol follows similar underlying principles. Enantiomeric excess $> 90\%$ in both (*R*)- and (*S*)-alcohol can be achieved accordingly.

## 5.1 Introduction

Deracemisation, as it literally suggests, is the reverse process of racemisation, which converts racemic mixtures to corresponding enantiomerically pure compounds. The deracemisation of secondary alcohols is an important approach to obtain enantiomerically pure alcohols which are essential building blocks in food, agrochemical, and pharmaceutical industries.[263–266] Based on the processes and mechanisms that the racemate is deracemised, common protocols include enantioconvergence[267], dynamic kinetic resolution[268], and cyclic deracemisation,[269] which are often operated in a two-stage approach.[268, 270, 271] This includes the combination of: **(i)** two enantio-complementary enantioselective enzymes;[272–275] **(ii)** a non-selective chemical agent/enzyme and an enantioselective enzyme;[263, 276–278] **(iii)** transition metals/organometallic catalysts and enzymes.[81, 279, 280] Apart from purified enzymes, the whole-cell systems are also available to carry out corresponding enantioselective reactions under similar working principles.[281–285] However, these methods are all inevitably exposed to the problem of compatibility of different components, which often results in a diminishment of catalytic activities in either stage (or both) and thus incurs a reduction of overall rate of deracemisation.[257]

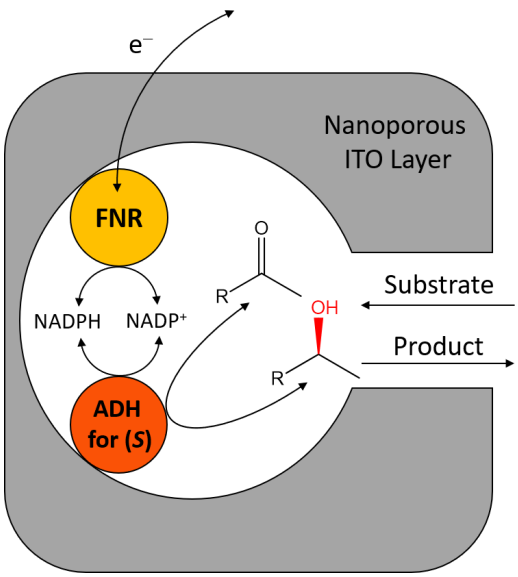
In the previous chapters, the application of Electrochemical Leaf to synthesise chiral compounds unidirectionally has been demonstrated. As FNR is capable of catalysing the interconversion of $NADP^+$/NADPH quasi-reversibly, minimal overpotential is required for efficient catalysis and almost 100% Faraday efficiency is achievable. Under this background, it is sensible to think whether the Leaf system can provide a solution to some of above-mentioned issues and offers a practical electrochemical deracemisation scheme.

The key to synthesise chiral compounds relies on the intrinsic properties of dehydrogenases that are specific on one enantiomer of the racemic mixture of which an exemplary demonstration is the interconversion between secondary alcohols and ketones catalysed by an enantioselective secondary alcohol dehydrogenase (*sec*-ADH,

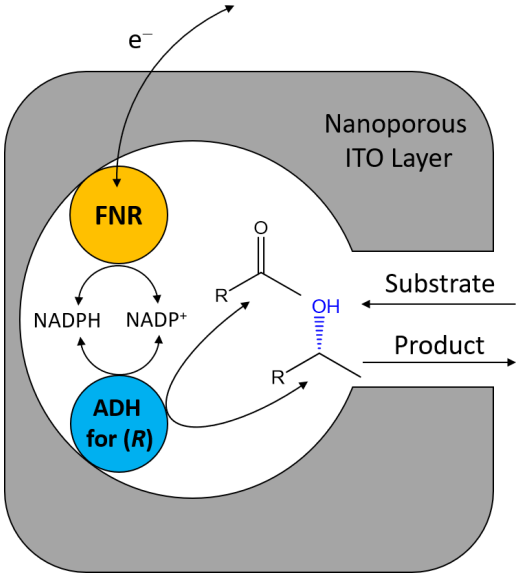
also known as ketoreductase[286]). Figure 5.1a shows the electrode that entraps FNR and an (*S*)-selective *sec*-ADH within the nanopores, by which NADP(H) is continuously recycled, with the resulting coupled reaction in the nanopores being:

$$(S)\text{-Alcohol} \rightleftharpoons \text{Ketone} + 2\,\text{H}^+ + 2\,\text{e}^- \tag{5.1}$$

This reaction is bidirectional and whether it is alcohol oxidation or ketone reduction that occurs depends on the applied potential. In the case of oxidising a racemic mixture of two enantiopure alcohols, *i.e.* a kinetic resolution, the (*S*)-alcohol is biotransformed into ketone, leaving the much slower (*R*)-alcohol accumulating in the bulk solution. When the potential is switched to a reductive value, the asymmetric reduction of the prochiral ketone occurs and (*S*)-alcohol is produced. Analogously, as shown in Figure 5.1b, the exploitation of an (*R*)-selective *sec*-ADH follows the same underlying mechanism but works with (*R*)-alcohol instead.




**(a)** When the coupled *sec*-ADH with FNR is (*S*)-selective, it prefers (*S*)-alcohol as the substrate for alcohol oxidation or the product for ketone reduction.




**(b)** When the coupled *sec*-ADH with FNR is (*R*)-selective, it prefers (*R*)-alcohol as the substrate for alcohol oxidation or the product for ketone reduction.

**Figure 5.1** An illustration showing the electrode in which the flavoenzyme FNR and a *sec*-ADH are entrapped within the ITO nanoporous layer.

The bidirectional nature of the reaction shown in Equation 5.1 is illustrated in

Figure 5.2 which shows the interconversion of the (*S*)-4-phenyl-2-butanol/4-phenyl-2-butanone redox couple under the cyclic voltammetry mode (detailed experimental conditions shown in the figure caption). The reaction was catalysed by a rotating (FNR + TeSADH W110A)@ITO/PGE electrode under equal concentrations of the redox form of the cofactor and substrate ([NADPH] = 2.5 $\mu$M, [$NADP^+$] = 2.5 $\mu$M, [(*S*)-4P2B] = 5 mM, [4-phenyl-2-butanone] = 5 mM). At pH 9.0, the oxidation and reduction currents are virtually equal when the same driving force was applied in each direction. Also, the potential at which the direction is switched corresponds closely to the formal potential of the (*S*)-4-phenyl-2-butanol/4-phenyl-2-butanone couple. This potential is *ca.* 20 mV more negative than that for the $NADP^+$/NADPH couple (–380 mV vs SHE) at pH 9.0.

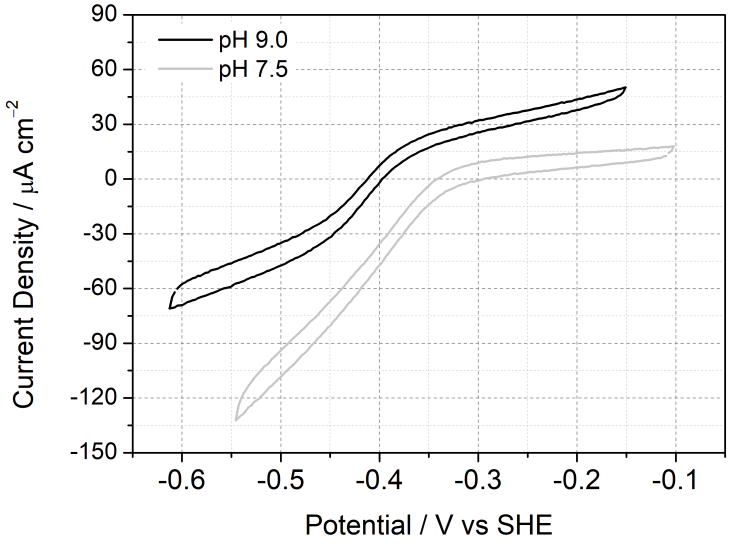



**Figure 5.2** Cyclic voltammograms showing the alcohol/ketone interconversion at pH 9.0 (black trace) and pH 7.5 (light gray trace). The reaction was catalysed by an (FNR + TeSADH W110A)@ITO/PGE electrode formed by dropcasting a 10 $\mu$L aliquot of FNR (294 $\mu$M) and TeSADH (120 $\mu$M). The electrode was rinsed by buffer before use and the Ar was purged the headspace of the cell throughout. Experimental conditions: scan rate = 5 mV $s^{-1}$, buffer = 50 mM TAPS + 1 mM $MgCl_2$ + 12 mM NaCl, [NADPH] = 2.5 $\mu$M, [$NADP^+$] = 2.5 $\mu$M, 25 °C, [(*S*)-4P2B] = 5 mM, [4-phenyl-2-butanone] = 5 mM, cell volume = 3 mL, rotation speed = 1,000 rpm. Adapted with permission from L. Wan *et al.*, Copyright 2021, American Chemical Society.[257]

The same reaction at pH 7.5 was carried out using the same electrode (light gray trace). To do this, the cell was under thorough cleaning and recharged with the same substrates at pH 7.5. The electrode was rinsed by buffer at required pH before being placed in the cell. It is shown that the acidification resulted in the alcohol/ketone formal potential shifting more positive than that for the $NADP^+$/NADPH couple.[1] This change of pH also makes the Leaf strongly favour reduction as kinetically *sec*-ADH enzymes have better activity for ketone reduction at lower pH.

In terms of efficiency and economy to obtain enantiopure secondary alcohols, the unidirectional kinetic resolution starting from the racemate or asymmetric reduction starting from ketones are conceptually inferior to deracemisation. The former approach leaves 50% pro- or meso-chiral ketones unreacted and the latter usually is not the first choice because the racemates are often economically, broadly and readily more accessible as the starting materials.[266]

As for electrochemical methods to achieve deracemisation or stereoinversion, there were a few examples, such as the syntheses of D-lactate, D-alanine, L-leucine, *etc.*,[287–289] which incorporated the direct non-enantioselective electrochemical process and the enantioselective enzymatic reactions. These cases, though are informative and thought-provoking, are not general because the unmodified electrodes, in most cases, are not designed for specialised reactions.

Figure 5.3 shows a scheme to produce enantiopure D-lactate.[288] The anode is piece of carbon felt and catalyses direct oxidation of NADH into $NAD^+$. The regenerated $NAD^+$ is exploited by the free NAD(H)-dependent L-lactate dehydrogenase (L-LDH) in the bulk solution that catalyses L-lactate into pyruvate. The electrode material of cathode is mercury on which non-enantioselective reduction of pyruvate occurs such that the ratio of the resulting D-lactate and L-lactate is 50% vs 50%. As L-LDH is only active on L-lactate, only this isomer can re-enter the next cycle and be catalysed into pyruvate again, leaving the D-lactate gradually becoming the dominant enantiomer. As the catalytic cycle goes on, it is expected that the amount

[1] $NADP^+$/NADPH ($2e^-/1H^+$): –30 mV per pH increase; ketone/alcohol ($2e^-/2H^+$): –60 mV per pH increase.

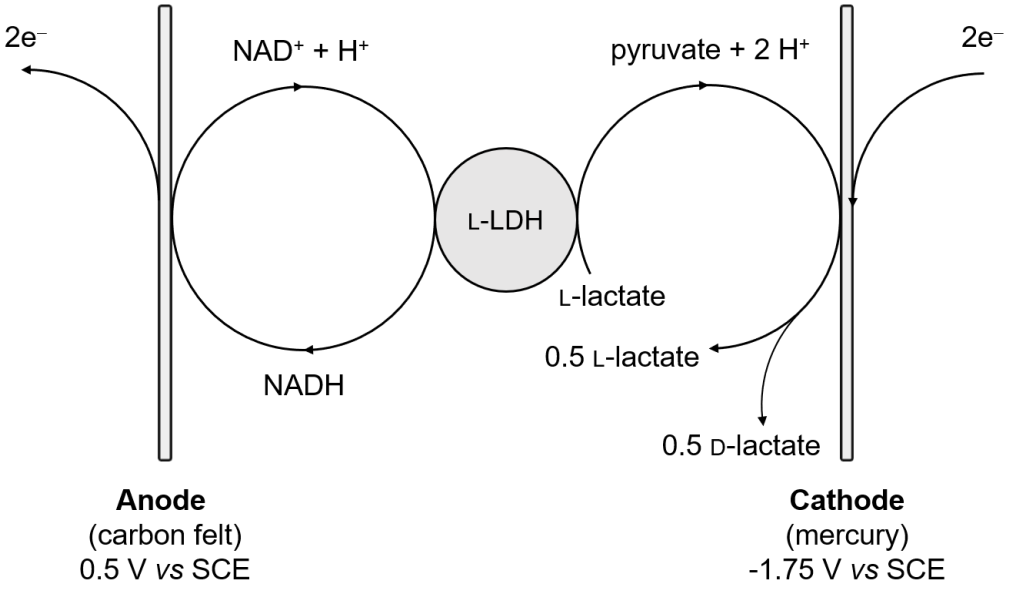



**Figure 5.3** The scheme of an electrochemical method to produce D-lactate. The starting substrate can be D-lactate, racemic D,L-lactate or pyruvate.[288]

of L-lactate decreases exponentially by 1/2 in each cycle and soon disappears to finish the deracemisation process. This method is quite similar to the classical cyclic deracemisation scheme.[280, 290] However, approaches like this has some inevitable drawbacks:

- Although the direct electrochemical regeneration of $NAD^+$ is achievable and well-established with 99.97% efficiency in each cycle,[291] very high oxidative potential 0.5 V vs SCE is required.
- As mentioned before, direct electrochemical regeneration of NADH is not easy if one wants to design a coupled reaction requiring NADH rather than $NAD^+$ as the cofactor. As the dimer $(NAD)_2$ and inactive 1,2-NADH and 1,6-NADH are all possible products of direct electrochemical process, mathematically the biologically active 1,4-NADH tends to vanish over a few cycles.
- The applied potential of non-enantioselective electrochemical reduction of pyruvate is –1.75 V vs SCE. At such an extremely negative potential, undesired side reaction like oxygen reduction occurs.

In short, previous electrochemical studies for deracemisation can only be achieved

under specific conditions using specific substrates and specialised electrode materials and hard to be extended to other systems.

In this thesis, three (*S*)-selective recombinant *sec*-ADH from *Thermoanaerobacter ethanolicus* 39E (TeSADH W110A, W110V and W110G) were purified. These TeSADH variants are the site-directed mutagenesis versions of the wildtype TeSADH to gain activities on phenyl-ring containing compounds. They are all active on (*S*)-alcohol but vary in $K_{\mathrm{m}}$, $k_{\mathrm{cat}}$ and more importantly, activities on (*R*)-alcohol. For a *sec*-ADH that is enantio-complementary to the (*S*)-selective TeSADH, the (*R*)-selective ADH *Lactobacillus kefir* (ADH LK) was purified. The kinetic data of these *sec*-ADH have been shown in Table 4.1 of Chapter 4.

Based on the relevant electrochemical results shown in the previous chapter (Chapter 4), to design a practical two-stage electrochemical reactor for deracemisation, the following conclusions are important:

- The oxidation of secondary alcohols is often seriously inhibited by the product ketones. As a result, 100% full oxidation of alcohol is hard to achieve unless some harsh experimental conditions are applied to push the chemical equilibrium to strongly favour alcohol oxidation.[292] Therefore, there must be some schemes that can overcome this conundrum.

- Racemisation is thermodynamically favourable and spontaneously occurs. In the case of the homogeneous TeSADH-W110A(G)-catalysed interconversion of alcohol/ketone, the racemisation effect was significant when [ADH] was well over 1 $\mu$M, which leads to the production of unwanted enantiomer in either of the two stages. To avoid this effect, one measure is to ensure that no enzyme stays in the bulk solution. Even so, the racemisation effect tends to be strengthened by the highly reversible confined enzymes in the pores, where an ADH-rich environment can be created, and all components involved in cascades were concentrated. This fact has been demonstrated clearly in the TeSADH-W110A(G)-catalysed experiments in the previous chapter (Chapter 4), where more (*R*)-alcohol than expected was always produced.

- *sec*-ADH with higher enantioselectivity is preferred for a possible two-stage deracemisation scheme to counteract the trend of racemisation, especially during the reduction stage to prevent the synthesis of undesired enantiomer. Under this standard, the most enantioselective (*S*)-selective TeSADH W110V should prevail over the less enantioselective TeSADH W110G and W110A.

- As shown in Figure 5.2, the oxidation is better to be carried out at pH 9.0, while for the reduction, pH 7.5 is more favoured.

## 5.2 Electrochemical Deracemisation to Produce (*R*)-4P2B

### 5.2.1 The Two-stage Scheme to Produce (*R*)-4P2B

Figure 5.4 shows a two-stage electrochemical deracemisation scheme to produce (*R*)-alcohol. The approach consists of two stages: the first one being (*S*)-selective oxidation of (*rac*)-alcohol and the second one being the (*R*)-selective reduction of 4-phenyl-2-butanone. The first stage is designed to consume the (*S*)-enantiomer of the racemic mixture to the prochiral ketone and leave the slower (*R*)-enantiomer keep unreacted in the cell. At the point when the first stage is finished, the second stage is then initiated to catalyse the ketone back to (*R*)-alcohol. In this scheme, the selected *sec*-ADH is TeSADH W110A because its activity to oxidise secondary phenyl-ring-containing alcohols is well-established. TeSADH W110G should also be available, but its relative high activity on (*R*)-alcohol is undesired. TeSADH W110V is the best one among the three TeSADH variants in terms of enantioselectivity, but this variant is not selected because of its relatively low activity on (*S*)-4P2B. For the ketone reduction step, the *sec*-ADH chosen is the (*R*)-selective ADH LK.

This deracemisation scheme is appreciated because ideally only 50% of the racemic mixture needs transforming, while the other 50% keeps unreacted throughout. However, as mentioned before, the experimental conditions for oxidation and reduction of a two-stage deracemisation experiment are often incompatible and diverging to one another.[293] In a one-pot homogeneous reactor, the addition of two enantio-

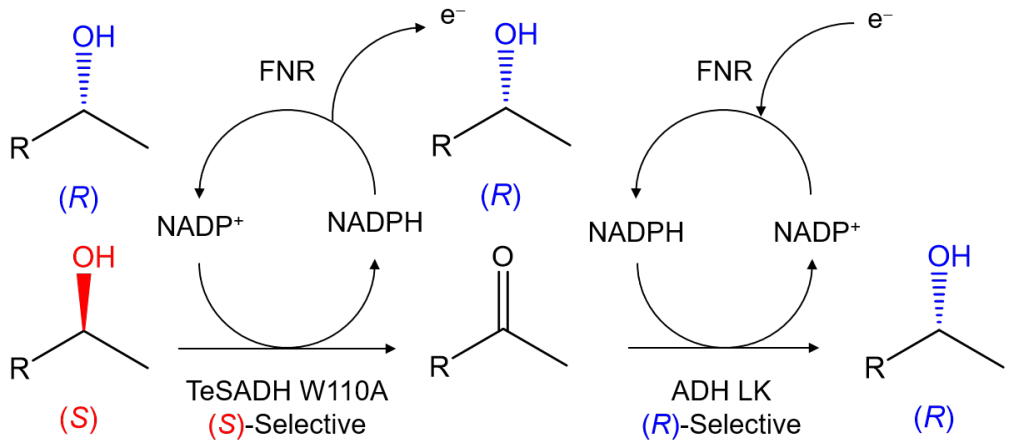



**Figure 5.4** A scheme showing the deracemisation of (*rac*)-alcohol to produce (*R*)-alcohol. This is achieved by (*S*)-selective oxidation catalysed by TeSADH W110A, followed by (*R*)-selective reduction catalysed by ADH LK.

complementary enantioselective *sec*-ADH would automatically make this system non-enantioselective at all. The biocatalytic methods adopted by previous studies often exploited whole-cell systems or used two independent NADP(H) and NAD(H) regenerating systems.[272, 283] On the other hand, with regard to the Electrochemical Leaf, a special feature is likely to overcome this conundrum: all effective working units to generate cofactors and synthesise species of interest being confined within the pores. That is to say, no enzyme is required in the bulk solution because catalysis occurs heterogeneously. Therefore, after the first-stage oxidation, an (*S*)-selective (FNR + TeSADH W110A)@ITO/Ti-foil electrode can be replaced by an (*R*)-selective (FNR + ADH LK)@ITO/Ti-foil electrode, by which enantioselectivity of the whole system is completely flipped over from being (*S*)- to (*R*)-selective. According to solution assay results (Table 4.1), the $k_{cat}$ of the (*R*)-selective ADH LK is 32.8 $s^{-1}$ on 4-phenyl-2-butanone and more importantly, while it has moderately good activity on (*R*)-4P2B, it does not show any observable activity on (*S*)-4P2B. This makes it a promising enzyme to reduce ketones and oxidise alcohols without much concern for the possible racemisation effect.

### 5.2.2 (*S*)-selective Alcohol Oxidation and (*R*)-selective Ketone Reduction

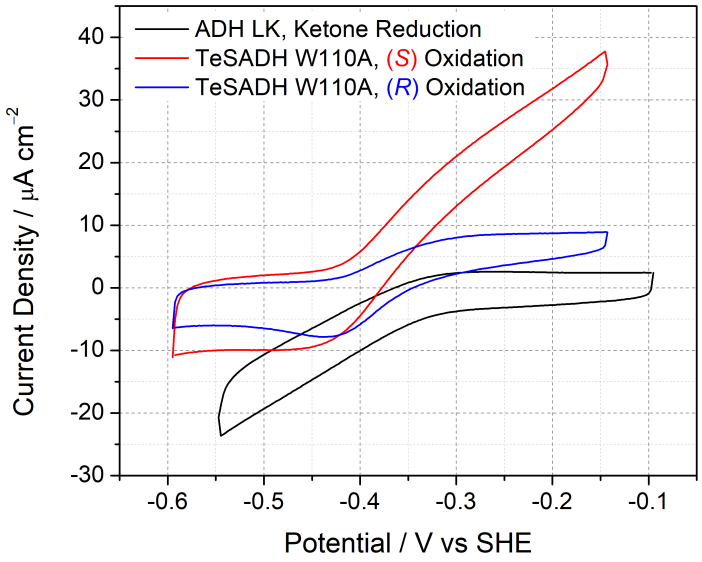



**Figure 5.5** Cyclic voltammograms showing the electrochemical interconversion of $NADP^+$/NADPH coupled to TeSADH W110A in the presence of (*S*)- (red trace) or (*R*)-4P2B (blue trace) at pH 9.0 (buffer = 50 mM TAPS + 1 mM $MgCl_2$) or to ADH LK (black trace) in the presence of 4-phenyl-2-butanone at pH 7.5 (buffer = 50 mM TAPS + 1 mM $MgCl_2$ + 25 mM NaCl). All experiments exploited a stationary (FNR + ADH)@ITO/ITO-glass electrode with active surface area 1.1–1.5 $cm^2$. The electrode was formed by dropcasting a 10 $\mu$L aliquot of concentrated FNR and ADH solution on the electrode. This was incubated at 4 °C for 15 minutes and then rinsed by required buffer before use. In the case for electrochemical oxidation, the concentrations of FNR and TeSADH W110A to be loaded were 155 and 140 $\mu$M, while for the electrochemical reduction, the corresponding concentrations of FNR and ADH LK were 310 and 82 $\mu$M. Experimental conditions: cell volume = 8 mL, 25 °C, [alcohols or ketone] = 5 mM, [NADP(H)] = 50 $\mu$M, scan rate = 2 mV $s^{-1}$. Ar was purged the headspace of the cell throughout. Adapted with permission from L. Wan *et al.*, Copyright 2021, American Chemical Society.[257]

Figure 5.5 shows the CVs of electrochemical oxidation of 5 mM (*S*)-4P2B (red trace) or (*R*)-4P2B (blue trace) at pH 9.0. These measurements were conducted with small stationary (FNR + TeSADH W110A)@ITO/ITO-glass electrodes which were formed by dropcasting an aliquot of concentrated FNR and TeSADH W110A. The

electrode was rinsed by required buffer before being placed into to the electrochemical cell (details shown in the figure caption). By comparing the activities using two enantiomers, the enantioselectivity of TeSADH W110A was reaffirmed.

The plot also includes the CV of electrochemical reduction of 5 mM 4-phenyl-2-butanone (black trace) catalysed by an (FNR + ADH LK)@ITO/ITO-glass electrode at pH 7.5. The activity was moderately good and linearly dependent on the applied potential, suggesting an electron transfer limited step, which is possibly due to relatively low FNR coverage (*ca.* 30 pmole $cm^{-2}$) at this pH.

Before moving on to carry out the continuous two-stage experiment, to investigate the outcomes of the oxidation/reduction half cycles, two separate electrochemical (*S*)-selective oxidation and (*R*)-selective reduction chronoamperometric experiments were carried out. Figure 5.6 shows the result of oxidation reaction starting with (*rac*)-4P2B. Enzymes were loaded by placing the raw ITO/Ti-foil electrode into a vial containing dilute FNR and TeSADH W110A overnight during which the solution was gently stirred. The electrode was rinsed by buffer before use through which one would expect that the catalysis is exclusively contributed by enzymes confined in the pores. FNR coverage for the as-prepared (FNR + TeSADH W110A)@ITO/Ti-foil electrode was approximately 101 pmole $cm^{-2}$. The measurement was initiated by injecting a 20 $\mu$L aliquot of $NADP^+$ to give the final concentration of 20 $\mu$M in the cell that was charged with 10.5 mM (*rac*)-4P2B. As expected, the current promptly increased to 400 $\mu$A shortly and then started to decrease gradually. After *ca.* 17 hours, the run was halted when the current dropped to a very low level. The conversion was 51.5% based on charge passed and the GC-FID analysis showed ee = 90.3% (*R*).

The CA result of a separate (*R*)-selective ketone reduction catalysed by ADH LK is shown in Figure 5.7. The electrode was formed by dropcasting an aliquot of concentrated FNR and ADH LK for 40 minutes at low temperature before use. The FNR coverage was estimated to be 41 pmole $cm^{-2}$. As before, the run was initiated by injecting $NADP^+$ to give 50 $\mu$M in the cell solution, following which the maximum current soon reached the highest level at approximately 140 $\mu$A. The measurement

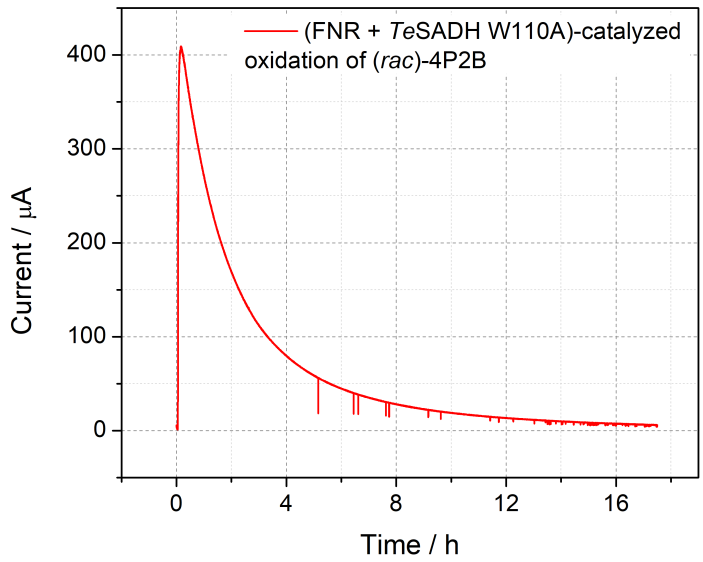



**Figure 5.6** The chronoamperogram showing the electrochemical oxidation of (*rac*)-4P2B. The experiment was catalysed by an (FNR + TeSADH W110A)@ITO/Ti-foil electrode (active surface area = 7.2 $cm^2$) which was formed by placing the raw ITO/Ti-foil electrode into a vial containing dilute FNR and TeSADH W110A (vial volume = 2.5 mL, [FNR] = 3.72 $\mu$M, [TeSADH W110A] = 2.4 $\mu$M) in the cold room overnight, during which the solution was gently stirred. During the measurement, the cell solution was stirred throughout. Experimental conditions: cell volume = 4.02 mL, [$NADP^+$] = 20 $\mu$M, [(*rac*)-4P2B] = 10.7 mM, 25 °C, applied potential = +0.071 V vs SHE, pH = 9.0, buffer 50 mM TAPS + 1mM $MgCl_2$. Adapted with permission from L. Wan *et al.*, Copyright 2021, American Chemical Society.[257]

was halted after 44 hours before the overall activity turned to a very low level at approximately 25 $\mu$A. The chirality of the cell solution afterwards was almost pure ($>$ 99% ($R$)), with *ca.* 7% ketone being unreacted in the main compartment of the cell. This reaffirms that the ADH LK has very high enantioselectivity favouring the ($R$)-alcohol.

The ee 90.3% ($R$) and $>$ 99% ($R$) achieved in separate oxidation and reduction half cycles suggest that a stepwise deracemisation scheme should be viable.

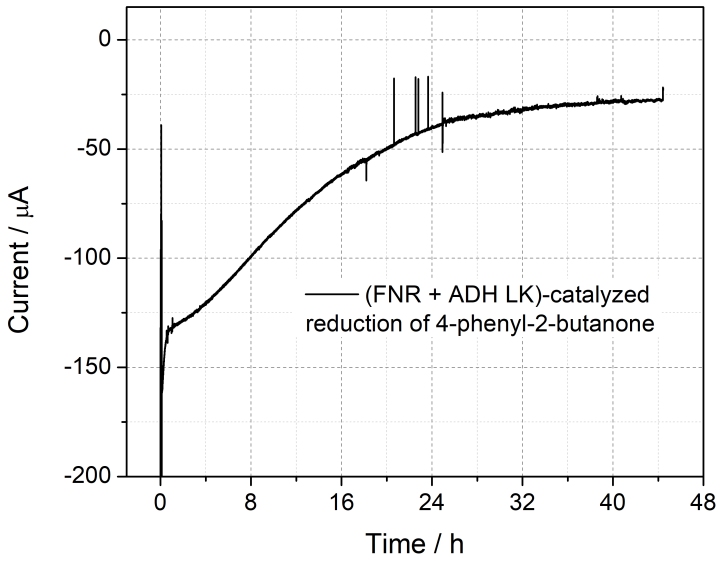



**Figure 5.7** The chronoamperogram showing the electrochemical reduction of 4-phenyl-2-butanone. The experiment was catalysed by an (FNR + ADH LK)@ITO/Ti-foil electrode (active surface area = 7.2 $cm^2$) which was formed by dropcasting a raw electrode with a 10 $\mu$L aliquot of concentrated FNR and ADH LK ( [FNR] = 310 $\mu$M, [ADK LK] = 47 $\mu$M). This electrode was incubated in a vial being placed in ice for 40 minutes and rinsed by pH 7.5 buffer. During the measurement, the cell solution was stirred throughout. Experimental conditions: cell volume = 4.02 mL, [$NADP^+$] = 50 $\mu$M, [4-phenyl-2-butanone] = 10.7 mM, 25 °C, buffer = 1mM $MgCl_2$ + 50 mM TAPS + 25 mM NaCl, applied reductive potential = –0.649 V vs SHE. Adapted with permission from L. Wan *et al.*, Copyright 2021, American Chemical Society.[257]

### 5.2.3 Two-stage Experiments to Produce (*R*)-4P2B

In order to achieve bulk solution transformation that is adequate for chiral GC analysis, larger electrodes (double-sided, 7.2 $cm^2$) were used with 4 mL cell volume for the two-stage deracemisation experiment.

After close inspection of the results of separate oxidation and reduction half cycles, it is estimated that a two-step deracemisation scheme should be feasible, since results from both runs show very high ee favouring the (*R*)-enantiomer. To combine the two separate stages together, after the first-stage electrochemical oxidation, the electrode is swapped from the (*S*)-selective to the (*R*)-selective. Also, the pH needs to be titrated from 9.0 to 7.5 to make the system shift to reduction favouring.

The timecourses for the two-stage electrochemical deracemisation are shown in Figure 5.8, with the red trace demonstrating the first-stage (*S*)-selective oxidation of (*rac*)-4P2B, catalysed by an (FNR + TeSADH W110A)@ITO/Ti-foil electrode (active surface area = 7.2 $cm^2$) formed using dilute enzyme solution in a glass vial (details shown in the figure caption). The experiment was initiated by injecting $NADP^+$ to give the final concentration of 50 $\mu$M in the stirred electrochemical cell.

The current soon rapidly climbed to more than 400 $\mu$A at potential +0.071 V vs SHE. The run was halted after 14 hours as the current declined to a very low level at which point according to coulometry, 45.7% ketone should have been produced. At this stage, an aliquot of concentrated HCl was injected into the cell to titrate the pH from 9.0 to 7.5 and the electrode was replaced by an electrode preloaded with FNR and ADH LK using the same method (details shown in the figure caption). Then the CA was resumed by applying a reductive potential –0.649 V vs SHE, prior to which the solution was gently bubbled with Ar for 10 minutes to remove traces $O_2$. In the rest of the measurement, Ar was purged the headspace of the cell. The initial reduction current was approximately 150 $\mu$A (black trace), and decreased to *ca.* 30 $\mu$A after 12 hours, at which point the measurement was stopped (based on coulometry, *ca.* 39.3% ketone should have been converted back to alcohol) and 91.9% ee (*R*) was recorded based on GC-FID analysis. This result reaffirms that all

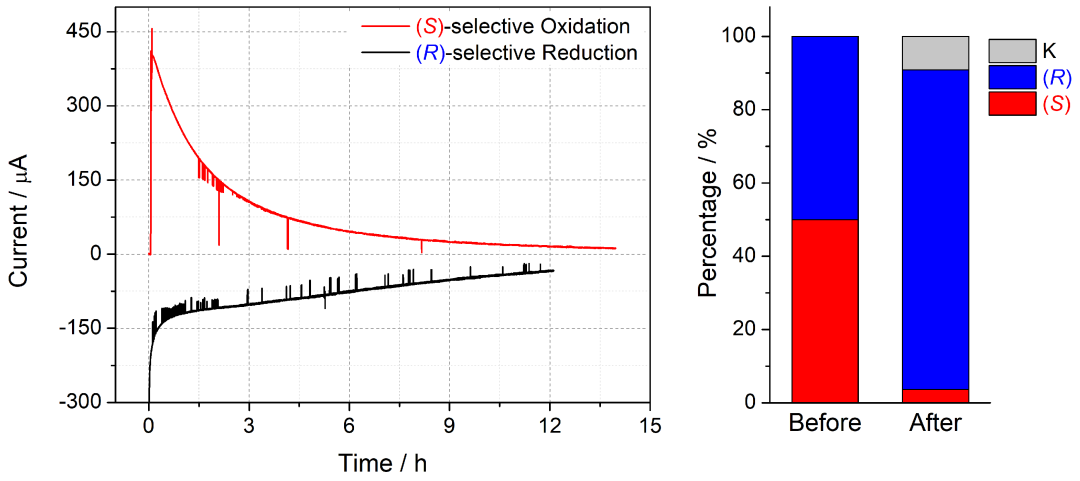



**Figure 5.8 Left:** Chronoamperograms of two-stage experiments to deracemise (*rac*)-4P2B and produce (*R*)-4P2B. The first-stage oxidation (red trace) was catalysed by an (FNR + TeSADH W110A)@ITO/Ti-foil electrode (active surface area = 7.2 $cm^2$) which was formed by placing the raw electrode into a vial containing dilute mixed FNR and TeSADH W110A (vial volume = 2.5 mL, [FNR] = 3.72 $\mu$M, [TeSADH W110A] = 1.44 $\mu$M, pH 9.0, buffer = 50 mM TAPS + 1mM $MgCl_2$) in the cold room overnight, during which the solution was gently stirred. The second-stage reduction (black trace) was catalysed by an (FNR + ADH LK)@ITO/Ti-foil electrode (active surface area = 7.2 $cm^2$). This electrode was prepared in a similar way as the one for oxidation, with [FNR] = 4.96 $\mu$M, [ADH LK] = 1.50 $\mu$M to load in pH 7.5 (50 mM TAPS + 1 mM $MgCl_2$ + 25 mM NaCl) buffer. Experimental conditions: cell volume = 4.02 mL, [$NADP^+$] = 50 $\mu$M, [(*rac*)-4P2B] = 10.5 mM, 25 °C, applied potential = +0.071/–0.649 V vs SHE. Ar was purged the headspace of the cell during reduction half cycle. **Right:** the bar chart showing the composition (in %) of the solution in the main compartment before and after the measurement. Adapted with permission from L. Wan *et al.*, Copyright 2021, American Chemical Society.[257]

(or almost all) active biocatalytic units work in the nanoporous zones rather than in the bulk solution. For the first-stage electrochemical enantioselective oxidation, though the electrode was washed repeatedly before being put into the cell, one can still argue that TeSADH W110A with no electroactivity can later diffuse outwards from the ITO nanopores to the bulk solution and works as homogeneous biocatalysts as most previous studies do. However, if a noticeable amount of (*S*)-selective enzyme keeps turning over during the next stage for (*R*)-selective reduction of ketone, this intervention will colossally attenuate the efficiency of the system and the final enantiomeric excess, which in our case, obviously did not happen at all.

The enantiomeric excess results are based on the alcohols collected from the main compartment of the electrochemical cell in a three-compartment set-up. As the porous glass which separates the Pt-containing sidearm and the main compartment of the cell is not a 100% perfect barrier to prevent materials crossover, there were some losses due to this effect. Figure 5.9 shows the GC-FID spectra of the cell solution collected in the main and Pt-containing compartments. The lower part of the figure shows the result of the main compartment. It is clear that the peak corresponding to (*R*)-alcohol is huge and the areas for those corresponding to (*S*)-alcohol and the ketone are very small. This suggests that the deracemisation process was almost complete. Also, as seen in the upper part of the figure, the main component of the Pt-containing compartment is also (*R*)-alcohol, but with much smaller peak area.

Table 5.1 lists detailed data of the cell solutions collected in both main and Pt-containing compartments. It is estimated that some of the alcohol and ketone molecules went through the porous glass to the Pt-containing sidearm during measurements. Also, there were minor losses due to evaporation.

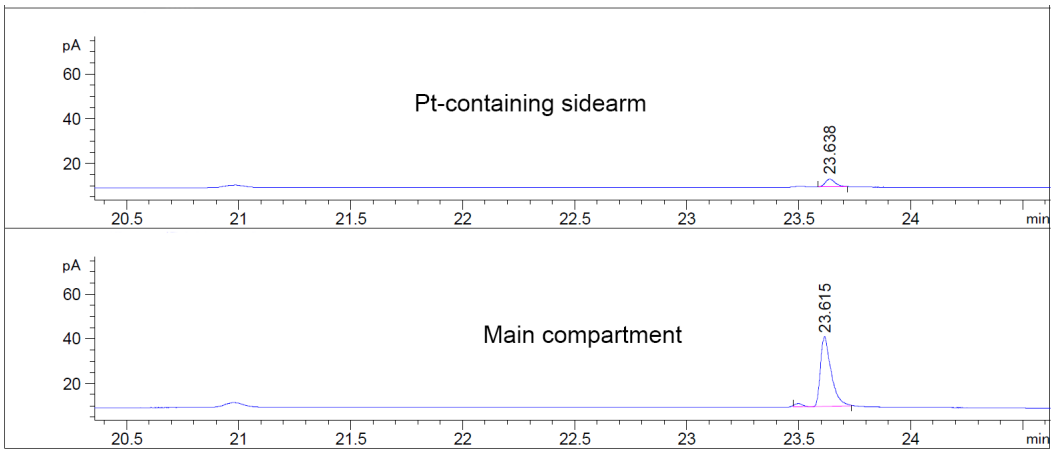



**Figure 5.9** GC-FID spectra of the sample collected in the main (lower part) and Pt-containing (upper part) compartments. In the spectrum band, the peaks at 20.8, 23.6, and 23.4 minutes represent 4-phenyl-2-butanone, (*R*)-4P2B, and (*S*)-4P2B, respectively. Adapted with permission from L. Wan *et al.*, Copyright 2021, American Chemical Society.[257]

**Table 5.1** Detailed results for the two-stage electrochemical deracemisation to produce (*R*)-4P2B.

| compartment | [alcohol][a] / mM | [ketone] / mM | integral area[b] | | | ee[c] / % |
|---|---|---|---|---|---|---|
| | | | (*S*) | (*R*) | ketone | (*R*) |
| main | 7.52 | 0.76 | 4.8 | 114.2 | 12.0 | **91.9** |
| platinum | 0.85 | 0.44 | 0.74 | 6.3 | 6.3 | 79.0 |

[a] The normalised concentration using 4 mL as the standard cell volume. 4 mL was the initial cell volume of the main compartment. For convenience, the calculated concentration of the cell solution in the Pt-containing sidearm also uses 4 mL as the standard cell volume. [b] The GC-FID signals were shown in Figure 5.9. The initial peak area of (*rac*)-4P2B substrate was 159.1. [c] Defined as $\left|\frac{c^{\mathrm{R}}-c^{\mathrm{S}}}{c^{\mathrm{R}}+c^{\mathrm{S}}}\right| \times 100\%$. Adapted with permission from L. Wan *et al.*, Copyright 2021, American Chemical Society.[257]

## 5.3 Electrochemical Deracemisation to Produce (*S*)-4P2B

### 5.3.1 The Two-stage Scheme to Produce (*S*)-4P2B

Analogous to the two-stage deracemisation to produce (*R*)-4P2B, a scheme to deracemise (*rac*)-4P2B and produce enantiopure (*S*)-4P2B is shown in Figure 5.10. This is simply achieved by inverting the sequential exploitation of the (*S*)- and (*R*)-selective electrode. In such a scheme, an ADH-LK-catalysed (*R*)-selective oxidation comes first, followed by an (*S*)-selective reduction catalysed by the TeSADH variant W110V. In terms of activity, this TeSADH variant is slower than W110A and W110G. What really makes this V variant stands out is that it has extremely high enantioselectivity the (*S*)-enantiomer (Table 4.1), thus avoiding the production of undesired (*R*)-4P2B during the reduction cycle.

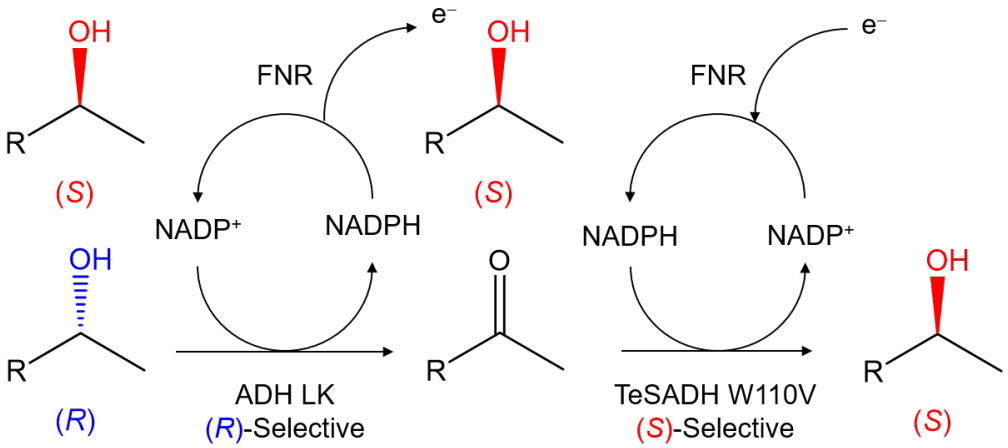



**Figure 5.10** A scheme showing the deracemisation of (*rac*)-alcohol to produce (*S*)-alcohol. This is achieved by (*R*)-selective oxidation catalysed by ADH LK, followed by (*S*)-selective reduction catalysed by TeSADH W110V.

### 5.3.2 (*R*)-selective Alcohol Oxidation and (*S*)-selective Ketone Reduction

The CVs of electrochemical oxidation for (*S*)- and (*R*)-4P2B catalysed by ADK LK are shown in Figure 5.11 (experimental details shown in figure caption). While decent activity on (*R*)-4P2B (blue trace) is observed, almost no signal due to coupled

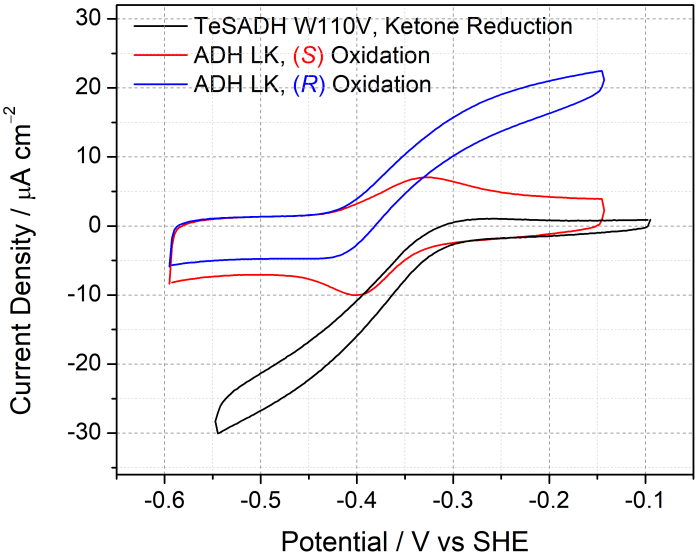



**Figure 5.11** Cyclic voltammograms showing the electrochemical interconversion of $NADP^+$/NADPH coupled to ADH LK in the presence of (*S*)- (red trace) or (*R*)-4P2B (blue trace) at pH 9.0 (buffer = 50 mM TAPS + 1 mM $MgCl_2$) or to TeSADH W110V (black trace) in the presence of 4-phenyl-2-butanone at pH 7.5 (buffer = 50 mM TAPS + 1 mM $MgCl_2$ + 25 mM NaCl). All experiments exploited (FNR + ADH)@ITO/ITO-glass electrodes with active surface area varying from 1.1–1.5 $cm^2$. The electrode was formed by dropcasting a 10 $\mu$L aliquot of concentrated FNR and ADH solution. This was incubated at low temperature for 15 minutes and then rinsed by buffer before use. In the case for electrochemical oxidation carried out at pH 9.0, the concentrations of FNR and ADH LK to be loaded were 155 and 82 $\mu$M, while for the electrochemical reduction at pH 7.5, the corresponding [FNR] and [TeSADH W110V] used were 310 and 124 $\mu$M. Experimental conditions: cell volume = 8 mL, 25 °C, [alcohols or ketone] = 5 mM, [NADP(H)] = 50 $\mu$M, scan rate = 2 mV $s^{-1}$. Ar was purged the headspace of the cell throughout. Adapted with permission from L. Wan *et al.*, Copyright 2021, American Chemical Society.[257]

reaction was observed for the case charged with (*S*)-4P2B, as the shape of the CV (red trace) was similar to the uncoupled NADPH oxidation as if there was no coupled downstream reaction at all. The electrochemical reduction catalysed by the (FNR + TeSADH W110V)@ITO/ITO-glass electrode (black trace), showed good coupling and catalytic current.

Figure 5.12 shows the electrochemical oxidation of (*S*)- (red trace) and (*R*)-4P2B (blue trace) exploiting rotating electrodes that were coloaded with FNR and ADH LK (experimental conditions shown in the figure caption). This was to reaffirm the enantioselectivity of ADH LK. The measurements were initiated by injecting $NADP^+$ to give the final concentration of 20 $\mu$M in the cell solution and the rotation speed for the PGE electrode was set at 1,000 rpm. For the (*R*)-4P2B-charged case, following cofactor injection, the activity soon climbed to the maximum value at 120 $\mu$A $cm^{-2}$. In contrast, for the (*S*)-4P2B, the largest activity after $NADP^+$ injection was almost negligible in the figure. The inset shows its zoomed-in view, confirming that there was still limited activity of oxidation at 1.2–1.5 $\mu$A $cm^{-2}$. Compared to its control experiment using the (*R*)-alcohol, the difference of activity was as large as 80−100 times. Considering the possible racemisation effect and an ADH-rich environment in the nanozones, the intrinsic enantioselective disparity could be even larger for ADH LK.

Two more runs were carried out to reaffirm the fidelity of bulk transformations separately. The CA of electrochemical oxidation of (*rac*)-4P2B catalysed by FNR and ADH LK is shown in Figure 5.13. As usual, the electrode was formed by placing the raw electrode in the dilute stirred enzyme solution overnight and the measurement was initiated by injecting $NADP^+$ in the cell charged with 10.7 mM (*rac*)-4P2B. The FNR coverage was calculated to be 156 pmole $cm^{-2}$. The experiment was run for 21 hours, at which point 45.1% alcohol was converted to ketone based on charged passed and the ee of the cell solution in the main compartment was determined to be 93% (*S*).

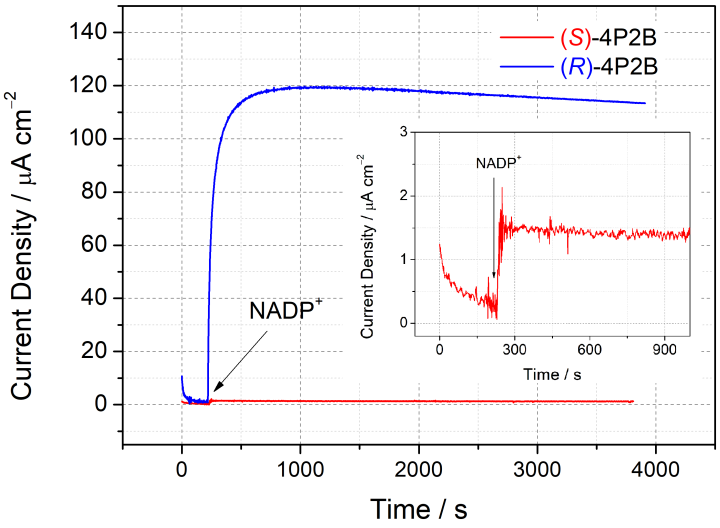



**Figure 5.12** Chronoamperograms of electrochemical oxidation of (*S*)- (red trace) and (*R*)-4P2B (blue trace) at pH 9.0 (buffer = 25 mM TAPS + 25 mM MES + 1 mM $MgCl_2$). The experiments were carried out using rotating (FNR + ADH LK)@ITO/PGE electrodes with active surface area varying from 0.031 – 0.034 $cm^2$. The electrode was formed by dropcasting a 10 $\mu$L aliquot of concentrated FNR and ADH LK solution. This was incubated at room temperature for 30 minutes and then rinsed by buffer before use. The concentrations of FNR and ADH LK to be loaded are 46.5 and 42.4 $\mu$M. During the measurement, the cell solution was stirred throughout. Experimental conditions: cell volume = 3 mL, 25 °C, [alcohols] = 10 mM, [$NADP^+$] = 20 $\mu$M, scan rate = 2 mV $s^{-1}$, electrode rotation speed = 1,000 rpm. Ar was purged the headspace of the cell throughout. The inset shows the magnified version of the CA using (*S*)-4P2B over the first 1,000 seconds.

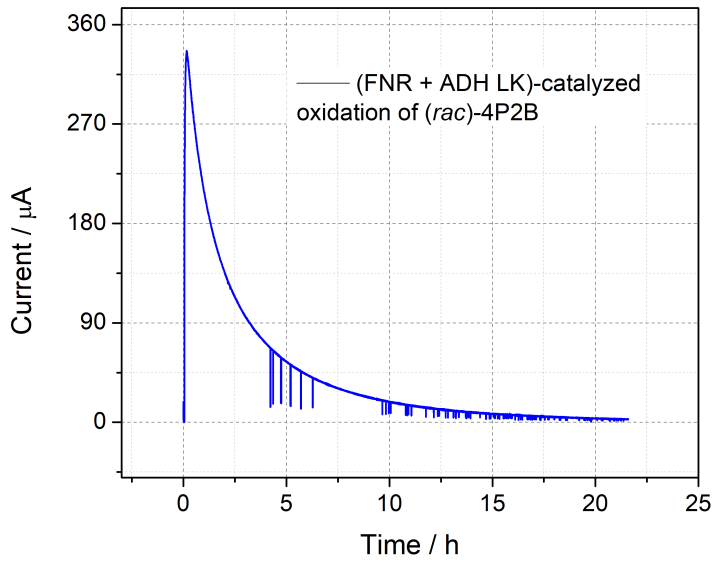



**Figure 5.13** The chronoamperogram of electrochemical oxidation of (*rac*)-4P2B (blue trace) at pH 9.0 (buffer = 50 mM TAPS + 1 mM $MgCl_2$). The reaction was catalysed by an (FNR + ADH LK)@ITO/Ti-foil electrode (active surface area = 7.2 $cm^2$) which was formed by placing the raw electrode into a vial containing dilute FNR and ADH LK (vial volume = 2.5 mL, [FNR] = 4.96 $\mu$M, [ADH LK] = 1.50 $\mu$M) in the cold room overnight, during which the solution was gently stirred. During the measurement, the cell solution was stirred throughout. Experimental conditions: cell volume = 4.02 mL, [$NADP^+$] = 50 $\mu$M, [(*rac*)-4P2B] = 10.7 mM, 25 °C, applied oxidative potential = +0.071 V vs SHE. Adapted with permission from L. Wan *et al.*, Copyright 2021, American Chemical Society.[257]

The CA of electrochemical reduction of 4-phenyl-2-butanone catalysed by FNR and TeSADH W110V is shown in Figure 5.14. Detailed experimental conditions are available in the figure caption. After overnight loading, the FNR coverage of the as-prepared electrode was approximately 49 pmole $cm^{-2}$. After the initiation of the CA, the maximum current once reached more than 240 $\mu$A and then started to decrease gradually over the next 16 hours. Based on GC-FID analysis, the chirality of the cell solution was essentially > 99% ($S$) and the unreacted ketone accounted for approximately 5.1% of the sample collected in the main compartment.

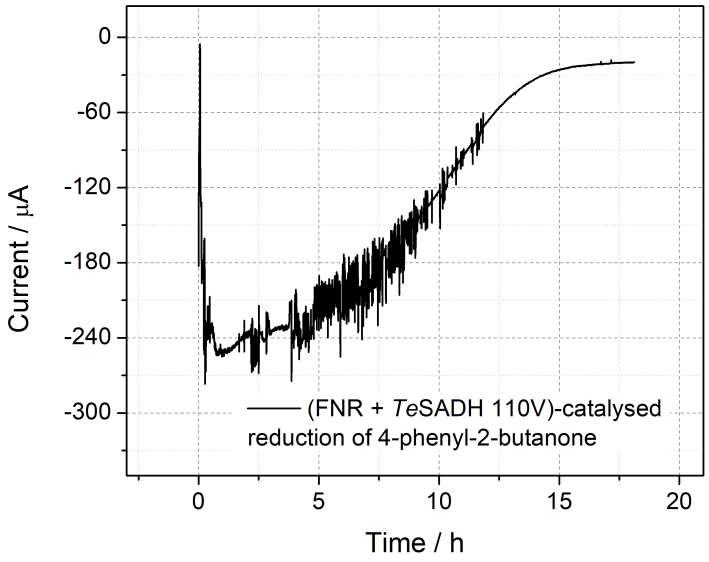



**Figure 5.14** The chronoamperogram of 4-phenyl-2-butanone reduction using TeSADH W110V as the coupled enzyme. The experiment was catalysed by an (FNR + ADH)@ITO/Ti-foil electrode (active surface area = 7.2 $cm^2$) prepared by placing the raw ITO/Ti-foil electrode into a vial containing stirred dilute FNR and TeSADH W110V (vial volume = 2.5 mL, [FNR] = 3.72 $\mu$M, [TeSADH W110V] = 1.3 $\mu$M) in the cold room overnight. During the measurement, the cell solution was stirred throughout. Experimental conditions: cell volume = 4.02 mL, [$NADP^+$] = 50 $\mu$M, [4-phenyl-2-butanone] = 10.7 mM, 25 °C, applied potential = –0.649 V vs SHE, pH = 7.5, buffer = 1 mM $MgCl_2$ + 50 mM TAPS + 25 mM NaCl. Ar was purged the headspace of the cell throughout. Adapted with permission from L. Wan *et al.*, Copyright 2021, American Chemical Society.[257]

The ee ~93% (*S*) and > 99% (*S*) achieved at the separate oxidation and reduction cycles suggest that the two-stage scheme to produce (*S*)-4P2B is feasible.

### 5.3.3 Two-stage Experiment to Produce (*S*)-4P2B

The result of the two-stage CA in order to electrochemically deracemise (*rac*)-4P2B and produce (*S*)-4P2B is shown in Figure 5.15 (experimental conditions shown in the figure caption).

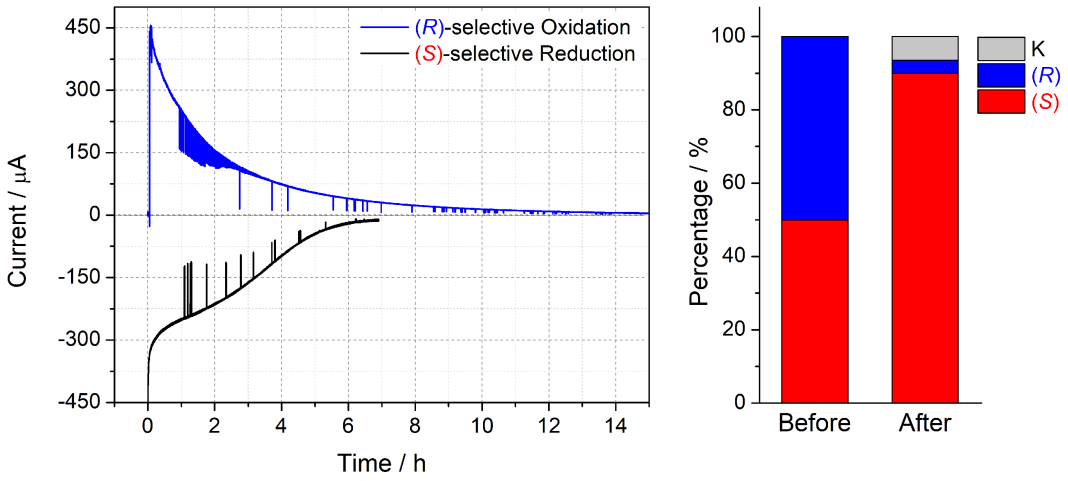



**Figure 5.15 Left:** Results of two-stage CAs to deracemise (*rac*)-4P2B and produce (*S*)-4P2B. The first-stage oxidation (blue trace) was catalysed by an (FNR + ADH LK)@ITO/Ti-foil electrode (active surface area = 7.2 $cm^2$) which was formed by placing the raw electrode into a vial containing dilute FNR and ADH LK (vial volume = 2.5 mL, [FNR] = 4.96 $\mu$M, [ADH LK] = 1.50 $\mu$M, pH 9.0, buffer = 50 mM TAPS + 1mM $MgCl_2$) in the cold room overnight, during which the solution was gently stirred. The reduction (black trace) was catalysed by an (FNR + TeSADH W110V)@ITO/Ti-foil electrode (active surface area = 7.2 $cm^2$). This electrode was prepared in a similar way as the one for oxidation, with [FNR] = 3.72 $\mu$M, [TeSADH W110V] = 1.30 $\mu$M to be loaded in pH 7.5 (50 mM TAPS + 1 mM $MgCl_2$ + 25 mM NaCl) buffer. Experimental conditions: cell volume = 4.02 mL, [$NADP^+$] = 50 $\mu$M, [(*rac*)-4P2B] = 10.5 mM, 25 °C, applied potential = +0.071/–0.649 V vs SHE. Ar was purged the headspace of the cell during the reduction cycle. **Right:** the bar chart showing the composition of the cell solution in the main compartment ( in %). Adapted with permission from L. Wan *et al.*, Copyright 2021, American Chemical Society.[257]

The blue trace shows the first-stage (*R*)-selective electrochemical oxidation catalysed by an (FNR + ADK LK)@ITO/Ti-foil electrode. This reaction was initiated by injecting a 20 $\mu$L aliquot of $NADP^+$ to give the final concentration 50 $\mu$M in the cell with applied potential +0.071 V vs SHE. The first-stage oxidation last for 15 hours, with the largest current once peaking at 400 $\mu$A initially, followed by progressive decrease in the rest of the run, at which point 43.2 % alcohol was converted to ketone, based on charge passed. Then the pH was titrated by an aliquot of concentrated HCl from 9.0 to 7.5, the electrode was replaced by an (*S*)-selective (FNR + TeSADH W110V)@ITO/Ti-foil electrode, and Ar was purged the headspace of the cell for 10 minutes to remove traces $O_2$. The ensuing second stage reduction was initiated by applying a reductive potential –0.649 V vs SHE, with the starting current at approximately 300 $\mu$A. The sample was collected after 7 hours when the current declined to a very low level at which point 40.2% ketone was converted back to alcohol based on coulometry and GC-FID analysis gave ee 92.4% (*S*) for the cell solution in the main compartment.

Detailed results for the two-stage experiment are shown in Table 5.2. The GC-FID spectra are shown in Figure 5.16. Crossover led to some alcohols and ketones staying in the Pt-containing compartment in the end, with lower degree of deracemisation 72.1% (*S*), as expected. There was also approximately 5% 4-phenyl-2-butanone unreacted. These facts were reflected by both $^1$H NMR and GC-FID.

**Table 5.2** Detailed results for the two-stage electrochemical deracemisation to produce (*S*)-4P2B.

| compartment | [alcohol][a] / mM | [ketone] / mM | integral area[b] | | | ee[c] / % |
|---|---|---|---|---|---|---|
| | | | (*S*) | (*R*) | ketone | (*S*) |
| main | 7.90 | 0.9 | 114.2 | 4.5 | 8.2 | **92.4** |
| platinum | 1.15 | 0.11 | 11.7 | 1.9 | 6.9 | 72.1 |

[a] The normalised concentration using 4 mL as the standard cell volume. 4 mL was the initial cell volume of the main compartment. For convenience, the calculated concentration of the cell solution in the Pt-containing sidearm also uses 4 mL as the standard cell volume. [b] Peaks of the species of interest shown in Figure 5.16. [c] Defined as $\left|\frac{c^{R}-c^{S}}{c^{R}+c^{S}}\right| \times 100\%$. Adapted with permission from L. Wan *et al.*, Copyright 2021, American Chemical Society.[257]

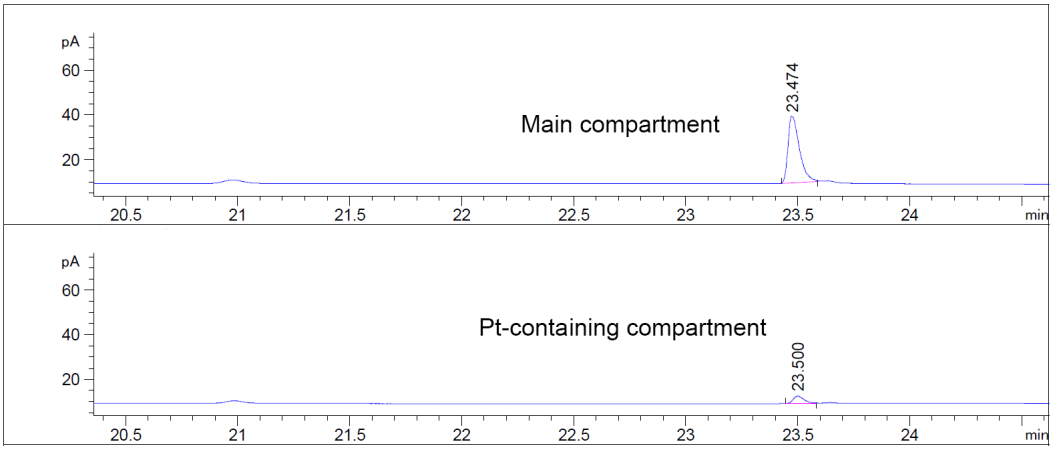



**Figure 5.16** GC-FID spectra for the samples collected in the main (upper part) and Pt-containing (lower part) compartments. Within the spectrum band, the peaks at 20.8, 23.6, and 23.4 minutes represent 4-phenyl-2-butanone, (*R*)-4P2B, and (*S*)-4P2B. Adapted with permission from L. Wan *et al.*, Copyright 2021, American Chemical Society.[257]

## 5.4 Conclusion and Perspectives

This chapter introduces a novel electrochemical approach to deracemise secondary alcohols. *sec*-ADH with enantio-complementary enantioselectivity, *i.e.* one (*S*)-selective and the other (*R*)-selective were chosen as the enzyme coupled to FNR within the ITO nanopores. A model example of electrochemical deracemisation

experiment was performed stepwise in an one-pot reactor, with the first step being enantioselective oxidation of the racemic secondary alcohol (*rac*)-4P2B catalysed by an enantioselective *sec*-ADH, followed by a reduction stage achieved by inverting the applied potential and enantioselectivity using a *sec*-ADH enantio-complementary to the previous one. The rate and progress of the model reaction – the deracemisation of (*rac*)-4-phenyl-2-butanol to produce either (*S*)- or (*R*)-enantiomer with more than 90% ee – were continuously monitored in real time.

The key to fulfil a successful electrochemical deracemisation lies in two points:

1. The exploitation of *sec*-ADH with very high enantioselectivity, especially in the reduction half cycle. Otherwise the thermodynamically favoured racemisation effect tends to occur.

2. It is important to make sure that no enzyme, especially the *sec*-ADH remains in the cell solution throughout the measurement, because this tends to support racemisation and attenuate the catalytic activities of the system over the two separate stages.

The scheme put forward in this chapter has the potential to be extended to broader enzyme-catalysed systems. Based on our previous study,[192] the exploitation of an (FNR + E2)@ITO/support electrode in a scaling-up scheme incorporating several tens to hundreds millilitres of cell solution was achievable, so it is therefore sensible to envisage that this clean, two-stage process should be widely applicable to deracemisation using much larger reactors and diversified enantio-complementary enantioselective dehydrogenases.

# Chapter 6

# Theories and Experimental Methods

## Abstract

This chapter is comprised of three sections. The first section introduces essential concepts and techniques of electrochemistry which are all relevant to this thesis, such as the electrode potential, the set-up of electrochemical cells, and Faradaic current. Cyclic voltammetry is the key technique to study thermodynamics and dynamics of electrode processes. While for chronoamperometry, one essential advantage is that the output signal is intuitive, as the rate of reactions can be quantified and monitored *in situ* through the current that flows. One can thus optimise experimental conditions to realise better catalysis accordingly.

The second section deals with experimental procedures involving enzymes. Detailed purification protocols of enzymes used in this thesis are first introduced. The methods to determine enzyme concentration and a brief outline of Michaelis-Menten kinetics are given later. Key parameters of enzyme kinetics such as $K_{\mathrm{m}}$, $k_{\mathrm{cat}}$ and $v_{\mathrm{max}}$ can be determined by an equation that is derived from Michaelis-Menten kinetics.

The last section first outlines experimental methods. The methods of electrochemical measurements and electrode formation are introduced first. Then other analytical techniques, including UV-Vis spectroscopy, GC-FID and NMR are also introduced. The last part gives a brief introduction of buffer solution.

## 6.1 Electrochemical Fundamentals and Techniques

To study electrochemistry, it is important to understand a set of terms, like the electrode, solvent, set-up, electrolyte, and catalyst, to name a few. This section will move on to introduce basic concepts and terms in electrochemistry, especially those involved in enzyme-linked electrochemical processes.

### 6.1.1 Basic Concepts

#### *6.1.1.1 Electrode*

The electrode is the central component of an electrochemical device. An electrode is the place where an electrochemical process occurs. It can be an **anode** when species of interest are oxidised and a **cathode** when species of interest are reduced. Keeping such an interpretation in mind is very important as sometimes to distinguish an anode and cathode might be confusing and also, the state of an electrode can be altered simply by switching the potential being applied to the electrode. For instance, in this thesis, the (FNR + E2)@ITO/support electrode was an anode during the first stage of the deracemisation scheme in the previous chapter as the Leaf catalysed the oxidation of NADPH. It was then turned into a cathode when the potential was switched to a reductive value such that the system was forced to regenerate NADPH from $NADP^+$.

Dynamic electrochemistry is more often carried out with a three-electrode system, as will be discussed in Section 6.1.1.5, in which electrodes are classified by their roles. In addition, as to electrode material and the way electroactive species respond to the change of applied potential, electrodes can also be categorised into the so-called first, second, and third electrodes.[294]

#### *6.1.1.2 Electrode Processes*

An electrode reaction involving $n$ electrons being transferred is given by:

$$\mathrm{Ox} + n\mathrm{e}^- \rightleftharpoons \mathrm{Red} \tag{6.1}$$

This process is heterogeneous as free electrons themselves cannot flow within the aqueous phase in which they must be carried by electrolytes and electron transfer must occur very close to the electrode surface. Generally speaking, the reaction comprises of the following steps:

1. Reactants in bulk solution diffuse to the electrode surface.

2. Electron transfer occurs.

3. Products diffuse from near the electrode surface to bulk solution.

Before and after the electrode reaction, coupled chemical reactions could occur, which can be either homogeneous or heterogeneous. The slowest step of all these processes is called the rate-determining step.

#### *6.1.1.3 Electrochemical Cell*

A device that is able to either transform chemical energy into electrical energy or conversely cause chemical reactions using electrical energy is called an electrochemical cell.

If cell reactions of a closed-circuit electrochemical cell can occur spontaneously, that is to say, no external driving force is required ($\Delta G < 0$), the cell is a **galvanic cell** (voltaic cell). Otherwise, when external driving force is required ($\Delta G > 0$), the cell is called an **electrolytic cell**.

The well-studied primary cell, secondary cell (rechargeable battery) and fuel cell are all galvanic cells. In industry, NaOH, $Cl_2$ and Al are all produced using the underlying principles of electrolytic cells. These applications of the electrochemical cell have shaped modern society.

#### *6.1.1.4 Electrode Potential*

A **working electrode** (WE) is the place where an electrode reaction of interest occurs. The value of the electrical potential drop ($\phi_{\mathrm{M}} - \phi_{\mathrm{S}}$) ($\phi_{\mathrm{M}}$ is the electrical potential of the working electrode and $\phi_{\mathrm{S}}$ is electrical potential of the aqueous phase) for a half reaction with one electron being transferred:

$$\nu_{\mathrm{A}}\mathrm{A} + \nu_{\mathrm{B}}\mathrm{B} + \ldots + \mathrm{e}^{-}(\text{metal}) \rightleftharpoons \nu_{\mathrm{C}}\mathrm{C} + \nu_{\mathrm{D}}\mathrm{D} + \ldots \tag{6.2}$$

is expressed as:

$$\phi_{\mathrm{M}} - \phi_{\mathrm{S}} = \Delta\phi^{\ominus} + \frac{RT}{F} \ln \left\{ \frac{a_{\mathrm{A}}^{\nu_{\mathrm{A}}} a_{\mathrm{B}}^{\nu_{\mathrm{B}}} \ldots}{a_{\mathrm{C}}^{\nu_{\mathrm{C}}} a_{\mathrm{D}}^{\nu_{\mathrm{D}}} \ldots} \right\} \tag{6.3}$$

Equation 6.3 is called the Nernst equation and is derived in Appendix A. However, it is clear that the absolute value of ($\phi_{\mathrm{M}} - \phi_{\mathrm{S}}$) cannot be measured using a mono-electrode set-up since some current is required to flow through the electrode such that the difference of potential can be probed, which in this set-up would not happen unfortunately.[295] To address this conundrum, a **reference electrode** (RE) is introduced to the system and the difference of electrical potential between the two electrodes becomes[1]:

$$\Delta\phi = (\phi_{\mathrm{M}} - \phi_{\mathrm{S}}) - (\phi_{\mathrm{ref}} - \phi_{\mathrm{S,ref}}) \tag{6.4}$$

If the difference of electrical potential corresponding to RE ($\phi_{\mathrm{ref}} - \phi_{\mathrm{S,ref}}$) stays fixed, the quantity of electrical potential involving WE ($\phi_{\mathrm{M}} - \phi_{\mathrm{S}}$) becomes:

$$\Delta\phi = (\phi_{\mathrm{M}} - \phi_{\mathrm{S}}) - (\phi_{\mathrm{ref}} - \phi_{\mathrm{S,ref}}) = (\phi_{\mathrm{M}} - \phi_{\mathrm{S}}) + \text{constant} \tag{6.5}$$

This equation implies that although the absolute value of electrode potential is not measurable, the change of any applied potential between the WE and RE only effects on the ($\phi_{\mathrm{M}} - \phi_{\mathrm{S}}$) term.

The **standard hydrogen electrode** (SHE) is a platinised platinum electrode

[1]Here, we assume that the current flowing through the two electrodes is tiny. So the $iR$ across the aqueous phase should be negligible.

at $P_{H_2} = 1$ atm and $a_{H^+} = 1$ for the reaction:

$$H^+ + e^- \,(\text{metal}) \rightleftharpoons \frac{1}{2}H_2\,(g) \tag{6.6}$$

for which the Nernst equation is:

$$(\phi_{H_2/H^+} - \phi_{S,Pt}) = \Delta\phi^{\ominus}_{H_2/H^+} + \underbrace{\frac{RT}{F}\ln\left\{\frac{a_{H^+}}{P^{1/2}_{H_2}}\right\}}_{0} \tag{6.7}$$

where the term $\frac{RT}{F}\ln\left\{\frac{a_{H^+}}{P^{1/2}_{H_2}}\right\}$ under standard conditions is mathematically zero and conventionally, the electrical potential of $\Delta\phi^{\ominus}_{H_2/H^+}$ is arbitrarily set to be 0, such that:

$$(\phi_{H_2/H^+} - \phi_{S,Pt}) = \underbrace{\Delta\phi^{\ominus}_{H_2/H^+}}_{0} + \underbrace{\frac{RT}{F}\ln\left\{\frac{a_{H^+}}{P^{1/2}_{H_2}}\right\}}_{0} = 0 \tag{6.8}$$

The point in introducing SHE is that it is the ideal standard RE and 'zero point' to which the potential of other commonly used RE (like Ag/AgCl or calomel electrodes) or any half reactions of interest can be precisely referenced. Using the SHE as the standard RE and combining Equations 6.6 (the reaction of SHE) and 6.2 (the half reaction of interest), the difference of electrical potential of the full cell reaction is:

$$\Delta\phi = (\phi_M - \phi_S) - (\phi_{H_2/H^+} - \phi_{S,Pt}) = (\Delta\phi^{\ominus} - \Delta\phi^{\ominus}_{H_2/H^+}) + \frac{RT}{F}\ln\left\{\frac{a^{\nu_A}_A a^{\nu_B}_B \ldots}{a^{\nu_C}_C a^{\nu_D}_D \ldots}\right\} \tag{6.9}$$

or:

$$E = E^{\ominus} + \frac{RT}{F}\ln\left\{\frac{a^{\nu_A}_A a^{\nu_B}_B \ldots}{a^{\nu_C}_C a^{\nu_D}_D \ldots}\right\} \tag{6.10}$$

where $E^{\ominus}$ is defined as the **standard electrode potential** (SEP) of the half reaction shown in Equation 6.2. In this new equation, $E^{\ominus} = E$ when the activities of all chemical species are in unity. With the well-defined SEP of half-cell potentials in

hand, we can easily derive the potential difference of any cell reaction ($E_{\text{cell}}$) involving half reactions of two electrodes simply using algebraic treatment. Also, based on the conclusion of thermodynamics, the relation between the change in Gibbs free energy and $E_{\text{cell}}$ can be translated into:

$$\Delta G = -FE_{\text{cell}} \tag{6.11}$$

More details can be seen in the following references.[295–297]

#### *6.1.1.5 The Set-up for Dynamic Electrochemistry*

When current starts to flow through the WE and RE at applied potential $E$, a slight difference from Equation 6.4 is that a new term – voltage drop $iR$ is introduced such that:

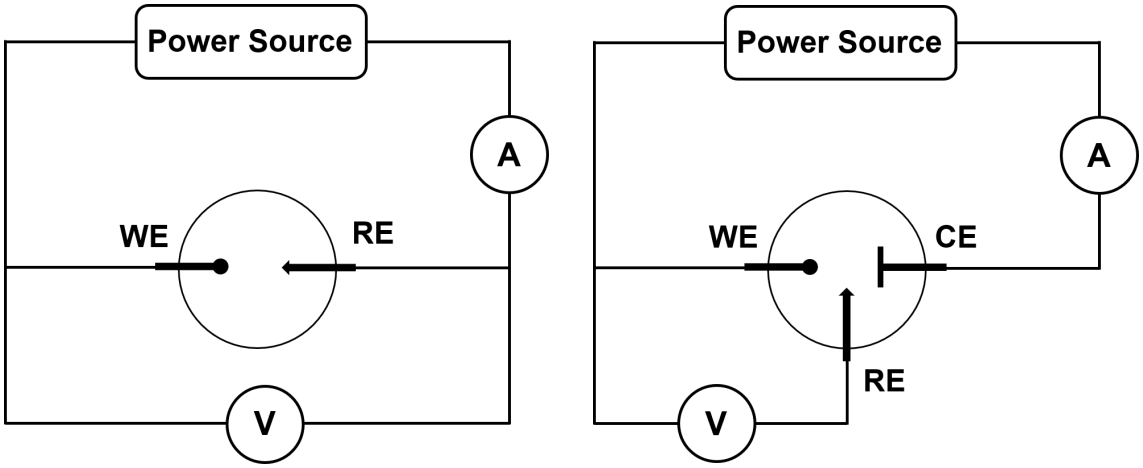
$$E = \underbrace{(\phi_{\text{M}} - \phi_{\text{S}})}_{E_{\text{WE}}} - \underbrace{(\phi_{\text{ref}} - \phi_{\text{S,ref}})}_{E_{\text{RE}}} + iR \tag{6.12}$$

where $i$ is the current, $R$ is the solution resistance.

**The two-electrode set-up** A two-electrode system consists of a WE and RE, in which the applied potential on WE is ideally a value referencing to the electrode potential of RE. The scheme for a two-electrode system is available in Figure 6.1a of Chapter 1.

Usually the two-electrode set-up works perfectly regarding potential measurement when only negligible current flows through and the term $iR$ is virtually 0. On the other hand, this approximation fails to hold when $iR$ is no longer negligible. As large $i$ leads to significant electrolysis in proximity to the RE where the chemical composition linked to the Nernst equation is altered. This results in drifting of the term $(\phi_{\text{ref}} - \phi_{\text{S,ref}})$.

In this thesis the two-electrode set-up was exploited to both the $H_2$-driven and the air-driven experiments under the fuel-cell mode. However, it should be mentioned that in these experiments, large current does flow through the WE (Electrochemical




**(a)** A scheme of set-up for a two-electrode cell.

**(b)** A Scheme of set-up for a three-electrode cell.

**Figure 6.1** Sketches of two-electrode and three-electrode schemes.

Leaf) and RE (platinised carbon) so that actually we do not know the exact electrode potential of the Leaf. The reason why these experiments are still self-consistent is that instead of the electrode potential of WE, it was the current that flowed through the electrodes that was measured. The 0 applied potential mimics situation that no external driving force is applied and the role that the potentiostat plays is an amperemeter.

**The three-electrode set-up** For most elaborate electroanalytical experiments, the introduction of a **counter electrode** (CE, or auxiliary electrode) is the answer for the problem as mentioned in the last paragraph. A simplified scheme for a three-electrode set-up is shown in Figure 6.1b.

The three-electrode set-up ensures that in most cases, the applied potential is exactly the value (or almost) on the WE referencing to the RE. Technically, the current flows through the WE and RE is negligible. This is to ensure that no significant electrolysis occurs on the RE; thus electrical potential of the RE keeps fixed during measurement. The current monitored by the potentiostat is the current flowing through the WE and CE. The CE and WE are often separated by a glass frit to prevent crossover of reactants. Also, a Luggin capillary is usually introduced between the WE and RE.[298]

### 6.1.2 Cyclic Voltammetry

Cyclic voltammetry is the most common and powerful electrochemical technique. The input signal – applied potential – is periodical. During one typical period, which is customarily called a cycle, the applied potential is swept back and forth between two values with a constant rate ($\nu$). The periodical input from a potentiostat to carry out a cyclic voltammetry experiment is shown in Figure 6.2. The measurement is initiated at $E_0$ which then linearly increased to $E_\lambda$, at which point the potential is then swept reversely back to $E_0$ with the same rate $\nu$. The plot that the resulting current is recorded against potential is called a cyclic voltammogram.

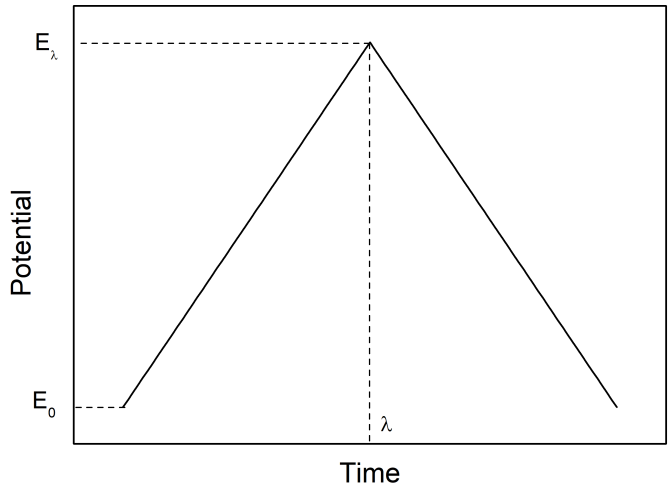



**Figure 6.2** The periodical input of cyclic voltammetry during one cycle.

#### *6.1.2.1 Non-Faradaic Current*

As the term 'non-faradaic' suggests, this type of current does not involve the transfer of electrons to and from chemical species, *i.e.* no redox reaction occurs.

Charge and discharge behaviour are the origin of non-faradaic current. When the applied potential $E$ changes, the double layer linked to the electrode surface tends to respond this change by adjusting the amount and distribution of surface charge. Such behaviour is equivalent to a capacitor and the resulting current can be

expressed like:

$$i = \frac{\mathrm{d}Q}{\mathrm{d}t} = \frac{\mathrm{d}(CE)}{\mathrm{d}t} \tag{6.13}$$

where $C$ is the capacitance linked to the double layer, $Q$ is the amount of charges. In voltammetric measurement, suppose $C$ and the derivative of applied potential $E$ are constant ($\frac{\mathrm{d}E}{\mathrm{d}t} = \nu$), equation (6.13) can be rearranged as:

$$i = C\frac{\mathrm{d}E}{\mathrm{d}t} = C\nu \tag{6.14}$$

This shows that the responding non-faradaic current $i$ is proportional to the scan rate $\nu$. In a cyclic voltammogram, the non-faradaic current leads to a rounded-corner-rectangle-like background, the area of which can be subtracted before further electrochemical analysis. The illustration of typical non-faradaic current is available in Figure 1.24.

#### *6.1.2.2 Faradaic Current I: Non-Turnover Signal*

The non-turnover signal involves the interconversion of a redox couple, but it does not contribute to any net product. In this thesis, this refers to the shift of redox states of the electroactive FNR that is entrapped within the ITO nanopores. The relation can be expressed as (also shown in Figure 1.17 of Chapter 1):

$$\mathrm{FAD} \underset{\mathrm{H^+, e^-}}{\overset{E1}{\rightleftharpoons}} \mathrm{FADH^{\cdot}} \underset{\mathrm{H^+, e^-}}{\overset{E2}{\rightleftharpoons}} \mathrm{FADH_2} \tag{6.15}$$

The reaction involves the sequential transfer of two electrons and to quantify the number of FNR molecules that are entrapped within the ITO nanozones, the equation $Q = nFA\Gamma_0^* = \frac{\text{Integration Area}}{\nu}$ that is derived in Appendix B can be used, in which $n$ is number of electrons that are transferred per molecule, $F$ is the Faraday constant, A is the active surface area of the electrode, $\Gamma_0^*$ is the average surface coverage of FNR and $\nu$ is the scan rate of CV. The scale of the redox current and the corresponding

peak current $i_{\mathrm{p}}$ are also derived in Appendix B with the expressions:

$$i = \frac{n^2F^2A\Gamma_0^*\nu}{RT}\frac{exp\left[\frac{nF}{RT}(E-E^{\ominus'})\right]}{\left\{1+exp\left[\frac{nF}{RT}(E-E^{\ominus'})\right]\right\}^2} \tag{6.16}$$

$$i_{\mathrm{p}} = \frac{n^2F^2A\Gamma_0^*\nu}{4RT} \tag{6.17}$$

Figure 6.3a shows the simulated CV of adsorbed redox species based on Equation 6.16. The area under the anodic wave is proportional to the quantity of charge that is required to oxidise the whole layer, *i.e.* $nFA\Gamma_0^*\nu$. Similarly, the total charge passed during the reverse scan (cathodic wave) should link to the complete reduction of the layer. Under ideal Nernstian conditions, the intensity of anodic peak $E_{\mathrm{pa}}$ should be equal to the cathodic peak $E_{\mathrm{pc}}$ which is symmetrical to one another along the horizontal axis.[298] Also, the width at half-height of the anodic or cathodic wave at 298 K is expressed as:

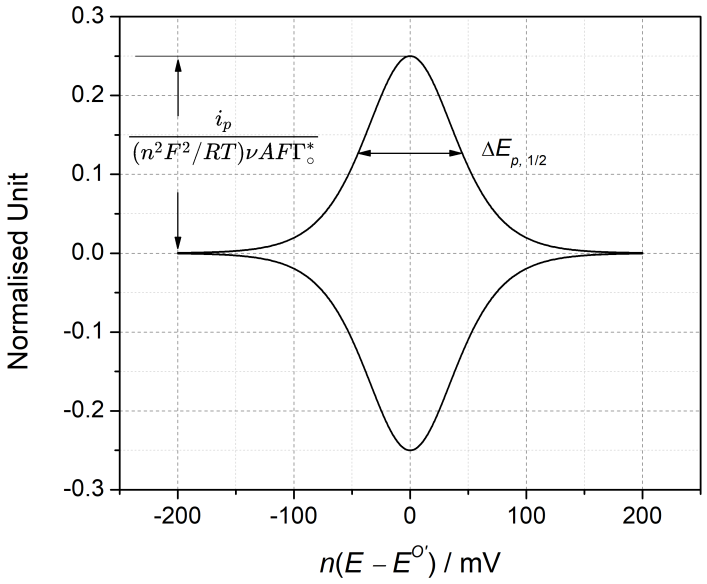
$$\Delta E_{\mathrm{p},1/2} = 3.53\frac{RT}{nF} = \frac{90.6}{n}\mathrm{mV} \tag{6.18}$$

For an ideal fully-cooperative two electron transfer case, the $\Delta E_{\mathrm{p},1/2}$ at 298 K should be 45 mV. With regard to FNR, however, as suggested by previous studies,[118] the conversion from the quinone state to the hydroquinone state is likely to be partially cooperative. The $\Delta E_{p,1/2}$ measured for FNR at pH 8.0 is approximately 57–59 mV.[117] The area and shape of the anodic or cathodic waves are also dependent on $n$. As shown in Figure 6.3b, compared to $n = 1$, the CV of $n = 2$ case is much sharper with bigger total area.

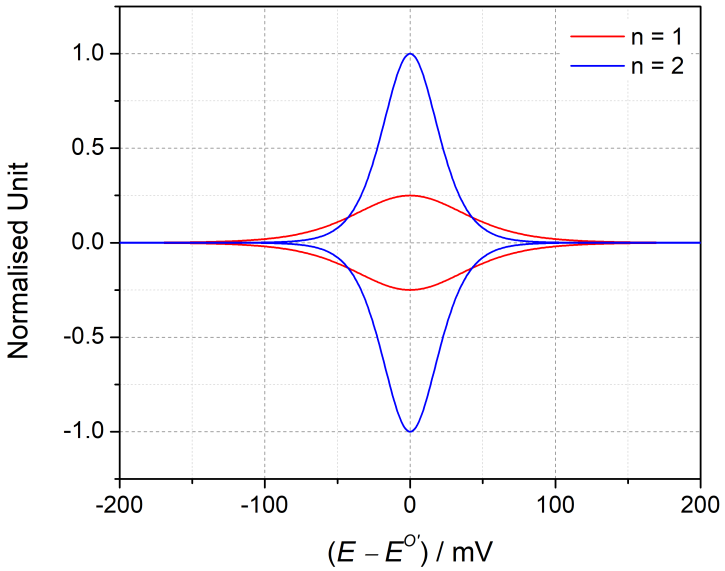
#### *6.1.2.3 Faradaic Current II: Catalytic Current*

The current that originates from added electroactive redox species and contributes to the total turnover in the bulk solution is the catalytic current. This situation is analogous to the case where the interconversion of $NADP^+$/NADPH is catalysed by FNR.

Figure 6.4 shows the CVs of simulated electrochemical catalytic reactions under




**(a)** The normalised unit here is $\frac{i_\mathrm{p}}{(n^2F^2/RT)\nu A\Gamma^*_\circ}$.




**(b)** An illustration for $n = 1$ and $n = 2$. Here the normalised unit is $\frac{i_\mathrm{p}}{(F^2/RT)\nu A\Gamma^*_\circ}$.

**Figure 6.3** Simulated CVs of oxidation and subsequent reduction of adsorbed redox species at 25 °C.

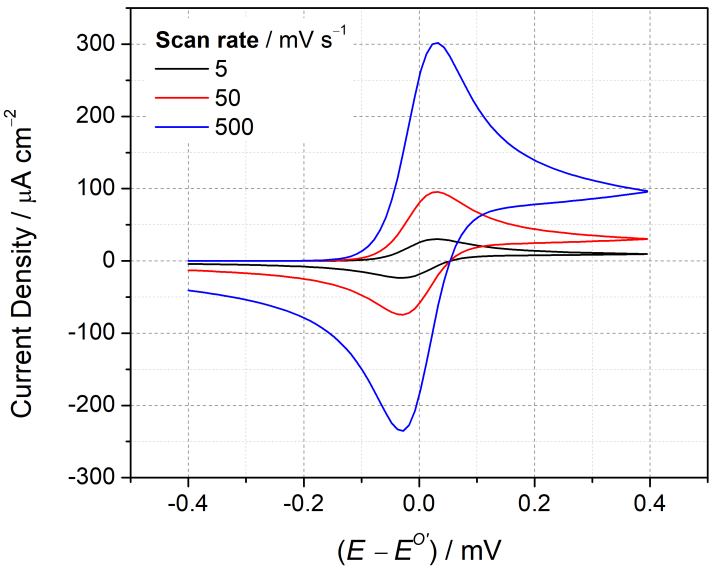



**Figure 6.4** Simulated CVs illustrating the catalytic current under different scan rates based on the electron transfer reaction $\mathrm{R} \xrightarrow{k_0} \mathrm{O} + \mathrm{e}^-$. Parameters for modelling: [R] = 50 $\mu$M, [O] = 0, $k_0$ = 50 m s$^{-1}$, 298 K, diffusion coefficient = $1 \times 10^{-7}$ m$^2$ s$^{-1}$.

ideal conditions such that the ratio between the redox couple O and R would be strictly Nernstian. The simulation was carried out using an open-source simulator.[299] The current for the electron transfer reaction $\mathrm{R} \xrightarrow{k_0} \mathrm{O} + \mathrm{e}^-$ is predicted by the Butler-Volmer equation:

$$I = AFk_0 \left[ c_\mathrm{R} \exp\left(\frac{\alpha_\mathrm{a} nF\eta}{RT}\right) - c_\mathrm{O} \exp\left(\frac{\alpha_\mathrm{c} nF\eta}{RT}\right)\right] \tag{6.19}$$

where $\alpha_\mathrm{a}$ and $\alpha_\mathrm{c}$ are the anodic and cathodic transfer coefficient, $A$ is the surface area of the electrode, $F$ is the Faraday constant, $R$ is the gas constant, $T$ is the temperature in Kelvin, $n$ is the number of electrons transferred, $c_\mathrm{O}$ and $c_\mathrm{R}$ are the surface concentration of oxidised and reduced forms of the redox species of interest, $\eta$ is the overpotential, and $k_0$ is the heterogeneous rate constant in m s$^{-1}$. The peak current is also an important indicator of the CV, which is expressed by the Randle-Ševcík equation:

$$I_\mathrm{p} = 0.4463\ nFAc_0 \left(\frac{nF\nu D}{RT}\right)^{1/2} \tag{6.20}$$

where $\nu$ is the scan rate of CV and $D$ is the diffusion coefficient. It is clear from the figure that as the catalytic current $I \propto \sqrt{\nu}$, every tenfold increase of scan rate is expected to lead to the growth the maximum peak current by $\sqrt{10}$. Additionally, compared to the currents due to non-faradaic output and the redox species adsorbed on the electrode which are proportional to the scan rate $\nu$, the scale of the catalytic rate is expected to be much clearer at a relatively slow scan rate. This is the reason why most of voltammetric measurements in this thesis were carried out at scan rate 1–5 mV $s^{-1}$.

#### *6.1.2.4 Faradaic Current III: Coupled Reaction*

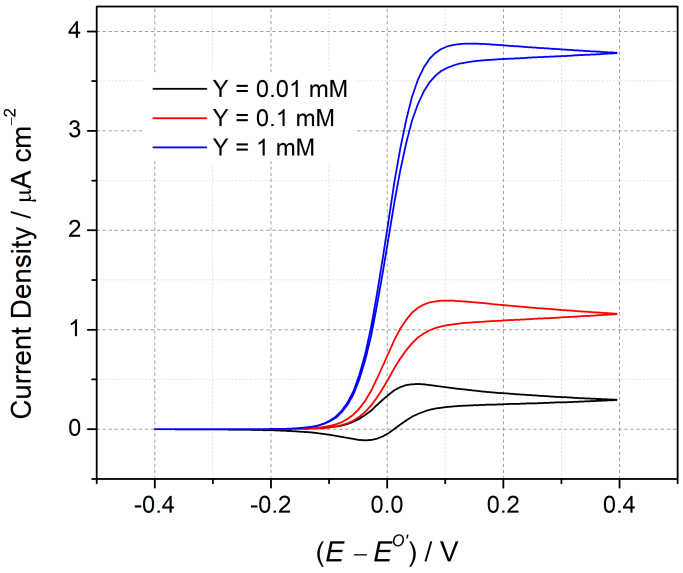
In the Electrochemical Leaf system, when a second enzyme is introduced into the nanopores which are pre-loaded with FNR, the homogeneous downstream reaction occurs such that a fast cofactor regeneration system can be established. This model is similar to the EC′ mechanism in dynamic electrochemistry, which can be summarised as:

$$\mathrm{R} \overset{\mathrm{k_0}}{\rightleftharpoons} \mathrm{O} + \mathrm{ne}^- \tag{6.21}$$

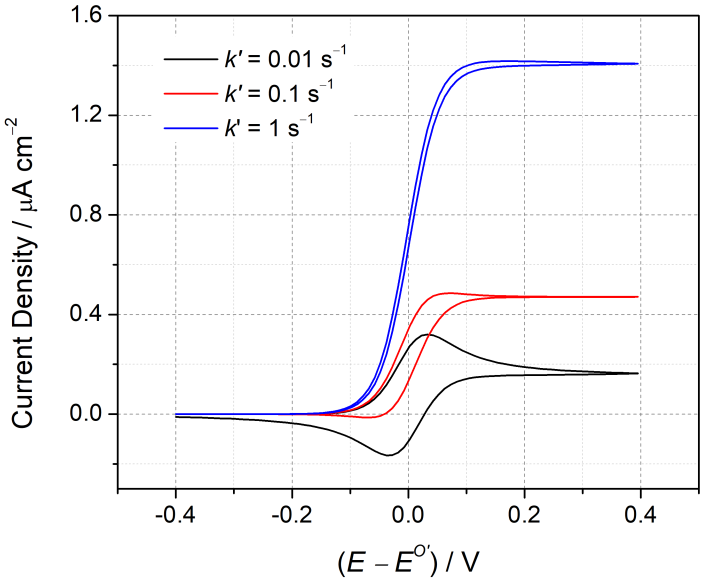
$$\mathrm{O} + \mathrm{Y} \xrightarrow{\mathrm{k'}} \mathrm{R} + \mathrm{products} \tag{6.22}$$

where R and O and are the reduced and oxidised forms of electroactive species of interest, Y is the co-substrate of the homogeneous reaction coupled to the electrode process, and $k'$ is the homogeneous rate constant of reaction.

The simulated CVs matching this mechanism are shown in Figure 6.5. Panel **a** shows the results modelled at different [Y]. It is clear that the ratio of [Y]/[R] largely determines the overall catalytic current. When the initial concentration of R and O are fixed, a larger ratio of [Y]/[R] would favour homogeneous reaction, resulting in more R being regenerated that can be conscripted for the ensuing electrode reaction. Analogously, the homogeneous rate constant of reaction $k'$ determines the rate of the homogeneous reaction. As shown in Figure 6.5b, a larger $k'$ substantially increases the overall catalytic rate.




**(a)** Simulated CVs demonstrating the catalytic current at different [Y]. Parameters for modelling: [R] = 50 $\mu$M, [O] = 0, $k_0$ = 10 m s$^{-1}$, $n$ = 1, $k'$ = 10 s$^{-1}$, scan rate = 5 mV s$^{-1}$, diffusion coefficient = 1 × 10$^{-9}$ m$^2$ s$^{-1}$.




**(b)** Simulated CVs demonstrating the catalytic current at a range of $k'$. Parameters for modelling: [R] = 50 $\mu$M, [O] = 0, $k_0$ = 10 m s$^{-1}$, $n$ = 1, Y = 1 mM, scan rate = 5 mV s$^{-1}$, diffusion coefficient = 1 × 10$^{-9}$ m$^2$ s$^{-1}$.

**Figure 6.5** Simulated CVs illustrate the catalytic current using the EC′ modelen. Here the potential axis ($E - E^{\circ'}$) is the overpotential of the electrode reaction.

### 6.1.3 Chronoamperometry

Under the chronoamperometry mode, the applied potential is hold at a constant value where the responding current is recorded. The graphical output is called a chronoamperogram (also timecourse, *i*-*t* curve in this thesis).

For a planar electrode, when significant electrolysis occurs, the resulting current of CA under stationary condition is proportional to the inverse of the square root of time, which is mathematically described by the Cottrell equation[2]: [296, 298]

$$i = \frac{nFAc_j^0\sqrt{D_j}}{\sqrt{\pi t}} \tag{6.23}$$

where $i$ is the current, $n$ is the number of electrons transferred, $F$ is the Faraday constant, $c_j^0$ is the starting concentration of the analyte $j$, $D_j$ is the diffusion coefficient of the analyte $j$. It is clear that as the CA carries on, the current $i$ is expected to gradually decrease to zero at time $t_\infty$ as depletion of the analyte $j$ occurs.

In this thesis, by design, electrochemical measurements to be performed are often limited by the enzyme at first when only FNR or the second enzyme is pre-loaded. Under such conditions, the CA is initiated by injecting the enzyme that limits the reaction.[3] This leads to the enzyme gradually going into the ITO nanopores and builds up the catalysis that is represented by current. Figure 6.6 shows the CA having this feature. At time 0, the current is virtually 0 because the essential component of the coupled reaction (either FNR or E2) is absent. Shortly after that, an aliquot of enzyme is injected into the bulk solution and then the enzyme starts to go into the pores. This leads to a continuous activation phase until the reaction is not limited by this enzyme any more. During this period, usually the increment of current over time due to the injection of enzyme is smaller and smaller. This can be understood by taking the first derivative of this *i*-*t* curve which tells the 'the change of change of

[2]For an electrode of another surface geometry, its corresponding Cottrell equation form is derived by solving the Fick's second law of diffusion with appropriate boundary conditions. In addition, this equation describes the current of chronoamperometry using a stationary electrode.

[3]Here, either the electrode is rotated or the cell solution is stirred such that the reaction is not limited by mass transport. Details can be seen in Section 6.1.4.

the rate'. As seen in the figure, the tangent value (red dash line) is initially very high and then starts to decrease. At the point when the current levels off, the tangent value should be 0 and this value could further decrease to a negative value in the following deactivation stage.

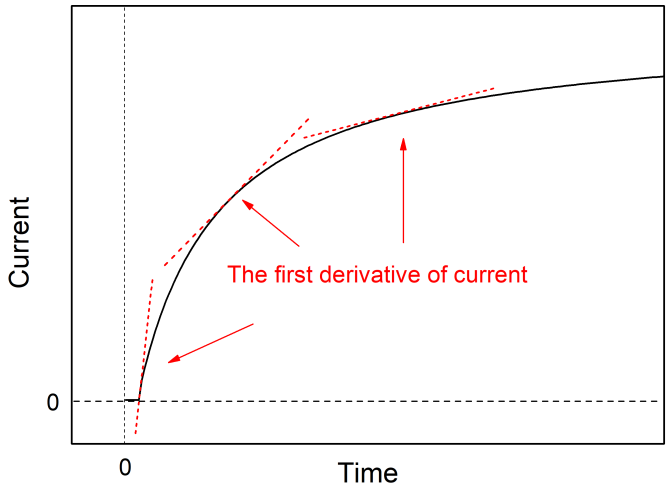



**Figure 6.6** An illustration of a typical CA that is initiated by injecting enzyme into the bulk solution.

During chronoamperometric measurement, the total charge passed $q$ corresponds to the number of electrons flowing to or from the substrates to form the products, which can be quantified by integrating the current versus time:

$$q = \int I \mathrm{d}t \tag{6.24}$$

The coulometry can then be converted to the yield of product by exploiting the Faraday's laws of electrolysis:

$$q = nzF \tag{6.25}$$

where $n$ is the amount of product (mole) and $z$ is the number of charges on the molecule of product.

### 6.1.4 Hydrodynamic Electrodes

When forced convection is introduced with the purpose of improving the mass transport situation in the bulk solution, the electrode under this influence is called a hydrodynamic electrode.[228] The electrode can still be stationary. In our case, a magnetic stirring bead could be introduced. Purging the cell solution by gas is also helpful. The direct outcome of introducing hydrodynamic force is that the current is expected to increase significantly depending on the scale of the forced convection.

The rotating disk electrode is commonly used in electroanalytical experiments as the current value monitored using this electrode can be quantified according to the Levich equation:

$$I = 0.62\ nFAD^{2/3}\omega^{1/2}v^{-1/6}[\mathrm{S}] \tag{6.26}$$

where $\omega$ is the electrode rotation rate, $D$ is the diffusion coefficient of substrate, $v$ is the kinematic viscosity, and [S] is the concentration of the substrate.

## 6.2 Enzyme

### 6.2.1 Enzyme Preparation and Purification

#### *6.2.1.1 Ferredoxin-NADP$^+$ reductase (FNR)*

The vector (aLICator, Thermo Scientific, N-terminal His-tag/EK, #K1251) containing the genes encoding FNR from *Chlamydomonas reinhardtii* and ampicillin resistance with a hexa His-tag at the N-terminal was used to transform *E. coli.* BL21-DE3 cells (New England Biolabs). The plasmid was grown overnight on Luria-Bertani (LB) agar plates containing 0.27 mM ampicillin. One positive colony was used to inoculate 100 mL LB (25 g $L^{-1}$) medium supplemented with ampicillin (final concentration, 0.27 mM) and was grown overnight at 37 °C in a shaking incubator (200 rpm). The overnight culture was diluted in the same medium (usually 15 mL into 500 mL medium, to give 6 × 500 mL per FNR preparation) and left grown at 37 °C and 200 rpm until the mid-log phase was reached (usually 2–3 hours, optical

density (OD) = 0.5) at which point isopropyl $\beta$-D-1-thiogalactopyranoside (IPTG) was added (final concentration of 1 mM) to induce the overexpression of FNR. After 3–4 hours of further growth, the cells were harvested and centrifuged at 6,000 rpm, 4 °C for 30 minutes. The cell pellets were resuspended in 50 mM HEPES buffer (pH = 7.4), supplemented with 150 mM NaCl and 10% V/V glycerol. The cells were disrupted by a French press through which the protein was released. The insoluble cell debris was removed by centrifugation at 45,000 rpm, 4 °C for 1 hour and then the supernatant which contained the enzyme was loaded onto a 5 mL His-Select$^{TM}$ $Ni^{2+}$ column (GE Healthcare) using an ÄKTA protein purification system. The column was first washed by buffer A (pH 7.4, 50 mM HEPES, 500 mM NaCl and 1mM dithiothreitol (DTT)) over 10 column volumes and the enzyme was eluted in the same buffer with a linear 1–100% gradient to reach buffer B (pH 7.4 50 mM HEPES, 500 mM NaCl, 250 mM imidazole and 1mM) over 10 column volumes. Fractions were centrifuged (3,000 rpm, 4 °C) to concentrate the protein using the Amicon Ultra 4 Merck 10 K centricons. The protein was then passed through a desalting column to remove the imidazole group, aliquoted, flash frozen in liquid nitrogen and stored at –80 °C before use.

#### *6.2.1.2 TeSADH W110A, W110G and W110V*

A pET28 vector containing the genes of W110A, W110G or W110V variants of the *sec*-ADH from *Thermoanerobacter ethanolicus* 39E with a hexa His-tag encoded at the N-terminal and also the genes conferring kanamycin resistance were used to transform *E. coli.* BL21 cells. Colonies were grown overnight on LB agar plates supplemented with 30 $\mu$g $mL^{-1}$ kanamycin. A positive single colony was then used to inoculate 100 mL of LB (25 g $L^{-1}$) medium containing kanamycin (30 $\mu$g $mL^{-1}$) and left grown overnight at 37 °C and 200 rpm. The overnight culture was diluted into TB autoinduction media (Formedium) supplemented with 30 $\mu$g $mL^{-1}$ kanamycin (usually 15 mL of culture into 500 mL medium, to give 6 × 500 mL per *sec*-ADH preparation) and was grown at 37 °C and 200 rpm for 16–20 hours. Additionally,

homemade autoinduction medium (500 mL), supplemented with 100 $\mu$L homemade trace elements can serve as an alternative for the TB autoinduction medium. The ingredients of the homemade medium and the solution of trace elements are shown in Table 6.1 and Table 6.2 respectively.

The cells were harvested and centrifuged at 4 °C, 4000 rpm for 30 minutes. The cell pellets were resuspended in 100 mM phosphate buffer (pH 7.7, 300 mM NaCl, 20 mM imidazole, and 10% V/V glycerol) and were disrupted using a French press from which the insoluble cell debris was removed by centrifugation at 45,000 rpm, 4 °C for 1 hour. The supernatant containing the protein was passed through a 0.45 $\mu$m filter and loaded onto a 5 mL His-Select$^{TM}$ $Ni^{2+}$ column (GE Healthcare) using an ÄKTA protein purification system. The column was washed by buffer A (pH 7.7, 100 mM phosphate 300 mM NaCl, 20 mM imidazole and 1 mM DTT) first over 10 column volumes and the enzyme was eluted from buffer A to buffer B (pH 7.7, 100 mM phosphate, 300 mM NaCl, 300 mM imidazole and 1 mM DTT) in a linear gradient. The harvested protein was dialysed overnight against 50 mM Tris-HCl buffer (pH 8.0), supplemented with 1 mM DTT, in order to remove imidazole. The protein was flash frozen in liquid nitrogen and stored at –80 °C before use.

**Table 6.1** Ingredients of the homemade TB autoinduction medium

| Formula | g $L^{-1}$ |
|---|---|
| Tryptone | 12 |
| Yeast extract | 24 |
| Ammonium sulphate $(NH_4)_2SO_4$ | 3.3 |
| Potassium dihydrogen phosphate $KH_2PO_4$ | 6.8 |
| Disodium hydrogen phosphate $Na_2HPO_4$ | 7.1 |
| Glucose | 0.5 |
| Lactose | 2.0 |
| Magnesium sulphate $MgSO_4$ | 0.15 |

**Table 6.2** Ingredients of the trace elements solution

| Formula | mM | Formula | mM |
|---|---|---|---|
| $FeCl_3 \cdot 6\,H_2O$ | 50 | $CaCl_2$ | 20 |
| $MnCl_2 \cdot 4\,H_2O$ | 10 | $ZnSO_4$ | 10 |
| $CoCl_2 \cdot 7\,H_2O$ | 2 | $CuCl_2 \cdot 2\,H_2O$ | 2 |
| $NiCl_2 \cdot 6\,H_2O$ | 2 | $Na_2MoO_4 \cdot 5\,H_2O$ | 2 |
| $Na_2SeO_3$ | 2 | $H_3BO_3$ | 2 |
| HCl | 50 | | |

The solution was prepared using deionised water, sterilised using a 0.45 $\mu$m filter and stored in room temperature.

#### *6.2.1.3 The Secondary Alcohol Dehydrogenase L. Kefir.*

The gene sequence encoding the *sec*-ADH from *Lactobacillus kefir* was available from reference A. Weckbecker *et al.* and was subsequently synthesised by GeneArt, Life Technologies, Thermo Scientific.[300] The vector (aLICator, Thermo Scientific, N-terminal His-tag/EK, #K1251) containing the as-prepared gene, which also encoded a hexa His-tag and the genes to confer ampicillin resistance was prepared using the ligation independent cloning (LIC) method. The forward and reverse primers designed for polymerase chain reaction (PCR) to amplify the gene were 5'- GGT GAT GAT GAT GAC AAG ACT GAT CGT TTA AAA GGC AAA GTA GCA ATT 3' and 5' GGA GAT GGG AAG TCA TTA TTG AGC AGT GTA TCC ACC ATC GAC AAC 3'.

The plasmid was grown overnight on LB agar plates containing 0.27 mM ampicillin. One positive colony was used to inoculate 100 mL LB (25 g $L^{-1}$) medium supplemented with ampicillin (final concentration, 0.27 mM) and was grown overnight at 37 °C in a shaker (200 rpm). The overnight culture was diluted in the same medium (usually 15 mL into 500 mL medium, to give 6 × 500 mL per *sec*-ADH preparation) and grown at 37 °C and 200 rpm until OD 0.5 was reached at which point IPTG was added (final concentration, 1.3 mM) to induce the overexpression of

this (*R*)-selective *sec*-ADH and meanwhile the temperature of the shaking incubator was reduced to 30 °C. The overexpression stage continued for *ca.* 20 hours at 250 rpm and then the harvested cell culture was centrifuged at 6,000 rpm, 4 °C for 30 minutes. The cell pellets were resuspended in cold 50 mM Tris-HCl buffer (pH 8.0, 500 mM NaCl, 1 mM $MgCl_2$, 10 V/V % glycerol) and disrupted using a French Press. The suspension was centrifuged at 45,000 rpm, 4 °C for 1 hour and the resulting supernatant was loaded onto a 5 mL His-Select$^{TM}$ $Ni^{2+}$ column using an ÄKTA protein purification system. After the column was washed by buffer A (50 mM Tris-HCl, 500 mM NaCl, 1 mM DTT, 1 mM $MgCl_2$, pH 8.0) over 10 column volumes, the protein was eluted by the same buffer with a linear gradient of imidazole to reach 250 mM (buffer B: 50 mM Tris-HCl, 500 mM NaCl, 1 mM DTT, 1 mM $MgCl_2$, 250 mM imidazole, pH 8.0) over 10 column volumes. The harvested enzyme was dialysed against 50 mM Tris-HCl buffer (pH = 8.0) containing 1 mM DTT overnight, aliquoted, flash frozen in liquid nitrogen and stored at –80 °C before use.

#### *6.2.1.4 L-Glutamate Dehydrogenase (GLDH)*

The L-glutamate dehydrogenase (GLDH) from bovine liver was purchased from Sigma-Aldrich. This enzyme was supplied in 10 mM phosphate buffer (pH 7.0), supplemented with glycerol and ammonium sulphate and was stored in 4 °C before use. The concentration of this enzyme (in mg $mL^{-1}$) varied among different batches from the supplier.

There are a few examples that the GLDH from *E. coli.* was used. This GLDH variant is more active than the commercially available one from bovine liver. Detailed protocol for purification and properties are available in the following reference.[192]

### 6.2.2 Determination of Enzyme Concentration

Concentration of newly purified or purchased enzymes can be quantified using the Bradford protein assay. This method, named after M. M. Bradford, is a colorimetric assay and is based on the absorption shift of a dye called Coomassie Brilliant Blue

G-250.[301] The original colour of such a dye is brown which turns into blue following the addition of protein. This is because a strongly bound noncovalent complex with the carboxyl group of amino acids is formed. The absorption at 595 nm is used to quantify the amount of complex, through which a protein with unknown concentration can be determined by comparing the absorption to that of a protein with known concentration.

In our case, the protein serving as the reference is the bovine serum albumin (BSA, 2 mg $mL^{-1}$) from Sigma-Aldrich. The Bradford dye reagent was purchased from Alfa Aesar.

### 6.2.3 Enzyme Kinetics

#### *6.2.3.1 Michaelis-Menten Kinetics*

The Michaelis-Menten kinetics is a model to describe the relation between the reaction rate and substrate concentration of enzyme-catalysed reactions.[302, 303] In a simplified scenario which involves a single substrate and a single product, the Michaelis-Menten equation is expressed as:

$$v = \frac{v_{\max}[\mathrm{S}]}{K_{\mathrm{m}} + [\mathrm{S}]} \tag{6.27}$$

where $v$ is the reaction rate, $v_{\max}$ is the maximum reaction rate, [S] is the substrate concentration, $K_{\mathrm{m}}$ is the Michaelis constant. Derivation of this equation is available in Appendix C. Also, $v_{\max} = k_{\mathrm{cat}}[\mathrm{E}]$ in which $k_{\mathrm{cat}}$ is the rate constant for the enzyme-catalysed reaction from the substrate to product and [E] is the concentration of the enzyme. A typical fitted curve matching this equation is shown in Fig 6.7.

In this equation, there are several pieces of useful information:

1. When $[\mathrm{S}] \gg K_{\mathrm{m}}$ (the enzyme is saturated with S), $v \to v_{\max}$, the reaction is a zero-order reaction.

2. When $[\mathrm{S}] \ll K_{\mathrm{m}}$ ([S] is very low), $v = \frac{v_{\max}}{K_{\mathrm{m}}}[\mathrm{S}]$. $v_0$ is proportional to [S], *i.e.* the reaction is first-order.

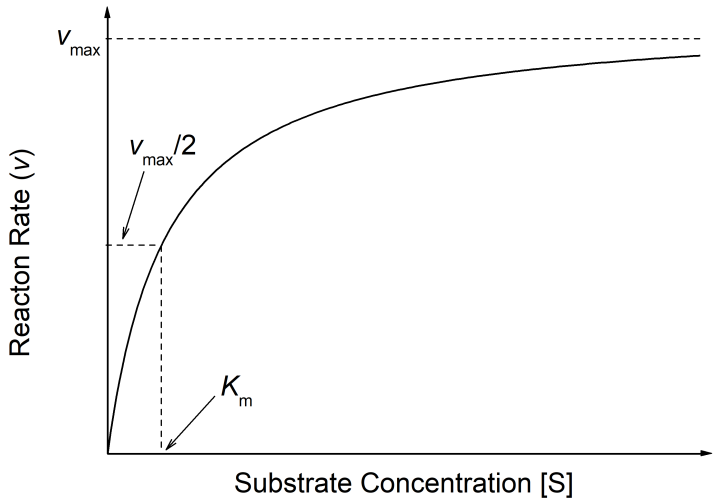



**Figure 6.7** A plot illustrates the effect of substrate concentration on reaction rate of enzyme-catalysed reaction. This is based on Michaelis-Menten kinetics.

3. When $[\mathrm{S}] = K_\mathrm{m}$, $v = \frac{1}{2}v_\mathrm{max}$.

When the biocatalytic activity is inhibited by the substrate, a modified version of Equation 6.27 is available[304]:

$$v = \frac{v_\mathrm{max}[\mathrm{S}]}{K_\mathrm{m} + [\mathrm{S}] + \frac{[\mathrm{S}]^2}{K_\mathrm{i}}} \tag{6.28}$$

where $K_\mathrm{i}$ is the substrate inhibition constant.

## 6.3 Experimental Methods and Materials

### 6.3.1 Electrochemical Measurements

Electrochemical experiments were carried out using the Ivium, PStrace or Multi-Channel Palmsens potentiostats. For experiments using the three-electrode set-up, Pt wire or mesh were exploited as the CE. The Pt CE should be flamed before use, with the purpose of removing possible impurities. The commonly used RE in this thesis were saturated calomel electrode (SCE) and Ag/AgCl (in 3M KCl). The mutual conversion of potential (V as the unit) between the SHE and SCE or AgCl

(in 3M KCl) at 25 °C are as follows:

$$E_{\mathrm{SHE}} = E_{\mathrm{SCE}} + 0.242 \tag{6.29}$$

$$E_{\mathrm{SHE}} = E_{\mathrm{Ag/AgCl}} + 0.211 \tag{6.30}$$

The conversion relation between the reversible hydrogen electrode (RHE) and SHE is:

$$E_{\mathrm{RHE}} = E_{\mathrm{SHE}} + 0.05916 \times \mathrm{pH} \tag{6.31}$$

Experiments under the fuel-cell mode were performed using the two-electrode set-up. In this case, a Pt-based electrode served as both RE and CE and the applied potential to the WE was 0 vs Pt. This mimics the situation where no external driving force is applied such that the cell reaction occurs spontaneously.

For electrochemical experiments requiring precise gas flow control, a mass flow controller was used (MFC, Sierra Instruments).

### 6.3.2 Electrode Fabrication

#### *6.3.2.1 The (FNR + E2)@ITO/support Electrode*

The conductive support for electrophoresis can be either Ti foil (thickness = 0.127 mm, Aldrich), pyrolytic graphite edge or ITO glass. The ingredient of every portion of solution for electrophoresis includes 0.02 g ITO nanopowder (Sigma-Aldrich), 10 mg iodine (Alfa Aesar) and 20 mL acetone (Aldrich). The mixture was sonicated for at least 45 minutes before use. The conductive support was sonicated in acetone, ethanol and distilled water sequentially, each for 15 minutes. Electrophoretic deposition was carried out at 10 V applied voltage. The conductive support to be deposited and the counter electrode (a piece of Ti foil or ITO glass) were connected to the power source and held in parallel with one another in 1–2 cm distance. The time applied for depositing the one-sided PGE and ITO glass was 6 minutes, while for the double-sided Ti foil, each side was deposited for at least 6 minutes separately. Figure 1.21 of Chapter 1 illustrates the as-prepared bare ITO/support electrodes.

Detailed procedure to load FNR and E2 to ITO/support electrode is available in Chapter 1.

After being used, the Ti foil can be recycled. This can be fulfilled by sonicating the electrode in ∼3.7% HCl to remove the old ITO layer. This is followed by sonication in acetone, ethanol and distilled water as mentioned before.

#### *6.3.2.2 The Platinised Carbon Electrode*

The Toray carbon paper (PTFE treated) was purchased from Alfa Aesar, cut into strips to fit the size of electrochemical cells and cleaned in the same way as the conductive support as mentioned before. The carbon paper was platinised by electrodeposition under the chronoamperometry mode (the cell solution was stationary). The electrolyte for electrodeposition contained 0.5 M $H_2SO_4$ (Fisher Chemical) and 5 mM $H_2PtCl_6$ (Aldrich).[222, 305, 306] Deposition was carried out sequentially in two stages. The duration for the first stage took 40 seconds at –0.32 V vs SHE. This was followed by 360 seconds at –0.25 vs SHE as the second stage.

### 6.3.3 Analytical Methods

#### *6.3.3.1 UV-Vis Spectroscopy*

The UV-Vis spectroscopy method measures the absorption intensity of species under ultraviolet and visible spectral regions of light. The 'Timedrive', 'Scan' and 'Waveprog' built-in modes of the Perkin-Elmer Lambda 19 UV-Vis spectrophotometer (program Lambda-SPX/P) were used for different purposes. The path length of the quartz cuvette is 10 mm and the slit is 1 nm.

**Waveprog mode** Under this mode, the adsorption of species is recorded at a designated wavelength in one go and the output data are discrete points. The concentration of enzymes used in this thesis was determined using the data collected using this mode. Details of the Bradford solution assay to determine protein concentration are available at Section 6.2.2.

**Scan mode** Under this mode, the wavelength of the incident light is linearly swept within a range. The resulting spectra can be used to quantify NADPH at 340 nm. This is achieved using the Beer-Lambert law:

$$A = \varepsilon l c \tag{6.32}$$

where A is the optical attenuation of the species, $\varepsilon$ is the molar attenuation coefficient, $l$ is the optical path length and $c$ is the concentration of the species. Figure 2.9 in Chapter 2 shows some typical output spectra under this mode.

**Timedrive mode** Under this mode, the absorption is recorded continuously over a time period at a designated wavelength of incident light. As the initial rate of NADP(H)-linked reactions can be determined by recording the linear production or consumption of NADPH, this mode was used to determine kinetics parameters of enzymes based on the Michaelis-Menten kinetics model.

#### *6.3.3.2 Nuclear Magnetic Resonance*

Samples were tested using a Bruker AVIIIHD 400 instrument, the results of which were analysed using the MestreNova software package. Two methods were used in this thesis for quantifying the concentration of product.

**Calibration curve** This method was used in Chapter 2 to quantify 2-oxoglutarate and L-glutamate. An NMR sample is composed of the cell solution and $D_2O$ in 90:10 ratio. The $^1H$ spectra under the water suppression mode are recorded, from which the characteristic peaks corresponding to the species of interest are quantified using the calibration curves which are fitted using a series of standard solutions with known concentration.

**The unlocked mode** NMR results in Chapter 3 and 5 were recorded using this method. Each NMR tube contains the cell solution and $D_2O$ in 90:10 ratio, and the capillary sealed with standard solution of (Trimethylsilyl)propionic-2,2,3,3-$d_4$

acid sodium salt (TMSP) inside with known concentration. The $^1$H spectra are recorded under the special unlocked water suppression mode. The concentration of cell solution is determined by comparing the ratio between the peak area of the compound of interest and that corresponding to TMSP. The chemical shift ($\delta$) of TMPS is at $-0.1$ ppm, with 9 H. The equation for calculating the species of interest is:

$$c = \frac{A}{\text{numbers of H corresponding to the peak}} \times \frac{B}{\frac{9}{C}} \tag{6.33}$$

where A = peak area of a characteristic peak of the solution in question, B = peak area of TMSP at $\delta$ $-0.1$, and C is the concentration of TMSP.

#### *6.3.3.3 GC-FID analysis*

The gas chromatography (GC) with flame-ionization detection (FID) analysis was carried out using a GC 6850 instrument fitted with an autosampler (Agilent) and a chiral BetaDex$^{TM}$ 325 column (30 m $\times$ 0.25 mm $\times$ 0.25 $\mu$m) (Supelco).

The protocol for GC-FID analysis is as follows: inlet temperature 200 °C, detector temperature 250 °C, oven 110 °C hold 20 min; 10 °C min$^{-1}$ to 200 °C, $R_t$ (4-phenyl-2-butanone) = 20.8 min, $R_t$ ((*R*)-4-phenyl-2-butanol) = 23.6 min, $R_t$ ((*S*)-4-phenyl-2-butanol) = 23.4 min.

Based on the absolute peak areas of the species, the ee and conversion can be determined accordingly.

### 6.3.4 Buffer Solution

#### *6.3.4.1 Borate and Phosphate Buffer*

The method to prepare the inorganic borate and phosphate buffers is similar, which is carried out by titrating a weak acid with its conjugate base or *vice versa*. For instance, to obtain 50 mM borate buffer, 50 mM $H_3BO_3$ and 12.5 mM $Na_2B_4O_7$ are first dissolved in distilled water or Milli-Q water (Millipore, 15.2 M$\Omega$ cm) separately. Then $Na_2B_4O_7$ solution is gradually titrated by $H_3BO_3$ solution until desired pH is reached.

Preparation of phosphate buffer follows a similar working principle. The ingredient includes $K_2HPO_4$ and $KH_2PO_4$.

#### *6.3.4.2 Good's Buffers*

The MES, TAPS, MOPS, CHES, HEPES and Tris buffers were used in this thesis. They are classified into the so-called Good's buffers which were described by N. E. Good and are commonly used for biological experiments.[307, 308]

To prepare these buffers with desired volume, concentration and pH, the compound of required mass is first weighed and dissolved into either distilled or Milli-Q water. The volume of added water should be slightly less than the required volume. After being stirred uniformly, concentrated NaOH is gradually titrated dropwise into the solution to finally reach the required pH. Last, water is replenished to give the correct final volume.

To increase the capacity of buffer over a broader pH range, the exploitation of a mixture of these buffers would work. For instance, the (MES + TAPS) buffer can cover pH 6–9; the working pH for (MOPS + CHES + TAPS) buffer varies from pH 7–10.

# References

(1) B. D. Engel, M. Schaffer, L. K. Cuellar, E. Villa, J. M. Plitzko and W. Baumeister, *Elife*, 2015, **4**, e04889.

(2) A. Schmid, J. Dordick, B. Hauer, A. Kiener, M. Wubbolts and B. Witholt, *Nature*, 2001, **409**, 258–268.

(3) H. E. Schoemaker, D. Mink and M. G. Wubbolts, *Science*, 2003, **299**, 1694–1697.

(4) R. A. Sheldon and S. van Pelt, *Chemical Society Reviews*, 2013, **42**, 6223–6235.

(5) J. B. van Beilen and Z. Li, *Current Opinion in Biotechnology*, 2002, **13**, 338–344.

(6) B. Sharma, A. K. Dangi and P. Shukla, *Journal of Environmental Management*, 2018, **210**, 10–22.

(7) C. Wandrey, A. Liese and D. Kihumbu, *Organic Process Research & Development*, 2000, **4**, 286–290.

(8) S. K. Ma, J. Gruber, C. Davis, L. Newman, D. Gray, A. Wang, J. Grate, G. W. Huisman and R. A. Sheldon, *Green Chemistry*, 2010, **12**, 81–86.

(9) C. R. Wescott and A. M. Klibanov, *Journal of the American Chemical Society*, 1993, **115**, 1629–1631.

(10) E. Vlasenko, M. Schülein, J. Cherry and F. Xu, *Bioresource Technology*, 2010, **101**, 2405–2411.

(11) J. Powlowski, S. Mahajan, M. Schapira and E. R. Master, *Carbohydrate Research*, 2009, **344**, 1175–1179.

(12) P. A. Fitzpatrick and A. M. Klibanov, *Journal of the American Chemical Society*, 1991, **113**, 3166–3171.

(13) I. P. Petrounia and F. H. Arnold, *Current Opinion in Biotechnology*, 2000, **11**, 325–330.

(14) A. Korkegian, M. E. Black, D. Baker and B. L. Stoddard, *Science*, 2005, **308**, 857–860.

(15) D. A. Kraut, K. S. Carroll and D. Herschlag, *Annual Review of Biochemistry*, 2003, **72**, 517–571.

(16) A. J. Mulholland, *Drug Discovery Today*, 2005, **10**, 1393–1402.

(17) H. Bisswanger, *Perspectives in Science*, 2014, **1**, 41–55.

(18) Y. Fu, Z. Callaway, J. Lum, R. Wang, J. Lin and Y. Li, *Analytical Chemistry*, 2014, **86**, 1965–1971.

(19) J. A. Wells and D. A. Estell, *Trends in Biochemical Sciences*, 1988, **13**, 291–297.

(20) P. V. Iyer and L. Ananthanarayan, *Process Biochemistry*, 2008, **43**, 1019–1032.

(21) R. Ciriminna and M. Pagliaro, *Organic Process Research & Development*, 2013, **17**, 1479–1484.

(22) M. Górecki, *Organic & Biomolecular Chemistry*, 2015, **13**, 2999–3010.

(23) U. Sauer, F. Canonaco, S. Heri, A. Perrenoud and E. Fischer, *Journal of Biological Chemistry*, 2004, **279**, 6613–6619.

(24) P. Wilkins and R. Wilkins, *Inorganic Chemistry in Biology*, Oxford University Press, 2005.

(25) C. S. Morrison, W. B. Armiger, D. R. Dodds, J. S. Dordick and M. A. Koffas, *Biotechnology Advances*, 2018, **36**, 120–131.

(26) F. Hollmann and A. Schmid, *Biocatalysis and Biotransformation*, 2004, **22**, 63–88.

(27) H. Wu, C. Tian, X. Song, C. Liu, D. Yang and Z. Jiang, *Green Chemistry*, 2013, **15**, 1773–1789.

(28) H. K. Chenault, E. S. Simon and G. M. Whitesides, *Biotechnology and Genetic Engineering Reviews*, 1988, **6**, 221–270.

(29) H. Zhao and W. A. Van Der Donk, *Current Opinion in Biotechnology*, 2003, **14**, 583–589.

(30) A. Angelastro, W. M. Dawson, L. Y. Luk and R. K. Allemann, *ACS Catalysis*, 2017, **7**, 1025–1029.

(31) A. Weckbecker, H. Gröger and W. Hummel, in *Biosystems Engineering I*, Springer, 2010, pp. 195–242.

(32) K. Drauz, S. Eils and M. Schwarm, *Chimica Oggi – Chemistry Today*, 2002, **20**, 15–21.

(33) G. Krix, A. Bommarius, K. Drauz, M. Kottenhahn, M. Schwarm and M.-R. Kula, *Journal of Biotechnology*, 1997, **53**, 29–39.

(34) B. Binay, D. Alagöz, D. Yildirim, A. Çelik and S. S. Tükel, *Beilstein Journal of Organic Chemistry*, 2016, **12**, 271–277.

(35) V. Tishkov and V. Popov, *Biochemistry*, 2004, **69**, 1252.

(36) W. Hummel and M.-R. KULA, *European Journal of Biochemistry*, 1989, **184**, 1–13.

(37) X. Wang, T. Saba, H. H. Yiu, R. F. Howe, J. A. Anderson and J. Shi, *Chem*, 2017, **2**, 621–654.

(38) Z. Shaked and G. M. Whitesides, *Journal of the American Chemical Society*, 1980, **102**, 7104–7105.

(39) W. Hummel, H. Schütte, E. Schmidt, C. Wandrey and M.-R. Kula, *Applied Microbiology and Biotechnology*, 1987, **26**, 409–416.

(40) K. Seelbach, B. Riebel, W. Hummel, M.-R. Kula, V. I. Tishkov, A. M. Egorov, C. Wandrey and U. Kragl, *Tetrahedron Letters*, 1996, **37**, 1377–1380.

(41) M. Wada, A. Yoshizumi, Y. Noda, M. Kataoka, S. Shimizu, H. Takagi and S. Nakamori, *Applied and Environmental Microbiology*, 2003, **69**, 933–937.

(42) H. Yun, Y.-H. Yang, B.-K. Cho, B.-Y. Hwang and B.-G. Kim, *Biotechnology Letters*, 2003, **25**, 809–814.

(43) H. R. Levy, F. A. Loewus and B. Vennesland, *Journal of the American Chemical Society*, 1957, **79**, 2949–2953.

(44) C. Wong, D. G. Drueckhammer and H. M. Sweers, *Journal of the American Chemical Society*, 1985, **107**, 4028–4031.

(45) L.-J. Wang, C.-X. Li, Y. Ni, J. Zhang, X. Liu and J.-H. Xu, *Bioresource Technology*, 2011, **102**, 7023–7028.

(46) K. Tauber, M. Hall, W. Kroutil, W. M. Fabian, K. Faber and S. M. Glueck, *Biotechnology and bioengineering*, 2011, **108**, 1462–1467.

(47) H. W. Adolph, P. Maurer, H. Schneider-Bernlöhr, C. Sartorius and M. Zeppezauer, *European Journal of Biochemistry*, 1991, **201**, 615–625.

(48) C. Drewke and M. Ciriacy, *Biochimica et Biophysica Acta (BBA)-Gene Structure and Expression*, 1988, **950**, 54–60.

(49) T. W. Johannes, R. D. Woodyer and H. Zhao, *Applied and Environmental Microbiology*, 2005, **71**, 5728–5734.

(50) T. W. Johannes, R. D. Woodyer and H. Zhao, *Biotechnology and Bioengineering*, 2007, **96**, 18–26.

(51) R. K. Singh, R. Singh, D. Sivakumar, S. Kondaveeti, T. Kim, J. Li, B. H. Sung, B.-K. Cho, D. R. Kim, S. C. Kim et al., *ACS Catalysis*, 2018, **8**, 11085–11093.

(52) K. Schneider and H. G. Schlegel, *Biochimica et Biophysica Acta (BBA)-Enzymology*, 1976, **452**, 66–80.

(53) B. Danielsson, F. Winqvist, J. Y. Malpote and K. Mosbach, *Biotechnology Letters*, 1982, **4**, 673–678.

(54) B. L. Hirschbein and G. M. Whitesides, *Journal of the American Chemical Society*, 1982, **104**, 4458–4460.

(55) L. G. Lee and G. M. Whitesides, *Journal of the American Chemical Society*, 1985, **107**, 6999–7008.

(56) W. Liu, S. Zhang and P. Wang, *Journal of Biotechnology*, 2009, **139**, 102–107.

(57) G. Carrea, R. Bovara, P. Cremonesi and R. Lodi, *Biotechnology and Bioengineering*, 1984, **26**, 560–563.

(58) G. Lemiere, J. Lepoivre and F. Alderweireldt, *Tetrahedron Letters*, 1985, **26**, 4527–4528.

(59) M. M. Musa, K. I. Ziegelmann-Fjeld, C. Vieille, J. G. Zeikus and R. S. Phillips, *The Journal of Organic Chemistry*, 2007, **72**, 30–34.

(60) C. H. Wong and G. M. Whitesides, *The Journal of Organic Chemistry*, 1982, **47**, 2816–2818.

(61) H. K. Chenault and G. M. Whitesides, *Bioorganic Chemistry*, 1989, **17**, 400–409.

(62) R. Wichmann and D. Vasic-Racki, *Technology Transfer in Biotechnology*, 2005, 225–260.

(63) B. R. Riebel, P. R. Gibbs, W. B. Wellborn and A. S. Bommarius, *Advanced Synthesis & Catalysis*, 2003, **345**, 707–712.

(64) H. Gao, J. Li, D. Sivakumar, T.-S. Kim, S. K. Patel, V. C. Kalia, I.-W. Kim, Y.-W. Zhang and J.-K. Lee, *International Journal of Biological Macromolecules*, 2019, **123**, 629–636.

(65) J. B. Jones, D. W. Sneddon, W. Higgins and A. J. Lewis, *Journal of the Chemical Society, Chemical Communications*, 1972, 856–857.

(66) K. Goldberg, K. Schroer, S. Lütz and A. Liese, *Applied Microbiology and Biotechnology*, 2007, **76**, 237–248.

(67) F. Hollmann, B. Witholt and A. Schmid, *Journal of Molecular Catalysis B: Enzymatic*, 2002, **19**, 167–176.

(68) M. Franke and E. Steckhan, *Angewandte Chemie International Edition*, 1988, **27**, 265–267.

(69) O. Abril and G. M. Whitesides, *Journal of the American Chemical Society*, 1982, **104**, 1552–1554.

(70) Y. Maenaka, T. Suenobu and S. Fukuzumi, *Journal of the American Chemical Society*, 2012, **134**, 367–374.

(71) R. Ruppert, S. Herrmann and E. Steckhan, *Journal of the Chemical Society, Chemical Communications*, 1988, 1150–1151.

(72) H. Maid, P. Böhm, S. M. Huber, W. Bauer, W. Hummel, N. Jux and H. Gröger, *Angewandte Chemie International Edition*, 2011, **50**, 2397–2400.

(73) M. M. Grau, M. Poizat, I. W. Arends and F. Hollmann, *Applied Organometallic Chemistry*, 2010, **24**, 380–385.

(74) R. Ruppert, S. Herrmann and E. Steckhan, *Tetrahedron Letters*, 1987, **28**, 6583–6586.

(75) C. E. Paul and F. Hollmann, *Applied Microbiology and Biotechnology*, 2016, **100**, 4773–4778.

(76) M. Poizat, I. W. Arends and F. Hollmann, *Journal of Molecular Catalysis B: Enzymatic*, 2010, **63**, 149–156.

(77) C. A. Denard, J. F. Hartwig and H. Zhao, *ACS Catalysis*, 2013, **3**, 2856–2864.

(78) V. Höllrigl, K. Otto and A. Schmid, *Advanced Synthesis & Catalysis*, 2007, **349**, 1337–1340.

(79) Z. J. Wang, K. N. Clary, R. G. Bergman, K. N. Raymond and F. D. Toste, *Nature Chemistry*, 2013, **5**, 100–103.

(80) F. Hildebrand and S. Lütz, *Chemistry–A European Journal*, 2009, **15**, 4998–5001.

(81) V. Köhler, Y. Wilson, M. Dürrenberger, D. Ghislieri, E. Churakova, T. Quinto, L. Knörr, D. Häussinger, F. Hollmann, N. Turner et al., *Nature Chemistry*, 2013, **5**, 93–99.

(82) T. Quinto, V. Köhler and T. R. Ward, *Topics in Catalysis*, 2014, **57**, 321–331.

(83) C. Kohlmann, W. Märkle and S. Lütz, *Journal of Molecular Catalysis B: Enzymatic*, 2008, **51**, 57–72.

(84) R. Wienkamp and E. Steckhan, *Angewandte Chemie International Edition*, 1982, **21**, 782–783.

(85) I. Carelli, R. Rosati and A. Casini, *Electrochimica Acta*, 1981, **26**, 1695–1697.

(86) J. Komoschinski and E. Steckhan, *Tetrahedron Letters*, 1988, **29**, 3299–3300.

(87) L. Gorton and E. Domínguez, *Reviews in Molecular Biotechnology*, 2002, **82**, 371–392.

(88) H. Jaegfeldt, *Journal of Electroanalytical Chemistry and Interfacial Electrochemistry*, 1981, **128**, 355–370.

(89) H. K. Chenault and G. M. Whitesides, *Applied Biochemistry and Biotechnology*, 1987, **14**, 147–197.

(90) P. J. Elving, W. T. Bresnahan, J. Moiroux and Z. Samec, *Journal of Electroanalytical Chemistry and Interfacial Electrochemistry*, 1982, **141**, 365–378.

(91) T. Kôno and M. Suekane, *Journal of the Agricultural Chemical Society of Japan*, 1958, **22**, 404–410.

(92) D. H. Fricks, J. T. Bechtel and A. Underwood, *Archives of Biochemistry and Biophysics*, 1973, **159**, 837–841.

(93) E. S. Kirkor and A. Scheeline, *European journal of biochemistry*, 2000, **267**, 5014–5022.

(94) B. A. Beaupre, B. R. Carmichael, M. R. Hoag, D. D. Shah and G. R. Moran, *Journal of the American Chemical Society*, 2013, **135**, 13980–13987.

(95) B. A. Beaupre, M. R. Hoag, J. Roman, F. H. Försterling and G. R. Moran, *Biochemistry*, 2015, **54**, 795–806.

(96) A. Damian, K. Maloo and S. Omanovic, *Chemical and Biochemical Engineering Quarterly*, 2007, **21**, 21–32.

(97) I. Ali, A. Gill and S. Omanovic, *Chemical Engineering Journal*, 2012, **188**, 173–180.

(98) I. Ali, T. Khan and S. Omanovic, *Journal of Molecular Catalysis A: Chemical*, 2014, **387**, 86–91.

(99) I. Ali, M. McArthur, N. Hordy, S. Coulombe and S. Omanovic, *Int. J. Electrochem. Sci*, 2012, **7**, 7675–7683.

(100) I. Ali, B. Soomro and S. Omanovic, *Electrochemistry communications*, 2011, **13**, 562–565.

(101) E. Siu, K. Won and C. B. Park, *Biotechnology Progress*, 2007, **23**, 293–296.

(102) F. Hildebrand, C. Kohlmann, A. Franz and S. Lütz, *Advanced Synthesis & Catalysis*, 2008, **350**, 909–918.

(103) D. C.-S. Tse and T. Kuwana, *Analytical Chemistry*, 1978, **50**, 1315–1318.

(104) Y. H. Kim and Y. J. Yoo, *Enzyme and Microbial Technology*, 2009, **44**, 129–134.

(105) K. Vuorilehto, S. Lütz and C. Wandrey, *Bioelectrochemistry*, 2004, **65**, 1–7.

(106) H.-K. Song, S. H. Lee, K. Won, J. H. Park, J. K. Kim, H. Lee, S.-J. Moon, D. K. Kim and C. B. Park, *Angewandte Chemie International Edition*, 2008, **47**, 1749–1752.

(107) M. T. Rawls, J. Johnson and B. A. Gregg, *Journal of Electroanalytical Chemistry*, 2010, **650**, 10–15.

(108) I. Schröder, E. Steckhan and A. Liese, *Journal of Electroanalytical Chemistry*, 2003, **541**, 109–115.

(109) C. M. Cadoux and R. D. Milton, *ChemElectroChem*, 2020.

(110) R. D. Milton and S. D. Minteer, *Journal of the Royal Society Interface*, 2017, **14**, 20170253.

(111) A. L. Ghindilis, P. Atanasov and E. Wilkins, *Electroanalysis*, 1997, **9**, 661–674.

(112) L. Gorton, A. Lindgren, T. Larsson, F. Munteanu, T. Ruzgas and I. Gazaryan, *Analytica Chimica Acta*, 1999, **400**, 91–108.

(113) A. Bassegoda, C. Madden, D. W. Wakerley, E. Reisner and J. Hirst, *Journal of the American Chemical Society*, 2014, **136**, 15473–15476.

(114) F. A. Armstrong, R. M. Evans and C. F. Megarity, *Methods in enzymology*, 2018, **599**, 387–407.

(115) F. A. Armstrong and J. Hirst, *Proceedings of the National Academy of Sciences*, 2011, **108**, 14049–14054.

(116) C. Léger, S. J. Elliott, K. R. Hoke, L. J. Jeuken, A. K. Jones and F. A. Armstrong, *Biochemistry*, 2003, **42**, 8653–8662.

(117) B. Siritanaratkul, C. F. Megarity, T. G. Roberts, T. O. Samuels, M. Winkler, J. H. Warner, T. Happe and F. A. Armstrong, *Chemical Science*, 2017, **8**, 4579–4586.

(118) B. Siritanaratkul, Ph.D. Thesis, University of Oxford, 2017.

(119) J. Cantet, A. Bergel, M. Comtat and J.-L. Séris, *Journal of Molecular Catalysis*, 1992, **73**, 371–380.

(120) J. Cantet, A. Bergel and M. Comtat, *Enzyme and Microbial Tchnology*, 1996, **18**, 72–79.

(121) P. Gros, C. Zaborosch, H. G. Schlegel and A. Bergel, *Journal of Electroanalytical Chemistry*, 1996, **405**, 189–195.

(122) K. Délécouls, P. Saint-Aguet, C. Zaborosch and A. Bergel, *Journal of Electroanalytical Chemistry*, 1999, **468**, 139–149.

(123) M. Yuan, M. J. Kummer, R. D. Milton, T. Quah and S. D. Minteer, *ACS Catalysis*, 2019, **9**, 5486–5495.

(124) Y. Kashiwagi and T. Osa, *Chemistry Letters*, 1993, **22**, 677–680.

(125) T. Osa, Y. Kashiwagi and Y. Yanagisawa, *Chemistry Letters*, 1994, **23**, 367–370.

(126) A. J. Fry, S. B. Sobolov, M. D. Leonida and K. I. Voivodov, *Denki Kagaku oyobi Kogyo Butsuri Kagaku*, 1994, **62**, 1260–1263.

(127) R. DiCosimo, C.-H. Wong, L. Daniels and G. M. Whitesides, *The Journal of Organic Chemistry*, 1981, **46**, 4622–4623.

(128) M. Ito and T. Kuwana, *Journal of Electroanalytical Chemistry and Interfacial Electrochemistry*, 1971, **32**, 415–425.

(129) A. L. de Lacey, M. T. Bes, C. Gómez-Moreno and V. M. Fernández, *Journal of Electroanalytical Chemistry*, 1995, **390**, 69–76.

(130) M. Schulz, H. Leichmann, H. Günther and H. Simon, *Applied Microbiology and Biotechnology*, 1995, **42**, 916–922.

(131) H. Günther, K. Walter, P. Köhler and H. Simon, *Journal of biotechnology*, 2000, **83**, 253–267.

(132) E. Katz and I. Willner, *Journal of the American Chemical Society*, 2003, **125**, 6803–6813.

(133) K. Cheikhou and T. Tzédakis, *AIChE journal*, 2008, **54**, 1365–1376.

(134) R. Jayabalan, M. Sathishkumar, E. Jeong, S. Mun and S. Yun, *Bioresource Technology*, 2012, **123**, 686–689.

(135) A. Bergel and M. Comtat, *Journal of Electroanalytical Chemistry and Interfacial Electrochemistry*, 1991, **302**, 219–231.

(136) D. Chen, D. Yang, Q. Wang and Z. Jiang, *Industrial & Engineering Chemistry Research*, 2006, **45**, 4110–4116.

(137) Z. Jiang, C. Lü and H. Wu, *Industrial & Engineering Chemistry Research*, 2005, **44**, 4165–4170.

(138) L. Zhang, M. Can, S. W. Ragsdale and F. A. Armstrong, *ACS catalysis*, 2018, **8**, 2789–2795.

(139) G.-L. Wang, J.-J. Xu and H.-Y. Chen, *Biosensors and Bioelectronics*, 2009, **24**, 2494–2498.

(140) K. A. Brown, D. F. Harris, M. B. Wilker, A. Rasmussen, N. Khadka, H. Hamby, S. Keable, G. Dukovic, J. W. Peters, L. C. Seefeldt et al., *Science*, 2016, **352**, 448–450.

(141) M. B. Wilker, K. E. Shinopoulos, K. A. Brown, D. W. Mulder, P. W. King and G. Dukovic, *Journal of the American Chemical Society*, 2014, **136**, 4316–4324.

(142) K. A. Brown, M. B. Wilker, M. Boehm, H. Hamby, G. Dukovic and P. W. King, *ACS Catalysis*, 2016, **6**, 2201–2204.

(143) R. Shi, Y. Cao, Y. Bao, Y. Zhao, G. I. Waterhouse, Z. Fang, L.-Z. Wu, C.-H. Tung, Y. Yin and T. Zhang, *Advanced Materials*, 2017, **29**, 1700803.

(144) X. Hao, J. Zhou, Z. Cui, Y. Wang, Y. Wang and Z. Zou, *Applied Catalysis B: Environmental*, 2018, **229**, 41–51.

(145) J. Ryu, S. H. Lee, D. H. Nam and C. B. Park, *Advanced Materials*, 2011, **23**, 1883–1888.

(146) I. Robel, V. Subramanian, M. Kuno and P. V. Kamat, *Journal of the American Chemical Society*, 2006, **128**, 2385–2393.

(147) W.-J. Ong, L.-L. Tan, Y. H. Ng, S.-T. Yong and S.-P. Chai, *Chemical Reviews*, 2016, **116**, 7159–7329.

(148) J. Huang, M. Antonietti and J. Liu, *Journal of Materials Chemistry A*, 2014, **2**, 7686–7693.

(149) Y. Wu, J. Ward-Bond, D. Li, S. Zhang, J. Shi and Z. Jiang, *ACS Catalysis*, 2018, **8**, 5664–5674.

(150) S. Roy, V. Jain, R. K. Kashyap, A. Rao and P. P. Pillai, *ACS Catalysis*, 2020, **10**, 5522–5528.

(151) D. H. Nam and C. B. Park, *ChemBioChem*, 2012, **13**, 1278–1282.

(152) W. Greschner, C. Lanzerath, T. Reß, K. Tenbrink, S. Borchert, A. Mix, W. Hummel and H. Gröger, *Journal of Molecular Catalysis B: Enzymatic*, 2014, **103**, 10–15.

(153) I. Willner and D. Mandler, *Enzyme and Microbial Technology*, 1989, **11**, 467–483.

(154) M. Lee, J. H. Kim, S. H. Lee, S. H. Lee and C. B. Park, *ChemSusChem*, 2011, **4**, 581–586.

(155) R. K. Yadav, J.-O. Baeg, G. H. Oh, N.-J. Park, K.-j. Kong, J. Kim, D. W. Hwang and S. K. Biswas, *Journal of the American Chemical Society*, 2012, **134**, 11455–11461.

(156) R. Ruppert and E. Steckhan, *Journal of the Chemical Society, Perkin Transactions 2*, 1989, 811–814.

(157) H. Gröger, F. Chamouleau, N. Orologas, C. Rollmann, K. Drauz, W. Hummel, A. Weckbecker and O. May, *Angewandte Chemie International Edition*, 2006, **45**, 5677–5681.

(158) H. Gröger, C. Rollmann, F. Chamouleau, I. Sebastien, O. May, W. Wienand and K. Drauz, *Advanced Synthesis & Catalysis*, 2007, **349**, 709–712.

(159) R. R. Wise and J. K. Hoober, *The Structure and Function of Plastids*, Springer Science & Business Media, 2007, vol. 23.

(160) R. Milo and R. Phillips, *Cell Biology by the Numbers*, Garland Science, 2015.

(161) C. F. Megarity, B. Siritanaratkul, R. A. Herold, G. Morello and F. A. Armstrong, *The Journal of Chemical Physics*, 2020, **153**, 225101.

(162) M. Shin, K. Tagawa and D. I. Arnon, *Biochemische Zeitschrift*, 1963, **338**, 84–96.

(163) C. F. Megarity, B. Siritanaratkul, R. S. Heath, L. Wan, G. Morello, S. R. FitzPatrick, R. L. Booth, A. J. Sills, A. W. Robertson, J. H. Warner et al., *Angewandte Chemie International Edition*, 2019, **58**, 4948–4952.

(164) J. A. Hermoso, T. Mayoral, M. Faro, C. Gomez-Moreno, J. Sanz-Aparicio and M. Medina, *Journal of Molecular Biology*, 2002, **319**, 1133–1142.

(165) N. Carrillo and E. A. Ceccarelli, *European Journal of Biochemistry*, 2003, **270**, 1900–1915.

(166) P. A. Karplus and H. R. Faber, *Photosynthesis research*, 2004, **81**, 303–315.

(167) Z. Deng, A. Aliverti, G. Zanetti, A. K. Arakaki, J. Ottado, E. G. Orellano, N. B. Calcaterra, E. A. Ceccarelli, N. Carrillo and P. A. Karplus, *Nature Structural Biology*, 1999, **6**, 847–853.

(168) L. Piubelli, A. Aliverti, A. K. Arakaki, N. Carrillo, E. A. Ceccarelli, P. A. Karplus and G. Zanetti, *Journal of Biological Chemistry*, 2000, **275**, 10472–10476.

(169) C. F. Megarity, B. Siritanaratkul, B. Cheng, G. Morello, L. Wan, A. J. Sills, R. S. Heath, N. J. Turner and F. A. Armstrong, *ChemCatChem*, 2019, **11**, 5662–5670.

(170) G. Kurisu, M. Kusunoki, E. Katoh, T. Yamazaki, K. Teshima, Y. Onda, Y. Kimata-Ariga and T. Hase, *Nature Structural Biology*, 2001, **8**, 117–121.

(171) C. Batie and H. Kamin, *Journal of Biological Chemistry*, 1984, **259**, 11976–11985.

(172) C. J. Batie and H. Kamin, *Journal of Biological chemistry*, 1984, **259**, 8832–8839.

(173) C. Batie and H. Kamin, *Journal of Biological Chemistry*, 1986, **261**, 11214–11223.

(174) F. A. Armstrong, R. M. Evans, S. V. Hexter, B. J. Murphy, M. M. Roessler and P. Wulff, *Accounts of chemical research*, 2016, **49**, 884–892.

(175) J. F. Evans and T. Kuwana, *Analytical Chemistry*, 1977, **49**, 1632–1635.

(176) A. M. Yacynych and T. Kuwana, *Analytical Chemistry*, 1978, **50**, 640–645.

(177) T. J. Davies, M. E. Hyde and R. G. Compton, *Angewandte Chemie*, 2005, **117**, 5251–5256.

(178) C. F. Blanford and F. A. Armstrong, *Journal of Solid State Electrochemistry*, 2006, **10**, 826–832.

(179) A. A. Gorodetsky and J. K. Barton, *Langmuir*, 2006, **22**, 7917–7922.

(180) C. F. Blanford, R. S. Heath and F. A. Armstrong, *Chemical Communications*, 2007, 1710–1712.

(181) S. Krishnan and F. A. Armstrong, *Chemical Science*, 2012, **3**, 1015–1023.

(182) O. Rüdiger, J. M. Abad, E. C. Hatchikian, V. M. Fernandez and A. L. De Lacey, *Journal of the American Chemical Society*, 2005, **127**, 16008–16009.

(183) J. Fontecilla-Camps and Y. Nicolet, *Metalloproteins: Methods and Protocols*, Humana Press, 2014.

(184) R. Elofson and R. Edsberg, *Canadian Journal of Chemistry*, 1957, **35**, 646–650.

(185) T. Osa and T. Kuwana, *Journal of Electroanalytical Chemistry and Interfacial Electrochemistry*, 1969, **22**, 389–406.

(186) L. Michaelis and E. S. Hill, *The Journal of General Physiology*, 1933, **16**, 859–873.

(187) K. Tagawa and D. I. Arnon, *Nature*, 1962, **195**, 537–543.

(188) F. L. Rodkey and J. Donovan Jr, *Journal of Biological Chemistry*, 1959, **234**, 677–680.

(189) J. Madoz, J. Fernández-Recio, C. Gómez-Moreno and V. M. Fernández, *Bioelectrochemistry and bioenergetics*, 1998, **47**, 179–183.

(190) J. Madoz-Gurpide, J. M. Abad, J. Fernandez-Recio, M. Velez, L. Vazquez, C. Gomez-Moreno and V. M. Fernandez, *Journal of the American Chemical Society*, 2000, **122**, 9808–9817.

(191) G. Morello, C. F. Megarity and F. A. Armstrong, *Nature Communications*, 2021, **12**, 1–9.

(192) B. Cheng, L. Wan and F. A. Armstrong, *ChemElectroChem*, 2020, **7**, 4672–4678.

(193) K. Kordesch, V. Hacker, J. Gsellmann, M. Cifrain, G. Faleschini, P. Enzinger, R. Fankhauser, M. Ortner, M. Muhr and R. R. Aronson, *Journal of Power Sources*, 2000, **86**, 162–165.

(194) E. Gülzow, *Journal of Power Sources*, 1996, **61**, 99–104.

(195) N. Sammes, R. Bove and K. Stahl, *Current Opinion in Solid State and Materials Science*, 2004, **8**, 372–378.

(196) P. Stonehart, *Journal of Applied Electrochemistry*, 1992, **22**, 995–1001.

(197) R. M. Ormerod, *Chemical Society Reviews*, 2003, **32**, 17–28.

(198) B. E. Logan, B. Hamelers, R. Rozendal, U. Schröder, J. Keller, S. Freguia, P. Aelterman, W. Verstraete and K. Rabaey, *Environmental Science & Technology*, 2006, **40**, 5181–5192.

(199) C. Santoro, C. Arbizzani, B. Erable and I. Ieropoulos, *Journal of Power Sources*, 2017, **356**, 225–244.

(200) J. A. Cracknell, K. A. Vincent and F. A. Armstrong, *Chemical Reviews*, 2008, **108**, 2439–2461.

(201) I. Willner, Y.-M. Yan, B. Willner and R. Tel-Vered, *Fuel Cells*, 2009, **9**, 7–24.

(202) X. Xiao, H.-q. Xia, R. Wu, L. Bai, L. Yan, E. Magner, S. Cosnier, E. Lojou, Z. Zhu and A. Liu, *Chemical Reviews*, 2019, **119**, 9509–9558.

(203) S. Calabrese Barton, J. Gallaway and P. Atanassov, *Chemical Reviews*, 2004, **104**, 4867–4886.

(204) L. Xu and F. A. Armstrong, *RSC Advances*, 2015, **5**, 3649–3656.

(205) L. Dos Santos, V. Climent, C. F. Blanford and F. A. Armstrong, *Physical Chemistry Chemical Physics*, 2010, **12**, 13962–13974.

(206) C. Kisker, H. Schindelin, A. Pacheco, W. A. Wehbi, R. M. Garrett, K. Rajagopalan, J. H. Enemark and D. Rees, *Cell*, 1997, **91**, 973–983.

(207) L. Xu and F. A. Armstrong, *Energy & Environmental Science*, 2013, **6**, 2166–2171.

(208) D. Burdette and J. Zeikus, *Biochemical Journal*, 1994, **302**, 163–170.

(209) J. Wiegel and L. G. Ljungdahl, *Archives of Microbiology*, 1981, **128**, 343–348.

(210) S. D. Minteer, P. Atanassov, H. R. Luckarift and G. R. Johnson, *Materials Today*, 2012, **15**, 166–173.

(211) L. B. Wingard Jr, C. H. Shaw and J. F. Castner, *Enzyme and Microbial Technology*, 1982, **4**, 137–142.

(212) K. Bych, M. H. Mikš, T. Johanson, M. J. Hederos, L. K. Vigsnæs and P. Becker, *Current Opinion in Biotechnology*, 2019, **56**, 130–137.

(213) M.-R. Kula, A. Buckmann, H. Hustedt, K. Kroner and M. Morr, in *Enzyme Engineering*, Springer, 1978, pp. 47–53.

(214) F. Sato, M. Togo, M. K. Islam, T. Matsue, J. Kosuge, N. Fukasaku, S. Kurosawa and M. Nishizawa, *Electrochemistry Communications*, 2005, **7**, 643–647.

(215) J. Xuan, M. K. Leung, D. Y. Leung and M. Ni, *Renewable and Sustainable Energy Reviews*, 2009, **13**, 1301–1313.

(216) L. Xia, K. Van Nguyen, Y. Holade, H. Han, K. Dooley, P. Atanassov, S. Banta and S. D. Minteer, *ACS Energy Letters*, 2017, **2**, 1435–1438.

(217) Y. H. Kim, E. Campbell, J. Yu, S. D. Minteer and S. Banta, *Angewandte Chemie International Edition*, 2013, **52**, 1437–1440.

(218) A. Ramanavicius, A. Kausaite and A. Ramanaviciene, *Biosensors and Bioelectronics*, 2008, **24**, 761–766.

(219) A. F. Wait, A. Parkin, G. M. Morley, L. dos Santos and F. A. Armstrong, *The Journal of Physical Chemistry C*, 2010, **114**, 12003–12009.

(220) E. Lojou, *Electrochimica Acta*, 2011, **56**, 10385–10397.

(221) R. D. Milton, R. Cai, S. Abdellaoui, D. Leech, A. L. De Lacey, M. Pita and S. D. Minteer, *Angewandte Chemie International Edition*, 2017, **56**, 2680–2683.

(222) L. Wan, C. F. Megarity, B. Siritanaratkul and F. A. Armstrong, *Chemical Communications*, 2018, **54**, 972–975.

(223) H. F. Fisher, in *Methods in Enzymology*, Elsevier, 1985, vol. 113, pp. 16–27.

(224) C. Frieden, *Annual Review of Biochemistry*, 1971, **40**, 653–696.

(225) I. Axelsson, *Journal of Chromatography A*, 1978, **152**, 21–32.

(226) P. Engel and K. Dalziel, *Biochemical Journal*, 1970, **118**, 409–419.

(227) J. E. Rife and W. Cleland, *Biochemistry*, 1980, **19**, 2321–2328.

(228) A. C. Fisher, *Electrode Dynamics*, Oxford University Press, 1996.

(229) S. Johnson and K. W. Smith, *Biochemistry*, 1976, **15**, 553–559.

(230) K. W. Smith and S. Johnson, *Biochemistry*, 1976, **15**, 560–565.

(231) D. H. Kim, K. F. Faull, A. J. Norris and C. D. Eckhert, *Journal of Mass Spectrometry*, 2004, **39**, 743–751.

(232) K. I. Ziegelmann-Fjeld, M. M. Musa, R. S. Phillips, J. G. Zeikus and C. Vieille, *Protein Engineering, Design & Selection*, 2007, **20**, 47–55.

(233) R. Devaux-Basseguy, A. Bergel and M. Comtat, *Enzyme and Microbial Technology*, 1997, **20**, 248–258.

(234) D. S. Burdette, V. Tchernajencko and J. G. Zeikus, *Enzyme and Microbial Technology*, 2000, **27**, 11–18.

(235) T. Eriksson, S. Björkman and P. Höglund, *European Journal of Clinical Pharmacology*, 2001, **57**, 365–376.

(236) L. Wan, R. S. Heath, B. Siritanaratkul, C. F. Megarity, A. J. Sills, M. P. Thompson, N. J. Turner and F. A. Armstrong, *Green Chemistry*, 2019, **21**, 4958–4963.

(237) S. L. Montgomery, J. Mangas-Sanchez, M. P. Thompson, G. A. Aleku, B. Dominguez and N. J. Turner, *Angewandte Chemie*, 2017, **129**, 10627–10630.

(238) M. Tavanti, J. Mangas-Sanchez, S. L. Montgomery, M. P. Thompson and N. J. Turner, *Organic & Biomolecular Chemistry*, 2017, **15**, 9790–9793.

(239) R. A. Sheldon, *Catalysis Today*, 2015, **247**, 4–13.

(240) G. Chen, Y. Zhou, Z. Long, X. Wang, J. Li and J. Wang, *ACS Applied Materials & Interfaces*, 2014, **6**, 4438–4446.

(241) J. E. Steves and S. S. Stahl, *Journal of the American Chemical Society*, 2013, **135**, 15742–15745.

(242) M. Pickl, M. Fuchs, S. M. Glueck and K. Faber, *Applied Microbiology and Biotechnology*, 2015, **99**, 6617–6642.

(243) L. Martínez-Montero, V. Gotor, V. Gotor-Fernández and I. Lavandera, *Green Chemistry*, 2017, **19**, 474–480.

(244) V. Prelog, *Pure and Applied Chemistry*, 1964, **9**, 119–130.

(245) J.-C. Mani, R. Pietruszko and H. Theorell, *Archives of Biochemistry and Biophysics*, 1970, **140**, 52–59.

(246) L. S. Al-Kassim and C. S. Tsai, *Biochemistry and Cell Biology*, 1990, **68**, 907–913.

(247) K. Niefind, J. Müller, B. Riebel, W. Hummel and D. Schomburg, *Journal of Molecular Biology*, 2003, **327**, 317–328.

(248) W. Hummel, *Applied Microbiology and Biotechnology*, 1990, **34**, 15–19.

(249) C. W. Bradshaw, W. Hummel and C. H. Wong, *The Journal of Organic Chemistry*, 1992, **57**, 1532–1536.

(250) D. S. Burdette, C. Vieille and J. G. Zeikus, *Biochemical Journal*, 1996, **316**, 115–122.

(251) E. Keinan, E. K. Hafeli, K. K. Seth and R. Lamed, *Journal of the American Chemical Society*, 1986, **108**, 162–169.

(252) M. M. Musa and R. S. Phillips, *Catalysis Science & Technology*, 2011, **1**, 1311–1323.

(253) C. Heiss, M. Laivenieks, J. G. Zeikus and R. S. Phillips, *Bioorganic & Medicinal Chemistry*, 2001, **9**, 1659–1666.

(254) A. E. Tripp, D. S. Burdette, J. G. Zeikus and R. S. Phillips, *Journal of the American Chemical Society*, 1998, **120**, 5137–5141.

(255) M. M. Musa, N. Lott, M. Laivenieks, L. Watanabe, C. Vieille and R. S. Phillips, *ChemCatChem*, 2009, **1**, 89–93.

(256) J. M. Patel, M. M. Musa, L. Rodriguez, D. A. Sutton, V. V. Popik and R. S. Phillips, *Organic & Biomolecular Chemistry*, 2014, **12**, 5905–5910.

(257) L. Wan, R. S. Heath, C. F. Megarity, A. J. Sills, R. A. Herold, N. J. Turner and F. A. Armstrong, *ACS Catalysis*, 2021, **11**, 6526–6533.

(258) P. Kokkonen, A. Beier, S. Mazurenko, J. Damborsky, D. Bednar and Z. Prokop, *RSC Chemical Biology*, 2021, **2**, 645–655.

(259) B. Wu, *Drug Metabolism Reviews*, 2011, **43**, 440–456.

(260) M. C. Reed, A. Lieb and H. F. Nijhout, *Bioessays*, 2010, **32**, 422–429.

(261) E. L. Eliel, S. H. Wilen and M. P. Doyle, *Basic Organic Stereochemistry*, John Wiley, 2001.

(262) M. M. Musa, R. S. Phillips, M. Laivenieks, C. Vieille, M. Takahashi and S. M. Hamdan, *Organic & Biomolecular Chemistry*, 2013, **11**, 2911–2915.

(263) E. Liardo, N. Róos-Lombardía, F. Morís, J. González-Sabín and F. Rebolledo, *European Journal of Organic Chemistry*, 2018, **2018**, 3031–3035.

(264) C. R. Shugrue and S. J. Miller, *Chemical Reviews*, 2017, **117**, 11894–11951.

(265) A. Lumbroso, M. L. Cooke and B. Breit, *Angewandte Chemie International Edition*, 2013, **52**, 1890–1932.

(266) C. C. Gruber, I. Lavandera, K. Faber and W. Kroutil, *Advanced Synthesis & Catalysis*, 2006, **348**, 1789–1805.

(267) M.-C. Gutiérrez, R. Furstoss and V. Alphand, *Advanced Synthesis & Catalysis*, 2005, **347**, 1051–1059.

(268) O. Verho and J.-E. Bäckvall, *Journal of the American Chemical Society*, 2015, **137**, 3996–4009.

(269) M. M. Musa, I. Karume, M. Takahashi, S. Hamdan and N. Ullah, *ChemistrySelect*, 2018, **3**, 10205–10208.

(270) M. M. Musa, F. Hollmann and F. G. Mutti, *Catalysis Science & Technology*, 2019, **9**, 5487–5503.

(271) S. C. Cosgrove, A. Brzezniak, S. P. France, J. I. Ramsden, J. Mangas-Sanchez, S. L. Montgomery, R. S. Heath and N. J. Turner, *Methods in enzymology*, 2018, **608**, 131–149.

(272) C. V. Voss, C. C. Gruber, K. Faber, T. Knaus, P. Macheroux and W. Kroutil, *Journal of the American Chemical Society*, 2008, **130**, 13969–13972.

(273) S. Yoon, M. D. Patil, S. Sarak, H. Jeon, G.-H. Kim, T. P. Khobragade, S. Sung and H. Yun, *ChemCatChem*, 2019, **11**, 1898–1902.

(274) W. Adam, M. Lazarus, C. R. Saha-Möller and P. Schreier, *Tetrahedron: Asymmetry*, 1998, **9**, 351–355.

(275) G. Shin, S. Mathew, M. Shon, B.-G. Kim and H. Yun, *Chemical Communications*, 2013, **49**, 8629–8631.

(276) K. Yasukawa, S. Nakano and Y. Asano, *Angewandte Chemie*, 2014, **126**, 4517–4520.

(277) G. A. Aleku, J. Mangas-Sanchez, J. Citoler, S. P. France, S. L. Montgomery, R. S. Heath, M. P. Thompson and N. J. Turner, *ChemCatChem*, 2018, **10**, 515–519.

(278) M. Alexeeva, A. Enright, M. J. Dawson, M. Mahmoudian and N. J. Turner, *Angewandte Chemie International Edition*, 2002, **41**, 3177–3180.

(279) F. G. Mutti, A. Orthaber, J. H. Schrittwieser, J. G. de Vries, R. Pietschnig and W. Kroutil, *Chemical Communications*, 2010, **46**, 8046–8048.

(280) N. J. Turner, B. Yuan, D. P. Debecker, X. Wu, J. Xiao and Q. Fei, *ChemCatChem*, 2020, **12**, 6191–6195.

(281) C. Magallanes-Noguera, M. M. Ferrari, M. Kurina-Sanz and A. A. Orden, *Journal of Biotechnology*, 2012, **160**, 189–194.

(282) C. E. Paul, I. Lavandera, V. Gotor-Fernández, W. Kroutil and V. Gotor, *ChemCatChem*, 2013, **5**, 3875–3881.

(283) C. V. Voss, C. C. Gruber and W. Kroutil, *Angewandte Chemie*, 2008, **120**, 753–757.

(284) Y.-L. Li, J.-H. Xu and Y. Xu, *Journal of Molecular Catalysis B: Enzymatic*, 2010, **64**, 48–52.

(285) B. Martín-Matute, M. Edin, K. Bogár and J.-E. Bäckvall, *Angewandte Chemie*, 2004, **116**, 6697–6701.

(286) E. L. Noey, N. Tibrewal, G. Jiménez-Osés, S. Osuna, J. Park, C. M. Bond, D. Cascio, J. Liang, X. Zhang, G. W. Huisman et al., *Proceedings of the National Academy of Sciences*, 2015, **112**, E7065–E7072.

(287) A. Anne, C. Bourdillon, S. Daninos and J. Moiroux, *Biotechnology and Bioengineering*, 1999, **64**, 101–107.

(288) A. E. Biade, C. Bourdillon, J. M. Laval, G. Mairesse and J. Moiroux, *Journal of the American Chemical Society*, 1992, **114**, 893–897.

(289) W. Märkle and S. Lütz, *Electrochimica Acta*, 2008, **53**, 3175–3180.

(290) W. Kroutil and K. Faber, *Tetrahedron: Asymmetry*, 1998, **9**, 2901–2913.

(291) J.-M. Laval, C. Bourdillon and J. Moiroux, *Biotechnology and Bioengineering*, 1987, **30**, 157–159.

(292) I. Karume, M. Takahashi, S. M. Hamdan and M. M. Musa, *ChemCatChem*, 2016, **8**, 1459–1463.

(293) C. V. Voss, C. C. Gruber and W. Kroutil, *Synlett*, 2010, **2010**, 991–998.

(294) W. R. Browne, *Electrochemistry*, Oxford University Press, 2018.

(295) R. G. Compton and G. H. Sanders, *Electrode Potentials*, Oxford University Press, 1996.

(296) R. G. Compton and C. E. Banks, *Understanding Voltammetry, Second Edition*, Imperial College Press, 2010.

(297) C. H. Hamann, A. Hamnett and W. Vielstich, *Electrochemistry, Second Edition*, Wiley-VCH, 2007.

(298) A. J. Bard and L. R. Faulkner, *Electrochemical Methods: Fundamentals and Applications, Second Edition*, John Wiley & Sons, Inc., 2001.

(299) S. Wang, J. Wang and Y. Gao, *Journal of Chemical Education*, 2017, **94**, 1567–1570.

(300) A. Weckbecker and W. Hummel, *Biocatalysis and Biotransformation*, 2006, **24**, 380–389.

(301) M. M. Bradford, *Analytical biochemistry*, 1976, **72**, 248–254.

(302) J. M. Berg, J. L. Tymoczko and L. Stryer, *Biochemistry, Fifth Edition*, W. H. Freeman, 2002.

(303) S. Sun, *Physical Chemistry, Second Edition*, Xiamen University Press, 2013.

(304) G. A. Hill and C. W. Robinson, *Biotechnology and Bioengineering*, 1975, **17**, 1599–1615.

(305) J. Liu, W. Hu, C. Zhong and Y. F. Cheng, *Journal of Power Sources*, 2013, **223**, 165–174.

(306) C. Zhong, W. Hu and Y. Cheng, *Journal of Power Sources*, 2011, **196**, 8064–8072.

(307) N. E. Good, G. D. Winget, W. Winter, T. N. Connolly, S. Izawa and R. M. Singh, *Biochemistry*, 1966, **5**, 467–477.

(308) N. E. Good and S. Izawa, in *Methods in Enzymology*, Elsevier, 1972, vol. 24, pp. 53–68.

(309) H. A. Heering, J. H. Weiner and F. A. Armstrong, *Journal of the American Chemical Society*, 1997, **119**, 11628–11638.

(310) J. P. Keener and J. Sneyd, *Mathematical physiology I: Cellular physiology*, Springer, 2009.

# Appendix

# A Derivation of Nernst Equation

In electrochemistry, a general half reaction with one electron transfer is expressed as:

$$\nu_{\mathrm{A}}\mathrm{A} + \nu_{\mathrm{B}}\mathrm{B} + \ldots + \mathrm{e}^{-}(\mathrm{metal}) \rightleftharpoons \nu_{\mathrm{C}}\mathrm{C} + \nu_{\mathrm{D}}\mathrm{D} + \ldots \tag{A.1}$$

where $\nu_i$ ($i$ = A, B, ..., C, D, ...) is the stoichiometric coefficient for species $i$, $\overline{\mu_i}$ is the electrochemical potential which is given as:

$$\overline{\mu_i} = \mu_i + z_i F \phi \tag{A.2}$$

where $\mu_i$ is the chemical potential of $i$, $z_i$ is the charge on molecule $i$, F is the Faraday constant, and $\phi$, also called Galvani potential, is the potential with respect to the phase – electrode, solution or gas – where species $i$ resides. The second term at the right-hand site of Equation (A.2) gives the electrical energy of species $i$. For any specific electrochemical reaction at equilibrium, we must have:

$$\sum_i \nu_i \overline{\mu_i} = 0 \tag{A.3}$$

Therefore, Equation (A.1) becomes

$$\begin{aligned} \nu_{\mathrm{A}}(\mu_{\mathrm{A}} + z_{\mathrm{A}} F \phi_{\mathrm{S}}) + \nu_{\mathrm{B}}(\mu_{\mathrm{B}} + z_{\mathrm{B}} F \phi_{\mathrm{S}}) + \ldots + (\mu_e + F\phi_{\mathrm{M}}) \\ = \nu_{\mathrm{C}}(\mu_{\mathrm{C}} + z_{\mathrm{C}} F \phi_{\mathrm{S}}) + \nu_{\mathrm{D}}(\mu_{\mathrm{D}} + z_{\mathrm{D}} F \phi_{\mathrm{S}}) + \ldots \end{aligned} \tag{A.4}$$

Here, the subscripts S and M attached to $\phi$ are abbreviations for 'solution' and 'metal' respectively. The conservation of electrical charge in Equation (A.1) requires:

$$\nu_{\mathrm{A}} z_{\mathrm{A}} + \nu_{\mathrm{B}} z_{\mathrm{B}} + \ldots - 1 = \nu_{\mathrm{C}} z_{\mathrm{C}} + \nu_{\mathrm{D}} z_{\mathrm{D}} + \ldots \tag{A.5}$$

By combining Equations (A.4) and (A.5), we have:

$$F(\phi_{\mathrm{M}} - \phi_{\mathrm{S}}) = \nu_{\mathrm{A}}\mu_{\mathrm{A}} + \nu_{\mathrm{B}}\mu_{\mathrm{B}} + \ldots - \nu_{\mathrm{C}}\mu_{\mathrm{C}} - \nu_{\mathrm{D}}\mu_{\mathrm{D}} + \mu_{\mathrm{e}^-} \tag{A.6}$$

In addition, the chemical potential of species $i$ is given by:

$$\mu_i = \mu_i^{\ominus} + RT \ln a_i \tag{A.7}$$

in which $a_i$ represents activity of species $i$ in solution (in the gas phase, $a_i$ should be the fugacity $f_i$ instead ). Substituting (A.7) to (A.6) gives

$$F(\phi_{\mathrm{M}} - \phi_{\mathrm{S}}) = F\Delta\phi^{\ominus} + RT(\nu_{\mathrm{A}} \ln a_{\mathrm{A}} + \nu_{\mathrm{B}} \ln a_{\mathrm{B}} + \ldots - \nu_{\mathrm{C}} \ln a_{\mathrm{C}} - \nu_{\mathrm{D}} \ln a_{\mathrm{D}} - \ldots) \tag{A.8}$$

or

$$\phi_{\mathrm{M}} - \phi_{\mathrm{S}} = \Delta\phi^{\ominus} + \frac{RT}{F} \ln \left\{ \frac{a_{\mathrm{A}}^{\nu_{\mathrm{A}}} a_{\mathrm{B}}^{\nu_{\mathrm{B}}} \ldots}{a_{\mathrm{C}}^{\nu_{\mathrm{C}}} a_{\mathrm{D}}^{\nu_{\mathrm{D}}} \ldots} \right\} \tag{A.9}$$

This is the general expression of the Nernst equation, in which the term

$$F\Delta\phi^{\ominus} = (\nu_{\mathrm{A}}\mu_{\mathrm{A}}^{\ominus} + \nu_{\mathrm{B}}\mu_{\mathrm{B}}^{\ominus}) + \ldots - (\nu_{\mathrm{C}}\mu_{\mathrm{C}}^{\ominus} + \nu_{\mathrm{D}}\mu_{\mathrm{D}}^{\ominus}) + \mu_{\mathrm{e}^-} \tag{A.10}$$

is a constant, provided the temperature and pressure are constant.

Relevant reading materials and analyses in depth are available in the attached references.[295, 297, 298]

# B Quantification of Non-Turnover Signal

The electrode process of the electroactive enzyme molecules adsorbed upon the electrode can take the form:

$$\mathrm{Ox} + n\mathrm{e}^- \rightleftharpoons \mathrm{Red} \tag{B.1}$$

where $n$ electrons are transferred between the interconversion of the reduced and oxidised form of the enzyme. During the measurement of cyclic voltammetry, considering the situation that electron transfer between the electrode and enzyme is fast, equilibrium is instantaneously approached soon after the potential is swept to a

new value; thus the reaction is Nernstian and can be expressed by:

$$E = E^{\ominus'} - \frac{RT}{nF} \ln \frac{\Gamma_{\text{Red}}}{\Gamma_{\text{Ox}}} \tag{B.2}$$

where $E$ is the electrode potential, $E^{\ominus'}$ is the formal potential, $R$ is the gas constant, $F$ is the Faraday constant, and $\Gamma_{\text{Red}}$ and $\Gamma_{\text{Ox}}$ refer to the surface coverage of the adsorbed enzyme in reduced and oxidised form. The current resulting from such an equilibrium is proportional to the rate of change in either oxidised or reduced form:

$$I = nFA\frac{\mathrm{d}\Gamma_{\text{Ox}}}{\mathrm{d}t} = -nFA\frac{\mathrm{d}\Gamma_{\text{Red}}}{\mathrm{d}t} \tag{B.3}$$

Assuming the total quantify of the adsorbed enzyme $\Gamma_0^*$ stays fixed throughout, we have:

$$\Gamma_0^* = \Gamma_{\text{Red}} + \Gamma_{\text{Ox}} \tag{B.4}$$

substituting which to (B.2) with algebraic rearrangement leads to:

$$\frac{\Gamma_{\text{Red}}}{\Gamma_{\text{Ox}}} = \frac{\Gamma_{\text{Red}}}{\Gamma_0^* - \Gamma_{\text{Red}}} = exp\left[-\frac{nF}{RT}(E - E^{\ominus'})\right] \tag{B.5}$$

After combining like terms in (B.5), we have:

$$\Gamma_{\text{Red}} = \frac{\Gamma_0^*}{1 + exp\left[\frac{nF}{RT}(E - E^{\ominus'})\right]} \tag{B.6}$$

and also:

$$\Gamma_{\text{Ox}} = \frac{\Gamma_0^* exp\left[\frac{nF}{RT}(E - E^{\ominus'})\right]}{1 + exp\left[\frac{nF}{RT}(E - E^{\ominus'})\right]} \tag{B.7}$$

Substituting results from either (B.6) or (B.7) into (B.3) yields:

$$I = \frac{n^2F^2A\Gamma_0^*}{RT} \frac{exp\left[\frac{nF}{RT}(E - E^{\ominus'})\right]}{\left\{1 + exp\left[\frac{nF}{RT}(E - E^{\ominus'})\right]\right\}^2} \frac{\mathrm{d}E}{\mathrm{d}t} \tag{B.8}$$

where the term $\frac{\mathrm{d}E}{\mathrm{d}t}$, also written as $\nu$, is the rate of potential change, *i.e.* the scan rate in cyclic voltammetry. We rewrite Equation (B.8) as:

$$I = \frac{n^2F^2A\Gamma_0^*\nu}{RT}\frac{exp\left[\frac{nF}{RT}(E-E^{\ominus'})\right]}{\left\{1+exp\left[\frac{nF}{RT}(E-E^{\ominus'})\right]\right\}^2} \tag{B.9}$$

and considering the fact that in cyclic voltammetry, $\nu$ is a constant, to get the peak current $I_\mathrm{p}$, we take the first derivative of $I$ against $E$, *i.e.* $\frac{\mathrm{d}I}{\mathrm{d}E}$. Then we determine the stationary point where $\frac{\mathrm{d}I}{\mathrm{d}E} = 0$ and get:

$$E_\mathrm{p} = E^{\ominus'} \tag{B.10}$$

$$I_\mathrm{p} = \frac{n^2F^2A\Gamma_0^*\nu}{4RT} \tag{B.11}$$

Moreover, the total charge passed $Q$ due to non-turnover signal of adsorbed enzymes can be expressed as:

$$Q = \int I\ \mathrm{d}t = \int \left(\frac{\mathrm{d}t}{\mathrm{d}E}\right) I\ \mathrm{d}E = \frac{1}{\nu}\int I\ \mathrm{d}E \tag{B.12}$$

Actually, the term $\int I\ \mathrm{d}E$ is the area under the redox peak in the cyclic voltammogram. By integrating B.12 using the expression in (B.9), we obtain:

$$Q = nFA\Gamma_0^* = \frac{\text{Integration Area}}{\nu} \tag{B.13}$$

through which we can determine $\Gamma_0^*$.

Relevant reading materials and analyses in depth are available in the attached references.[294, 309]

# C Derivation of Michaelis-Menten Equation

The model can be expressed as the following relation:[302]

$$\mathrm{S} + \mathrm{E} \underset{k_{-1}}{\overset{k_1}{\rightleftharpoons}} \mathrm{ES} \underset{k_{-2}}{\overset{k_2}{\rightleftharpoons}} \mathrm{P} + \mathrm{E} \tag{C.1}$$

Here, an enzyme binds with substrate S and forms an ES complex, with $k_1$ and $k_{-1}$ as the forward and reverse rate constants respectively. Catalysis continues until

the formation of product P and the release of the enzyme E. Also, this process is reversible with rate constants $k_2$ and $k_{-2}$. When time closes zero, we can simply consider there is no back reaction from E + P to ES ($k_{-2}$[P][E] $\approx 0$). Thus, we have:

$$\mathrm{S} + \mathrm{E} \underset{k_{-1}}{\overset{k_1}{\rightleftharpoons}} \mathrm{ES} \overset{k_2}{\rightleftharpoons} \mathrm{P} + \mathrm{E} \tag{C.2}$$

The initial catalytic rate $v_0$ is the rate of product formation when [P] is relatively small. This is written as:

$$v_0 = (\frac{\mathrm{d[P]}}{\mathrm{d}t})_0 = k_2[\mathrm{ES}] \tag{C.3}$$

The initial concentration of the enzyme, $\mathrm{E}_0$, can be expressed as:

$$[\mathrm{E}]_0 = [\mathrm{E}] + [\mathrm{ES}] \tag{C.4}$$

Considering a quasi steady state at which the intermediate concentration [ES] keeps constant, we have:

$$\frac{\mathrm{d[ES]}}{\mathrm{d}t} = k_1[\mathrm{E}][\mathrm{S}] - k_{-1}[\mathrm{ES}] - k_2[\mathrm{ES}] = 0 \tag{C.5}$$

After combining like terms, we have:

$$[\mathrm{ES}] = \frac{k_1[\mathrm{E}][\mathrm{S}]}{k_2 + k_{-1}} \tag{C.6}$$

It should be mentioned that in (C.6), only $[\mathrm{E}]_0$ is fixed; therefore we need to express [ES] as the function of $[\mathrm{E}]_0$. Substituting (C.4) into (C.6), we have:

$$[\mathrm{ES}] = \frac{k_1[\mathrm{E}]_0[\mathrm{S}]}{(k_{-1} + k_2) + k_1[\mathrm{S}]} \tag{C.7}$$

We next define the maximum catalytic rate $v_{\max}$ as:

$$v_{\max} = k_2[\mathrm{E}]_0 \tag{C.8}$$

and the Michaelis constant $K_{\mathrm{m}}$ as:

$$K_{\mathrm{m}} = \frac{k_{-1} + k_2}{k_1} \tag{C.9}$$

After combining (C.7), (C.8), and (C.9), the enzyme-catalysed reaction rate can be expressed as:

$$v_0 = \frac{v_{\mathrm{m}}}{K_{\mathrm{m}} + [\mathrm{S}]} \tag{C.10}$$

Equation (C.10) is the well-known Michaelis-Menten equation.

Relevant reading materials and analyses in depth are available in the attached references.[302, 310]